# INFLUENCE OF HYDRODYNAMICS ON CONTROLLING ALGAL GROWTH IN THE YTHAN ESTUARY, SCOTLAND

**KHRUEWAN CHAMPANGERN**

**MA**

SUBMITTED IN FULFILMENT OF REQUIREMENTS FOR THE DEGREE OF DOCTOR PHILOSOPHY

FEBRUARY 2019


SCHOOL OF GEOGRAPHICAL AND EARTH SCIENCES

COLLEGE OF SCIENCE AND ENGINEERING

UNIVERSITY OF GLASGOW

SUPERVISED BY

PROF. TREVOR HOEY, DR. RHIAN THOMAS, AND DR. EDWARD MITCHARD

# Declaration

The contents of this thesis are results of my own work except where material from other sources has been fully acknowledged. The thesis has not been submitted for any other degree at the university of Glasgow or any other institutes. The views and opinions are mine and not necessary those of any other person or organisation unless attributed.

Khruewan Champangern

February 2019

# Abstract

KEYWORDS: Eutrophication, River Ythan estuary, Algal mats, Delft3D hydraulic model, Hydrodynamics, Remote Sensing

The estuary of the River Ythan, North-East Scotland, UK, is a Site of Special Scientific Interest (SSSI) located in Forvie National Nature Reserve (NNR) and listed under the Ramsar Convention on Wetlands of International Importance. This site has long been affected by eutrophication despite designation as a nitrate vulnerable zone (NVZ) under the EU Nitrates Directive (ND) in 2000. Annual proliferation of macroalgal mats in the estuary results in decreases in the number of the invertebrates, major food sources for terns, waders and wildfowl, which causes a serious ecological problem in the estuary. It is critical to understand water circulation in the estuary in response to river flows and tides, to assess the role of hydrodynamics on controlling nutrient movement and the distribution and density of annual macroalgal blooms. This understanding will contribute a deeper knowledge of estuarine eutrophication for use in developing management strategies and mitigation measures. This study aims to understand the role of hydrodynamics on controlling annual macroalgal mat formation in the Ythan estuary by simulating water circulation, nutrient concentrations and pathways in the estuary using the Delft3D model. In addition, the study aims to evaluate potential of using remote sensing data for aiding model calibration and validation.

The results from the study reveal that hydrodynamics play a key role in controlling macroalgal growth in the estuary. Interaction between seasonal river flows and tides not only helps to create optimal water quality conditions which facilitate algal growth, but also influences nutrient movements across the estuary resulting in high nutrient availability in particular areas. In addition to hydrodynamics, tributary inflows and the timing of nutrient release from these tributaries impact nutrient concentrations and transport directions in the areas surrounding their input to the estuary. Areas of high nutrient availability coupled with low flow velocities (lower than 0.06 m/s) particularly on mudflats along the main channel, driven by interactions of river flow, tides and bed characteristics, have long durations of nutrient enrichment, and so much of the Ythan estuary is prone to eutrophication. As hydrodynamics along with the timing of nutrient inputs play

key roles in controlling macroalgal growth, strategies and mitigation measures to modify hydrodynamics to prevent long residence time are required, as well as guidelines on the timing of release of wastewater from tributaries. The study also demonstrates advantages of using remote sensing in conjunction with modelling studies. Remote sensing data are very valuable for model calibration and validation as well as for estuarine ecological management to study impacts of eutrophication and other disturbances.

# Table of Contents

# List of Figures

# List of Tables

# Acknowledgements

First and foremost, I would like to thank my supervisor, Professor Trevor Hoey, for his continuous support and guidance throughout my research work. He has always given his deep insights and put in effort for the benefit of this thesis. He is my mentor and a better supervisor for my PhD study beyond the imagination. Apart from my supervisor, I will not forget to express the gratitude to rest of the team: Dr. Rhian Thomas and Dr. Edward Mitchard for giving encouragement and sharing helpful comments. I would also like to sincerely thank my thesis committee members, Dr. Helene Burningham and Dr. Brian Barrett not only for their time and extreme patience, but for their invaluable intellectual contributions to help me improve this thesis, which I have gladly embraced.

Very special thanks go to Ministry of Science and Technology of Thailand for giving me the opportunity to carry out my doctoral research and for their financial support. My sincere thanks also go to GISTDA for Worldview-2 data, SEPA (Susan Stevens, Kirsten Gray, Clare Scanlan, Matthew Blackburn) for providing remote sensing and water quality data and for sample collection, Oceanlab (Stewart Chalmers) for advice and support for fieldwork, Kenneth Roberts, Thomas Lachendro, and Charlie Gilles for fieldwork assistance and sediment analysis data. I thank my fellow graduate students particularly Julia Stockamp, Ning An, Julius Mngumi, Charlie Gilles, and Shahmy Said for being great companions and for the fun-time we spent together in Glasgow.

Finally, and most importantly, my loves and heartfelt thanks go to my family: my parents, my aunt, my brother, and Wissawa Jenjob for supporting me physically and spiritually throughout my study and my life in general. They are the most important people in my world, and I dedicate this thesis to them.

# Chapter 1: Introduction

Estuaries have long been important to humans and both terrestrial and marine flora and fauna. The majority of large cities globally are located on estuaries and the coast (Cracknell, 1999, Wolanski and Elliott, 2016). They have been popular areas for urban development because they provide economic benefits such as transport routes, tourism and recreational activities as well as high levels of food production from their high biological productivity (Wolanski et al., 2004). Estuaries are also important and diverse habitats that provide a unique ecosystem for plants, birds, mammals, fish, and other living organisms such as microbes, plankton, benthic flora and fauna, and nekton to live, feed, and reproduce (Kennish, 2002, McLusky et al., 2004).

Estuaries receive inflows of fresh water and sediment from their catchments and saltwater from the sea (Wolanski and Elliott, 2016). Increases in the demands for water and land from urban, industrial, and agricultural developments to serve rapid human population growth put many estuaries under pressure (McLusky et al., 2004). The development of towns and cities along with changes in agricultural practices leads to a large amount of municipal and industrial effluents and increased nutrients, in particular nitrogen (N) and phosphorus (P), in many estuaries (Nedwell et al., 2002). Excess nutrients from industries and the use of fertilizers which lead to eutrophication is one of main threats to the environmental future of estuaries (De Jonge et al., 2002, Kennish, 2002).

## 1.1 Eutrophication in estuaries

Eutrophication has been described by Schramm and Nienhuis (1996) as "…the process of natural or man-made enrichment with nutrient elements, mainly N and P, beyond the maximum critical level of the self-regulatory capacity of a given system for a balanced flow and cycling of nutrients". They also define hypertrophication (nutrient pollution) as "…over-enrichment or excess supply of nutrients beyond the maximum critical self-regulatory level to an extent that detrimental processes cause irreversible changes in aquatic communities, as long as nutrient levels are not reduced". According to Smith et al. (1999), coastal marine waters which are in a eutrophic condition usually have either large supply of the sum parameter of all organic and inorganic nitrogen compounds (total

nitrogen, TN), of 350-400 ($mg.m^{-3}$) or chlorophyll a (Chl-a) of 3-5 ($mg.m^{-3}$). Whilst under hypertrophic conditions, TN is higher than 400 ($mg.m^{-3}$) and Chl-a is greater than 5 ($mg.m^{-3}$). Those locations having TN lower than 260 ($mg.m^{-3}$) or having Chl-a less than 1 ($mg.m^{-3}$) are categorised as having normal water conditions (Oligotrophic conditions).

Nutrients transported from catchments into estuaries that accelerate eutrophication are usually either in form of suspended sediment or water soluble forms of nitrite ($NO_2^-$), nitrate ($NO_3^-$), ammonium ($NH_4^+$), and phosphate ($PO_{43}^-$) (Yin and Harrison, 2000). In addition to these anthropogenic nutrients, $NH_4^+$ and $NO_3^-$, the preferred forms of nutrients for phytoplankton can be produced naturally in estuaries by bacteria living in the water through nitrogen fixation, nitrification, and decomposition processes. Moreover, the bacteria can generate P from waste or death of living organism into $PO_{43-}$, which is also a preferable food source for algae (Yin and Harrison, 2000).

A common symptom of eutrophication in estuaries is rapid increase in production of algae (Smith et al., 1999, Young et al., 1999), which eventually results in reduction of dissolved oxygen (DO) due to decomposition of dead algae by bacteria. Significant decrease in dissolved oxygen leads to hypoxia (DO < 2 mg/l) and anoxia (DO = 0). During hypoxia living organisms are stressed and will seek to move away. Some of those that cannot or do not manage to leave will die when the water reaches anoxic conditions (Wolanski and Elliott, 2016). In addition to causing reduction of DO, overabundance of floating algae hinders light penetration to water column causing decline of aquatic plants (Wolanski and Elliott, 2016). These algae also generate unpleasant odour in water, and the accumulation of foam and scum on water surface, which reduces recreational and commercial values of estuaries (Wolanski and Elliott, 2016).

Eutrophication in estuaries also leads to large macroalgal blooms forming on sediments of intertidal zones in particular *Ulva, Enterotnorpha, Cladophora and Chaetomorpha* species (Jones and Pinn, 2006, Lavery and McComb, 1991).These fast growing macroalgae usually dominate blooms on mudflats of intertidal zones as they can take up nutrients, particularly nitrate and phosphate, 4-6 times faster than slower growing species (Pederson and Borum, 1997). Although macroalgae are commonly found on intertidal mudflats (Jones and Pinn, 2006), the large blooms that occur during periods of high nutrient levels in estuaries produce the

most dramatic effects on estuarine systems (Jones and Pinn, 2006, Martins et al., 2001, Raffaelli, 1999, Taylor, 1999).The presence of large algal mats also hinders wading birds reaching their prey (Jones and Pinn, 2006, Wolanski and Elliott, 2016). In addition, the macroalgal blooms affect populations of benthic micro algae or microphytobenthos (MPB), a primary producer that supports other living organisms living in the mudflats (Underwood, 2010). As a result, there is a reduction of the food source for higher consumers in estuarine food webs as well as decreased physical stability of mudflat sediments (Underwood, 2010). Decomposition of macroalgae by bacteria and large amounts of organic matter underneath the mats leads to the development of hypoxic and anoxic conditions in sediments, which results in a reduction in benthic invertebrate communities (Lavery and McComb, 1991, Wolanski and Elliott, 2016). As a result predators, including both birds and fish, higher in the food chain lose their feeding areas (Lavery and McComb, 1991, Jones and Pinn, 2006).

Eutrophication is a major water quality concern worldwide (Wolanski et al., 2004). Globally, 415 hypoxic and eutrophic coastal systems were identified by Selman et al. (2010). The highest densities of hypoxic coastal systems are found along the coastlines of North America, Europe, and the East China Sea where are areas of very high population density, whilst eutrophic coastal systems are found along coastlines throughout the world (Figure 1-1). The global spatial pattern of eutrophic/hypoxic waters reflects the susceptibility of estuarine and coastal environments to nutrient loading resulting from anthropogenic impacts. High population density leads to greater eutrophication problems compared with areas of low density population. However, in low population density areas that have intensive agricultural activities, eutrophication can be significant, as seen in some areas of Eastern Baltic Sea and East Africa (Figure 1-1).

Some estuaries in high population density areas are in recovery, particularly in North America, Europe, and the east of Australia (Figure 1-1). This suggests that awareness, control, and management of eutrophication problems have been applied to those areas. However, only a small proportion of the degraded systems worldwide have seen successful recovery. Thus, more attention and greater understanding of eutrophication problems is still required. In Europe, there are 168 eutrophic and hypoxic coastal areas with 106 further areas of concern.

In the UK, several estuaries have increased N and P concentrations, resulting in high levels of chlorophyll-a and abundant algal communities. The main sources of nutrients to estuaries, including agriculture fertilizers and sewage discharges, reach estuaries through river runoff and, in some cases, groundwater (Maier et al., 2009). Since the introduction of the EU Nitrates Directive (1991; 91/676/EEC) intended to reduce water pollution caused by nitrates from agricultural land, only slight changes in N loads have been documented (Maier et al., 2009). Hypoxic coastal areas in the UK can still be found in Southwest England, Northeast England, West of Scotland, and North-Eastern Scotland, whilst some of the coastal estuarine systems located in Northwest England, and Central West Coast and Central East Coast Scotland are in recovered status (Figure 1-2).

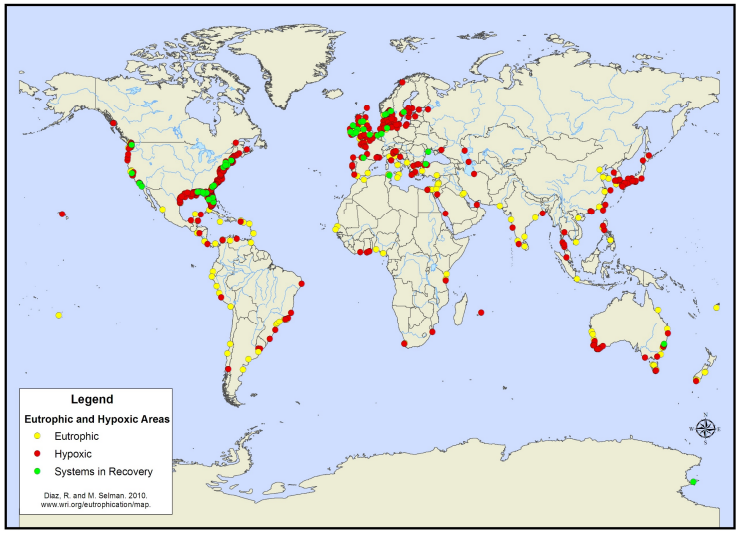


**Figure 1-1:** World hypoxic and eutrophic coastal areas in 2010 (Selman et al., 2010)

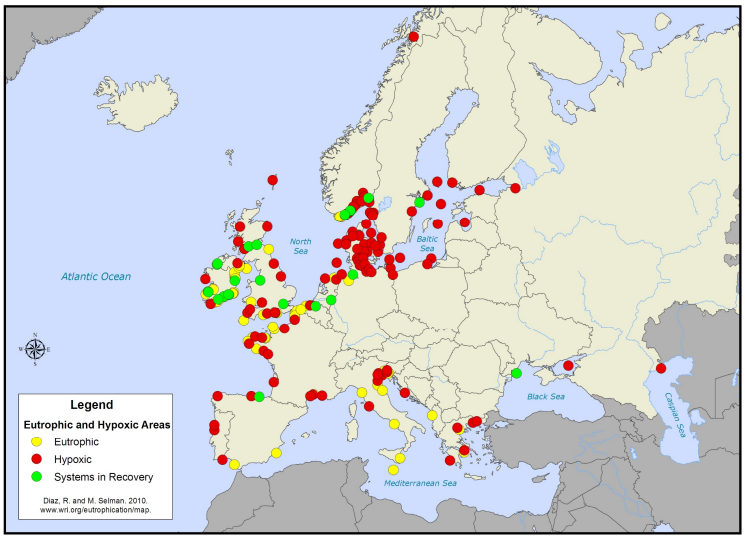


**Figure 1-2:** Coastal eutrophic and hypoxic areas of Europe in 2010 (Selman et al., 2010)

## 1.2 Eutrophication in the Ythan estuary, Scotland

### 1.2.1 Site introduction

The Ythan estuary (2.00°W, 57.34°N), located in a 690 $km^2$ intensive arable catchment in Aberdeenshire on the northeast coast of Scotland, is the study site for this project. It is a small estuary, with an area of approximately 6.82 $km^2$ (Flemming, 2011), and is 11 km long from the small town of Ellon to the river mouth at the North Sea. The estuary is elongated and shallow with an average water depth along the main channel of 2.2 m. Average width is 300 m, with a maximum of 620 m at the Sleek of Tarty (Baird and Milne, 1981, Balls et al., 1995, Leach, 1971, Raffaelli, 1999) (Figure 1-3).

The Ythan is the focus of this study as it is rich in aquatic and terrestrial life and is designated as a Site of Special Scientific Interest (SSSI) (Taylor, 1999). In addition, much of the estuary lies in Forvie National Nature Reserve (NNR) and is listed under the Ramsar Convention on Wetlands of International Importance (Nature.scot, 2009). However, the estuary has had long term eutrophication since the 1990s. As it is home to the largest breeding colony of eiders in Britain, four species of breeding terns and many wildfowl and waders (Nature.scot, 2009), the observed prolific growth of algal mats on mudflats (Figure 1-4) is a serious and damaging ecological problem.

Algal growth causes mortality among the invertebrates that live in the mudflats and consequent reductions of bird and fish populations that inhabit the estuary (Raffaelli, 1999, Soulsby et al., 1982, Taylor, 1999). According to Nature.scot (2009), green macroalgal blooms forming mat-like surfaces have caused drastic decreases in the number of the invertebrates such as *Corophium* (mud shrimps), a major food for waders, especially redshank and shelduck, in this estuary. At the present, the Ythan estuary is within a regional Nitrate Vulnerable Zone (NVZ) (Figure 1-5) where long-term management activities to address the eutrophication, problem have been implemented. The Ythan is a good case study for understanding the causes of, and potential solutions to, the eutrophication problem in estuaries with small population and extensive agricultural catchments. Insights from this study can be applied to other estuarine systems with similar characteristics and issues.


**Figure 1-3:** Worldview image acquired on 20 April 2015 showing the Ythan Estuary, Aberdeenshire, Scotland and water quality buoy and river flow measuring station locations; inset showing the Ythan estuary location (red box) and Nitrate Vulnerable Zone (NVZ) (blue area).


**Figure 1-4:** Macro algal mats developed on mudflats in the upper estuary (A) and at the estuary mouth (B); images taken during field work in 2014.

### 1.2.2 Current strategies for eutrophication management

Present understanding is that nitrogen is the most plausible causal factor exacerbating algal growth in the Ythan (Edwards et al., 2003). As a result, the strategies and policies for dealing with eutrophication in the Ythan are based on preventing and controlling the loss of nitrogen to watercourses. The action programme is being implemented within is the framework provided by designation of a nitrate vulnerable zone (NVZ). The Ythan estuary has been designated as a NVZ since 2000 under the EU Nitrates Directive (ND).

The purpose of designation of the NVZ is to protect human health and living resources from surface water and groundwater pollution caused by agricultural practices. The measures, known as an Action Programme, have been implemented in the NVZ to minimise diffuse pollution (substances contributing to eutrophication, in particular $NO_3^-$ and $PO_{43}^-$) from the storage and application of fertilisers, keeping of livestock, cultivation of land, application of pesticides, and operating sheep dipping facilities. According to Gov.scot (2008), the measures include limiting livestock manure loading at 170 kg N/ha, limits on the time and place for the storage of solid manure (heaps cannot remain in the same place more than 12 months and cannot return to the same place until at least 24 months have passed), no use of a slurry high trajectory splash plate spreaders, no use of nitrogen fertiliser in waterlogged soils, on soils frozen for longer than 12-hours or on flooded land, no use of chemical nitrogen fertilisers during a period from 15th September to 20th February, and no use of organic manures (1st September to 31st December for shallow or sandy soils; 15th October to 31st January for all other soils). Full lists of the action programme in the NVZ can be seen in Guidelines for Farmers in Nitrate Vulnerable Zones available on the Scottish Government web site and full lists of the regulations to control the diffuse pollution are available on the Farming and Water Scotland website.

Under the action programme, the Scottish Government carries out a review of the NVZs to inspect water quality status at least every 4 years (Gov.scot, 2008). The review reports in 2009 and 2013 showed that the application of chemical nitrogen fertilisers in the NVZ had decreased significantly. There was a 42% reduction from 113 kg N/ha applied to grass in 2001 to 66 kg N/ha in 2008, and a 24% reduction from 147 kg N/ha (2001) to 111 kg N/ha (2008) to tillage crops. Similar reductions were also found in use of chemical phosphate fertilisers. The reports also found improvements in the use manures and slurry, which became more efficiently used as a resource rather than a waste. As a result, losses of manures and slurry to watercourses decreased. In addition, only a few watercourses were found to have nitrate concentrations as high as 40 mg/l. However, the nitrate concentrations in ground waters, which are most likely to be contaminated by slurry seepage, have not shown overall improvement and the abundance of macroalgal mats in the Ythan estuary annually has remained. Thus, no changes to the current NVZ

boundary, which includes the Ythan estuary, were proposed in the latest review (Gov.scot, 2015b).

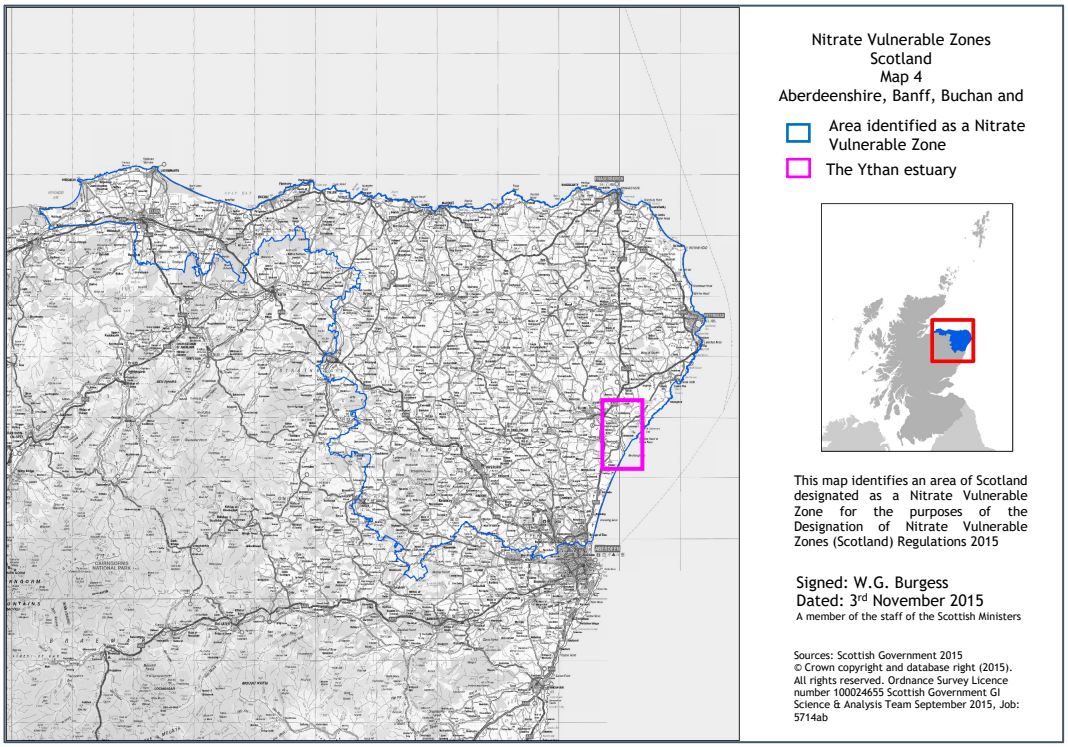


**Figure 1-5:** Nitrate Vulnerable Zone boundary, covering Aberdeenshire, Banff, Buchan, and Moray, modified from Gov.scot (2015a).

### 1.2.3 Previous studies into eutrophication

Many studies have been carried out in the Ythan estuary to identify the causes and effects of eutrophication so that the most suitable solutions can be put in place. However, specific causes of the locations and densities of macroalgal blooms and the mechanisms involved have not been fully identified. This section reviews previous studies to provide more specific information related to eutrophication in the Ythan, and identifies the knowledge gaps that this project seeks to address.

Green macroalgal blooms have been reported during summers since 1954 in the Ythan (Raffaelli, 1999, Taylor, 1999). *Enteromorpha spp.*, *Chaetomorpha Linum*, and *Ulva Lactuca* are mainly green macroalgal that develop on intertidal mudflats in the estuary (Raffaelli, 1999). They typically begin to grow in spring and reach their highest biomass from summer to the beginning of autumn (Raffaelli, 1999, Taylor, 1999). Although there is evidence of green macroalgal blooms since the 1950s, a significant increase in the blooms has been found since the 1990s, by when catchment land use had changed to high nitrogen demand crops such as wheat, barley, and oilseed rape (Raffaelli, 1999).

Figure 1-6 shows the much greater abundance of algal mats from 1986-1997 compared to baseline data from 1954 and 1969, with the exception of low macro algal cover in 1996 due to flooding in winter 1995/6. The flood event was likely to have removed nutrients and dead algae from the estuary resulting in a dramatic decrease in algal growth in the following season (Raffaelli, 1999). The areas covered by algal mats correspond with increased areas of wheat and oil seed rape in the catchment from 1985 to 1990, and barley plantation from 1960 to 1990 (Figure 1-7).

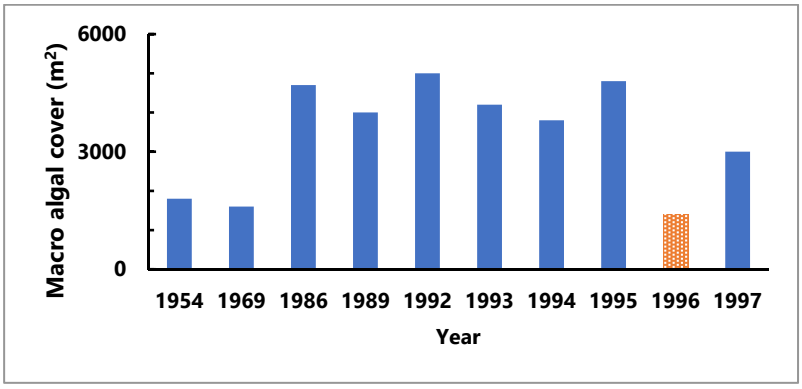


Figure 1-7: Area covered by macro algal mats (density > 1 kg.m$^{-2}$) on mudflats from 1954-1997, modified from Raffaelli (1999).

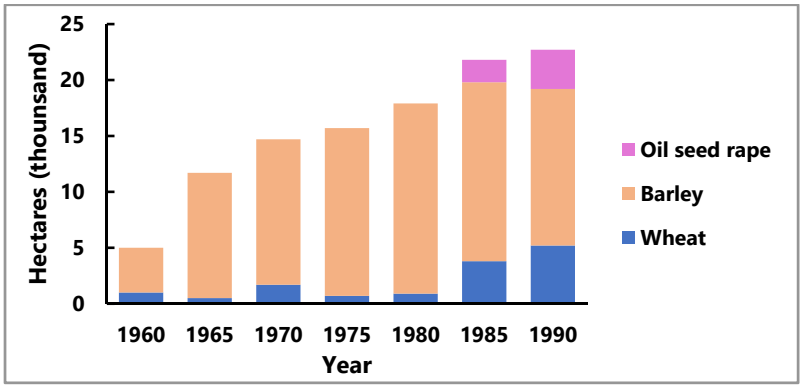


Figure 1-6: Changes of land use in the Ythan catchment, modified from Raffaelli (1999).

The changes of land use were also in accordance with increasing trends of the concentration and loads of total nitrite and nitrate nitrogen input (total oxidised nitrogen, TON) from the river to the estuary (Figure 1-8A). Comparing TON to salinity at different locations in the estuary during high tide, TON concentrations in the 1990s were significantly greater than in the 1960s (Figure 1-8B).

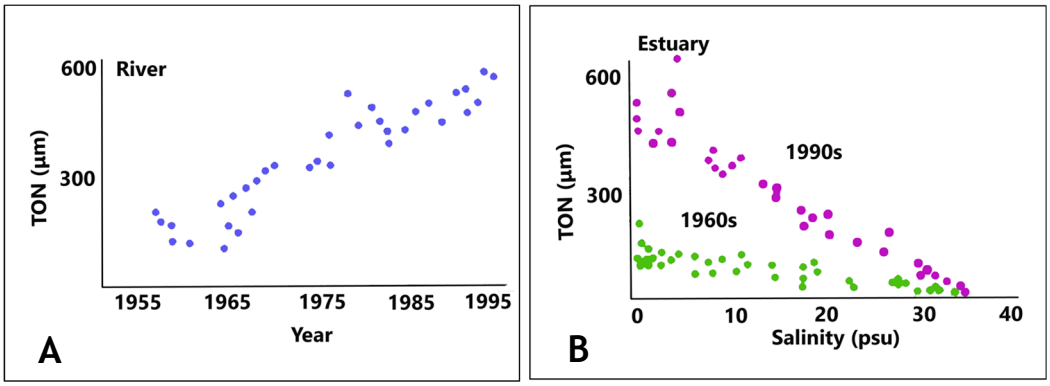


**Figure 1-8:** Trends in TON concentrations in the Ythan river (A) and in the estuary (B), modified from Raffaelli (1999).

According to Pugh (1998) and Raffaelli (1999), during the 1990s nutrient inputs to the estuary were predominantly from agricultural lands (95% of N) (Table 1-1), with domestic sewage treatment works from two towns, Ellon and Newburgh, close to the estuary contributing less than 5% (Table 1-1).

**Table 1-1:** Nitrogen loadings (tonnes.yr$^{-1}$) to the estuary from riverine input and two domestic sewage works located at the head of the estuary (Ellon) and west of the estuary (Newburgh). Data from Pugh (1998) and modified from Raffaelli (1999).

| Source of N input | N load (tonnes.yr-$^{1}$) |
|---|---|
| River | 2000 |
| Sewage from Ellon | 40 |
| Sewage from Newburgh | 4 |

No significant change in P inputs has been recorded over 30-40 years (Raffaelli, 1999). These figures suggest that increases in N inputs, which are more likely to be associated changing agricultural activities in the catchment, provide the nutrients that lead to elevated macroalgal bloom extent in the estuary (Raffaelli, 1999, Raffaelli, 2000). Supporting this reasoning is the unusual occurrence of extensive macroalgal mats at the head of the estuary which is mostly affected by fresh river water inputs (Raffaelli et al., 1999).

Even though N inputs from the river seems to be the cause of increased macroalgal blooms in this estuary, seasonal variation of nutrients from riverine inputs makes

the relation between nutrient supply and macroalgal development contentious. Lyons et al. (1993) found that high loads of $NO_3$-N usually occurred in winter and autumn then greatly reduced during spring and summer when macroalgae begin to grow and reach their peak blooms with the highest biomass (Balls et al., 1995, Edwards et al., 2003, Maier et al., 2009, Raffaelli, 1999). During the periods with highest loads of $NO_3$-N (late autumn to winter), there have been no reports of extensive macroalgal blooms. This pattern could be explained by unsuitable autumn conditions such as high turbidity, low water and air temperature, short daylight hours and less sunlight penetration (Boyle et al., 2004, Kennish, 2002, Young et al., 1999). The abundance and growth of macroalgal mats found during spring-summer when nutrient inputs are lower (Raffaelli, 1999, Raffaelli et al., 1999, Taylor, 1999) indicates that the quantity of nutrients supplied from the river may not be the main cause of macroalgal growth during the growing season.

According to the review of the NVZ 2013 by the Scottish Gov.scot (2015a), a source of nutrients that may contribute to the annual occurrence of eutrophication in the estuary is groundwater. Apart from nutrient loading from riverine inputs, long term changes of climate, changes of estuary hydraulics due to change of bathymetry, and changes of sediment type are among the factors considered as potential causes of algal blooms in the estuary (Raffaelli et al., 1999). However, no casual links have been demonstrated between those factors and macro algal growth patterns (Raffaelli et al., 1999).

Long term trends of weather for the area show some changes of spring temperature which coincides with high algal biomass, but these temperature changes are not yet consistent over a long time period and cannot explain the observed long term trend of algal biomass (Raffaelli, 1999). In other estuaries, changes of hydrography as a result of topographic modification appear to impact algal biomass (Raffaelli et al., 1998). In the Ythan case, there is no historical record of channel maintenance, such as dredging that may affect water levels. In addition, mean water levels along the estuary, recorded in 1969 by Leach (1971) and in 1995 by Raffaelli (1999), show no significant change, which implies stability of the main channel since 1969. In this regard, exacerbation of macro algal blooms by hydrodynamic changes caused by channel modification is considered unlikely in the Ythan (Raffaelli et al., 1999). Sediment types were also inspected by Raffaelli et al. (1999) and compared with those recorded in 1960s by Anderson (1971), using

four broad categories including mud ( > 2 φ Phi scale), sand (0 to 2 φ), gravel (0 to -2 φ), pebbles and stones (< -2 φ). The results suggest no significant change of sediment types over the last 30 years (Raffaelli et al., 1999). However, sediment properties are closely related to the locations of macro algal blooms in the Ythan (Raffaelli et al., 1999). Sediment characteristics, specifically the abundance of organic matter in the sediments, could be significant as $NH_4^+$ and P found in organic matter generated from decomposition of buried macroalgae can support macro algal growth (Lavery and McComb, 1991, Raffaelli, 1999, Raffaelli et al., 1999). In addition, acting as both a source and a sink of N could enable sediments to have an important role in controlling macroalgal blooms in the Ythan (Lavery and McComb, 1991, Raffaelli, 1999, Raffaelli et al., 1999).

The presence of organic material within the sediments suggests that nutrients from this organic material may aid macroalgal growth during summer when river nutrient input is lowest. However, if this is a case the blooms should mainly be found in areas of fine sediments which appear to have the highest organic matter concentrations. Against this suggestion, coarse sediments (sand) with lower organic matter concentrations, particularly near the mouth of the estuary, are found to support macroalgal growth in all years (Lavery and McComb, 1991, Raffaelli, 1999, Raffaelli et al., 1999). Thus, it is not likely that nutrients from within the sediments alone support the blooms at the mouth of the estuary. The possibility that N from riverine inputs, ground water, and N derived from sediments further up the estuary and transported to the mouth by the interaction of freshwater and tides, exacerbates the blooms at the mouth of the Ythan is highly likely. The interaction of river flow with the tides would thus be a crucial mechanism controlling nutrient transport and hence macroalgae growth. In addition, there is evidence that flow velocity also controls macroalgae growth. Evidence for this is the decrease in macroalgal cover in 1996 after a major flood event occurred in winter 1995 (Raffaelli, 1999) (Figure 1-4). High flow velocity during the flood event flooded out nutrients and dead algae to the sea as a result of decrease in macroalgal cover in summer months 1996 (Raffaelli, 1999).

Although hydrodynamics has been studied extensively in many estuaries, there has been little work on this in the Ythan. Comprehension of hydrodynamics, in particular the interaction of fresh and sea water, flow velocity, and nutrient movement pathways may explain the presence of macroalgal blooms in this

estuary. In addition, understanding the hydrodynamics may lead to explanation of the role of other factors apart from nutrients, such as sunlight, temperature and biological processes (Kennish, 2002, Young et al., 1999) which have been widely recognised as important factors for eutrophication (Boyle et al., 2004, Kennish, 2002, Young et al., 1999). Figure 1-9 shows the range of important factors controlling estuary eutrophication, including salinity (Martins et al., 2001), stability of the water column, nutrients, water turbidity, and water residence time (Kennish, 2002, Martins et al., 2001, Su et al., 2004, Yin and Harrison, 2000, Zhang et al., 2015, Zhu et al., 2007) which have each been found to have either direct or indirect association with algal growth (Maier et al., 2012, Young et al., 1999). However, the importance of these factors vary according to the location, physical and environmental characteristics of estuaries, catchment size and land use, and climate (Kennish, 2002, Martins et al., 2001, Wallace and Gobler, 2015).

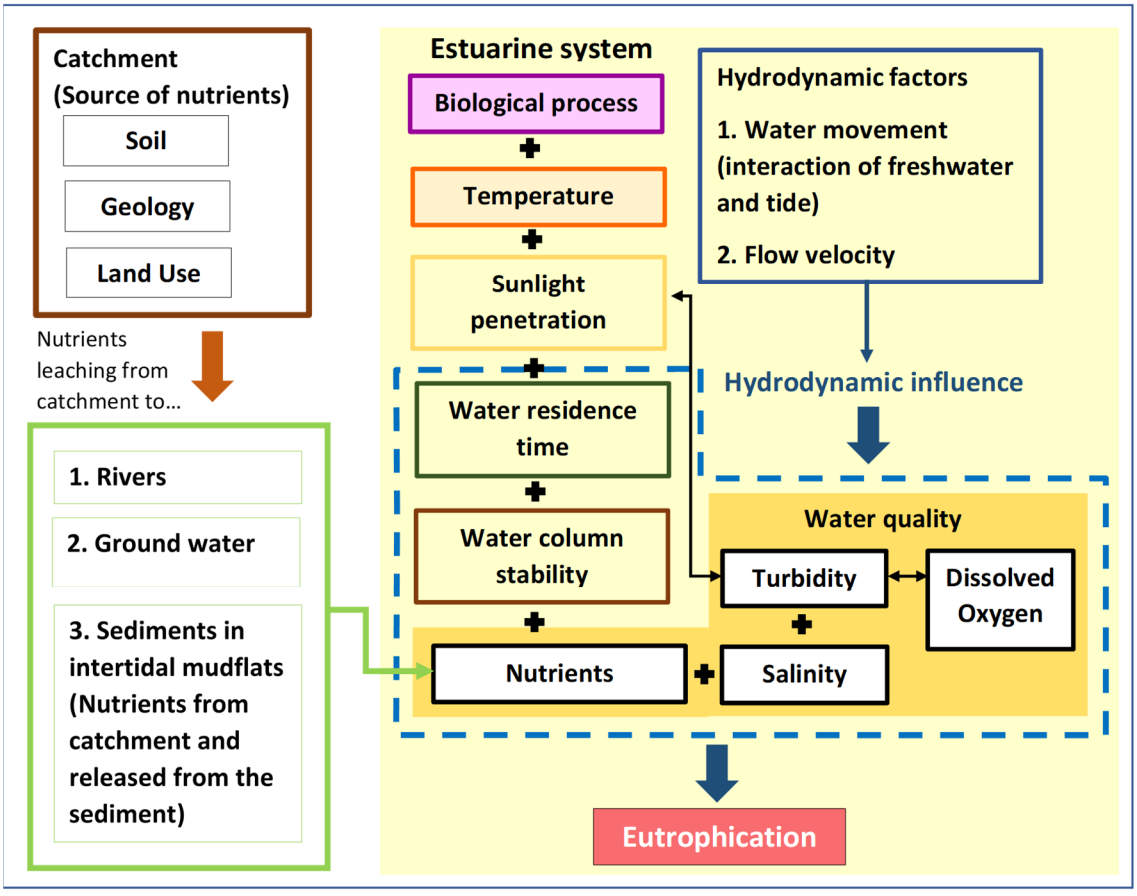


**Figure 1-9:** The factors controlling eutrophication and potential algal growth in estuaries.

## 1.3 Role of hydrodynamics in the estuary

Hydrodynamics estuaries are controlled by interactions between river discharge, tides, waves, currents, winds, temperature and precipitation as well as geomorphological factors such as estuary shape and bathymetry (Robins et al., 2016, Zou et al., 2016). The hydrodynamic interactions help to regulate nutrient fluxes and the transport of other pollutants (Robins et al., 2016, Tapia González et al., 2008, Zou et al., 2016). Importantly, hydrodynamics governs water residence times (Defne and Ganju, 2015). Bidirectional flows help nutrients and other pollutants to stay in the system as long as new waters renew, or mix with, old water that contains pollutants (Defne and Ganju, 2015). Poor flushing and long residence times, which are associated with small freshwater volumes and low tidal and wave forcing during summer months tend to retain nutrients within the system leading to eutrophication (Defne and Ganju, 2015, Martins et al., 2001, Tapia González et al., 2008). Conversely, efficient flushing and short residence times that result from increases in river flow and tidal energy particularly during late autumn and winter (Robins et al., 2016, Zou et al., 2016) lead to estuaries being more resilient to nutrient loading (Defne and Ganju, 2015, Martins et al., 2001, Tapia González et al., 2008).

In addition to reducing nutrient retention, effective flushing, which typically results from high flow velocities and turbulence, can reduce eutrophication symptoms as strong mixing and highly turbulent flows can rapidly oxygenate the entire water column and reduce eutrophication (Robins et al., 2016, Zou et al., 2016). High flow velocities can also release nutrients from sediments into the water column (Robins et al., 2016, Zou et al., 2016). Although this release increases nutrient availability, sediment instability, turbulence and high levels of turbidity in the water column prevent favourable conditions for algal growth (Jassby and Van Nieuwenhuyse, 2005, Martins et al., 2001, Robins et al., 2016, Zou et al., 2016). In contrast, stratified waters (fresh water overflowing denser sea water) usually develop when low river flow coincides with low tidal and wave energy which are more favourable conditions for algal growth (Jassby and Van Nieuwenhuyse, 2005).

Spatial and temporal variation of salinity is also influenced by the bidirectional flows of freshwater and sea water. Increased river flows move the limit of saline intrusion towards the estuary mouth, and potentially flushes nutrients and

pollutants out to sea (Martins et al., 2001). Conversely, low river flow enables salinity intrusion further into estuaries (Defne and Ganju, 2015). As tidal volume changes significantly every few hours and river flow changes over timescales form hours to days depending on the size of the river, it is possible that both well mixed water and strongly stratified water can occur simultaneously at different locations in an estuary (Defne and Ganju, 2015, Jassby and Van Nieuwenhuyse, 2005).

Estuarine hydrodynamics can also be strongly influenced by other factors including winds, waves and precipitation, each of which can affect mixing and circulation and can affect flushing times (Defne and Ganju, 2015). However in the UK, the influence of waves is generally minor as tidal energy is usually dissipated by either sand banks or bars at the mouths of estuaries (Robins et al., 2016). This suggests that within-estuary hydrodynamics are the main factor to be considered as causes for eutrophication. The hydrodynamics in the Ythan estuary have not been documented, and investigating these processes may help to explain long term patterns of macroalgal blooms in the estuary. The next section reviews previous studies of estuarine hydrodynamics emphasising hydrodynamic modelling approaches.

### 1.4 Previous studies into hydrodynamic modelling for estuarine studies

Estuarine hydrodynamics are complex due to interactions between tidal and river flows. Modelling to help understanding of estuarine hydrodynamics is needed to inform sustainable estuarine management. Several numerical models have been developed for, and applied to, estuarine studies (French, 2008). For instance, Duarte et al. (2002) estimated residence time, current velocity and salinity distribution under different scenarios using the DUFLOW model to help understand macroalgal growth in Mondeo estuary, Portugal. Ferrarin and Umgiesser (2005) used Shallow water Hydrodynamic Finite Element Model (SHYFEM) to simulate hydrodynamic circulations using forcing from river flow, tides, and wind to comprehend temporal salinity and temperature variations in the Cabras lagoon, Italy. Zhou et al. (2014) studied the impacts of construction of a barrage on salinity and water levels in the Severn estuary, UK using the Environmental Fluid Dynamics Code (EFCD). In the Ythan, simulation of saltwater and total oxidized nitrogen (TON) distributions under varying river flows using one-dimensional salt intrusion model developed by Gillibrand and Balls (1998) is the only known study of hydrodynamics. Gillibrand and Balls (1998) concluded that an increase

in freshwater discharge causes elevated TON concentrations. Among available hydrodynamic models, Delft3D is recognised as one of the most cost (time) effective and robust models (Deltares, 2017b, Hsu et al., 2006, Lesser et al., 2001, List et al., 2006). It can be used in two-or three-dimensions to simulate flow, transport, and biogeochemical process in estuaries, near shores, rivers and lakes. The model results are available in different formats for visualization and animation, some of which can be converted into different formats including GIS shapefiles (https://oss.deltares.nl/web/delft3d/about). The model has been successfully implemented in several estuarine studies around the world, specifically as it can be used to model pollutant transport (Baptistelli, 2015, Breemen, 2008, Brown et al., 2014, Cho et al., 2016, Fagherazzi et al., 2014, Hu et al., 2009, Williams et al., 2013, Zarzuelo et al., 2017).

For example, Delft3D FLOW (hydrodynamic module) and Delft3D PART (Particle tracking module) were applied together by Bonvin et al. (2013) to study micropollutant movement from a wastewater outfall in Lake Geneva and hence used to assess ecotoxicological risk. The movement of micropollutants and their spatial extent were simulated under four different wind conditions in 2010-2011. The simulations showed that winds significantly affect the currents in Lake Geneva and that a plume of micropollutants usually moved both east and west from the outfall covering a distance of over 300 m from the outfall. This spatial extent became larger during periods of thermal stratification in summer. Bonvin et al. (2013) note that the model was successfully validated and showed good agreement with measured winds, currents and temperature profiles as well as with electrical conductivity data. The simulations also helped to define ecotoxicological risk zones and identified the micropollutants which contribute to the risk. Using a similar approach, the dispersion of effluent discharge released from sewage works in Santos Bay, Brazil was assessed by Baptistelli (2015). The model showed the strong influence of tides from both northeast and southwest directions which dominated effluent dispersion in the bay. These results were verified, showed good agreement with field data and were used as supporting information for sewage works management in the bay (Baptistelli, 2015).

Brown et al. (2014) also used the hydrodynamic and particle tracking modules in Delft3D to predict freshwater flows and transport of dissolved organic carbon (DOC) after Hurricane Irene in Neuse River Estuary (NRE), USA. DOC was modelled

as a conservative tracer transported to the estuary, the model excluded biogeochemical processes but accounted for the physical parameters which influenced the DOC flux, including river discharge and wind forces. The model revealed that the storm caused increased freshwater discharge and DOC concentrations, and predicted that 19 times pre-storm DOC concentrations were exported from the river into the estuary during the storm. According to Brown et al. (2014), the model performance was good, it provided reliable results and is applicable to the transport of other materials or pollutants.

In an open water application, Van Der Meulen et al. (2015) simulated spatial and temporal transport patterns and accumulation areas of microplastics, Polyethylene (PE), Polystyrene (PS), Polyvinylchloride (PVC) and Polyethylene terephthalate (PET) in the North Sea. The model employed hydrodynamic data from existing long-term Delft3D Flow simulations of the North Sea. The plastic particles were treated as a conservative substance, which were continuously released into the North Sea through the river discharges by influence of advection and diffusion/dispersion (random component). The simulation showed that PE microplastic particles were transported towards the northeast of the North Sea and tended to float on the sea surface. In contrast, the heavier PS, PVC, and PET particles descended to the seabed and randomly accumulated in coastal areas. Their study provides an overview of the plastic distribution, which can be linked to possible sources such as rivers, ships and beaches, and informs approaches to monitor coastal and marine environments. In addition, the particle tracking module Delft3D-PART enabled modelling of future scenarios regarding the input of plastics to the sea (Van Der Meulen et al., 2015).

Apart from hydrodynamic and transport modelling, Delft3D has also been used as a tool for estuarine management, for example in a study of morphological changes due to storm surges in the Yangtze Estuary and Hangzhou Bay, China (Hu et al., 2009). In the above studies, Delft3D has consistently provided reliable results for modelling both hydrodynamics and the transport of either conservative and non-conservative substances in estuarine, coastal and open sea areas. Although Delft3D has not been used to simulate nutrient fluxes, its capability and credibility from earlier studies supports the use of Delft3D to simulate hydrodynamics and nutrient transport in the Ythan estuary, with the aim of improving understanding of

complex interactions between tides and fresh water flows and of the subsequent transport of nutrients.

## 1.5 Remote sensing for estuarine studies

Remote sensing from airborne and spaceborne platforms, which can provide a synoptic view of an estuary at different wavelengths, spatial and time scales, has long been used in coastal and estuarine studies and management (Klemas, 2010, Ouellette and Getinet, 2016). Applications of remote sensing include monitoring water quality such as suspended sediment concentration (SSC) (Chen et al., 2007) and chlorophyll-a concentration (Keith, 2014), classifying wetlands and monitoring their changes, predicting landcover trends (Klemas, 2010, Lee and Yeh, 2009, LeMarie et al., 2006), studying shoreline changes (Li and Damen, 2010), mapping coastal topography and bathymetry (Klemas, 2010), monitoring sea surface temperature, and detecting oil spill movement (Klemas, 2010).

With ongoing rapid development of remote sensing technologies, a wide variety of remotely sensed data are readily available, ranging from low to very high spatial and wavelength resolutions (Benz et al., 2004, Klemas, 2010). The selection of appropriate remote sensing data is required to obtain useful information that fits the purpose of particular studies (Benz et al., 2004). The main requirements for data selection include understanding both sensor characteristics and the properties of the objects of interest, which together directly define the scale of the study (Benz et al., 2004). The sensor characteristics, which play a key role in data selection are including spatial, spectral, and temporal resolutions (pixel size, wavelength range, and repetition frequency) (Kerle et al., 2004, Lillesand et al., 1994, Wulder et al., 2004). Pixel size is referred to area on the ground whilst wavelength range is a total range of the spectrum that can be detected by the sensor. As for, repetition frequency is the time lapse of capturing two images at the same area (Kerle et al., 2004, Lillesand et al., 1994, Wulder et al., 2004).

Low spatial resolution sensors such as MODIS and NOAA AVHRR, which provide a large coverage image with multi-spectral bands are often used for monitoring changes of object of interest at national and global scale (Hussain et al., 2013, Wulder et al., 2004). Whilst moderate spatial resolution sensors providing finer spatial resolution such as SPOT-5, Landsat TM, ETM+, ASTER are suitable for the regional scale study (Coppin et al., 2004, Hussain et al., 2013). Very high spatial

resolution data such as QuickBird, IKONOS, GeoEye, and Worldview-2 are often used for local scale studies as they provide very detailed information (Hussain et al., 2013, Wulder et al., 2004). With a wide range of very high spatial resolution sensors (Wulder et al., 2004), the use high resolution data has been continuously increasing even though trading-off low ranges of wavelength for high spatial data sometimes needs (Hussain et al., 2013, Wulder et al., 2004). However, with rapid development, some sensors provide satisfaction in both spatial resolution and ranges of wavelength (Gould and Arnone, 1997, Mumby et al., 1997, Mumby et al., 1999, Mutanga et al., 2012, Omar, 2010). Thus, high spatial resolution sensors are likely to play a key role in wetlands and estuarine and coastal zone applications (Mumby et al., 1997, Mutanga et al., 2012, Turner et al., 2003, Wulder et al., 2004).

Among a wide variety of high spatial resolution sensors, Worldview-2 (WV-2) and Compact Airborne Spectral Imager (CASI) provide wide spectral ranges while remain satisfied spatial resolution (Gould and Arnone, 1997, Mumby et al., 1997, Mumby et al., 1999, Mutanga et al., 2012, Omar, 2010). Worlview-2 is a commercial high spatial resolution satellite that was launched by the Digital Globe company in 2009. It provides coverage of an area about 16.4 $km^2$ and 8 sensor bands with very high spatial resolution (Panchromatic: 0.46 m Ground Sampling Distance, GSD at nadir, 0.52 m GSD at 20° off-nadir, and Multispectral: 1.85 m GSD at nadir, 2.07 m GSD at 20° off-nadir). The 8 sensor bands are including coastal blue (400-450 nm), blue (450-510 nm), green (510-580 nm), yellow (585-625 nm), red (630-690 nm), red-edge (705-745 nm), and two the near-infrared bands (Near-IR1: 770-895 nm; Near-IR2: 860-1040 nm) (DigitalGlobe, 2010, Mutanga et al., 2012, Omar, 2010).

The new coastal blue band is useful for mapping shallow coastal bathymetry and submerged vegetation in shallow coastal and estuarine environments. While the new yellow band, which corresponds to the absorption range of minor plant pigments, may be used to detect yellowness of vegetation or vegetation stress (Marchisio et al., 2010, Oumar and Mutanga, 2013). The new red-edge band, which is centred in the transition zone between high absorption by chlorophyll in the red region and high reflection by the spongy mesophyll cells in the near infrared region is valuable in improving vegetation classification, estimating chlorophyll content, and measuring plant health (Carle et al., 2014, Mutanga et al., 2012). The new

infrared band is less affected by atmospheric influences than NIR1, which enables broader vegetation analysis and biomass studies. With these advantages, Worldview-2 data have been utilised for many estuarine studies, in particular to help distinguish complexity of estuarine biodiversity (Carle et al., 2014, McCarthy et al., 2015, Mutanga et al., 2012, Rapinel et al., 2014, Reshitnyk et al., 2014). For example, the data have been used by Carle et al. (2014) to classify diverse and heterogeneous coastal wetlands in the Wax Lake delta, southern Louisiana, USA using a Support Vector Machine (SVM) classifier. Their results demonstrate that red-edge and coastal blue bands improve classification of marsh species distributions with high overall classification accuracy of 75% better than results derived from using 4 band high resolution sensors such as IKONOS and QuickBird (Carle et al., 2014). Worldview-2 data have also been used to define the parameters for a decision tree classifier, which provided results with very high accuracy of 82% for wetland areas and 90% for non-wetland areas in vegetation mapping of Fort De Soto State Park, Tampa Bay (Florida), USA (McCarthy et al., 2015). In addition, Worldview-2 has been used to map underwater algae in the north coast of British Columbia, Canada using the Maximum Likelihood (ML) classifier. The results show that Worldview-2 could classify green algae (*Ulva spp.*), brown algae (*Fucus spp.*) and eelgrass (*Zosteramarina*) in regions shallower than 3m with a total accuracy of 75% (Reshitnyk et al., 2014).

Compact Airborne Spectrographic Imager (CASI) data is a hyperspectral sensor having a capability to detect 19 spectral bands with 1m spatial resolution. The number of wavelength can even be adjusted according user requirements (Wulder et al., 2004). CASI have also been demonstrated to be able to map intertidal surfaces and saltmarsh vegetation in several studies. For instance, Hunter and Power (2002) used CASI data to identify intertidal habitats at Crayford Marsh and Dartford Creek, UK using two different classifiers. The Spectral Angle Mapper (SAM) and ML performance were assessed. The results show that ML produced the most accurate map at overall accuracy of 68% for Crayford Marsh and 53% for Dartford Creek. They also state that CASI data were useful for identifying intertidal habitats, in particular salt-marsh and sediments, although there were confusions on classifying in some classes. Valle et al. (2015) used CASI data to map 13 habitats on intertidal and subtidal zones of Oka estuary, Basque Country, Spain. In their study, the CASI data were adjusted to 25 spectral bands with 2m ground sampling

distance in order to improve the classification. These spectral bands were selected based on the spectral signature of different habitat types for classification using ML. Their results revealed that a 10 band combination produced the most accurate classification with 92% of mean producer accuracy and 94% of mean user accuracy (Valle et al., 2015).

Increase in availability and technologies of multiple sensors from very coarse to very high spatial resolution gives researchers the choice to select the best suits for purposes of studies. Variety of spatial and spectral resolution data also make distinguishing species and understanding aspects of biodiversity in estuarine and coastal zones feasible. In addition, it benefits to understanding object of interest across a range of scales (Hussain et al., 2013, Turner et al., 2003). For the Ythan, a compact small size estuary (523 $km^2$), the use of high spatial resolution data seems to suit for extracting detailed ecological information. Using high spatial and spectral resolution images to distinguish algal mat boundaries from mudflats and to map algal mat location with better accuracy was also recommended by Green (2010). WorldView-2 and CASI data, both of which have been proved to have good performance for identification of intertidal habitats and which exhibit high potential for providing meaningful information, are good candidates for this high complexity estuarine ecosystem.

### 1.6 Research motivation

The global importance of estuaries has led to considerable advances in the understanding of their hydrodynamics and ecology in recent years (Defne et al., 2011, Kench, 1999, Largier et al., 1997, Lillebø et al., 2005, Martins et al., 2001, Trancoso et al., 2005). Many of these advances have resulted from studies of particular estuaries, and all estuaries have specific physical and biological environments which affect their nutrient dynamics (Kennish, 2002, Martins et al., 2001, Wallace and Gobler, 2015). The complex interactions between the supply of nutrients, freshwater inflows, and the tidal cycle, which are required to comprehend nutrient transport in an estuary are not fully understood. In the Ythan, previous studies (Edwards et al., 2003, Raffaelli, 1999) demonstrate that the concentration of nutrients derived from both high-organic sediments and the water column is likely to be one of the most significant factors facilitating macroalgal blooms on intertidal mudflats. It is thus important to study water circulation in response to river flow and tides to assess the role of hydrodynamics

on controlling movement of nutrients and as such the distribution and density of annual macroalgal blooms in this estuary. This understanding will contribute a deeper knowledge of estuarine eutrophication in general, which can be applied in the Ythan to deal with this environmental problem and to find suitable strategies and mitigation measures.

To study hydrodynamics and hence nutrient transport, this study uses the Delft3D model which has been proved robust and reliable in several estuarine studies as described earlier. The expected results of the modelling are hydrodynamic characteristics and nutrient pathways, which could reveal how hydrodynamics and nutrient availability link to the locations and intensity of the algal blooms. To ensure that the model is reliable, calibration and validation are required. These steps typically rely on time series field data. Thus, in any modelling study in which cost and time are limited, using conventional in-situ field measurement for calibration and validation requires long time series of data at different locations which may not be available.

Likewise, Ythan estuary, the availability of long-term data is limited. There are only two time-series datasets available, which are the SEPA maps of algae coverage and SEPA water chemistry buoy data at one location. To overcome these limitations, remote sensing data are utilised in this study to helping the model validation and calibration process. Specifically, WV-2, CASI, and Landsat-8 data are used to identify boundaries of exposed mudflats and the estuary channels for modelled hydrodynamic validation and to identify areas of algal blooms for modelled nutrient dynamic validation. In addition, they are used to support understanding of macroalgal bloom behaviour in the Ythan. The Delft3D model outputs and remote sensing data are evaluated their potential for modelling hydrodynamics and nutrient pathways and for aiding model validation, respectively.

## 1.7 Research questions

The specific research questions that the thesis seeks to answer are:

- What are the patterns of water (river and ocean) circulation in the estuary?
- How are nutrients transported in the estuary?
- How do hydrodynamics influence macroalgal growth?

- Can remote sensing data and Delft3D model be used to support modelling hydrodynamics, nutrient concentrations and pathway in estuarine study effectively?

## 1.8 Research aims

The overall aim of this project is:

- To understand role of hydrodynamics on controlling annual macroalgal mat formation on tidal flats in the Ythan estuary by simulating water circulation, nutrient concentrations and pathways in the estuary using the Delft3D model

In delivering this aim, the project has the following secondary aims:

- To evaluate the potential of using the Delft3D model for modelling hydrodynamics and nutrient pathways
- To evaluate the potential of using remote sensing data for aiding model calibration and validation, and as a management tool

## 1.9 Thesis outline

This thesis is composed of eight chapters. The first chapter introduces the background, objectives/aims, and scope of the study. The second chapter outlines research design/ methods, details of the data used, and the description of the Delft3D model, particularly Delft3D-FLOW and Delft3D-PART modules, which are used for modelling hydrodynamics and nutrient pathways. Chapter three outlines the environment surrounding the Ythan estuary including, the Ythan catchment characteristics, geomorphology, river flow, tide, water quality, and sediment characteristics. All of which are used as supporting information for interpretation of modelled hydrodynamics and nutrient dynamics. Chapter four explains how remote sensing data are utilised for sensitivity test and model validation. In addition, the chapter describes how remote sensing data are used to study algal growth behaviour through the time. In chapter five, sensitivity test and model validation are outlined. Chapter six demonstrates the use of the Delft3D-FLOW and Delft3D-PART modules coupled with the optimal model parameter setting derived from chapter five to simulate hydrodynamics, nutrient concentrations and pathways under specific flow conditions (high flow and low flow events). Chapter seven is an overall discussion and assessment of the Delft3D model performance

and the potential of using remote sensing data for aiding sensitivity test and model validation. The last chapter is conclusion of influence of hydrodynamics, nutrient concentrations and pathways on algal blooms in the Ythan estuary.

# Chapter 2: Research design and methods

This chapter is divided into three parts. The first part describes the overall research design, developed to achieve the research aims and answer the research questions listed in Chapter 1. The second part is a full description of the data used in this study as well as their sources. The last part is an explanation of the methods and techniques employed for collecting and analysing the data.

## 2.1 Research design

To understand the role of hydrodynamics in controlling annual macroalgal mat formation on tidal flats, which is the main purpose of this study, it is necessary that patterns of water circulation in the estuary, and hence of nutrient transport, are clearly understood. To achieve the aim of the study, an overall plan was developed (Figure 2-1). A review of catchment characteristics including the river network, settlement locations, land cover, soil, and geology were carried out at the beginning of the study. Following this, a review of the geomorphology of the estuary itself is presented, and this information is used to provide an initial understanding of the hydrodynamic characteristics of the estuary. Then, the patterns of sediment grain size and organic concentration variation across the estuary are examined, as grain size also affects hydrodynamics. The grain size and the concentration of organic matter in the sediments, together may control algal mat formation. Changes in mudflat location and extent in the estuary were also undertaken as the morphodynamics of the estuary also influence hydrodynamics.

Following from a review of the physical setting of the estuary and its catchment, an analysis of river flow and tides is presented as these water inputs are the drivers of estuary hydrodynamics. In addition, water quality data including temperature, pH, DO, turbidity, and chlorophyll-a from a buoy located in the lower region of the estuary (Figure 1-3) are used to examine their association with river flow and tide. In this section, chlorophyll-a data are the main focus and are used as a proxy for nutrients. The water quality data are analysed together with river flow and tide information to provide better understanding of the influences of river flow and tides on changes in the amount of chlorophyll-a and its transport behaviour in the estuary. Following this analysis of secondary data, simulation of water circulation using the Delft3D model was conducted.

However, before applying Delft3D to the study site, the Ythan estuary, the sensitivity of the model outputs to parameters including bottom roughness, horizontal eddy viscosity, and horizontal eddy diffusivity are assessed using remote sensing data. In addition to these sensitivity tests, model validation was carried out. Measured water depths and NDWI (Normalized Difference Water Index) derived from WV-2 and Landsat-8 were used in verifying modelled hydrodynamics, while NDVI (Normalized Difference Vegetation Index), which is a proxy for the density of macroalgal blooms, was used for verifying the spatial linkage between observed locations of macroalgal bloom and modelled nutrient concentrations and pathways. After the model parameter settings have been optimised and the model results are considered satisfactory, the model is applied to the study site to simulate hydrodynamics, nutrient concentrations and pathways during both high and low river flow events and under different tidal conditions. The Delft3D FLOW module is used for hydrodynamic simulations and Delft3D PART is used for modelling nutrient concentrations and pathways. The hydrodynamic data generated by the FLOW module are employed within Delft3D PART for modelling nutrients. The nutrient concentrations and pathways are modelled as a conservative tracer transported from each release point (the river and tributaries) to the estuary.

In this study, remote sensing data are not only utilised to support sensitivity testing and model validation but also to investigate macroalgal bloom behaviour in the Ythan estuary over several years, from which the persistence of hydrodynamic patterns in the estuary can be inferred. In summary, the project research design contains four main elements to satisfy the study aims: (a) a review of the physical setting; (2) analysis of hydrological characteristics and their interaction with water quality; (3) modelling hydrodynamics and nutrient pathways; and, (4) analysis of intertidal substrates. These elements fill information gaps between the two main datasets for the Ythan (Figure 2-2), as well as providing valuable new datasets for further studies covering different space and time scales (Figure 2-2).

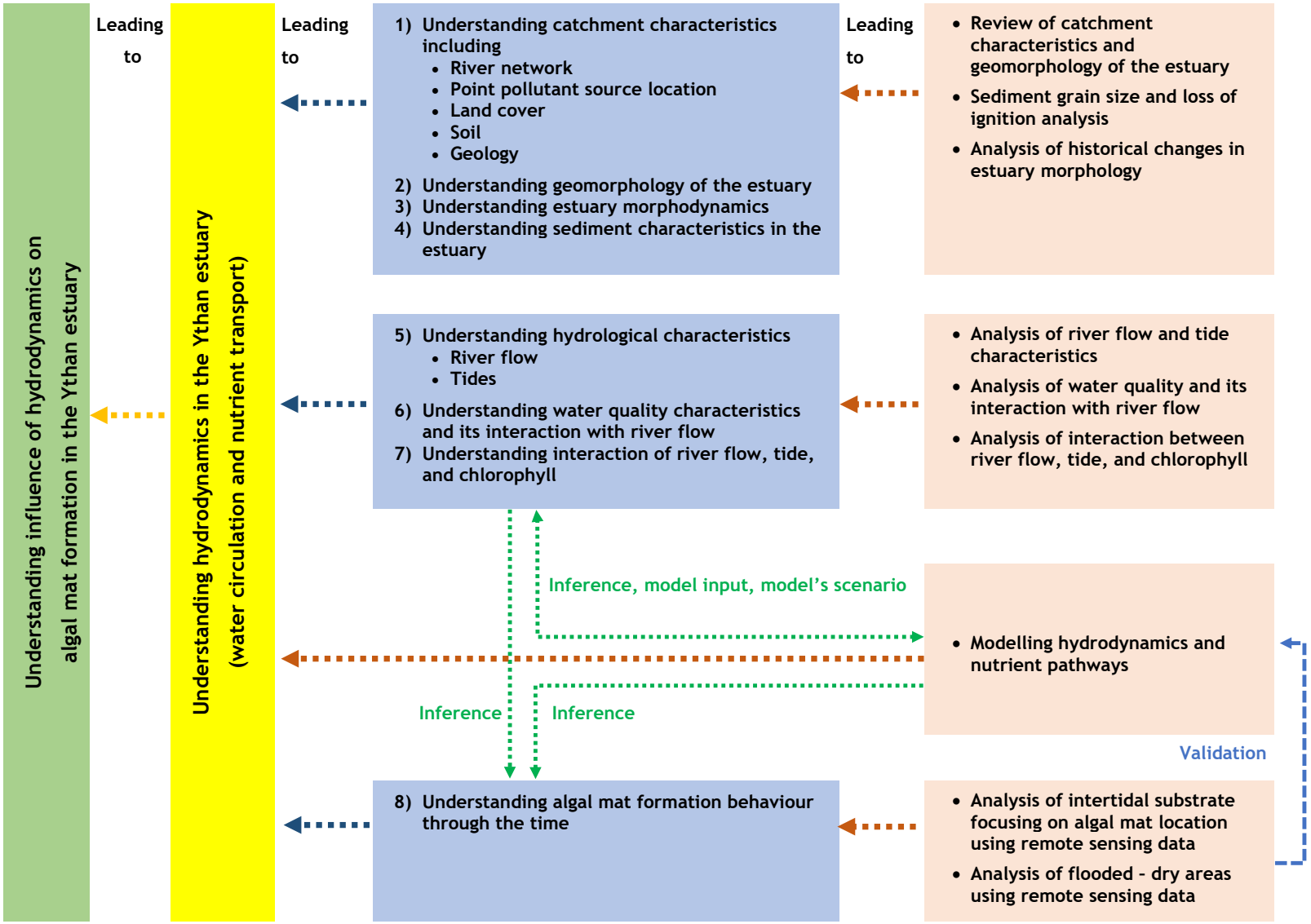


**Figure 2-1:** Outline of the framework used in this research

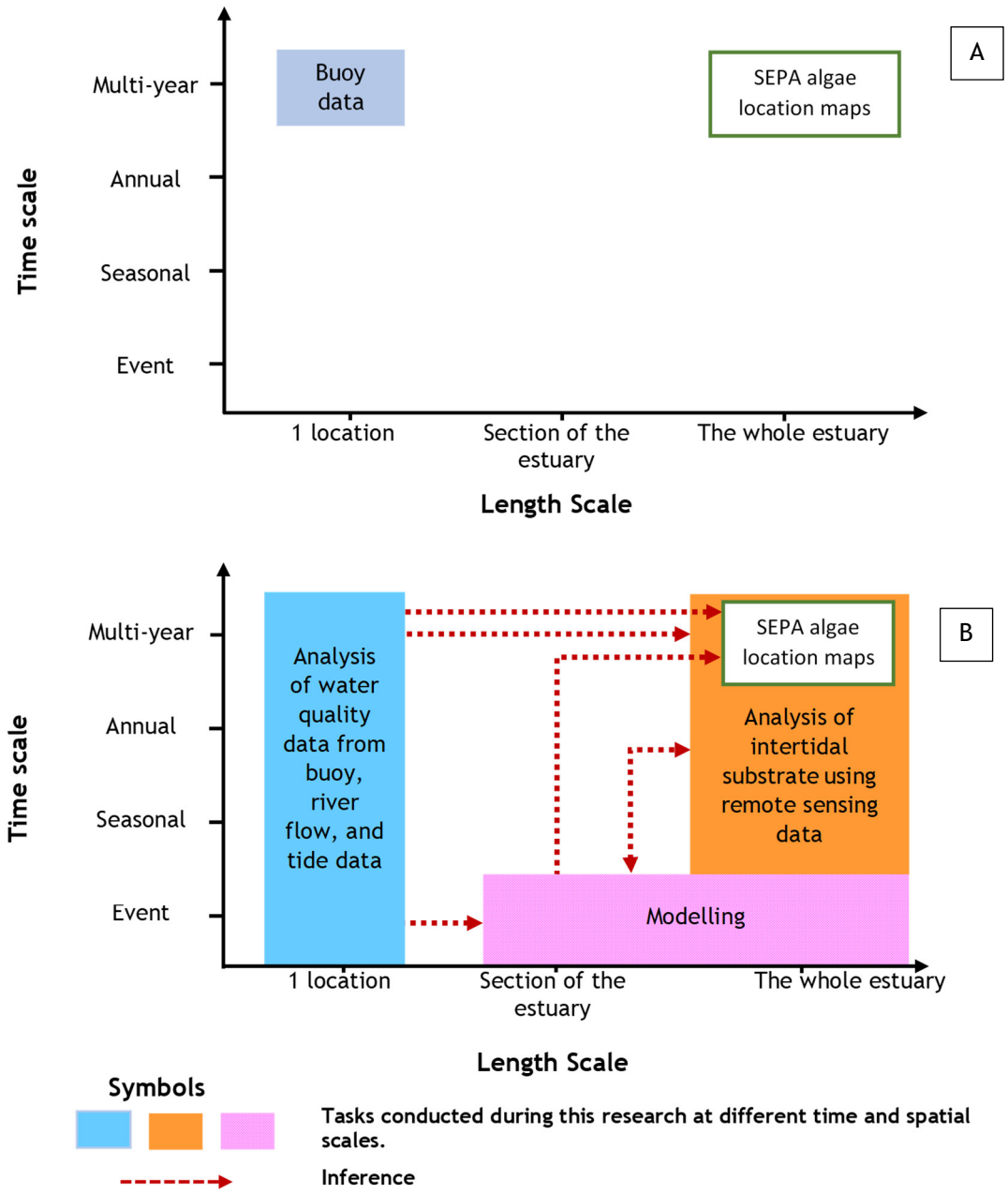


**Figure 2-2:** Data available before the project (A) and tasks conducted during this research at different time and spatial scales (B) providing information at different time scale and different spatial scale.

## 2.2 Data used

A list of primary, secondary, and remote sensing data to be used in this study is presented in Tables 2-1 and 2-2.

**Table 2-1:** Data type, source and purpose of use

| No. | Data | Details | Year | Source | Purpose of use |
|---|---|---|---|---|---|
| 1. | River flow | 15 - minute interval data collected at Ellon gauge station (Figure 1-3). | 2009<br>2011<br>2014<br>2015 | Scottish Environment Protection Agency (SEPA), UK | • To characterise hydrological characteristics<br>• To study interactions of between river flow, water quality, and tides<br>• To use as model input for hydrodynamic and nutrient pathway modelling |
| | | Daily mean flow data collected at Ellon gauge station (Figure 1-3). | 1983 - 2016 | National River Flow Archive (NRFA), UK | • To characterise hydrological characteristics |
| 2. | Water quality<br>• Temperature<br>• pH<br>• Dissolved Oxygen (DO)<br>• Turbidity<br>• Chlorophyll-a<br>• Salinity | 15 - minute interval data collected by a floating buoy and daily mean water temperature and salinity of fresh water all of which collected at Ellon gauge station (Figure 1-3).<br>The buoy data were available in some months and years as the SEPA buoy occasionally stopped operating, and has not operated since October 2013. | 2009<br>2010<br>2011<br>2013 | SEPA, UK | • To analyse water quality characteristics<br>• To study interactions between river flow and water quality<br>• To study interactions between chlorophyll-a, river flow, and tide<br>• To use in model sensitivity testing |
| 3. | Sea surface temperature and salinity of sea water | Daily mean | 2009 | Copernicus Marine Environment Monitoring Service (http://marine.copernicus.eu/services-portfolio/access-to-products/) | • To use in model sensitivity testing |

| No. | Data | Details | Year | Source | Purpose of use |
|---|---|---|---|---|---|
| 4. | Tidal level | 15-minute interval data measured by a tide gauge at Aberdeen port (approximately 22 km away from the Ythan estuary (Green, 2010). | 2009<br>2011<br>2014<br>2015 | British Oceanographic Data Centre (BODC), UK | • To study general sea level characteristics<br>• To study interactions between chlorophyll-a, river flow, and tide<br>• To use as model input for hydrodynamic and nutrient pathway modelling |
| 5. | Sediment grain size | 7 surface sediment samples | 04/03/2014 | Self-analysed | • To study sediment grain size distribution |
| | | 64 surface sediment samples | 12/08/2014 | (Lachendro, 2016) | • To map sediment grain size distribution |
| 6. | Organic matter | 64 surface sediment samples | 12/08/2014 | (Lachendro, 2016) | • To map organic content in sediments |
| 7. | Algal patch location | Shapefile format | 11/09/2009<br>14/07/2011<br>12/08/2014 | SEPA, UK | • To study conditions associated with algal growth<br>• To verify algal mat locations derived from this study |
| 8. | LiDAR DEM | ERDAS Imagine IMG format, 2.0 m pixel size | 11/09/2009 | SEPA, UK | • To use coupled with measured bed elevations for DEM creation |
| 9. | Measured bottom bed elevation | 5,566 measured points | 10/09/2015 | Self-collected | • To use, coupled with LiDAR DEM, as bathymetric input to the estuary DEM |
| 10. | Measured water depth | 5,566 measured points | 10/09/2015 | Self-collected | • To validate model results |

| No. | Data | Details | Year | Source | Purpose of use |
|---|---|---|---|---|---|
| 11. | Wind speed | Daily mean data collected at Aberdeen airport. | 1-15/09/2009 | WeatherOnline Ltd.- Meteorological Services's website (http://www.weatheronline.co.uk/) | • Model inputs to model nutrient concentrations and pathways |
| 12. | Wind direction | 6 - hour interval data collected at Aberdeen airport | 1-15/09/2009 | WeatherOnline Ltd.- Meteorological Services's website (http://www.weatheronline.co.uk/) | • Model inputs to model nutrient concentrations and pathways |
| 13. | Biomass | 21 algal patches | 10-13/08/2009 | SEPA, UK | • To validate NDVI data |
| | | 9 algal patches | 16-17/08/2011 | | |
| 14. | Landsat-5 | Details in Table 2-2 | 04/07/1989<br>25/10/2010 | US Geological Survey (USGS), USA | • To study change in mudflat location and extent |
| 15. | Landsat-8 | Details in Table 2-2 | 30/08/2013<br>30/09/2015<br>28/02/2016<br>09/10/2016 | US Geological Survey (USGS), USA | • To create NDWI and NDVI for sensitivity test, model validation, and studying algal growth behaviour |
| 16. | CASI | Details in Table 2-2 | 11/09/2009<br>14/07/2011 | SEPA, UK | • To create NDVI for model validation and for studying algal growth behaviour |
| 17. | Worldview-2 (WV-2) | Details in Table 2-2 | 20/04/2015<br>09/05/2016 | Geo-informatics and Space Technology Development Agency (GISTDA), Thailand | • To create NDWI and NDVI for sensitivity test, model validation, and studying algal growth behaviour |

**Table 2-2:** Satellite data and aerial photograph characteristics

| Data | Wavelength (nm)/ Centre Wavelength (nm) for CASI | | Spatial resolution | Swath width | Revisit time | Acquisition dates | Source |
|---|---|---|---|---|---|---|---|
| WV-2 | Panchromatic (450-800)<br>Band 1 Coastal (400-450)<br>Band 2 Blue (450-510)<br>Band 3 Green (510-580)<br>Band 4 Yellow (585-625) | Band 5 Red (630-690)<br>Band 6 Red edge (705-745)<br>Band 7 Near infrared (NIR)1 (770-895)<br>Band 8 Near infrared (NIR)2 (860-1040) | 0.50 m (pan)<br>1.85 m (ms) | 16.4 km | 1.1 days | 20/04/2015<br>09/05/2016<br>The images were acquired during cloud free conditions (<10%), and low tide | GISTDA, Thailand |
| CASI | Band 1 442.80; 13.10<br>Band 2 486.70; 11.40<br>Band 3 510.35; 12.15<br>Band 4 555.65; 13.55<br>Band 5 575.70; 6.59<br>Band 6 597.15; 7.15<br>Band 7 609.70; 5.40<br>Band 8 625.25; 5.75<br>Band 9 641.80; 8.50<br>Band 10 661.80; 3.90 | Band 11 673.90; 8.10<br>Band 12 684.80; 11.00<br>Band 13 691.85; 4.25<br>Band 14 702.05; 2.95<br>Band 15 711.05; 6.05<br>Band 16 749.20; 6.70<br>Band 17 854.35; 12.45<br>Band 18 877.75; 10.85<br>Band 19 958.95; 9.85 | 1.00 m | 512 pixels across swath | - | 11/09/2009<br>14/07/2011<br>The images were acquired during cloud free conditions (<10%), and low tide | SEPA, UK |
| Landsat-5 | Band 1 Blue (450–520)<br>Band 2 Green (520-600)<br>Band 3 Red (63-690) | Band 4 Near-Infrared (760-900)<br>Band 5 Shortwave-Infrared (550-1750)<br>Band 7 Mid-Infrared (2080-2350) | 30.0 m (ms) | 185.0 km | 16 days | 04/07/1989<br>25/10/2010 | USGS, USA |

| Data | Wavelength (nm)/ Centre Wavelength (nm) for CASI | | Spatial resolution | Swath width | Revisit time | Acquisition dates | Source |
|---|---|---|---|---|---|---|---|
| Landsat-8 | Band 1 - Ultra blue (435-451)<br>Band 2 - Blue (452-512)<br>Band 3 - Green (533–590)<br>Band 4 - Red (636-673)<br>Band 5 - Near Infrared (NIR) (851-879) | Band 6 - Shortwave Infrared (SWIR) 1 (1566-1651)<br>Band 7 - Shortwave Infrared (SWIR) 2 (2107-2294)<br>Band 8 - Panchromatic (503- 676)<br>Band 9 - Cirrus (1363-1384)<br>Band 10 - Thermal Infrared (TIRS) 1 (10600–11190)<br>Band 11 - Thermal Infrared (TIRS) 2 (11500-12510) | 15.0 m (pan)<br>30.0 m (ms)<br>100.0 m (TIRS) (resampled to 30.0 m) | 185.0 km | 16 days | 30/08/2013<br>30/09/2015<br>28/02/2016<br>09/10/2016<br>The images were acquired during cloud free conditions (<10%), and low tide | USGS, USA |

## 2.3 Methods

In this section, the methods and techniques used for collecting and analysing data are explained.

### 2.3.1 Sediment sampling

Since macroalgae are normally found on intertidal mudflats (Raffaelli, 1999, Raffaelli, 2000, Wolanski et al., 2004), investigating sediment types and organic matter concentrations is required to understand potential favourable sediment types for algal growth, as well as to inform assessment of hydrodynamic patterns in the estuary, and to aid in selecting roughness parameter values for hydrodynamic modelling. Initial inspection of sediments in the estuary took place on March 4, 2014 during low tide. Surface sediment samples were collected from seven different sites, selected from areas where algal mats often developed from 2000-2009 (Gov.scot, 2011, Green, 2010). Five of the seven sites (sites 1, 2, 3, 4, and 7) were in the middle estuary and two (5 and 6) were in the upper estuary

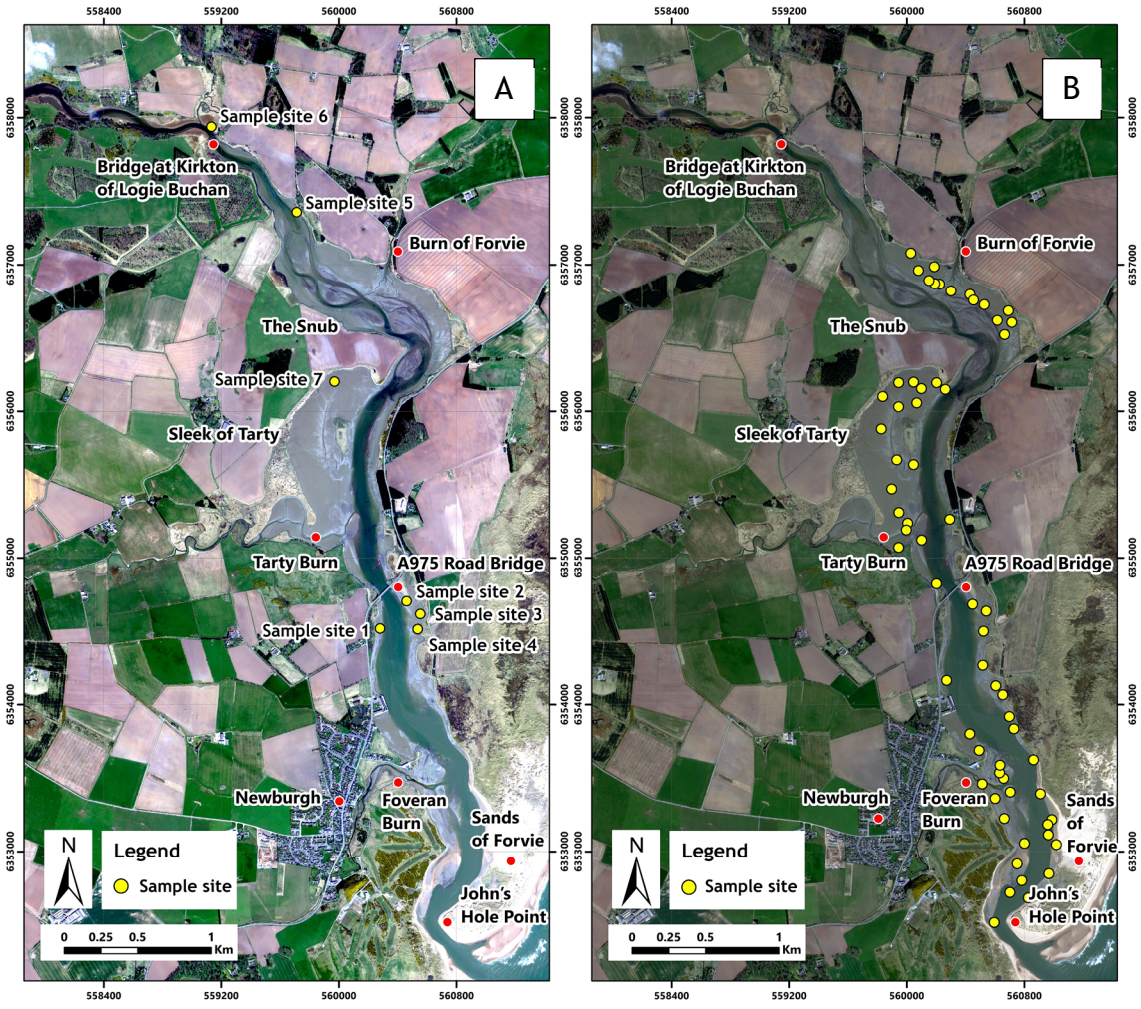


**Figure 2-3:** Surface sediment sample sites during the first field survey on 04/03/2014 (A) and sample sites collected by SEPA on 12/08/2014 (B).

(Figure 2-3A). Further sediment type investigations took place on August 12, 2014. This time, 62 surface sediment samples were collected from across the entire estuary by SEPA (Figure 2-3B).

### 2.3.2 Sediment grain size and loss on ignition analysis

The seven samples were analysed in the laboratory to obtain sediment grain size, following the method of Swift (2002). To prepare the samples they were dried overnight at 450°C in a furnace to remove all organic materials. Then, each individual sample was crushed and ground with a mortar and pestle to break up aggregates. Following this, the sample was sieved to remove particles larger than 2000 micron, which cannot be measured by the Coulter LS230 which has a size range of 0.4-2000 micron. Then, Calgon, a dispersing agent made of 35g sodium hexa-metaphosphate, 7g sodium carbonate, and 1 litre of distilled water, was added to each sample to ensure dispersion and to prevent sediments from aggregating when in solution. The sample was then placed in an ultrasonic bath for 3 minutes to further dispersion. Once this process was completed, the prepared samples were analysed using a Beckman-Coulter LS230 laser diffraction particle size analyser. Three repeat measurements were made for each sample to check for consistency (Swift, 2002).

The 62 sediment samples collected by SEPA were analysed by Lachendro (2016) using the procedure described above, and their loss on ignition was determined to obtain the organic matter concentrations. Further details of the methods are explained by Lachendro (2016). The median grain size and organic matter concentration (expressed as a % by mass) were plotted against sediment median size, and mapped to assess the relationship between sediment median size and the location of high organic matter. An interpolation map of sediment grain size was also created and then overlaid by macro algal mat location and algal type collected on August 12, 2014 by SEPA to examine the relationship between sediment type and organic matter concentration and macroalgal development.

Interpolation used the ordinary Kriging interpolator in the Geostatistical Analyst module of ArcGIS10.1 as it considers the degree of autocorrelation between input points (Johnston et al., 2001) and it produced the best overall result (the smallest root mean square error, average standard error, mean standard error, and root-

mean-square standardized errors) compared to interpolated maps derived from other interpolators.

### 2.3.3 Analysis of historical changes in estuary morphology

The long-term locational stability of mudflats is an important element of the dynamics in the estuary. Historical maps including scanned Ordnance Survey maps from 1901 (Figure 2-4) and 1957 (Figure 2-5A) provided by the National Library of Scotland (NLS), a scanned aerial photo taken in 1988 (Figure 2-5B) and Landsat-5 acquired in 1989 and 2010 were used to assess the magnitude of changes in the location and extent of mudflats over time. These changes from 1901-1988 were investigated using the process shown in Figure 2-6.

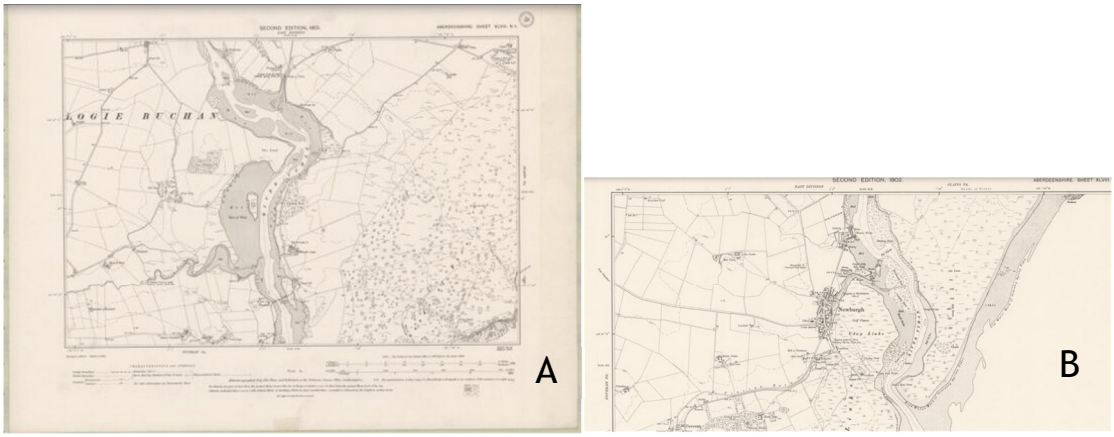


**Figure 2-4:** Scanned Ordnance Survey maps constructed in 1901 upper part (A) and lower part (B) of the estuary.

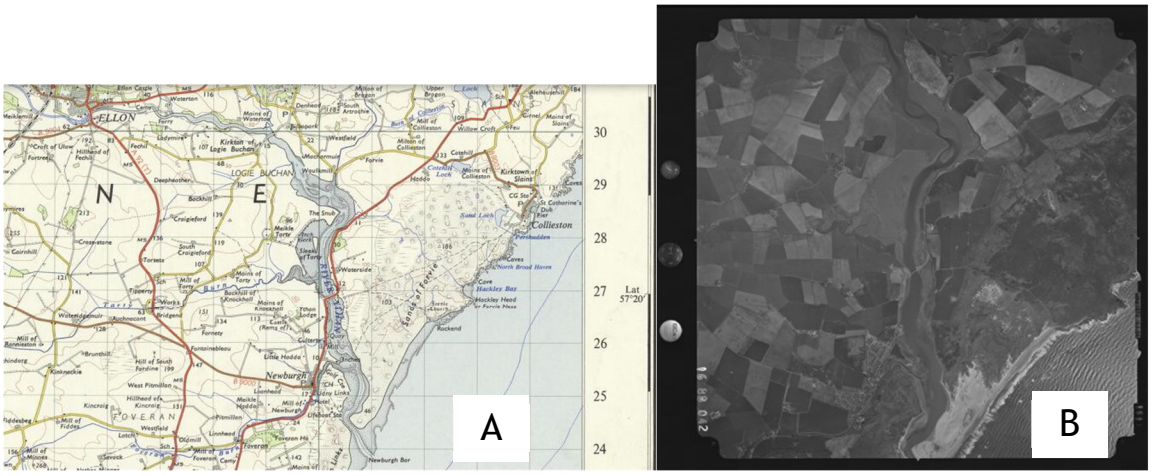


**Figure 2-5:** A scanned Ordnance Survey map constructed in 1957 (A) and a scanned aerial photo taken in 1988 (B).

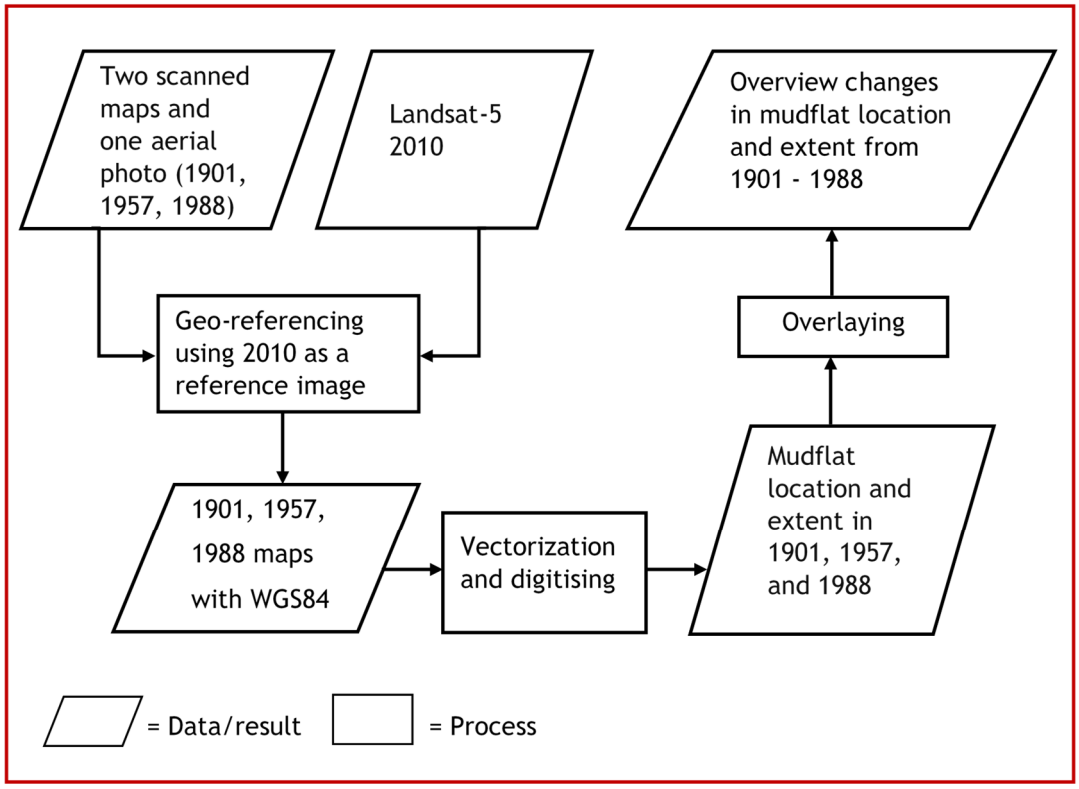


**Figure 2-6:** The process for studying changes in mudflat location and extent from 1901-1988.

Changes from 1989 to 2010 were assessed using image differencing. This technique is chosen as it is straightforward and produces easy to interpret results. Two satellite images are pre-processed and perfectly aligned so that corresponding pixels coincide. The difference between the two images is a direct subtraction (Equation 2-1), pixel by pixel (Coppin et al., 2004, Green et al., 1994, Hayes and Sader, 2001, Lu et al., 2004). The differencing uses a suitable satellite image band, in this case one that differentiates. For this study, a Landsat-5 images acquired in 1989 and 2010 are used. The near infrared band (NIR) (band 4) of LANSAT-5 is used as this band is considered to be the most suitable for differentiating land and water (Frazier and Page, 2000, Jensen, 1996). The pre-processing steps for the two images are given in Figure 2-7.

$$Difference\ image = First\ image\ (2010) - Second\ image\ (1989) \qquad \textit{Equation 2-1}$$

Where $Difference\ image$ is the result and the NIR band (band 4) of Landsat-5 is used.

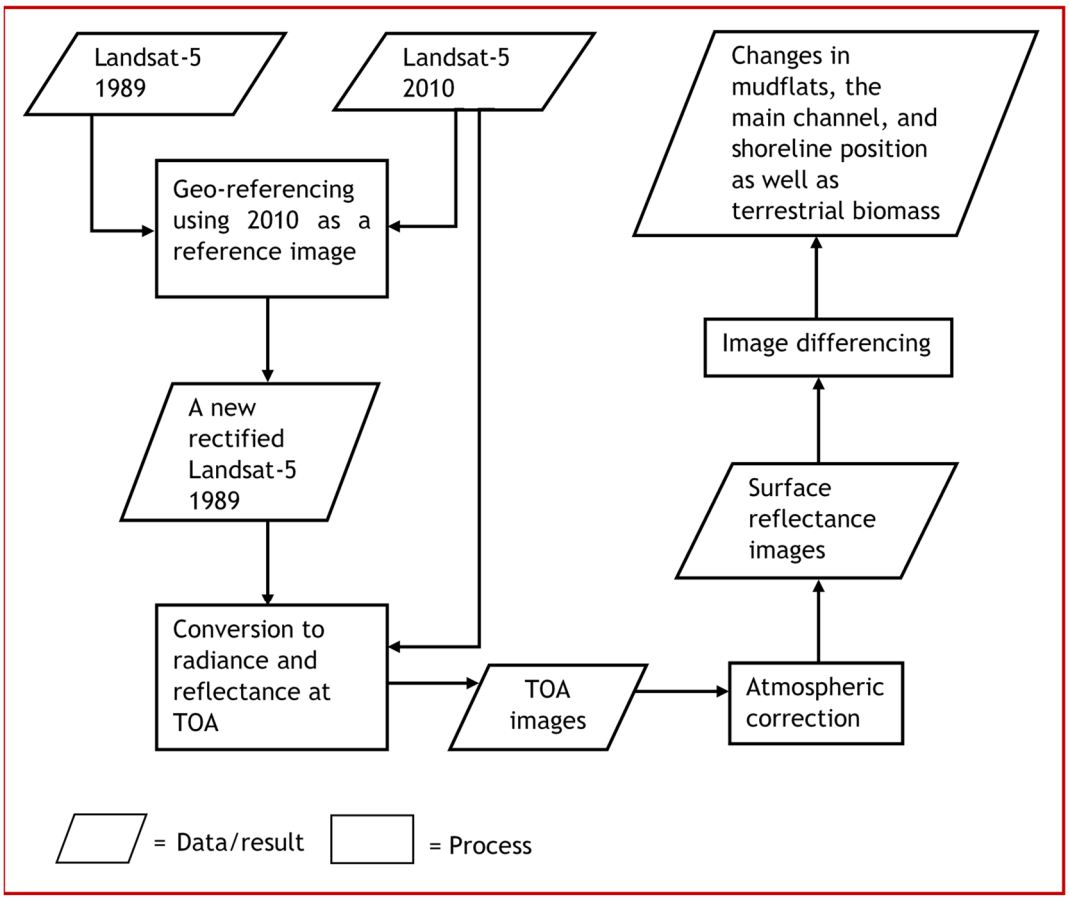


**Figure 2-7:** Flow chart shows the pre-process for image differencing method.

### 2.3.4 Analysis of river flow and tide level

#### 2.3.4.1 River flow

Daily mean flows during 1983 - 2016 (33.39 years) were plotted using hydrological year dates (1st October - 30th September) to understand long-term river flow patterns. Mean, maximum and minimum flows on each day of the year were also computed to determine seasonal patterns and the degree of variability throughout the year. 15-minute interval river flows (2009, 2011, 2014, and 2015) were also plotted to provide greater detail on the nature of typical flow events in the Ythan. Flow duration curves were calculated across the full period of record, present the data as the proportion of time that river flows were less than the specified values. All statistical computations for the analysis of river flow were made using Microsoft Excel 2016.

#### 2.3.4.2 Tides

Mean, maximum and minimum values from 15-minute interval data from 2009-2013 were plotted to assess patterns and extremes. All of the tide data were computed and plotted using Microsoft Excel 2016.

### 2.3.5 Analysis of water quality data

Time-series, using a 15-minute sampling interval, of water quality data were collected by a floating buoy from 2009, 2010, 2011, and 2013 (see Figure 1-3 for location). Data include water temperature, pH, DO, turbidity, and chlorophyll-a. Time series plots were used to show the general characteristics of water quality variation and their relationships with river flow. To understand changes in water quality parameters from 2009-2013, anomaly for each season were analysed. Correlations were calculated between river flow and each of the water quality parameters, and also between the different water quality parameters. All statistical data were processed using Microsoft Excel 2016 and Minitab. This study does not use multivariate analysis of the water quality indicators as the main focus is the influence of hydrodynamics on algal growth, and hence how the interaction of river flow and tides affects nutrient fluxes in the estuary. As the detailed water quality data come from only one location, it is not possible to use these data alone to assess the role of water quality in algal growth.

### 2.3.6 Analysis of interaction between river flow, tide, and chlorophyll-a

The time series behaviour of chlorophyll-a relative to river flow, and tides were investigated at different time scales (seasonal and event scales) to identify influences on the concentration of chlorophyll-a in the estuary. Data from 2009 were the main focus as there were occurrences of prolific algal blooms in this year (Gov.scot, 2011) and there were unusual high flow events in the summer. The selected events which were based on amount of chlorophyll and changes of river flows were as follows;

- Moderate chlorophyll-a coinciding with high flow in winter (19-24 Feb 2009)
- High chlorophyll-a coinciding with low flow in spring (27-31 May 2009)
- High chlorophyll-a coinciding with low flow in summer (dry summer) (8-12 Jun 2009)

- High chlorophyll-a coinciding with high flow in summer (wet summer) (17-21 Jul 2009)
- High chlorophyll-a coinciding with high flow in autumn (19-25 Nov 2009)

### 2.3.7 Hydrodynamic and nutrient modelling using Delft3D

Delft3D was chosen for this study as firstly, the form of hydrodynamic equations in the model are suitable for predicting the flows in shallow coasts and estuaries where the horizontal length is larger than the vertical, conditions appropriate to the Ythan estuary. Secondly, the model has been successfully applied in shallow coasts and estuaries (Baptistelli, 2015, Bonvin et al., 2013, Brown et al., 2014, Elhakeem et al., 2015, Hu et al., 2009, Lesser et al., 2004, Shaeri et al., 2017, Van Der Meulen et al., 2015, Zhao et al., 2017). Lastly, Delft3D is very time effective in term of computational efficiency compared with other commonly used models (Deltares, 2017b, Hsu et al., 2006, Lesser et al., 2001, List et al., 2006, Symonds et al., 2017, Teng et al., 2017). Consequently, this model provides the shortest runtimes, which typically are several hours (Symonds et al., 2017).

Delft3D has been developed by Deltares, an independent institute working on water, subsurface and infrastructure research in the Netherlands (https://oss.deltares.nl/web/delft3d/about). Delft3D is a modelling system that has the capability in both two-and three-dimensions to simulate flow, sediment transport, waves, water quality and ecology. Delft3D is comprised of six modules including Delft3D-FLOW, Delft3D-WAVE, Delft3D-MOR, Delft3D-PART, Delft3D-WAQ, and Delft3D-ECO, all of which can be applied for any type of open water study such as lakes, river, estuaries and coastal areas.

Delft3D-FLOW is capable of simulating hydrodynamic and transport phenomena resulting from tidal and meteorological forcing. Delft3D-WAVE and Delft3D-MOR are designed to simulate ocean waves and short-crested waves generated by wind in coastal and estuarine systems, and to simulate sediment transport and resulting morphodynamic behaviour. Delft3D-PART can predict the spatial concentration distribution of substances within the water, and can be used to model both non-conservative and conservative substances, while Delft3D-WAQ and Delft3D-ECO are to simulate the behaviour of water quality parameters resulting from decay processes and the transformation of variables between different states in the aquatic environment. Each of the modules can be accessed through embedded

graphic user interface menus and can be executed independently or in combination with other modules through communication files. In addition, utility programmes developed for pre-processing and post-processing, such as RGFGRID for generating grids, QUICKIN for preparing bathymetry, and QUICKPLOT for visualising simulation results, are available in the Delft3D system. In this study only Delft3D-FLOW and Delft3D-PART are utilised, and the theoretical background of these modules is described in the next section.

#### 2.3.7.1 General background of Delft3D-FLOW

Delft3D-FLOW is a core module of Delft3D, which solves the unsteady shallow-water equations in two-dimensions (one computational layer) or three-dimensions. Delft3D-FLOW comprises four main groups of equations for solving full Navier Stokes equations including the horizontal momentum equation, continuity equation, transport equation, and turbulence closure model. In Delft3D, the vertical momentum equation is reduced to a hydrostatic pressure relation as vertical accelerations are assumed to be small and are not taken into account.

Delft3D-FLOW uses an orthogonal curvilinear grid, which can curve along the boundary of the model domain, to provide high computational accuracy. The equations can be formulated in either orthogonal curvilinear co-ordinates or spherical co-ordinates. Using curvilinear co-ordinates, the free surface level and bathymetry are given relative to a flat horizontal plane whereas using spherical co-ordinates they are relative to the World Geodetic System 1984 datum (WGS84). The main equations used in the module are given in the following section (Deltares, 2014).

#### 2.3.7.2 Governing equations in Delft3D-FLOW

- ***The horizontal momentum equation***

The horizontal momentum equations in x- and y- directions (where x is parallel to the main flow direction, and y- is orthogonal to this) are:

$$\frac{\partial U}{\partial t}+u\frac{\partial U}{\partial x}+v\frac{\partial U}{\partial y}+\frac{\omega}{h}\frac{\partial U}{\partial \sigma}-fV=-\frac{1}{\rho_0}P_x+F_x+\frac{1}{h^2}\frac{\partial}{\partial \sigma}\left(v_V\frac{\partial u}{\partial \sigma}\right) \qquad \textit{Equation 2-2}$$

$$\frac{\partial V}{\partial t}+u\frac{\partial V}{\partial x}+v\frac{\partial V}{\partial y}+\frac{\omega}{h}\frac{\partial V}{\partial \sigma}-fU=-\frac{1}{\rho_0}P_y+F_y+\frac{1}{h^2}\frac{\partial}{\partial \sigma}\left(v_v\frac{\partial v}{\partial \sigma}\right) \qquad \textit{Equation 2-3}$$

in which the horizontal pressure terms, $P_x$ and $P_y$ are based on Boussinesq approximation, and are given by

$$\frac{1}{\rho_0}P_x = g\frac{\partial\zeta}{\partial x} + g\frac{h}{\rho_0}\int_\sigma^0\left(\frac{\partial\rho}{\partial x} + \frac{\partial\sigma'}{\partial x} + \frac{\partial\rho}{\partial\sigma'}\right)d\sigma' \qquad \textit{Equation 2-4}$$

$$\frac{1}{\rho_0}P_y = g\frac{\partial\zeta}{\partial y} + g\frac{h}{\rho_0}\int_\sigma^0\left(\frac{\partial\rho}{\partial y} + \frac{\partial\sigma'}{\partial y} + \frac{\partial\rho}{\partial\sigma'}\right)d\sigma' \qquad \textit{Equation 2-5}$$

$F_x$ and $F_y$, the horizontal Reynold's stresses are determined using the eddy viscosity concept, which is described by Rodi (1993). The concept is simplified into the following definitions:

$$F_x = v_H\left(\frac{\partial^2 U}{\partial x^2} + \frac{\partial^2 U}{\partial y^2}\right) \qquad \textit{Equation 2-6}$$

$$F_y = v_H\left(\frac{\partial^2 V}{\partial \mathrm{x}^2} + \frac{\partial^2 V}{\partial \mathrm{y}^2}\right) \qquad \textit{Equation 2-7}$$

- ***The depth-averaged continuity equation***

The depth-averaged continuity equation is derived from integrating the continuity equation over the total depth, in which the kinematic boundary conditions are at the water surface and bed levels. The depth-averaged continuity equation is given by:

$$\frac{\partial\zeta}{\partial t} + \frac{\partial[h\bar{U}]}{\partial x} + \frac{\partial[h\bar{V}]}{\partial y} = s \qquad \textit{Equation 2-8}$$

where $S$ represents the contributions per unit area due to the discharge or withdrawal of water, evaporation, and precipitation.

- ***Transport equation***

Delft3D-FLOW solves the advection-diffusion equation for mass transport by using horizontal and vertical viscosity ($v_H$, $v_V$) and diffusivity ($D_H$, $D_V$). The advection-diffusion equation is:

$$\frac{\partial[hc]}{\partial t} + \frac{\partial[hUc]}{\partial x} + \frac{\partial[hVc]}{\partial y} + \frac{\partial[\omega c]}{\partial\sigma} = h\left[\frac{\partial}{\partial x} + \left(D_H\frac{\partial c}{\partial x}\right) + \frac{\partial}{\partial y}\left(D_H\frac{\partial c}{\partial x}\right)\right] + \frac{1}{h}\frac{\partial}{\partial\sigma}\left[D_v\frac{\partial c}{\partial\sigma}\right] + hS \qquad \textit{Equation 2-9}$$

in which $S$ represents source and sink terms per unit area, as above.

For 2D simulation, the total horizontal eddy viscosity coefficient is composed of three elements and is defined by

$$v_H = v_{SGS} + v_V + v_H^{back} \qquad \textit{Equation 2-10}$$

and the total horizontal eddy diffusivity is defined in the same way as

$$D_H = D_{SGS} + D_V + D_H^{back} \qquad \textit{Equation 2-11}$$

Although 2D depth averaged simulation requires only two parameters, which are background horizontal viscosity, $v_H^{back}$ and background horizontal eddy diffusivity $D_H^{back}$ defined by the user, $v_H$ can be calculated from addition of $v_H^{back}$ and $v_{SGS}$, a computed value derived from the SGS-turbulence model (see Deltares (2014) for further information).

Likewise, $D_H$ can be calculated from addition of $D_H^{back}$ and $D_{SGS}$ derived from the sub-grid scale turbulence model, which is presented by Uittenbogaard (1998). In addition, horizontal large eddy simulation (HLES) can be used in calculating $v_H$ and $D_H$ (Uittenbogaard, 1998, Uittenbogaard and Van Vossen, 2004, Van Vossen, 2000). Using this approach, the values computed in the HLES sub-grid model are added to $v_H^{back}$ and $D_H^{back}$. For 3D simulations, $v_V$ and $D_V$ , are computed using a selected turbulence closure model as explained below.

- ***Turbulence closure models***

Several turbulence closure models implemented in Delft3D-FLOW are based on the eddy viscosity concept (Tikhomirov, 1991). The available turbulence closure models for determining $v_V$ and $D_V$ are: 1) constant eddy viscosity and diffusivity coefficients; 2) Algebraic Eddy viscosity closure Model (AEM); 3) k-L turbulence closure model; and, 4) k-ε turbulence closure model.

The first model is the simplest although under some conditions it can lead to laminar flow being predicted as it is based on a constant, user-specified, value. The second model does not use transport equations but uses algebraic/analytical formulas to determine the turbulent kinetic energy (k) and the mixing length (L). The third closure model involves one transport equation to find k but still uses the same algebraic/analytical formula as the second model to find L. In the last model, k and the dissipation, ε are produced by shear stress. All of turbulence closure models are extensively described in Deltares (2014).

#### 2.3.7.3 General background of Delft3D-PART

Delft3D-PART uses two or three-dimensional flow calculations from the Delft3D-FLOW module to simulate transport of conservative, or simple decaying, substances. Delft3D-PART is a deterministic model, except for the processes related to the random displacement of the particles for which a random-walk (Monte Carlo) method is used to simulate the stochastic nature of particle movement due to fluid turbulence. The movements of particles in water are governed by both advection due to the currents, and to horizontal and vertical dispersion as a consequence of fluid turbulence (Deltares, 2017a).

The simulation of particle movement separates the advection and diffusion components into two steps. Firstly, advection due to shear stresses from the bed surface and wind at the top of the free surface, is computed. The second step is the random walk step, in which the direction of movement is random and is related to horizontal and vertical dispersion. For each simulation, the horizontal and vertical dispersion coefficients are the required main input parameters for the random processes. The horizontal and vertical dispersion coefficients (Deltares, 2017a) are described as follows.

#### 2.3.7.4 Horizontal dispersion in Delft3D-PART

The horizontal dispersion coefficient is time dependent. Soon after release of particles at a specified location in the model domain, the plume of particles is relatively small and their mixing is influenced by local turbulence only. However, as the plume of particles becomes dispersed, larger-scale turbulence increasingly contributes to mixing. The horizontal dispersion coefficient is defined as:

$$D_{x,y} = at^b \qquad \textit{Equation 2-12}$$

in which $a$ and $b$ are coefficients that are obtained in calibrating the model (Bent et al., 1991), and $b$ is in the range 0 to 1. The time $t$ is defined from $t = 0$, the release time for the dispersing particles.

#### 2.3.7.5 Vertical dispersion in Delft3D-PART

In a well-mixed, horizontally uniform flow, the vertical dispersion coefficient is estimated from the mixing length and the turbulent kinetic energy as:

$$D_Z(Z') = \frac{k}{\sigma_C}\, h\,(1 - Z')\sqrt{Z'}\sqrt{U_{*b}^2 Z' + U_{*s}^2\,(1 - Z')} \qquad \textit{Equation 2-13}$$

where $Z' = Z - h$

Note that the $Z$ co-ordinate is defined downwards from the water surface, i.e. $Z = 0$ is at the surface and $Z = H$ is at the bottom.

#### 2.3.7.6 Boundary condition and open boundaries

To solve the differential equations described earlier requires that suitable boundary conditions are specified for all open boundaries. There are four available main types of boundary condition: water level, velocity, discharge, and Riemann, each of which is suitable to be applied in different situations. These boundary conditions can be used in combination to improve computational results. There is no rule for selecting boundary conditions, but satisfactory computational results from other modelling can be used as criteria to determine the best choice of boundary condition. Boundary conditions are often obtained from field measurements but can also be outputs from a large model into which a smaller model is nested.

In Delft3D, using linear interpolation, boundary conditions can be specified for unlimited boundary points along open boundaries. However, it is recommended that open boundaries are far from areas of interest so that the areas are unaffected by any physically unrealistic flows caused by the boundary condition itself and/or interpolation along the boundary. For this study, the open boundaries used in the model are a sea boundary and a fresh water boundary. The sea boundary is situated close to mouth of the estuary while the fresh water boundary is situated further up the river upstream of the tidal limit (Figure 2-8).

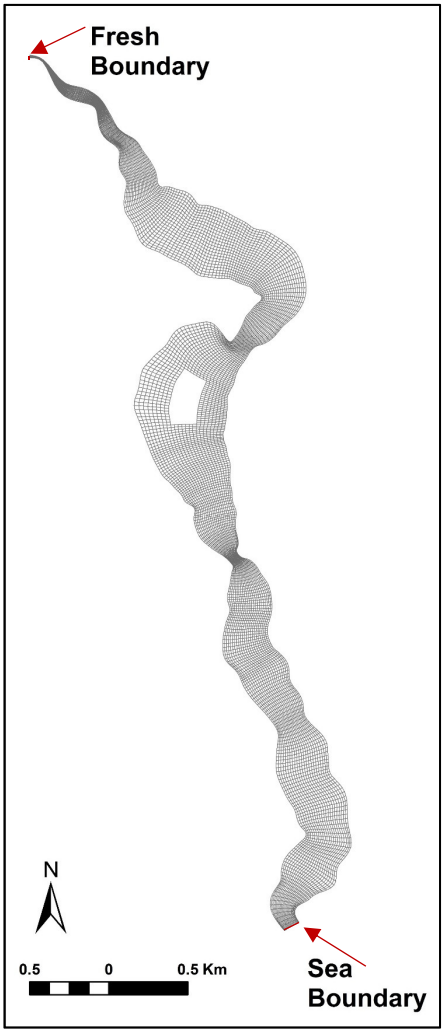


**Figure 2-8:** Open boundary locations for the model domain

### 2.3.7.7 Bottom roughness

In the Delft3D Flow module, a roughness coefficient is used to measure the resistance to the flow from the bed. This coefficient can be defined as a constant value over the whole area (uniform value) or as a spatially varying value (non-uniform value). The software allows for roughness to be computed in several ways as follows:

A) Manning coefficient, $n$, for which a typical value for an estuary is 0.02 ($m^{1/3}/s$) (Deltares, 2014, Lesser et al., 2004). This is converted within the model to the Chezy coefficient, $C$ computed by

$$C = \frac{h^{1/6}}{n}$$ *Equation 2-14*

B) Colebrook-White coefficient (Deltares, 2014), of which typical values are in the range 0.15 – 0.01 m, or less than 0.01 for smooth surfaces, is computed by

$$Cw = 18.\,log_{10}\left(\frac{12h}{k_s}\right) \qquad \textit{Equation 2-15}$$

C) Chezy coefficient, for which a first estimate can be computed from (Deltares, 2014)

$$C = 25 + h \qquad \textit{Equation 2-16}$$

For this study, the Chezy coefficient recommended by Deltares (2014) was used, as this is the simplest and produced numerically stable results.

#### 2.3.7.8 Numerical stability

The Courant-Friedrichs-Lewy (CFL) condition is used to indicate the numerical accuracy and stability of computations. The CFL number is a relation between flow speed and model time step. As the magnitude of the time step determines the total computational time, it is desirable to choose the largest time step which preserves numerical stability to reduce the total computational time.

In general, where the model domain has large differences of bottom geometry, and hence spatially varied flow properties, Courant numbers should not exceed 10 (Luijendijk, 2001). However, this value is a guide and the appropriate limit can vary between different model domains, and is spatially variable. Sensitivity testing is advised to find the largest time step which provides accurate, numerically stable, results. The CFL number for two-dimensional problems is defined by

$$CFL = 2\Delta t\sqrt{gh\left(\frac{1}{\Delta x^2}+\frac{1}{\Delta y^2}\right)} \qquad \textit{Equation 2-17}$$

#### 2.3.7.9 Installing Delft3D

Installing the Delft3D model starts from downloading pre-and post-processing Graphic User Interface (GUI) and the source codes for the required modules, all of which are available on Deltares' website. The GUI utilities programmes are run on the Windows platform, while the source codes of FLOW module (tagged 4440) can

be compiled on either Window or Linux platforms. For this study, Ubuntu version 12.04.1 LTS 64 bit was chosen for the compilations as all prerequisites including OpenSSh-server, Subversion, GNU autotools, GNU autoconf, libtool, g++, expat, gfortran, mpich2, flex, bison, libreadline6-dev, libexpat1-dev, libopenmpi-dev do not required licenses.

It is noted that the shell scripts of Delft3D-PART module are available to use after finishing FLOW module compilation. However, Delft3D-PART GUI still needs to be downloaded from Deltares' website. In addition, some editing on Delft3D-PART GUI scripts is required so as to make Delft3D-PART GUI appear on the main Delft3D-FLOW GUI.

#### 2.3.7.10 Bathymetry creation

The model inputs required for hydrodynamic and nutrient modelling using Delft3D model are river flow, tide, and bathymetry. However, no digital elevation model for the estuary was available and this needed to be created by merging data from different sources. An existing terrestrial LiDAR DEM, collected and processed by SEPA, was combined with self-collected single beam echo sounder data. The LiDAR DEM was provided in ERDAS Imagine IMG format with 2 m pixel size. The data were quantified from a near-infrared LiDAR system flown over the estuary on 11/09/2009, the same day that CASI data were acquired. However, the collection time of those data was different resulting in different tidal stage and water surface extent. As near-infrared light cannot penetrate the water surface, elevation values derived from the LiDAR data in inundated areas tend to represent the water surface rather than bottom elevation. Thus, only the elevation values from dry areas (exposed mudflats) were used to represent bottom elevation.

LiDAR elevation values for inundated areas were replaced with interpolated bottom elevations derived from an echo sounder survey. The surface water elevation from the LiDAR DEM could not be masked out by using the main channel extracted from the CASI data, as there were different acquisition times for the two datasets which therefore had different tidal levels and water surface extents. The water surface extent in the CASI image, particularly in the lower region of the estuary, was notably narrower than in the LiDAR DEM (Figure 2-9).

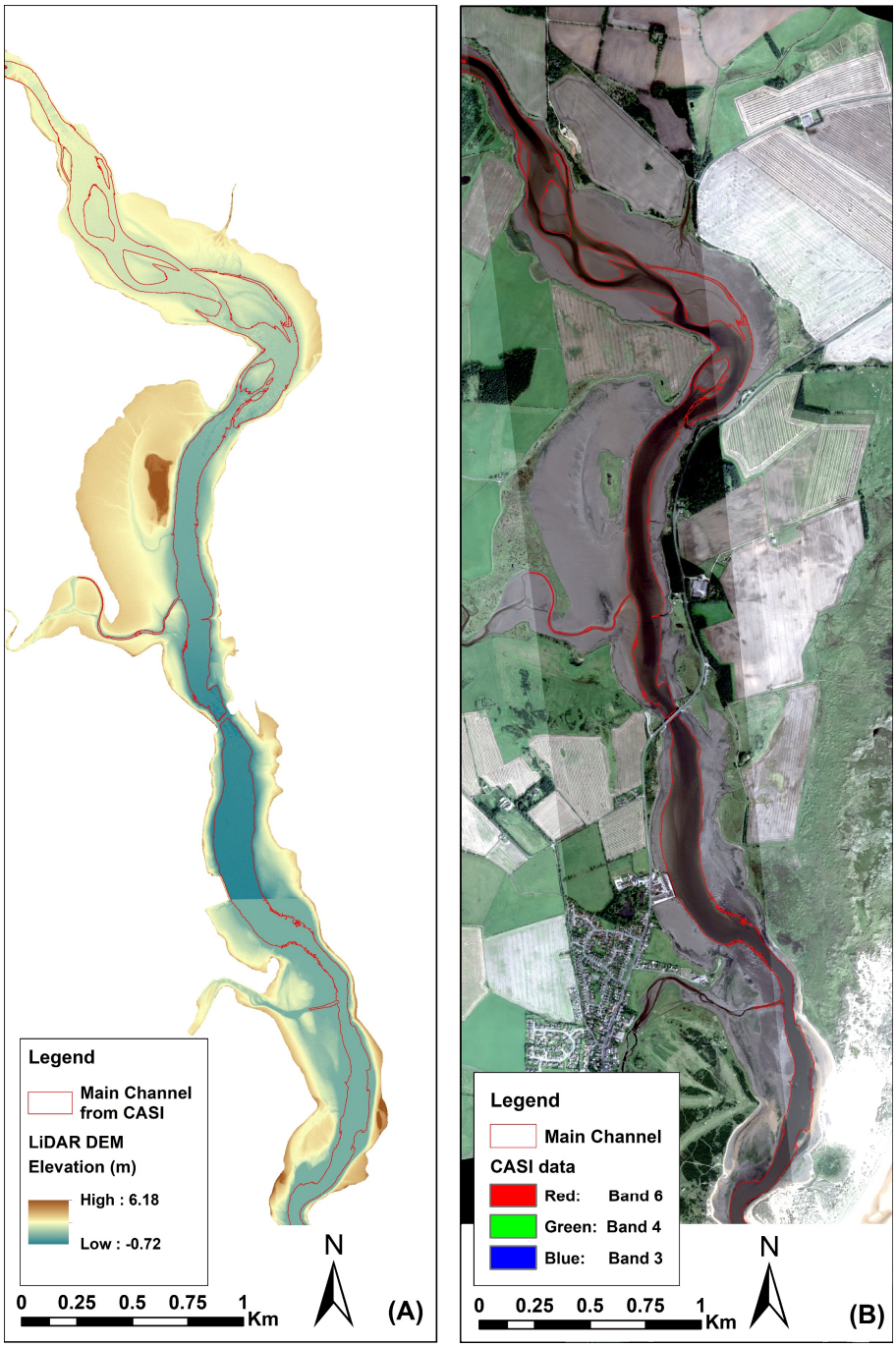


**Figure 2-9:** (A) LiDAR DEM, (B) CASI data acquired on the same day as LiDAR DEM at a different acquisition time, and the main channel in the LiDAR DEM (blue) overlaid with the main channel location extracted from the CASI data (red polygon) (A).

An echo sounder survey was carried out to collect bottom elevation followed by establishing an empirical relationship between elevation values from echo sounder and the LiDAR DEM. Elevation values in the main channel from the echo sounder are reliable and were interpolated and used to replace the LiDAR DEM data in inundated areas. Details of the steps in this process are as follows;

- ***Echo-sounder survey and LiDAR DEM validation***

A boat survey was conducted using a GPS-based single-beam acoustic echo sounding system to obtain bottom elevations in the main channel of the estuary on 10/09/2015 at high tide. During the survey, mean tide level referenced to chart datum measured at Aberdeen port ranged between 3.6 – 4.0m. The weather during the survey was sunny with no rain. Temperature was 16°C and wind direction was towards the south with light to moderate wind force at 13 km/h (gentle breeze), according to information from the weather station at Aberdeen airport (https://goo.gl/UD88y5).

The survey system comprised a GPS Leica 1200 base station located on the river bank, and both a GPS receiver (the rover) and a single beam echo sounder, Sonarmite V 3.0, mounted in line on a rigid pole on the boat (Figure 2-10). The sounder has acoustic pulse with a single frequency of 235 KHz and beam spread approximately 8 to 10 degrees with sound velocity range of 1400 to 1600m/sec. With its narrow beam width, the sounder can present a depth measurement at a more discrete point under the survey. OSGB1936 and ODN were defined as the horizontal and vertical reference systems for the GPS base station setups respectively. The survey system was operated by transmitting position and elevation data from the base station to the rover mounted in the boat, and water depths were collected by the single beam echo sounder while the boat moved along the survey transects.

The sounder was set to record measured depth every 2 seconds. 20 transects were surveyed along the main channel of the estuary in the lower region and 24 further transects in the central region so that elevation data quantified from the survey would represent real bottom elevation as much as possible (Figure 2-11). However, the survey was not carried out from the bottle neck at the Snub upward to Bridge at Kirkton of Logie Buchan in the upper region (Figure 1-3) as this area has limited accessibility by boat. To avoid any uncertainty produced by the model due to unreliable bottom elevation, this area is used as a buffer area in the model and is excluded from the modelling results.

To ensure good coverage, the survey also used ArcGIS software connected to a real time handheld GPS to locate the boat relative to a high-resolution satellite image. The background WV-2 image acquired on 20/04/2015 during low tide was used to help sail the boat along the designed transects. This technique reduced the risk that the boat entered shallow water resulting in possible damage, and also reduced the time and cost of the survey. After the survey, the bottom elevations were calculated from elevations derived from GPS minus the length from the GPS antenna to the echo sounder and minus the depth recorded by the echo sounder (Mastin and Fosness, 2009). The method is shown in Figure 2-10. The maximum depth value calculated from the survey was -4.85 m and the shallowest depth value was 1.08 m. The calculated bottom elevation values were used to create cross-section profiles for comparison with cross-section profiles derived from the LiDAR DEM, to represent the true shape of the main channel of the estuary.

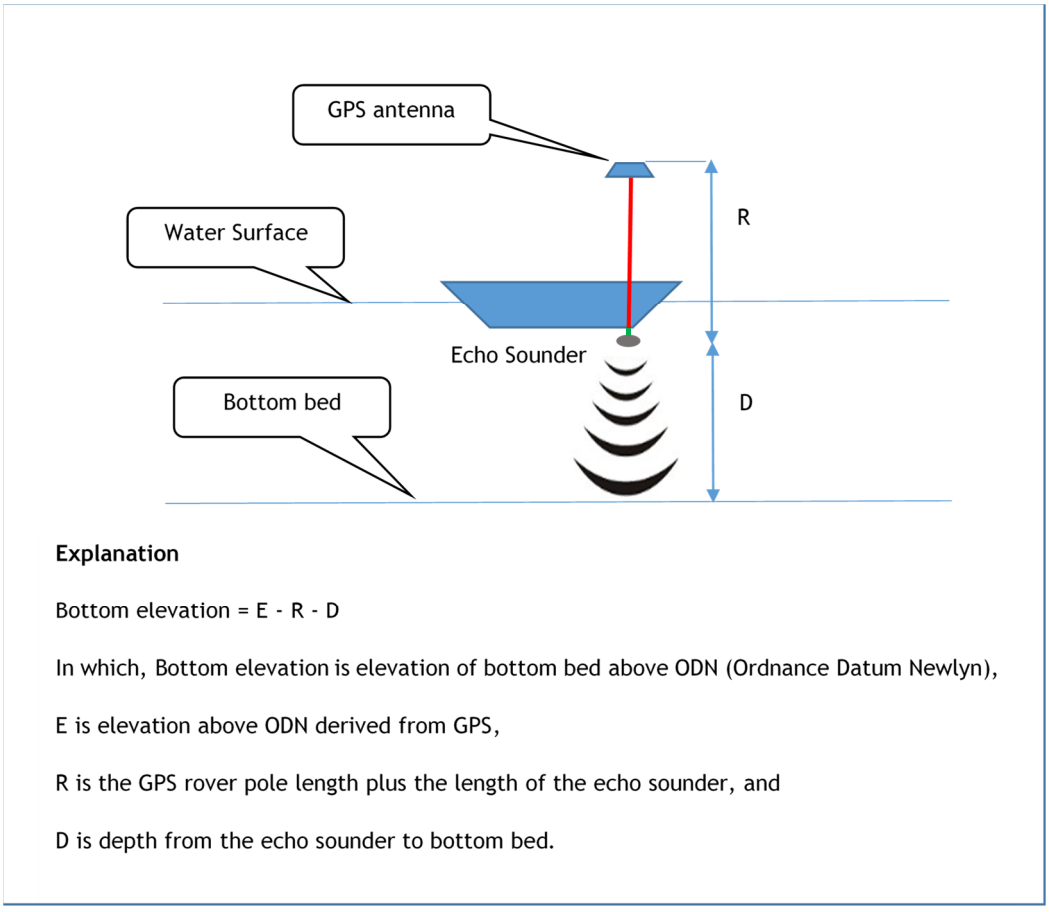


**Figure 2-10:** Boat survey system comprising of the rover and echo sounder mounted on the boat and explanation of bottom elevation measurement. The figure is adapted from Mastin and Fosness (2009).

LiDAR DEM validation was also carried out on the same day that the boat survey was conducted. GPS Real-Time Kinematic (RTK) technique, which gives potential accuracy of ±0.02m (Brown et al., 2006, Wolf and Ghilani, 2008, Woo et al., 2018), was used for the validation. The RTK was used to measure elevation at eight validation points, spread across the estuary (Figure 2-11). The RTK base station, located close to Ocean Lab's boat garage (Figure 2-11) was used to define the horizontal and vertical reference systems. The reference systems used were OSGB1936 National Grid (Ordnance Survey Great Britain 1936) OSGB 1936 as the horizontal reference and the ODN (Ordnance Datum Newlyn) as the vertical reference.

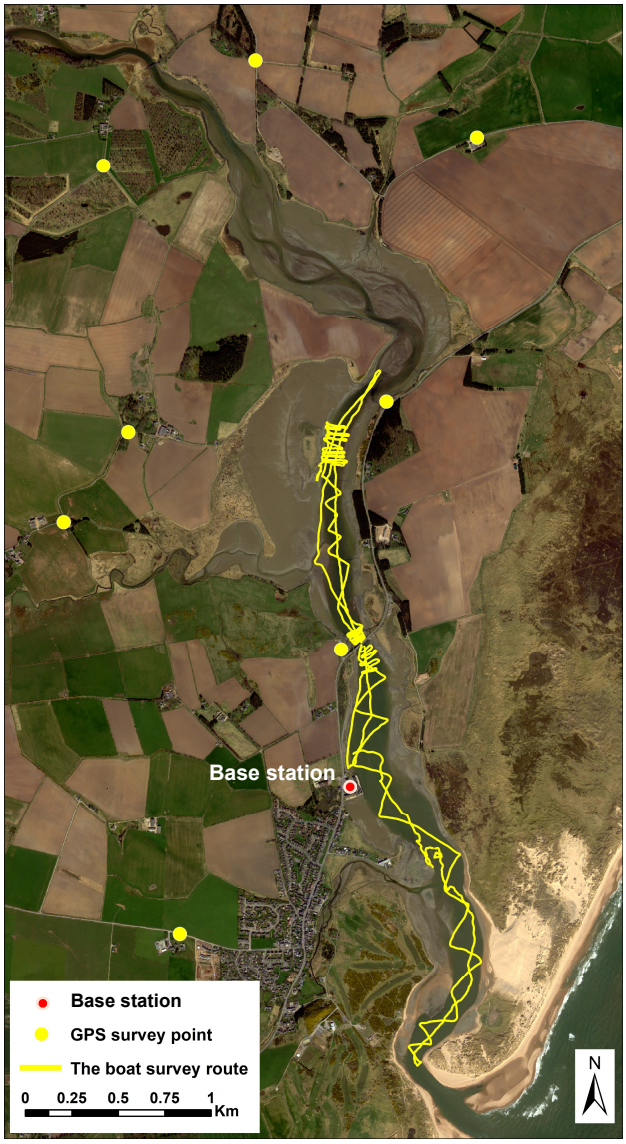


**Figure 2-11:** The bathymetric survey routes in the main channel of the estuary conducted on 10/09/2015, and GPS validation point locations.

Once the base station was set-up, the receiver (rover) was moved to each validation point. The real-time position and elevation obtained from the base station at the validation point were computed from the baseline between the base station and the rover and the known coordinates of the base station. Each point was measured three times to get an average position and elevation. Elevations of the eight validation points derived from GPS RTK measurements are shown in Table 2-3.

**Table 2-3:** Coordinates and elevations at validation points

| Validation point | Easting | Northing | GPS height (m) | LiDAR DEM height (m) | Residual (m) |
|---|---|---|---|---|---|
| GPS01 | 400100 | 826776 | 5.20 | 5.19 | -0.01 |
| GPS02 | 400344 | 828113 | 6.10 | 6.14 | 0.04 |
| GPS03 | 400832 | 829540 | 19.04 | 19.05 | 0.01 |
| GPS04 | 399639 | 829954 | 20.10 | 20.12 | 0.02 |
| GPS05 | 398819 | 829386 | 15.28 | 15.36 | 0.08 |
| GPS06 | 398953 | 827949 | 15.50 | 15.55 | 0.05 |
| GPS07 | 398606 | 827461 | 14.30 | 14.32 | 0.02 |
| GPS08 | 399231 | 825241 | 18.11 | 18.19 | 0.08 |

The elevations from the LiDAR DEM at the validation points are higher than elevations measured by GPS RTK by an average of 0.04 m with mean error 0.01 m. This slight bias is within the expected range; in general, the high correspondence suggests that the LiDAR DEM has very high relative accuracy (as needed for the model), and very good absolute accuracy. Since the LiDAR DEM provides high elevation accuracy, this study uses elevation from the LiDAR DEM as a reference and any systematic bias from areas inundated at the time of LiDAR data collection is subtracted based on the echo sounder data to retain the accuracy of the LiDAR DEM.

- ***Relationships between bottom elevation of the LiDAR DEM and the single beam echo sounder***

The 5,566 bottom elevation points collected from echo sounder survey were used to assess the correlation with the elevations from the LiDAR DEM. The results show that the LiDAR DEM has a positive relationship to the sounder data for bottom elevations higher than 0.1m OD [$R^2$ = 0.84], whilst for bottom elevations below 0.1 m OD the LiDAR DEM elevations fall into two groups, one at c.0m and one at -0.4m OD, and there is no correlation with the sounder data (Figure 2-12).

Hence, elevation values higher than 0.1 m found in the LiDAR DEM are considered to be reliable, whereas those lower than 0.1 m OD are not. To avoid errors from the two clusters of LiDAR elevations that show no correlation with the echo sounder data (Figure 2-12), only LiDAR DEM values greater than + 0.1 m are used directly in the estuary DEM. These data are merged with the interpolated bottom elevation obtained by the echo sounder, as explained in the next section.

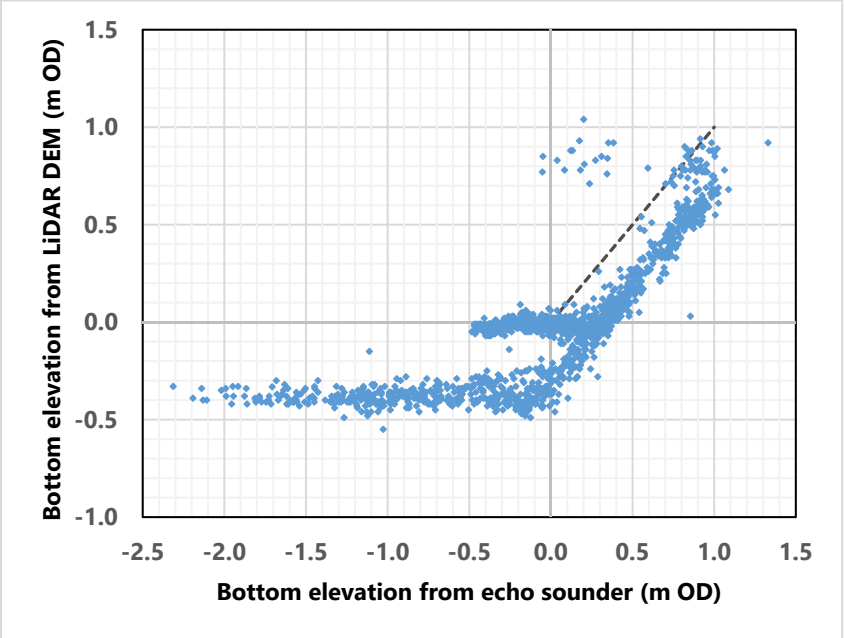


**Figure 2-12:** The bottom elevation from the terrestrial LiDAR DEM against echo sounder data. Note the different x- and y-axis scales.

- ***Interpolation of bottom elevation from echo sounder data***

Interpolation was applied to the data to predict bottom elevation values at unmeasured locations in the main channel, based on measured values from the echo sounder. Areas where bottom elevation values are lower than +0.1m in the LiDAR DEM were replaced by elevations interpolated using the function Geostatistical Analyst coupled with Spatial Analyst Tools in ArcGIS. Kriging was used to interpolate bed elevation in the man channel. Four different Kriging techniques including Simple Kriging (SK), Ordinary Kriging (OK), Universal Kriging (UK), and Empirical Bayesian Kriging (EBK) were tested to obtain the optimal predicted bottom elevations. The workflow to create new bathymetric data is shown (Figure2-13).

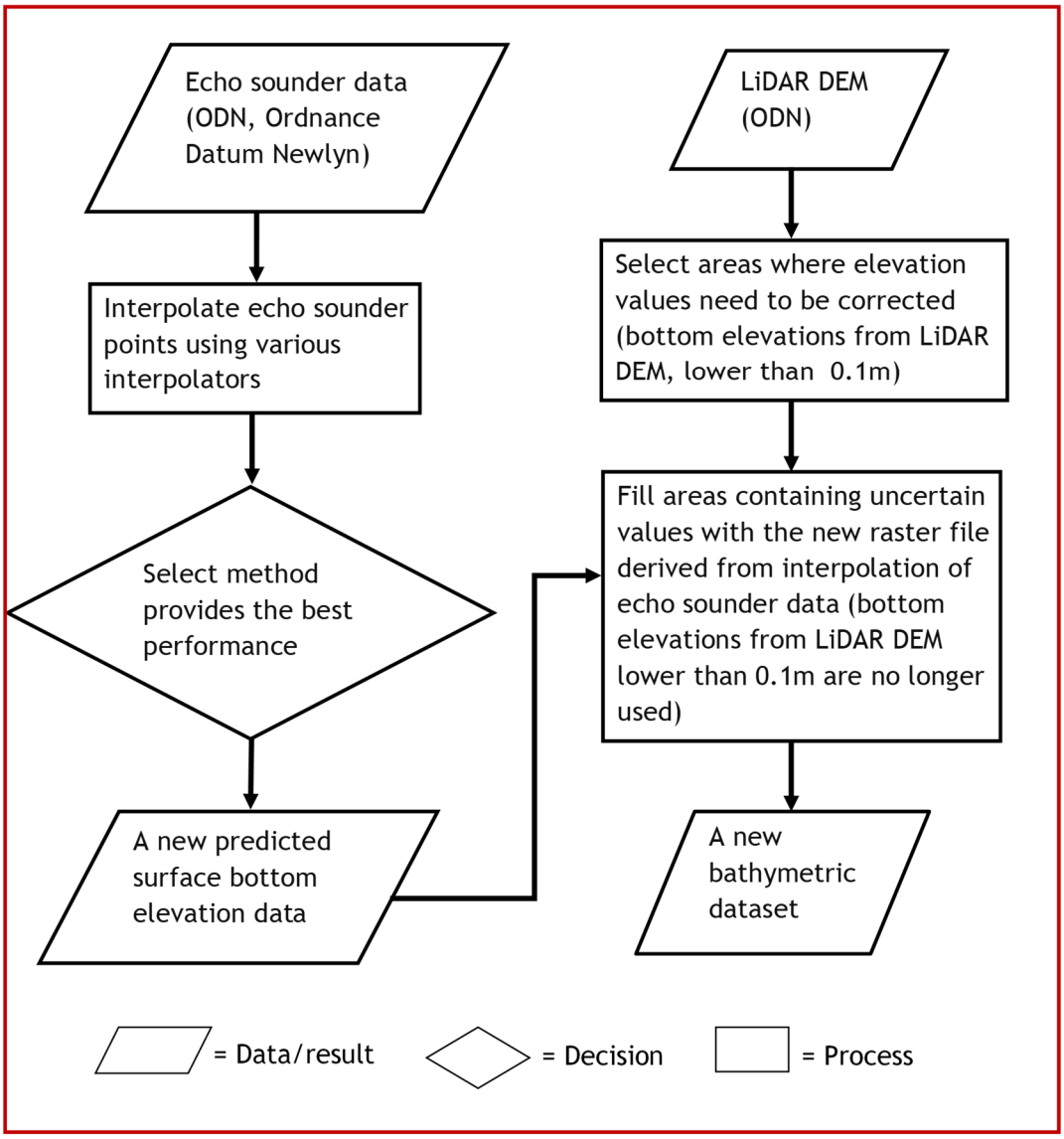


**Figure 2-13:** The workflow for creating a new bathymetric data

Cross validation showed that Empirical Bayesian Kriging provided the best results giving the smallest root mean square error, average standard error, mean prediction error (closest to 0), and root-mean-square standardized errors (closest to 1) (Table 2-4). After the interpolation process, the predicted bottom elevation was integrated into the LiDAR DEM data to obtain the new DEM for the entire estuary (Figure 2-14), which is used as the topographic input for the Delft3D model.

Table 2-4: Analysis and assessment of interpolation techniques

| Method | RMS (m) | Mean prediction error (m) | RMS standard prediction (m) | Average standard error | Maximum depth (m) |
|---|---|---|---|---|---|
| SK | 0.19 | -0.03500 | 0.318 | 0.604 | -3.91 |
| OK | 0.13 | -0.00059 | 0.418 | 0.326 | -4.40 |
| UK | 0.13 | -0.00059 | 0.567 | 0.247 | -4.40 |
| EBK | 0.12 | 0.00056 | 0.923 | 0.127 | -5.17 |

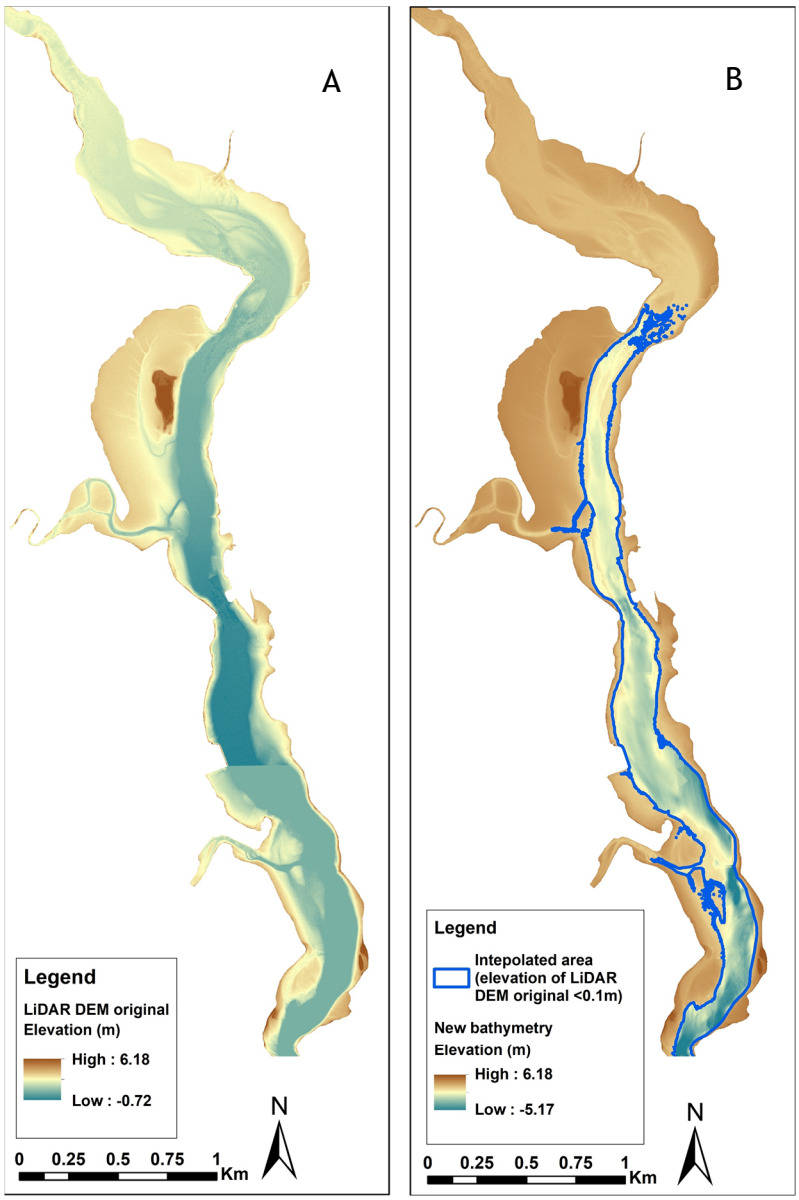


Figure 2-14: Bottom elevation from using EBK kriging technique (B) compared to the original LiDAR DEM (A).

#### 2.3.7.11 Model parameter testing and model assessment

- ***Model parameter testing***

Before using Delft3D to simulate hydrodynamics and nutrient pathways at specific flow and tide conditions, overall sensitivity testing of the key physical and numerical parameters in the model was undertaken. The bottom roughness, horizontal eddy viscosity, and horizontal diffusivity were varied to find their optimal values for use in the model domain. This testing used the one-factor-at-a-time (OFAT) approach, where one parameter is varied at a time while keeping all other parameters fixed (Cariboni et al., 2007, Saltelli et al., 2008). OFAT results indicate the robustness of the results to changes in each individual parameter (Pannell, 1997). The extent of inundated areas derived from the ratio image derived from the NDWI analysis using WV-2 and Landsat-8 were used in selecting model parameter settings.

- ***Model assessment***

After determining model sensitivity to the parameters mentioned previously, and selecting the most suitable values of each parameter to use across the model domain, the last step is assessing the credibility of the model results. Anderson and Bates (2001) note that the validity of a model can be categorised into two elements, conceptual validation and performance validation. Conceptual validation involves assessment of model structure. Performance validation involves comparing modelled data with independent data, preferably measured but potentially from other model outputs. This study focuses on how well the model predicts hydrodynamics and nutrient pathways and does not aim to adjust model formulation, although the parameter values (Chezy coefficient, eddy viscosity, and eddy diffusivity) are based on sensitivity tests. Hence, the second type of assessment is relevant here. Measured data and results from image processing are compared with the model results to assess the effects of the applied physical and numerical parameters on model predictions.

*a) Using measured water depths for modelled water depth assessment*

Due to funding availability, the buoy data and water depth data measured by echo sounder during the boat survey are the only field data available for model validation. The measured water depths, which are derived from the same datasets

used to create the new bathymetric data used as model input, were used to assess the quality of water depths modelled using 15-minute interval river flow and sea level data as boundary conditions. The boat survey took about one hour to cover the lower region and some parts of the central region of the estuary during high tide conditions, but the modelled water depths were simulated every 15 minutes. Thus, survey transects that have collection times that correspond closely to the output times of the modelled water depths are selected for validation. The measured and modelled water depths are plotted against each other to understand the performance of the model.

*b) Using NDWI for assessing modelled flooded-dry areas*

The ratio image derived from the NDWI technique was used for validating the delimitation of flooded and dry areas by the model. The ratio image, which represents areas covered with water (flooded areas) and exposed mudflats (dry areas), revealed those areas at the time when the WV-2 image was taken, 11:30 am, on 20 April 2015 and the Landsat- 8 image was taken, 11:10 am, on 30 September 2015. These ratio images then were used as references to compare with the modelled water depths simulated at 11:30 am and 11:10 am on the same dates. The threshold depth, a numerical parameter to determine wet/dry condition of a grid cell in the model, was set as 0.001 m. Thus, any grid cell in the model that had water depth higher than this threshold value was considered wet.

Since a raster format is the natural output of satellite data and is simple to manipulate (Chang, 2006, Mitchell, 1999), this study used comparison between a raster modelled water depth files and a raster ratio image files to assess the delimitation of flooded and dry areas by the model. The modelled water depths simulated at 11:10 am and 11:30 am were exported to a grid file format with the same grid size (15m and 0.5m) as a grid file of the ratio images. Then, the raster modelled water depth file and the ratio image were reclassified into flooded and dry groups. The files were later compared using the Con tool in the Raster calculator function in ArcGIS. The matching areas of modelled water depths and ratio images and wet/dry in error can be identified using simple multiple conditional expressions (equations 2-18 to 2-21).

$$Matching\ flood =$$

$$Con\ (("ratio\_image"\ ==\ 1)\&("modelled\_waterdepth"\ ==\ 100), 1000, 0) \quad \textit{Equation 2-18}$$

$$Matching\ dry =$$

$$Con\ \big((\text{ratio\_image}\ ==\ 2)\&(\text{modelled\_waterdepth}\ ==\ 200), 2000, 0\big) \quad \textit{Equation 2-19}$$

$$Flood\ in\ error =$$

$$Con\ \big((\text{ratio\_image}\ ==\ 2)\&(\text{modelled\_waterdepth}\ ==\ 100), 999, 0\big) \quad \textit{Equation 2-20}$$

$$Dry\ in\ error =$$

$$Con\ \big((\text{ratio\_image}\ ==\ 1)\&(\text{modelled\_waterdepth}\ ==\ 200), -999, 0\big) \quad \textit{Equation 2-21}$$

where 1 is the index value for flooded areas in the ratio image, 2 is the value for dry areas, 100 is for flooded areas in the modelled water depth data, 200 is the value for modelled dry areas, 1000 is assigned to matched flooded areas, 2000 to matching dry areas, 999 for areas flooded in error in the model and -999 for areas that the model has as dry in error. 0 is assigned for mis-matched areas.

*c) Using NDVI for modelled nutrient concentration and pathway assessment*

The NDVI in early autumn 2009 and late spring 2015 were used to assess modelled nutrient concentrations and transport pathways. The nutrient behaviour was derived from simulation of a conservative tracer using the Delft3D-PART module. The tracer input was not scaled to the magnitude of actual nutrient input, with 1kg of conservative tracer instantaneously released from the upstream fresh water boundary (River Ythan input) as the input for the simulation.

The modelled nutrient concentrations during the slow current period around high tide, which lasts for approximately three hours, were the focus in this study since this slack water condition enables nutrients to be taken up by plants more than in flood or ebb conditions (Davies and Ugwumba, 2013). The normally distributed modelled nutrient concentrations were categorised into five zones: level five (very high), level four (high), level three (medium), level two (low), and level one (very low). The class breaks above and below the mean at intervals of half, one, one-half, two, and three deviations of the mean. The strength of the linear relationship between NDVI and nutrient concentration zone was assessed using Pearson correlation. In addition, a group of NDVI pixels in each of the nutrient concentration zones was extracted using the Extract by Mask tool in Spatial Analysis, ArcGIS. The distributions of these extracted NDVI values were examined

using box plots. Details of the model parameter testing, and the model assessment are presented in Chapter 5.

#### 2.3.7.12 Modelling hydrodynamics, nutrient concentrations and pathways for specific scenarios

After finishing sensitivity testing and model validation, the selected optimal values of the model parameters and model settings were used to simulate hydrodynamics, nutrient concentrations and pathways as follows.

- ***Modelling hydrodynamics at specific flow conditions***

Hydrodynamics were simulated at different river flow conditions (high and low flows) to help to understand patterns with different river flow inputs. Modelling hydrodynamics in 2009 was the focus in this study as in this year the estuary was severely affected by algal blooms (Gov.scot, 2011). High flow, particularly in late winter and early spring, which is likely to carry large quantities of nutrients to the estuary before the summer algae blooming period was the main focus. As a comparison, a low flow event (mid-spring and late summer), which is expected to transport lesser nutrient quantities was also investigated. Additionally, high flow in autumn was studied to understand seasonal variations of hydrodynamic patterns in the estuary. Hydrodynamics from events in 2011 and 2015 were also simulated to understand inter-annual variations. Furthermore, hydrodynamics during both spring and neap tide conditions were studied to understand the effects of different tidal forcing. In all cases, the modelled hydrodynamics were then used for modelling nutrient concentrations and pathways.

- ***Modelling nutrient concentrations and pathways at specific scenarios***

The conservative tracer simulation was used to model patterns of nutrient concentration and transport pathways during high and low flow events. Four release points were identified to create realistic scenarios for the locations of nutrient input. Release point 1 was located at the upstream fresh water boundary (River Ythan input) and release points 2-4 were located at the three tributaries to the estuary. The tracer simulation used two scenario types. In the first group of scenarios, the tracer was released from a single release point during both the flood tide and the ebb tide. In this group, tracer was first introduced from release point 1, then from release points 2, 3, and 4, respectively. In the second group of scenarios, tracer was released from the four release points at one time on each

of the flood and ebb tides. The instantaneous release of 1kg of conservative tracer was used as the tracer input for all simulations. The tracer input was not scaled to actual nutrient input. It was simulated to understand nutrient movement and nutrient concentrations in the estuary, which can be applicable to other sites having the same problem as the Ythan. Details of the two scenarios are presented in Chapter 6. The modelled nutrient concentrations and pathways can be used to inform explanations of algal mat locations in the Ythan estuary.

### 2.3.8 Analysis of intertidal substrate

Remote sensing data were not only used to calculate the NDWI and NDVI, which were used as proxies for flooded and dry areas and location of macroalgae growth in model validation, the data were also used to study macroalgal bloom behaviour in the estuary, which are explained in Chapter 4.

# Chapter 3: The Ythan estuary and its surrounding environment

This chapter outlines the characteristics of the River Ythan catchment, including its geology, land cover, soil, geology, river network, population in the catchment, and sewage point sources. The hydrology (river flow and tides), geomorphology, sediments (grain size, organic matter), macroalgal bloom location, and changes in mudflat location and extent are described. Data on water quality, including temperature, pH, DO, turbidity, and Chlorophyll-a, are presented to give an initial understanding of the influence of river flow on water quality in the estuary. Interactions between river flow, tides and Chlorophyll-a, which is used as a proxy for nutrient concentration in the estuary, are analysed to understand the influence of river flows and tides on nutrient concentrations. The environment throughout the catchment provides insight into the controls over physical and hydrological characteristics of the estuary, which can be used to explain the hydrodynamics and nutrient fluxes in the Ythan estuary.

## 3.1 Characteristics of the river Ythan catchment and surrounding areas

The River Ythan catchment occupies a total area of 690 $km^2$. It is categorised as a gently rolling lowland (Morris and Morris, 2005, Nature.scot, 2009), and its rises to higher areas in the west reaching a maximum of 380.4 m above sea level. The catchment average annual rainfall is approximately 800 mm (Morris and Morris, 2005, Nature.scot, 2009) with average annual air temperature of 10.9°C, a summer average of 14°C, and a winter average of 3.2°C (Nature.scot, 2009). The catchment physical characteristics are as follows;

### 3.1.1 River network

The catchment includes the main River Ythan and 45 tributaries. The main river is approximately 63 km in length, of which 8 km lies within the estuarine area (Domburg et al., 1998, Morris and Morris, 2005) (Figure3-1). Apart from the River Ythan, there are four small tidal rivers connected to the Ythan estuary, Burn of Forvie and Burn of Auchmacoy in the north, and Tarty Burn and Foveran Burn in the west (Figure3-1). The straightening and deepening of river channels for land drainage are commonly found in the catchment and surrounding the estuary

(Morris and Morris, 2005), a result of high intensity agricultural activities in the area.

### 3.1.2 Land cover

Agriculture dominates land use in the catchment and the total area of agricultural land in the catchment remained reasonably constant from 1960 -1990 (Domburg et al., 1998). According to Land Cover Map 2007, agriculture dominates land use in the catchment, with 57.9% of the area used for arable/ horticultural farming and 32.3% being improved grass land. The remaining area mainly consists of woodland (6.9%), heather/bog (1.9%), and urban (1.3%) (Figure3-2) and there are no reports of significant land cover change in the catchment since 2007.

### 3.1.3 Soil

Agricultural lands in the catchment generally consist of a mixture of brown forest soil, one of the most the fertile soils in Scotland (Domburg et al., 1998), noncalcareous gleys, poorly drained soils which largely support grassland agriculture, and humus-iron podzols, acidic and nutrient deficient soils that support a number of uses (Domburg et al., 1998). In terms of soil texture and drainage properties, freely draining sandy loam soils dominate the western, higher, parts of the catchment, with loamy and sandy textures toward the east (Figure 3-3). Sandy clay loam soils are mostly found surrounding the estuary, which suggests that the catchment become less well drained towards the east (Domburg et al., 1998). Regarding these characteristics, the soils in the Ythan catchment belongs to the hydrological soil type (HOST) class 17, which is classified as relatively free draining soils with a large storage capacity overlying hard impermeable rocks with little or no storage capacity (Domburg et al., 1998).

### 3.1.4 Geology

According to Geology Map 2008 and Tetzlaff et al. (2011), the Ythan catchment is mostly underlain by metamorphic rocks with very low permeability, including psammite, pelite, and semi-pelite (Figure 3-4). Although normally hard and highly impermeable, weathering processes can create fractures within the upper few metres of the rock, resulting in small quantities of groundwater occupying these fractures (Tribe and Ball, 2005).

### 3.1.5 Population and sewage point sources

The population density is low, being ≈ 44 persons.km$^{-2}$(Edwards et al., 2003).The two largest towns are Ellon, at the head of the estuary close to the upper tidal limit, with population ≈ 10,000 and Newburgh located close to the sea with population ≈ 1400 (Aberdeenshire.gov.uk, 2016, Edwards et al., 2003, Gillibrand and Balls, 1998).There are four sewage works, one sewage farm and three sluices in the catchment and surrounding the estuary (Figure 3-1). The Ellon sewage works (Figure 3-1) contributes the largest discharges of P (≈25 kg/day) and N (≈75 kg/day); however, this nitrate load is less than 5% of the total load in the river (Raffaelli, 1999). The second largest point source is from Newburgh sluice (Figure 3-1), which releases about 8 kg/day of N and 2.6 kg/day of P (Raffaelli, 1995, Raffaelli, 1999).

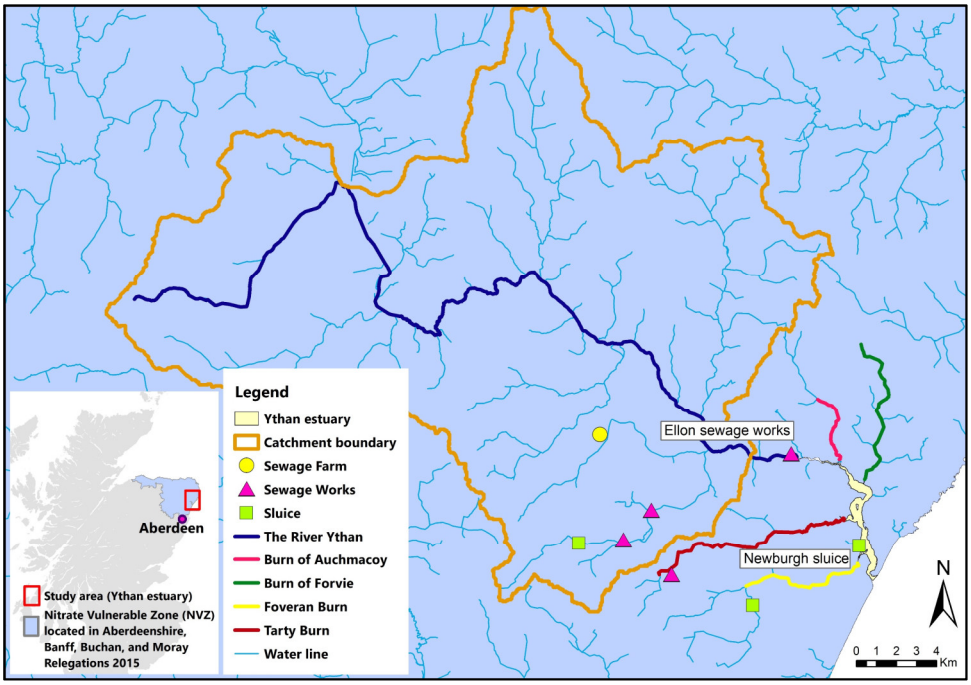


**Figure 3-1:** Rivers and nutrient point sources in the River Ythan catchment and areas surrounding the estuary in 2017 (source: OS Open Rivers 2017 and Points of Interest 2017, downloaded from EDINA Digimap Ordnance Survey Service [http://digimap.edina.ac.uk], 29 Jan 2018).

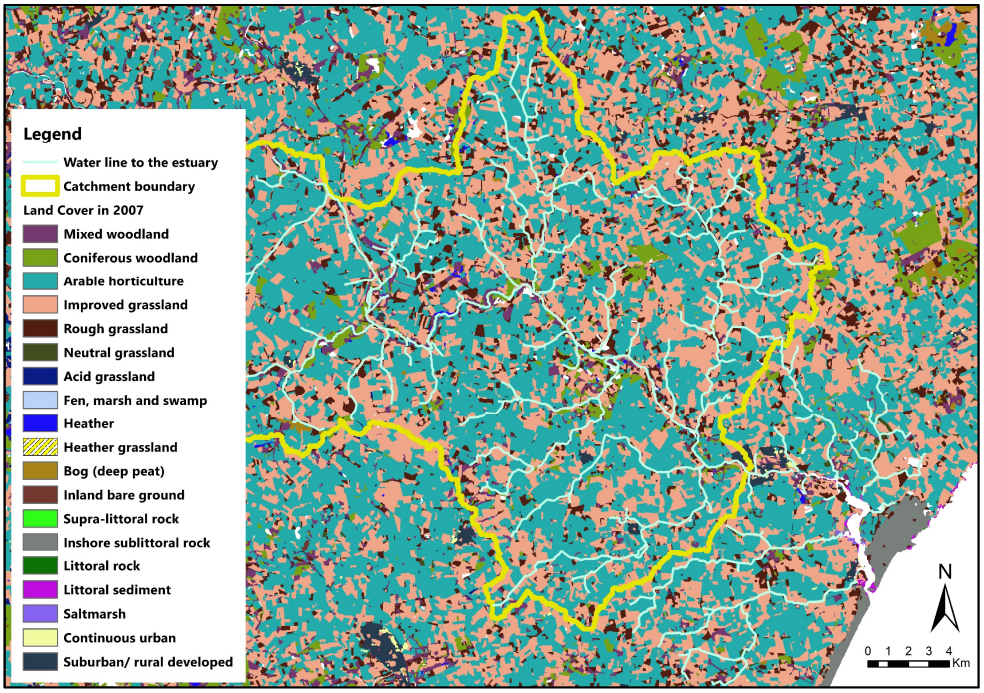


**Figure 3-2:** Land cover in the River Ythan catchment and areas surrounding the estuary in 2007 (source: Land Cover Map 2007, downloaded from EDINA Environment Digimap Service [http://digimap.edina.ac.uk], 29 Jan 2018).

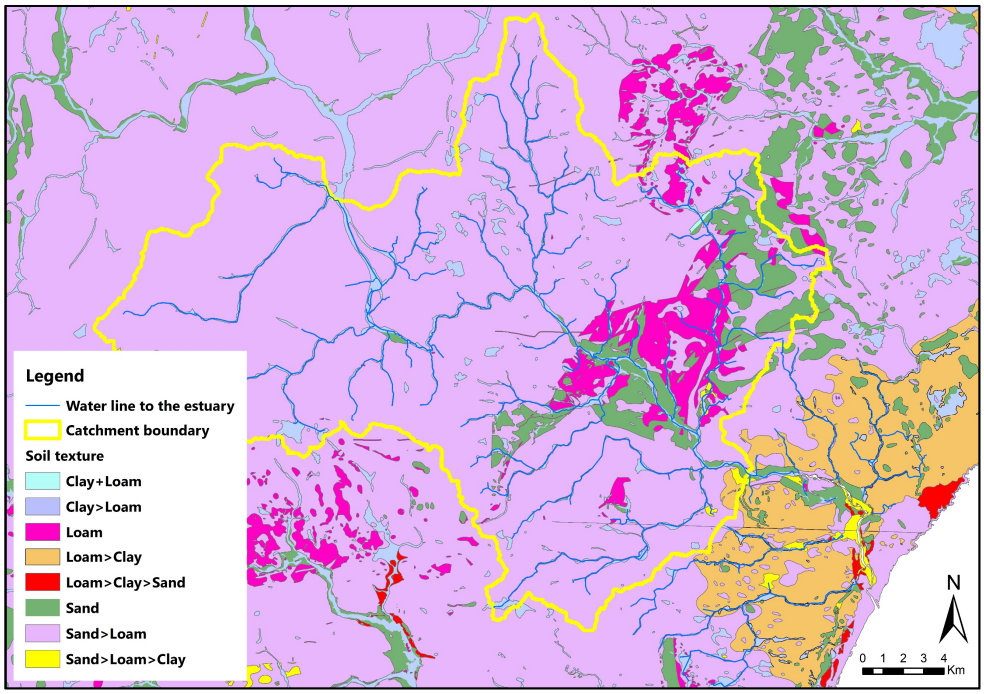


**Figure 3-3:** Soil texture in the River Ythan catchment and areas surrounding the estuary in 2011 (source: Soil Parent Material Model, downloaded from EDINA Environment Digimap Service [http://digimap.edina.ac.uk], 29 Jan 2018).

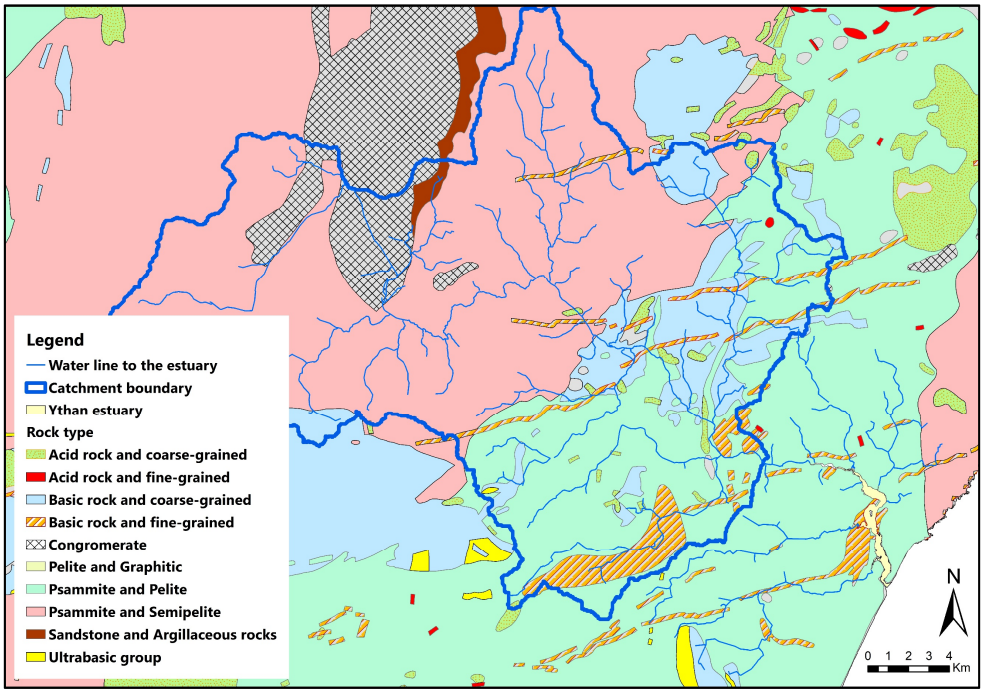


**Figure 3-4:** Underlying geology of the River Ythan catchment and areas surrounding the estuary (source: DiGmapGB-250 updated 2008, downloaded from EDINA Environment Digimap Service [http://digimap.edina.ac.uk], 29 Jan 2018).

## 3.2 River flow characteristics

Figure 3-5 shows that a consistent overall pattern in the flow in the Ythan with no obvious long-term trend. The seasonal variation in precipitation (Figure 3-6) produces a consistent winter peak and continuous reduction to low summer flow levels. In most years there are one or more events that exceed 50 $m^3/s$, but over one six-year period, 1989-94, flow never exceeded 40 $m^3/s$, which corresponds to years with extensive algal mat development (Figure 1-6). The seasonal variation leads to highest daily mean flow in December-January of most years (Figure 3-6).

The summer dry period (July - August; days 272-334) has generally low flows but intense rainfall events can produce significant summer floods with peaks of over 30 $m^3/s$ (Figure 3-6). Very low flows, less than or equal to 5 $m^3/s$, can also occur at any time of year except for late winter (February; days 124-152). High flows, over 30 $m^3/s$, represent 2.0% of the time (Figure 3-7). The two years of this study include a relatively dry year, 2015, and 2016 which included the highest flow recorded during the period since 1985 (Figure 3-5). During 2016, 4.0% of days exceeded 20 $m^3/s$ and 2.0% exceeded 50 $m^3/s$. In contrast, during 2015 the highest flow was 50 $m^3/s$, 2.0% of days had flow exceeding 20 $m^3/s$ (Figure 3-7).

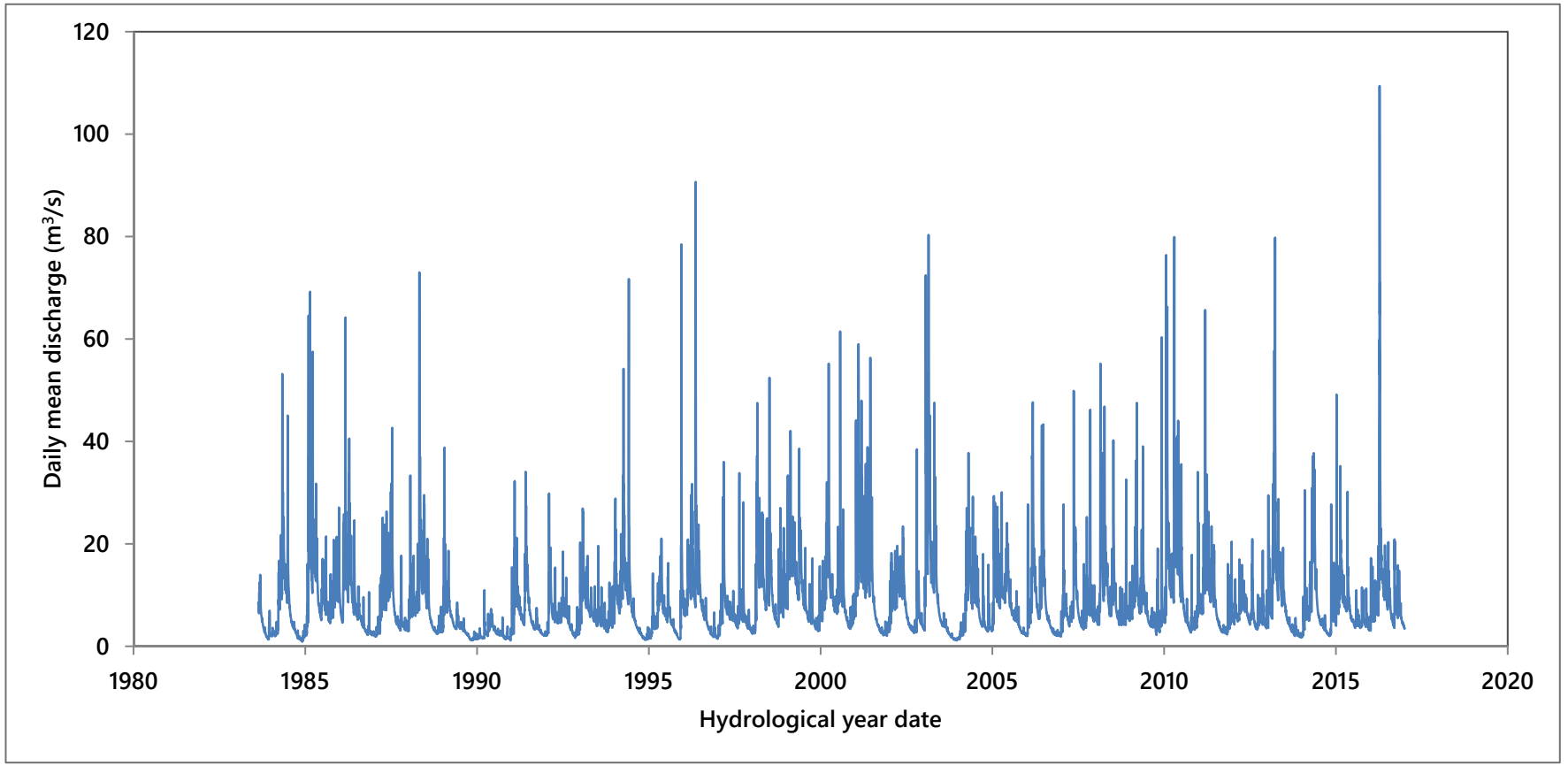


**Figure 3-5:** Daily mean flow for the full period of record (1985-2016); source: NRFA; location of measurement (Ellon), SEPA site code 10003.

Note: hydrological year starts on 1st October.

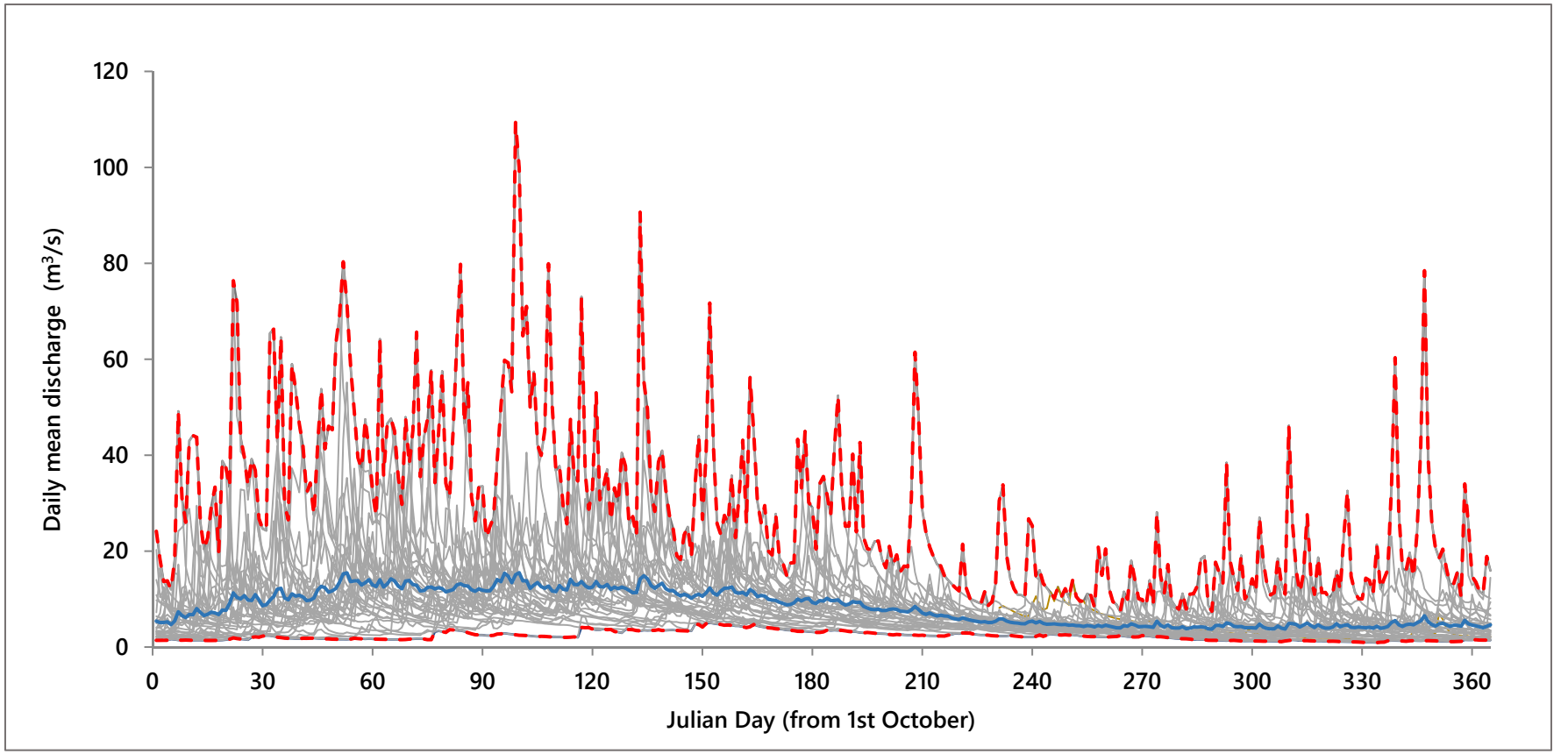


**Figure 3-6:** Daily mean flow for each day of every year of record (grey lines); the maximum value (red), overall mean (blue), and the minimum (red) recorded on each day of the year. February 29th has been excluded from the calculations.

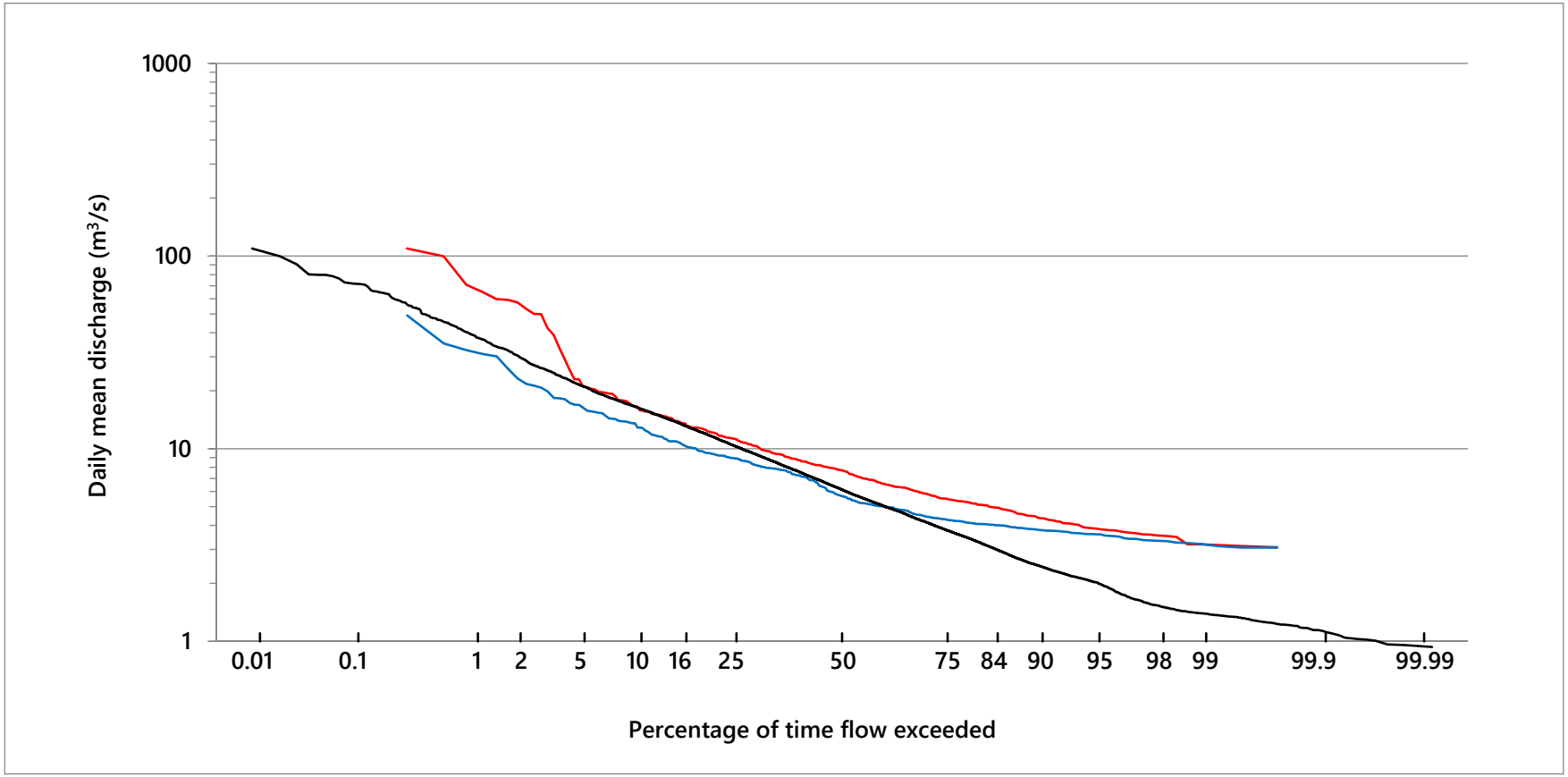


**Figure 3-7:** Flow duration curve for the full period of record, 2015, and 2016; all data (19/5/1983 onwards) (black), 2014/15 (blue), 2015/16 (red).

## 3.3 Tidal characteristics

According to Leach (1971), the Ythan estuary has a semi diurnal tide; two high and two low tides a day. The tidal range decreases from 4 m at the mouth to about 1m at the Snub (Figure 1-3) (Gillibrand and Balls, 1998, Leach, 1971). The farthest point upstream where the river is affected by tides is at the town of Ellon (Gillibrand and Balls, 1998). The flushing time of the estuary has been estimated as ranging between one tidal cycle and 5-12 days (Balls et al., 1995, Leach, 1971). The extent of salt water intrusion into the estuary varies seasonally in relation to the amount of freshwater discharged (Leach, 1971, Baird and Milne, 1981, Gillibrand and Balls, 1998).

Measured 15-minute interval tidal levels from 2009 - 2013 show inter- and intra-annual fluctuations. There is no evidence of extreme high tide levels. Mean minimum [maximum] daily tidal levels ranged from 0.1 – 3.0 m [3.0 m – 5.0 m] above CD in 2009, 0.0 – 3.2 m [3.1 – 4.2 m] in 2010, 0.0 – 3.2 m [3.0 m – 5.1 m] in 2011, and 0.0 - 2.0 m [3.0 m - 5.2 m] in 2013 (Figure 3-10). Mean daily tidal ranges were 1.2 m - 4.5 m above CD (mean range 3.0 m) in 2009, 1.8 m – 4.6 m above CD (mean range 2.9 m) in 2010, 1.5 m – 4.3 m above CD (mean range 3.0 m) in 2011, and 1.4 m - 4.6 m above CD (mean range 3.0 m) in 2013 (Figure 3-8). Salinity in the estuary varies according interaction of river flow and tide. The high salinities are in low river flow months with average maximum of 36.06 ppt and minimum of 0.41 ppt and mean of 18.23 ppt.

Although average annual mean spring and neap tides from 2009 - 2013 were slightly different, average annual maxima, minima and daily tidal range were mostly equivalent over this period (Table 3-1), suggesting low variation of tidal levels in the north-east coast of Scotland. Spring tides produced higher ranges than neap tides, on average 41.3% greater. These ranges are important as spring tides with greater tidal ranges may exert greater influence on nutrient transport patterns in the estuary than neap tides, for similar river flow conditions.

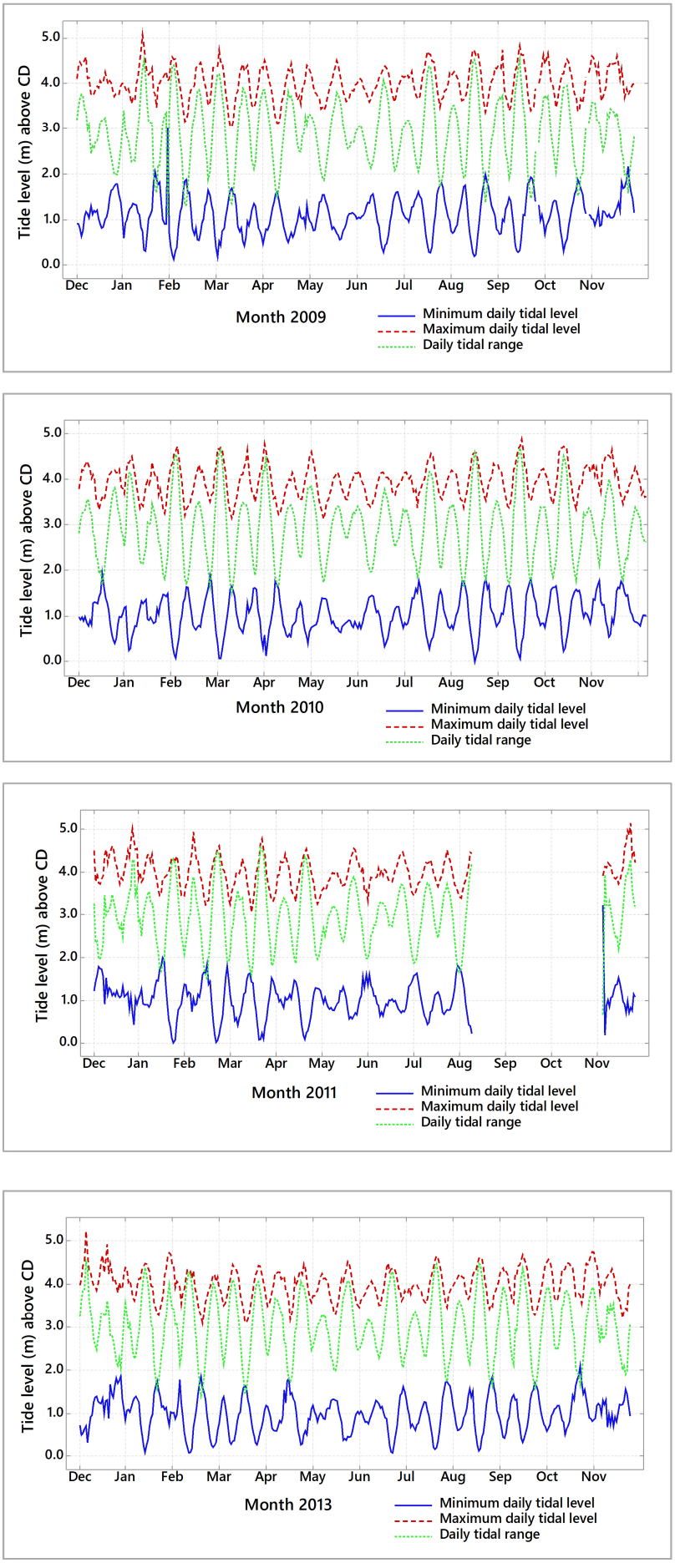


**Figure 3-8:** Mean maximum (red), minimum (blue) and range (green) of tide data from 2009-2013 (tide data from BODC).

**Table 3-1:** Average tide level from 2009 to 2013 (tide level above CD)

| | 2009 | 2010 | 2011 | 2013 |
|---|---|---|---|---|
| Average maximum | 4.0 | 4.0 | 4.0 | 4.0 |
| Average minimum | 1.1 | 1.0 | 1.0 | 1.0 |
| Average neap tide | 2.2 | 2.4 | 2.3 | 2.2 |
| Average spring tide | 3.3 | 3.2 | 3.0 | 3.4 |
| Average tidal range | 3.0 | 2.9 | 3.0 | 3.0 |

## 3.4 Types of estuary

Estuaries can have of a range of different geological and geomorphological origins, as explained in Fairbridge (1980) and Perillo (1995). The main types of estuary are briefly described below.

### 3.4.1 Fjord estuaries

This estuary type is created by glacial erosion as advancing glaciers shape river valleys into long narrow u-shaped channels with steep sides and a characteristic shallow sill at the seaward end of the channels (ABPmer, 2011, Fairbridge, 1980, Perillo, 1995) (Figure 3-9A). Seawater floods into the valleys creating the estuaries after glacial retreat (ABPmer, 2011, Fairbridge, 1980, Perillo, 1995). Fjord estuaries are the deepest estuary type (Perillo, 1995). With their channel profile, fresh water inputs tend to be larger than seawater, which is obstructed by sill at the mouth. As a result, there is a poor flushing particularly from the deeper parts of the estuary (Davidson, 2016, Perillo, 1995).

### 3.4.2 Fjard estuaries

The estuaries are also created by advancing glaciers but they have channels that are shorter, shallower, and broader than those of fjord estuaries (ABPmer, 2011, Fairbridge, 1980, Perillo, 1995). In addition, they have more irregular shapes and often no main channel (Fairbridge, 1980, Perillo, 1995). They are usually located along relatively low relief coasts with mud flats, salt marshes, and flood plains (ABPmer, 2011) (Figure 3-9B). As these estuaries are more exposed to wave and tide action due to their shallow topography, flushing tends to be faster than in fjord estuaries (Davidson, 2016, Perillo, 1995).

### 3.4.3 Ria estuaries

Ria estuaries are drowned river valleys (ABPmer, 2011, Fairbridge, 1980, Perillo, 1995), formed by a substantial rise in sea level, submergence of the lower reaches of the river valley due to tectonic subsidence, or a combination of both (Davidson, 2016). Rias typically have widening funnel shapes with deep, narrow and well-defined channels (Britannica, 1998) (Figure 3-9C). Mudflats and salt marshes are found in ria estuaries (ABPmer, 2011), and while they often have several branching tributaries they can also be straight with no significant branches (Davidson, 2016). As ria estuaries have no barrier or delta complexes at their entrances, the estuaries are strongly influenced by tides resulting in well-mixed water conditions (Britannica, 1998, Davidson, 2016, Hume and Herdendorf, 1988).

### 3.4.4 Coastal plain estuaries

This type of estuary also has its origin as a submerged river valley formed as a result of rising sea levels (Davidson, 2016, Perillo, 1995). They have a funnel shaped planform and are formed in areas of low relief (Figure 3-9D) (Davidson, 2016, Perillo, 1995). These estuaries often contain extensive mudflats, saltmarshes, sand flats and floodplains alongside meandering main channels which deepen and widen towards the mouth (ABPmer, 2011, Davidson, 2016). The beds of these estuaries are usually sediments, with mud often in the upper regions and coarser sediments found towards the mouth. Maximum depths in such estuaries are generally less than 30m (Davidson, 2016). Fresh water in the estuaries is relatively small compared with the tidal volume and so tides dominate circulation patterns in the estuaries (Davidson, 2016, Perillo, 1995).

### 3.4.5 Bar-built estuaries

Bar-built estuaries occur when ocean waves and/or tidal currents transport sediments shoreward, building up bars at the entrance of the estuaries (Morrissey and Sumich, 2012, Ross, 1995) (Figure 3-9E). These estuaries are shallow, are usually found on very low relief coasts and they have deposits of silts, muds and sands near their mouths (ABPmer, 2011). They often also have seasonal variation of fresh water inputs (Prandle and Lane, 2015) and large volumes of sediments may be transported from the river into the estuary during floods. Because of the constriction at the mouth, tidal current velocities can be high in this area but

rapidly reduce in the wider parts further inland (Morrissey and Sumich, 2012, Ross, 1995). Where the estuary mouth bar is ephemeral being eroded during periods of river flooding or strong tidal currents, such estuaries have been referred to as blind estuaries (Figure 3-9F)(Davidson, 2016, Friedrichs and Wright, 1997, Hume and Herdendorf, 1988, Ross, 1995).

### 3.4.6 Delta front estuaries in ephemeral distributaries

Delta front estuaries are typically found on shallow coasts with weak tidal currents (Davidson, 2016, Perillo, 1995, Ross, 1995). They occur when river-derived sediments accumulate at the mouth of the river as a delta, the shape of which depends on the interaction between the size of the river input and the ocean waves and tidal currents that erodes these sediments (Davidson, 2016) (Figure 3-9G). As the slope of the river channels decreases downstream towards the delta front, the river channels often bifurcate into a short network of distributaries, creating a delta front estuary (Bianchi and Allison, 2009, Davidson, 2016, Ross, 1995).

### 3.4.7 Compound estuaries

Compound estuaries are those that have complex origins with some characteristics of more than one estuary type. This complexity reflects their evolution through time resulting from interactions between sea level, marine energy, fluvial dynamics and tectonic processes (Davidson, 2016, Hume and Herdendorf, 1988, Ross, 1995) (Figure 3-9H).

The Ythan estuary originates in a region of low relief and exhibits characteristics of a bar-built estuary (Figure 3-9E) as a large mobile sand dune complex (Sands of Forvie) extends northwards from the mouth of the estuary. The dunes are comprised of sands carried offshore by the river and shoreward by ocean waves, winds, and tidal currents (Flemming, 2011, Nature.scot, 2009). The dunes which are approximately 20 m high (Nature.scot, 2009), provide protection from winds for the estuary and also help to dissipate tidal energy. The Ythan also exhibits some characteristics of coastal plain estuaries (Figure 3-9D), including the occurrence of mudflats and saltmarshes along the main channel, coarser sediment deposition towards the estuary mouth, and progressive changes in the shape of the main channel cross-section towards the mouth.

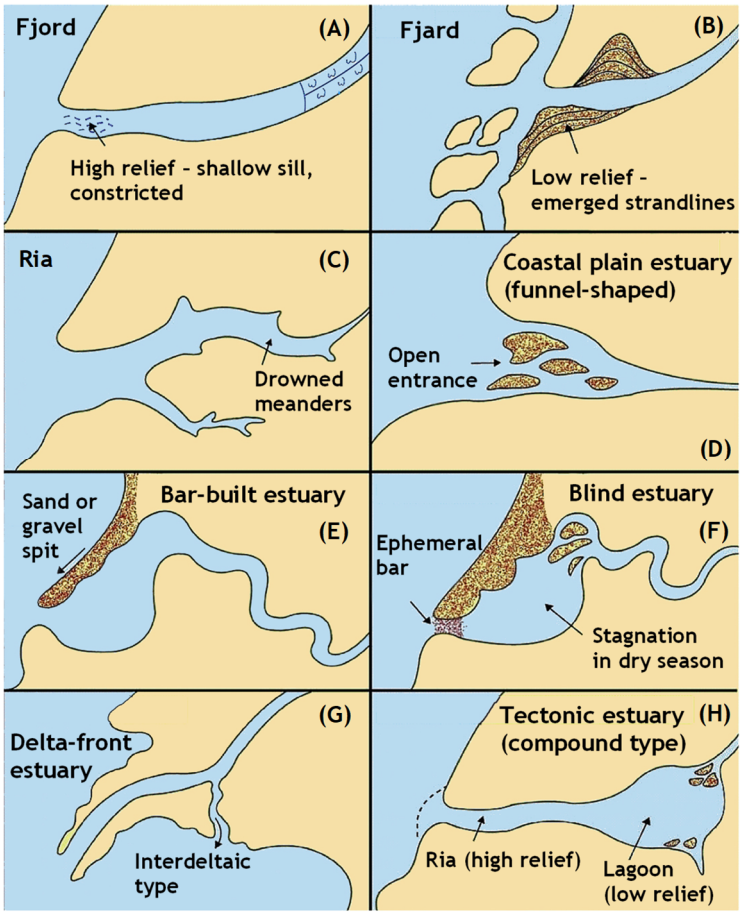


**Figure 3-9:** Estuary type classified by geomorphology. Modified from Fairbridge (1980) and Flemming (2011).

## 3.5 Mixing process in the Ythan estuary

In addition to the shape of the estuary, mixing process and tidal range (Dalrymple et al., 1992, Flemming, 2011), both of which control the nature of water circulation, are also important aspects in defining estuarine characteristics (Dalrymple et al., 1992, Flemming, 2011). In terms of mixing processes, the ratio between the tidal flux and the fluvial discharge is used to identified three types of mixing conditions in the estuary (Dalrymple et al., 1992, McFeeters, 1996, Reading, 1996). A ratio of <20 is typical for well-stratified or salt-wedge estuaries, 20-200 indicates partially stratified estuaries, and ratios >200 are indicative of well-mixed estuaries (Dalrymple et al., 1992, McFeeters, 1996, Reading, 1996).

### 3.5.1 Well-stratified estuaries (or salt-wedge estuary)

Well-stratified estuaries occur when river flows discharge rapidly into the sea, hence are found where tidal currents are relatively weak (Dalrymple et al., 1992, McFeeters, 1996, Reading, 1996). As a result, advection of fresh water to the sea dominates over the transport of sea water upstream. In this mixing condition, a sharp boundary between fresh water and seawater is created as fresh water, which is less dense than seawater, is buoyant above a wedge of saltwater (Molles, 2010, Ross, 1995) (Figure 3-10A).

### 3.5.2 Partially mixed estuaries

In partially mixed estuaries, fresh water mixes with seawater at all depths but the water in the lower layers remains more saline than the top layers. In addition, the salinity gradually decreases from the mouth of the estuary upstream (Ross, 1995) (Figure 3-10B). Well-mixed estuaries occur when fresh water discharge is relatively low and weaker than tidal currents (Ross, 1995).

### 3.5.3 Well-mixed estuaries

In well-mixed estuaries, the fresh water is mixed by interaction with strong tidal currents so that the salinity is the same from the upper to the lower layers of the water column. The spatial pattern of salinity in well-mixed estuaries is similar to that in partially mixed estuaries, being highest at the mouth and progressively decreasing upstream towards the source river (Ross, 1995) (Figure 3-10C).

Estuaries can be classified according to their tidal range, and tidal ranges <2m, between 2-4 m, and >4m are classified as microtidal, mesotidal, and macrotidal estuaries, respectively (Boothroyd, 1978, Dalrymple et al., 1992, McFeeters, 1996, Reading, 1996). According to Flemming (2011), microtidal estuaries are usually small and are likely to be well stratified. Conversely, macrotidal estuaries, which are often large and shallow, tend to be well mixed. Mesotidal estuaries, in which river flow usually has little influence on tidal dynamics (Prandle and Lane, 2015) tend to be well mixed and to develop partially stratified water in some areas. Flemming (2011) and Prandle and Lane (2015) note that the classification of estuaries according to mixing processes leads to estuaries changing from one type to another in response to changes in river flow or changes in tidal forcing due to neap-spring tidal cycles.

The average tidal range in the Ythan estuary is not more than 4 m, and the ratio between the tidal prism and river flow during neap tides is about 10:1 and 20:1 during spring tides (Leach, 1971, Baird and Milne, 1981, Gillibrand and Balls, 1998). The estuary can thus be classified as a well-mixed mesotidal estuary. Although the tidal dominance of the Ythan estuary results in well-mixed water particularly in the deep main channel, some stratification of the water column can also develop, and has been observed in the upper part of the estuary from the Snub to the bridge at Kirkton of Logie Buchan (Raffaelli, 1999, Raffaelli, 2000).

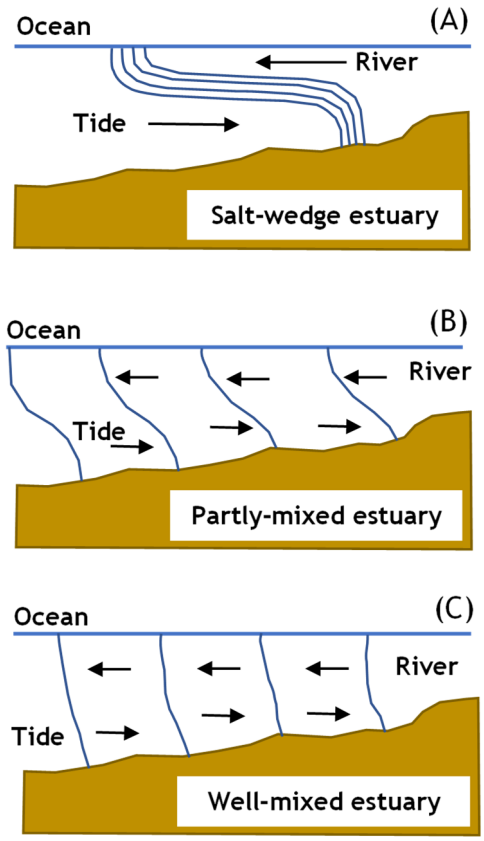


**Figure 3-10:** Classification of estuaries according to mixing process; (A) stratified estuary (salt-wedge), (B) partially mixed estuary, (C) well-mixed estuary, modified from Valle-Levinson (2010).

## 3.6 Sediment characteristics of the Ythan estuary

Analysis of seven grain-size samples shows that sediment size distributions in the estuary were positively (coarse) skewed. There is variability between the sediment size distributions as the mud flats and salt marshes in this estuary are comprised of sediments from more than one source. The sorting and skewness depended on sample location. Coarse silt (44.2 - 62.5 µm) was dominant at sample sites 1, 2, 3,

4 and 7 (central region; Figure 2-3). Fine sand was the modal size at sample sites 5 and 6 (upper region). Substrates at the seven sample sites can be seen in Figure 3-11. The results from the 62 samples collected by SEPA on August 12, 2014, reveal that fine sediments (medium coarse silt, 44.2-62.5 μm) were predominant in samples collected from the upper and central regions of the estuary, where algal mats normally developed. In contrast, coarser sand-sized sediments, were found in samples collected from the lower region. These results correspond to the results derived from sediment grain size analysis from the seven surface sediment samples taken during the first field visit.

As for organic matter, there is a non-linear relationship between sediment grain size and organic matter with Pearson correlation of -0.62 ($p<0.001$) (Figure 3-12), with organic matter concentration being low (<1%) in sediments >240 μm, and only exceeding 2% in the finer sediments (median size <80 μm). The spatial distribution of organic matter concentration shows the association between higher organic matter values and fine sediment deposits (central region of the estuary) with less organic matter in coarser samples (lower region) (Figures 3-13A, B).

Interpolation of median sediment grain size to produce a predictive map of sediment size (Figure 3-14), coarse silts dominate in the upper region from Burn of Forvie across to Snub and in the extensive mudflats in the central region. Very fine and fine sands are mainly found at the tributary mouth bars at Tarty Burn and Foveran Burn and areas close to the Sands of Forvie and John's Hole Point in lower region. Superimposing the macro algal mat location data (collected by SEPA on August 12, 2014) on the predicted sediment grain size map shows a high degree of correspondence with the distribution of high organic concentration fine sediments.

However, macroalgal mats are also found in some areas where there are coarser sediments with lower organic concentrations, in particular at the tributary mount bars at Tarty Burn and Foveran Burn and areas close to the estuary mouth (Figure 3-14B). In addition, *Chaetomorpha* and *Ulva* species dominate in the central and upper region where salinity levels are likely to be less due to the dilution effect of fresh water. However, *Chaetomorpha* can also be found at tributary mouths in the lower estuary where fresh water also has an influence. *Enteromorpha*, conversely are only found in the lower region where salinity is higher (Figure 3-14A).

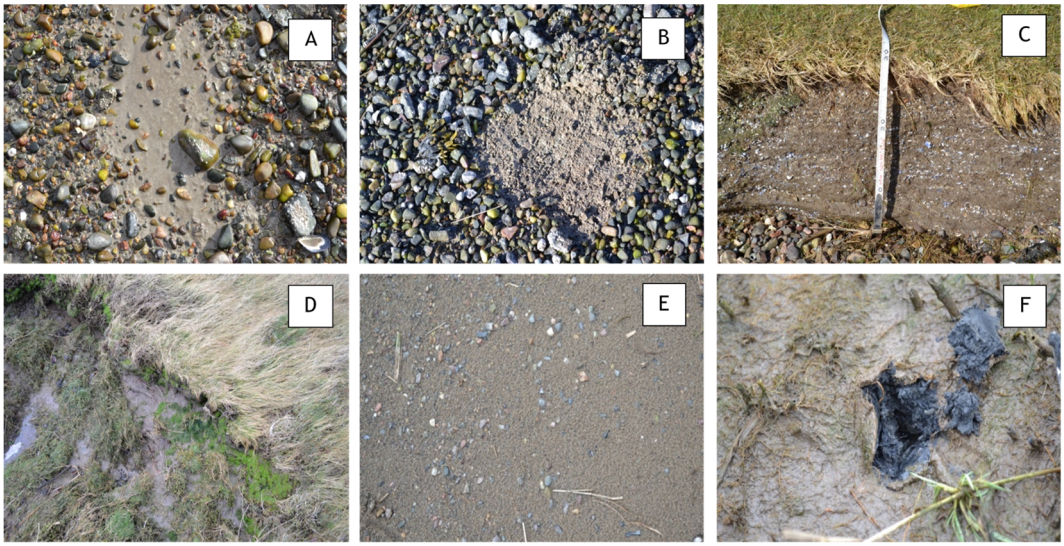


Figure 3-11: Substrates at sample sites: (A) sample site 1; (B) sample site 2 - note that the coarse gravel surface layer has been removed in part of the image to show the underlying fine sediments; (C) sample site 3; (D) sample site 7; (E) sample site 5; (F) sample site 6. See Figure 2-3 for sample locations.

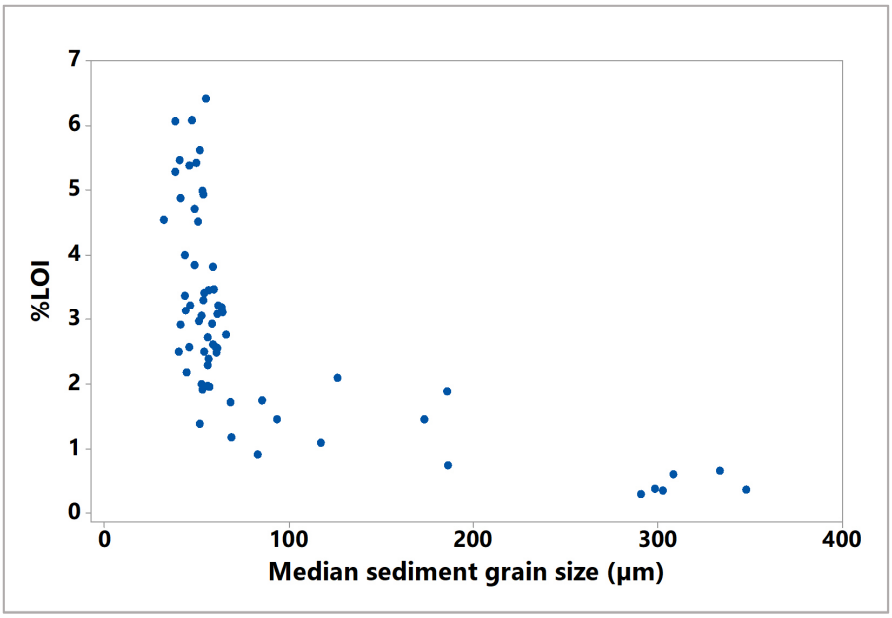


**Figure 3-12:** Non-linear relationship between sediment grain size and percentage Loss on Ignition (%LOI).

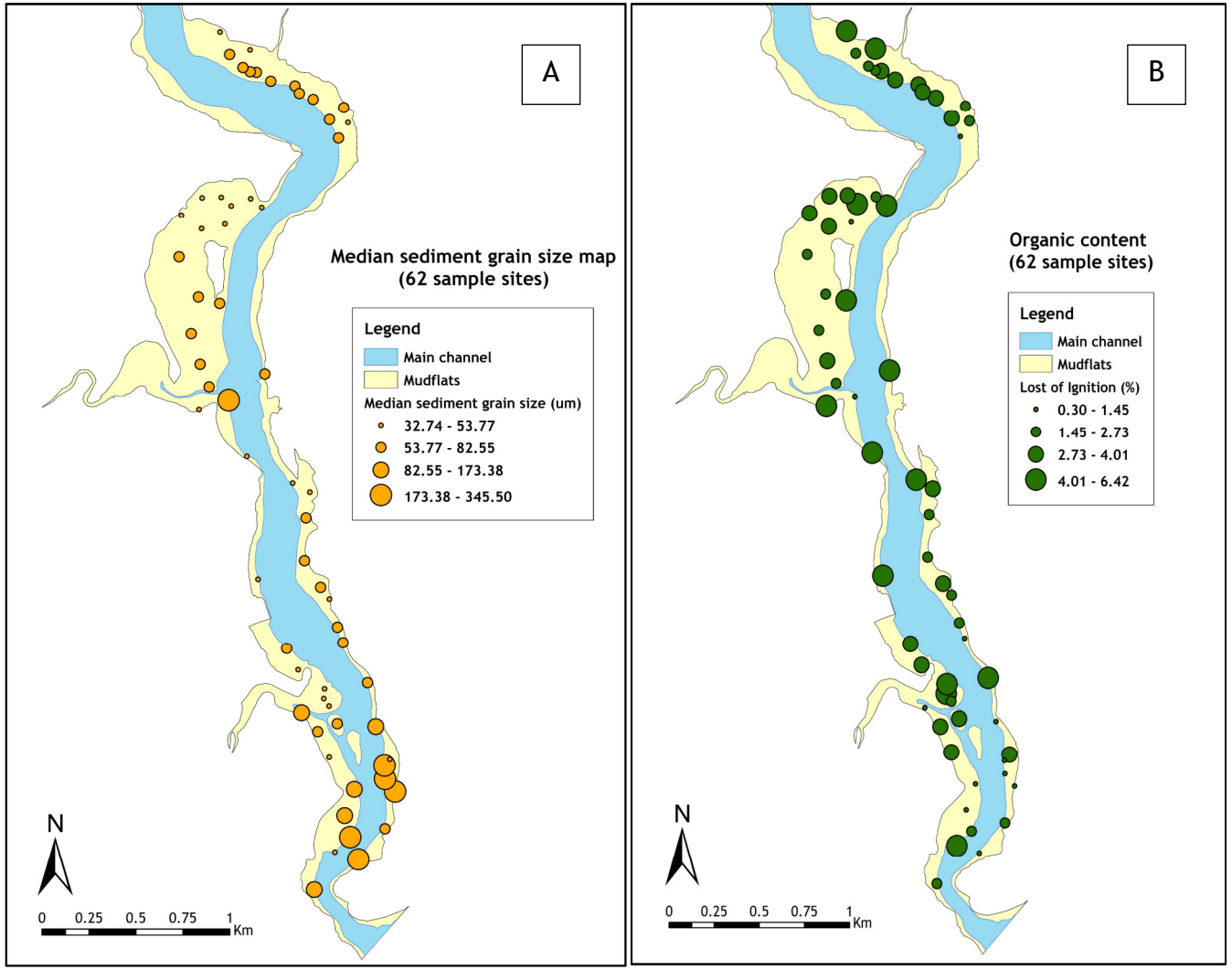


**Figure 3-13:** (A) Median sediment grain size; (B) Organic content (%) along the estuary.

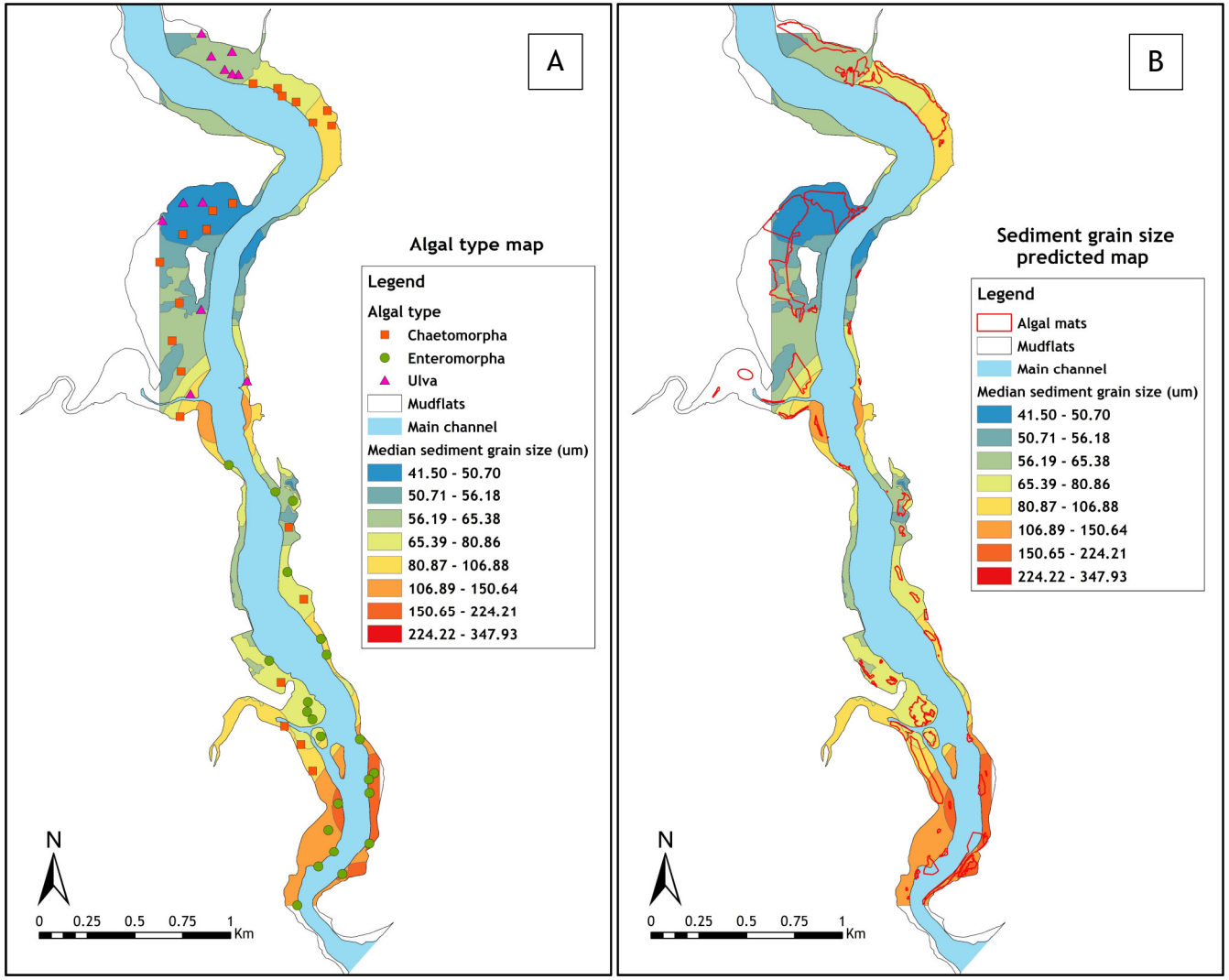


**Figure 3-14:** Predicted sediment grain size overlaid by algal type (A) and algal mat locations (B).

## 3.7 Bed of the estuary and its dynamics

The estuary bed is comprised of mudflats, sand flats, and mussel beds, all of which except the mussel beds, which remain beneath a small creek, are exposed during low tide. Mudflats and saltmarshes occupy about 185 ha, mostly in the central region. Sand flats are mainly found in the lower and upper regions (Baird and Milne, 1981, Leach, 1971, Raffaelli, 1999, Raffaelli, 2000). From the historical map overlay, mudflat extent and the position of the main channel in the estuary from 1901 (Figure 3-15A) to 1957 (Figure 3-15B) show no significant change. The upper and central regions of the estuary are particularly stable. In 1988 a branch channel was disconnected (Figure 3-15C), which may be due to local sedimentation blocking the upper part of this channel. The exposed mudflats and saltmarshes have remained in the same locations with approximately the same extent from 1901-1988. It is noted that mismatches of the channel edge found in the lower region (Figure 3-16) result from different water levels during mapping surveys and image acquisition.

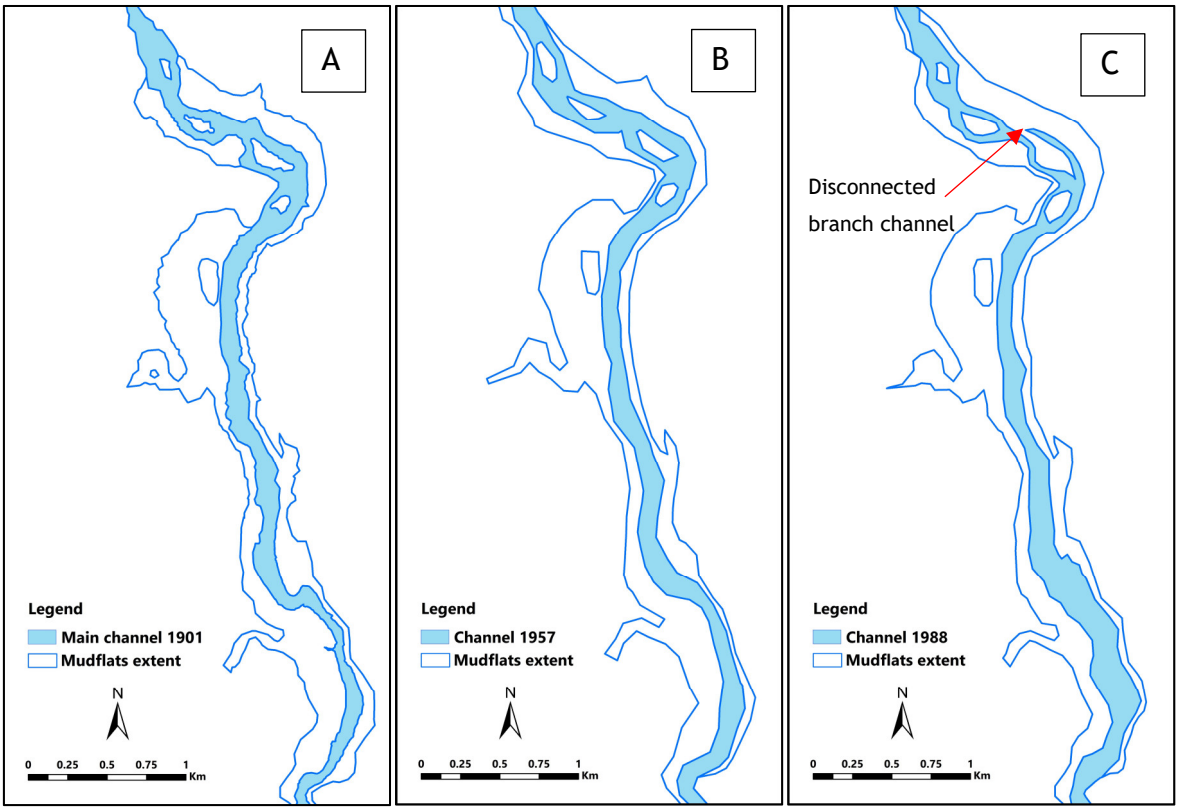


**Figure 3-15:** Main channel and mudflat extent derived from vectorization of the scanned maps constructed in 1901 (A) and 1957 (B), and from digitising of the scanned aerial photo in 1988 (C).

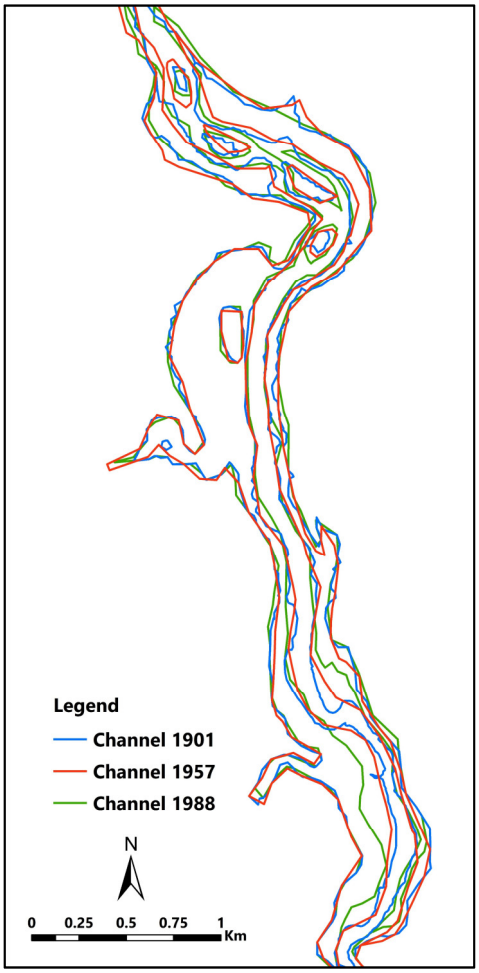


**Figure 3-16:** The channel and mudflat boundaries showing no significant change in mudflat location and extent from 1901 - 1988.

Analysis of images from 2010 and 1989 also suggest no significant changes in the boundaries and extent of mudflats or the main river channel (very light yellow), although slight positive changes of NIR values over the mudflats can be found from 1989 to 2010 (light yellow) (Figure 3-17). High positive changes (dark purple) found along the coast line reflect coastal deposition occurring after 1989. The areas of high negative changes (dark brown) represent lower biomass in agricultural areas in 2010 compared to 1989, as the 1989 image is from July (summer) and that in 2010 from October (autumn, after harvest) (Figure 3-17).

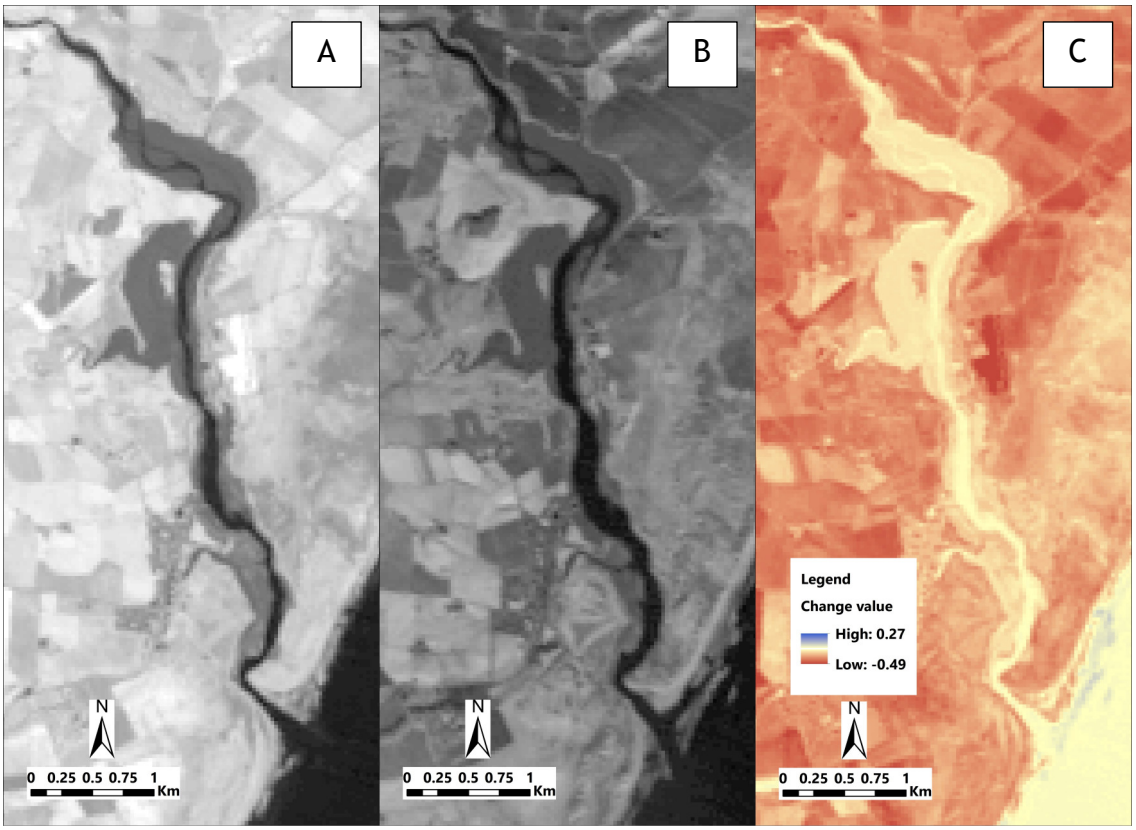


**Figure 3-17:** Landsat-5 data band 4 (NIR; showing mud flats, the creek, and shoreline position as well as terrestrial biomass) acquired on 4 July 1989 (A) and 25 October 2010 (B) over the Ythan, and the difference image (C) derived from change detection analysis of (A) and (B).

The bottom elevation derived from the boat surveys reveals cross-section profiles that have natural channel shapes, compared to the profiles created from the LiDAR DEM. The boat survey shows deeper channels than the LiDAR DEM, and the offset difference is especially large towards the middle of the main channel (Figure 3-18). Small offsets were found in shallower areas, most of which were mudflat areas that were closer to the river bank, suggesting the LiDAR and echo sounder agree well in shallow water (Figure 3-19). According to echo sounder survey, longitudinal profile of the main channel from the bottle neck in upper region toward the mouth of the estuary exhibits very low gradient; however, there are some steep areas occur locally as shown in Figure 3-20.

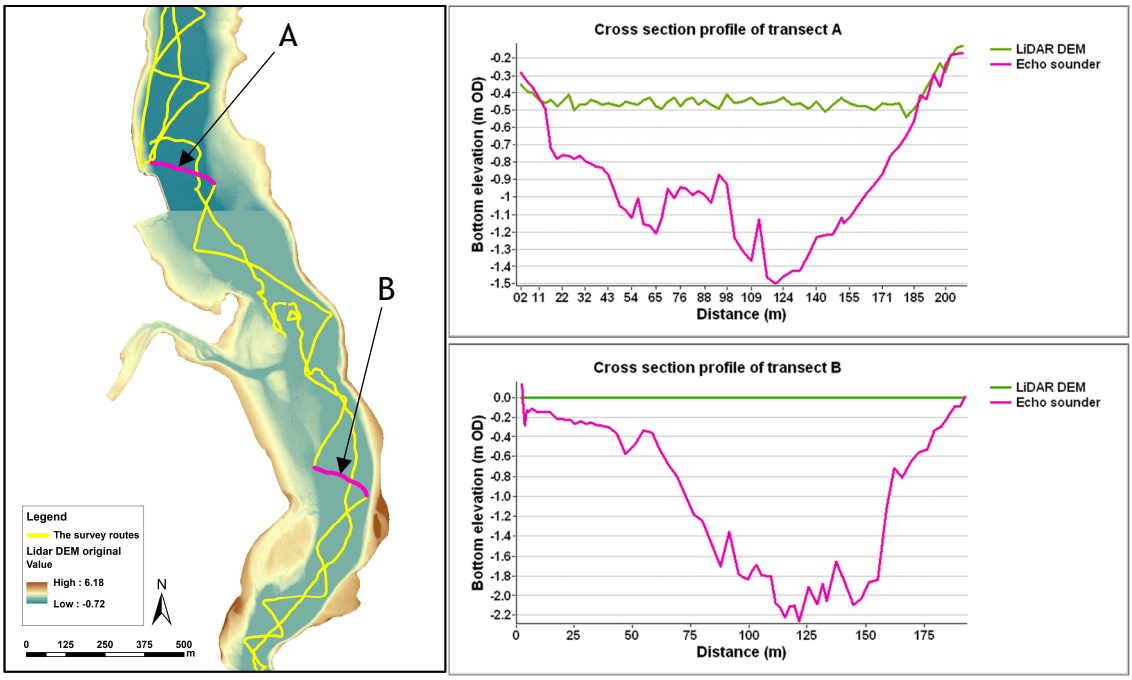


**Figure 3-18:** Boat survey routes in lower region of the estuary with LiDAR DEM original as a background. Comparison of cross sections from terrestrial LiDAR DEM and the echo sounder at transect A and transect B. Distances are from the left side of the channel.

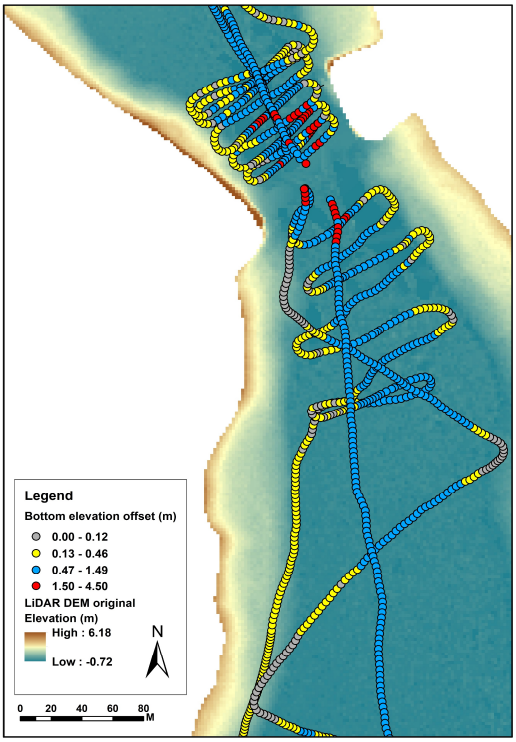


**Figure 3-19:** Offset elevation values of LiDAR DEM and echo sounder: offset values are low in shallower water close to the river bank, while higher offsets are found in the deeper middle of the channel.

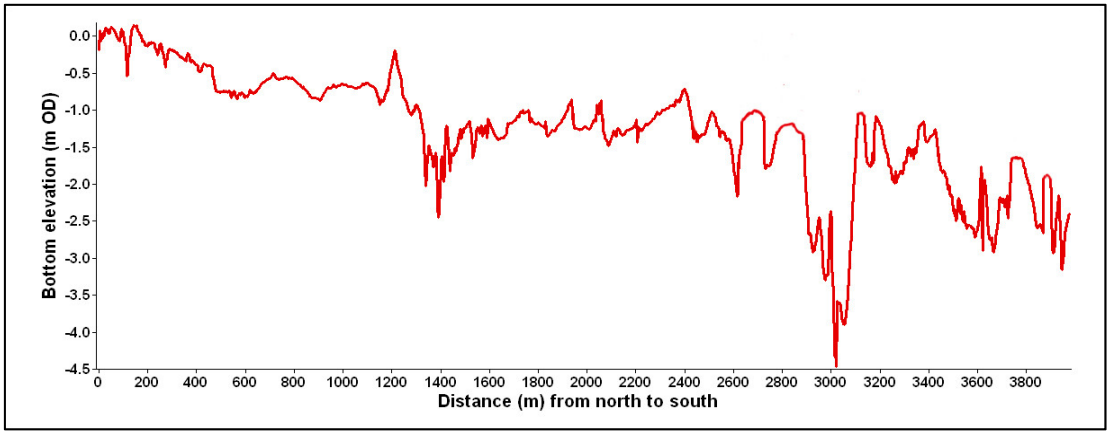


**Figure 3-20:** Longitudinal profile of the main channel from the channel bottleneck in upper region toward the mouth of the estuary (north to south).

## 3.8 Water quality in the estuary and its interaction with river flow

### 3.8.1 Water temperature (WT)

Water temperature in the Ythan changes seasonally. The temperature gradually rose from winter to a summer maximum, and continually fell from autumn to winter (Figure 3-21). The average temperature in summer ranged from 14.1 – 14.5 °C with average max 20.97 °C and average min 9.92°C, whereas in winter the average temperature ranged from 3.7- 5.3 °C. In addition to the seasonal effect, water temperature was influenced by the of river discharge, resulting from weather conditions. Pearson's correlation shows that river flow was inversely related to WT with a correlation coefficient of -0.47 ($p < 0.001$) in 2009 and -0.76 ($p < 0.001$) in 2011 (Table 3-7).

The relationship suggests that high river flow entering the estuary causes a drop in water temperature, while low river flow generally leads to increased water temperature. Fluctuations in WT, possibly due to variations in river flow, can be seen year to year (Table 3-2; Figure 3-22). WT in 2010 was the lowest of all the years of data, whilst WT in 2013 was the highest, especially during summer and autumn. Although WT significantly changes every year, the inter-annual variability of WT in least in summer, which reflects consistent summer weather conditions in the Ythan.

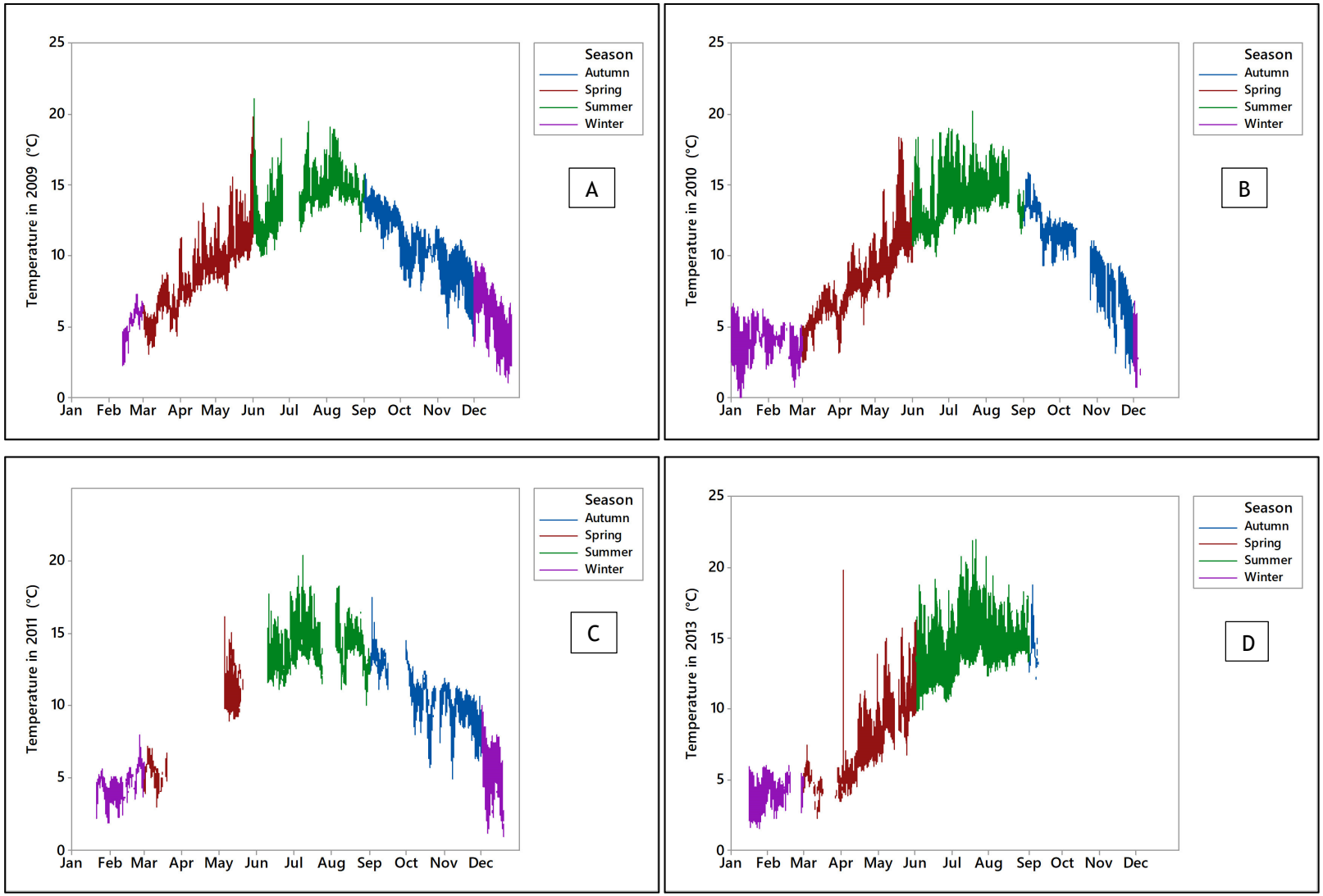


**Figure 3-21:** Water temperature in 2009 (A); 2010 (B); 2011 (C); 2013 (D); data from SEPA buoy (see Table 2-1 for details)

**Table 3-2:** Temperature (°C) anomaly (%) for each season

| Season | 2010 | 2011 | 2013 |
|---|---|---|---|
| Winter | -30.2% | 21.6% | -15.6% |
| Spring | -5.8% | 9.9% | -14.6% |
| Summer | 0.0% | 0.0% | 2.8% |
| Autumn | -4.7% | 6.9% | 33.3% |

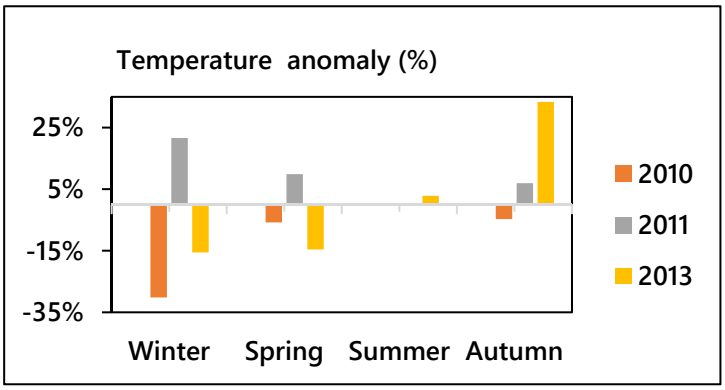


**Figure 3-22:** Temperature anomaly (%) from 2009 to 2010, 2010 to 2011, and 2011 to 2013

### 3.8.2 pH

pH values in the Ythan are also seasonally dependent, rising gradually from late winter to summer and then dropping continually from the start of autumn (Figure 3-23). High pH values were found during spring to summer with average values 8.1-8.2, with low pH values in winter and autumn, averages being 7.6 - 8.1. This pattern leads to pH values being negatively correlated with river discharge, with (Pearson's correlation coefficient for 2009 data $R$ = -0.5, p <0.001 and for 2011 $R$ = -0.7, p <0.001) (Table 3-7). These strong negative relationships suggest the predominance of river flow over control sea water intrusion in the estuary as far upstream as the measuring buoy. Annual variability in pH from 2009 to 2013 was relatively low, with less than 6% variation between years. The lowest changes were in spring and summer while there was slightly higher variation in autumn and winter (Table 3-3; Figure 3-24). These changes correspond closely with the annual changes of WT, which confirms the influence of river flow on controlling both WT and pH in the Ythan.

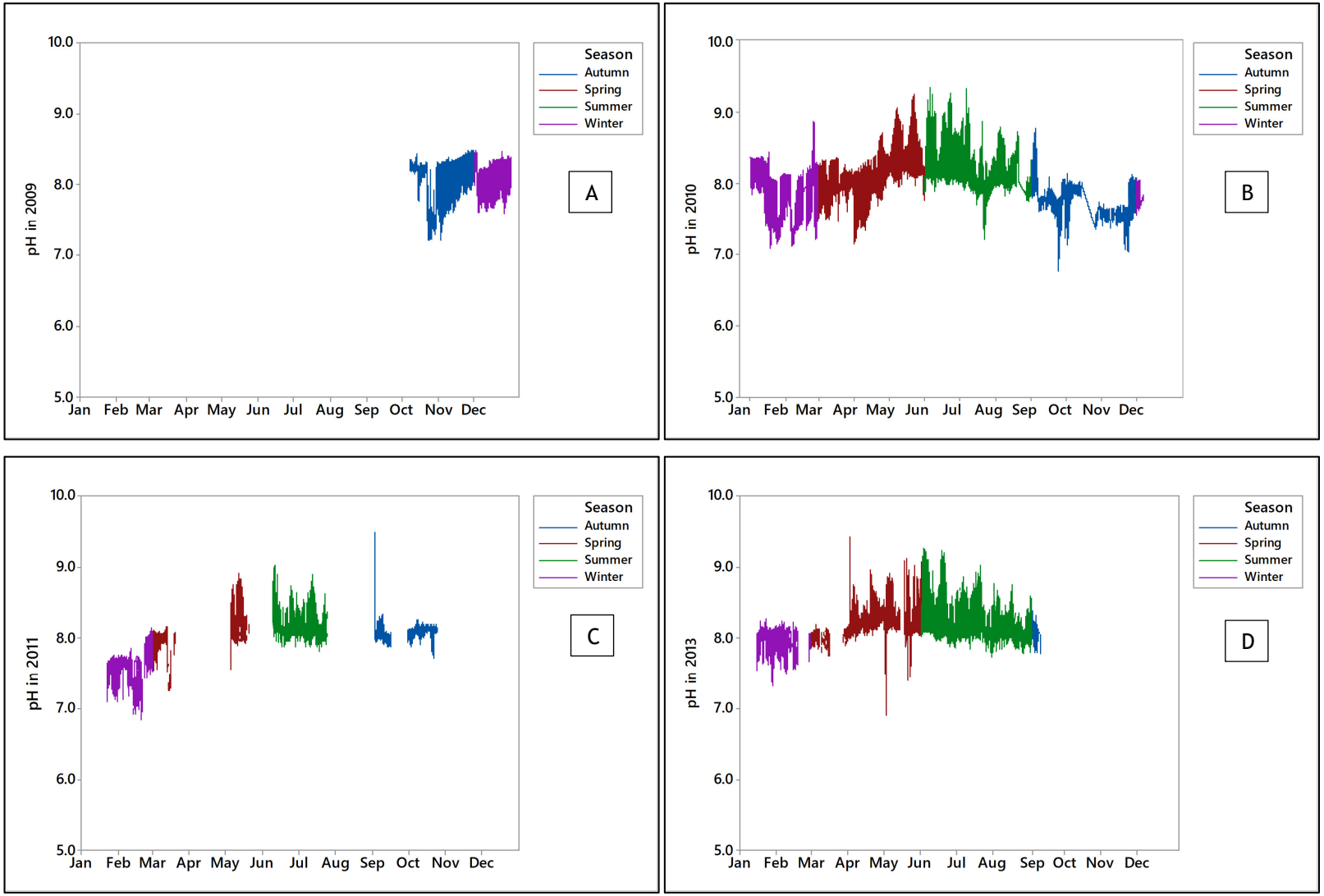


**Figure 3-23:** pH values in 2009 (A); 2010 (B); 2011 (C); 2013 (D) data from SEPA buoy (see Table 2-1 for details)

Table 3-3: pH anomaly (%) for each season

| Season | 2010 | 2011 | 2013 |
|---|---|---|---|
| Winter | -3.75% | -2.56% | 5.26% |
| Spring | - | 0.00% | 1.23% |
| Summer | - | 0.00% | 1.23% |
| Autumn | -3.80% | 5.19% | 0.00% |

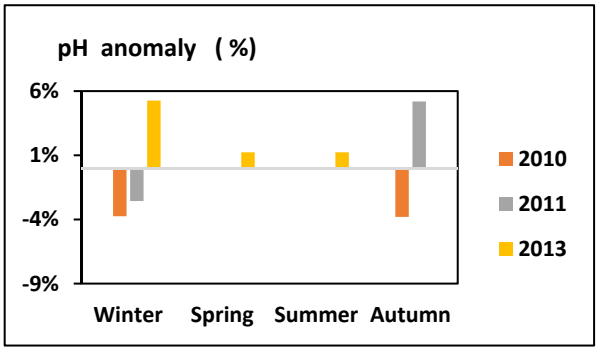


Figure 3-24: pH anomaly (%) from 2009 to 2010, 2010 to 2011, and 2011 to 2013

### 3.8.3 Dissolved oxygen (DO)

DO gradually declined from late winter to summer and recovered again from late summer to mid-winter (Figure 3-25). The lowest DO occurs in summer, ranging from 8.9 mg/L to 9.4 mg/L. The annual v-shaped trends of DO mean that it is positively related to river flow with correlation coefficients of 0.3 and 0.6 (both p values < 0.001) in 2009 and 2011 (Table 3-7). In addition to river flow, DO had significant negative relationships with WT ($R$ = -0.6 (2009) and -0.7 (2011) (both p <0.001). These relationships show that high river flows at low temperature, most likely in winter, are associated with large amounts of DO in the estuary. In summer, low river flows at high temperature tend to have less DO in the water column. Annual changes of DO seem to depend on the river discharge entering the estuary. The positive changes of DO from 2009 - 2010 and again from 2011-2013 reflect increases in river flow in the latter years. The reduction in DO from 2010 to 2011 reflects an overall reduction in river flow. The decreases in DO in the autumns from 2011 - 2013 may be due to decreased river flow which coincided with prolific algal blooms as a result of warm temperatures (Table 3-4; Figure 3-26). This interpretation is supported by negative correlation coefficients between DO and Chlorophyll-a, which suggests that increased Chlorophyll-a relates to decreased DO (Table 3-8).

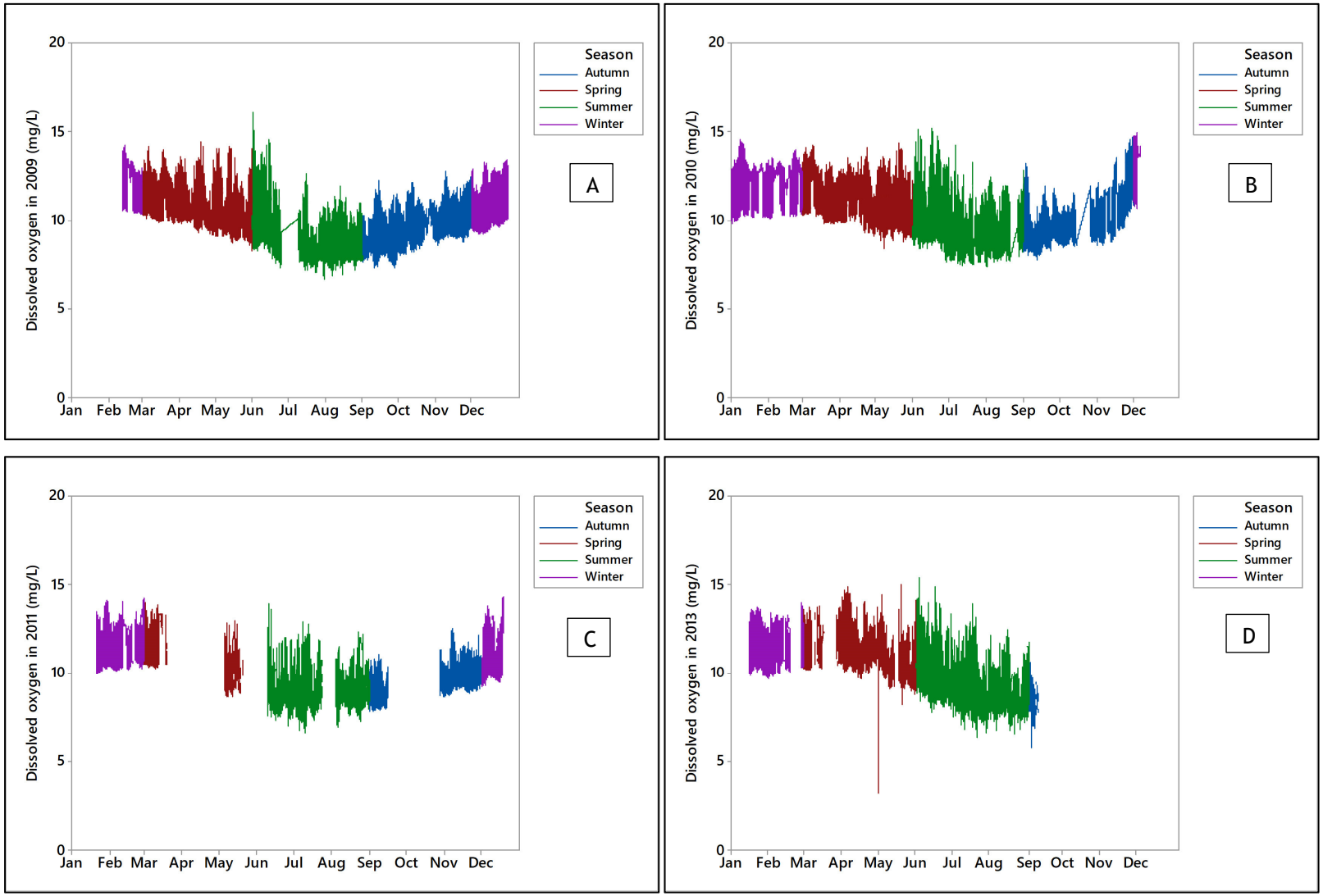


**Figure 3-25:** Dissolved oxygen in 2009 (A); 2010 (B); 2011 (C); 2013 (D); data from SEPA buoy (see Table 2-1 for details)

Table 3-4: DO (mg/L) anomaly (%) for each season

| Season | 2010 | 2011 | 2013 |
|---|---|---|---|
| Winter | 7.8% | -5.6% | 0.9% |
| Spring | 3.7% | -4.5% | 3.7% |
| Summer | 3.3% | -5.3% | 2.2% |
| Autumn | 4.1% | -5.9% | -11.6% |

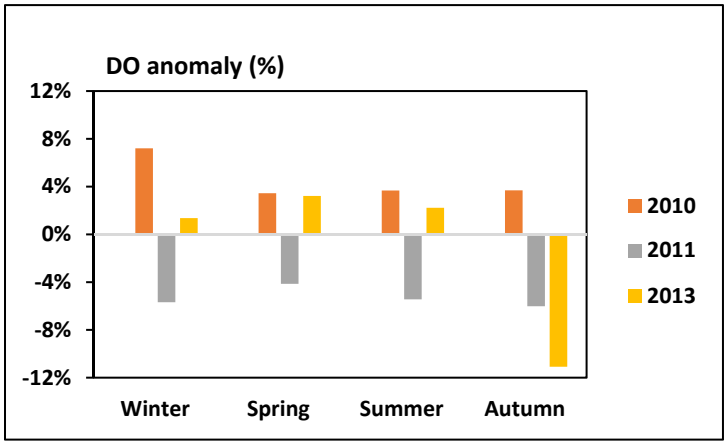


Figure 3-26: DO anomaly (%) from 2009 to 2010, 2010 to 2011, and 2011 to 2013

### 3.8.4 Turbidity

Turbidity in the Ythan varied seasonally and from year to year. High turbidity was mostly found in spring, summer, and autumn with average range of turbidity from 12.6 NTU - 83 NTU in 2009 - 2013 (Figure 3-27, 3-28; Table 3-5). In winter, when river discharge was higher, turbidity only ranged from 12.3 NTU – 33.8 NTU. This suggests that river flow is not the only parameter controlling turbidity in the water column, which is supported by a low correlation coefficient between turbidity and river flow ($R$ = 0.14; p <0.001) (Table 3-7). However, positive correlation coefficients between turbidity and Chlorophyll-a (Table 3-8) suggest that biological productivity during low flow, warm months causes increases in both Chlorophyll-a and turbidity.

### 3.8.5 Chlorophyll-a

Different patterns of Chlorophyll-a concentration are observed in different years. In 2009, the high chlorophyll-a period started from late spring and extended to autumn, with the highest values in summer and autumn.

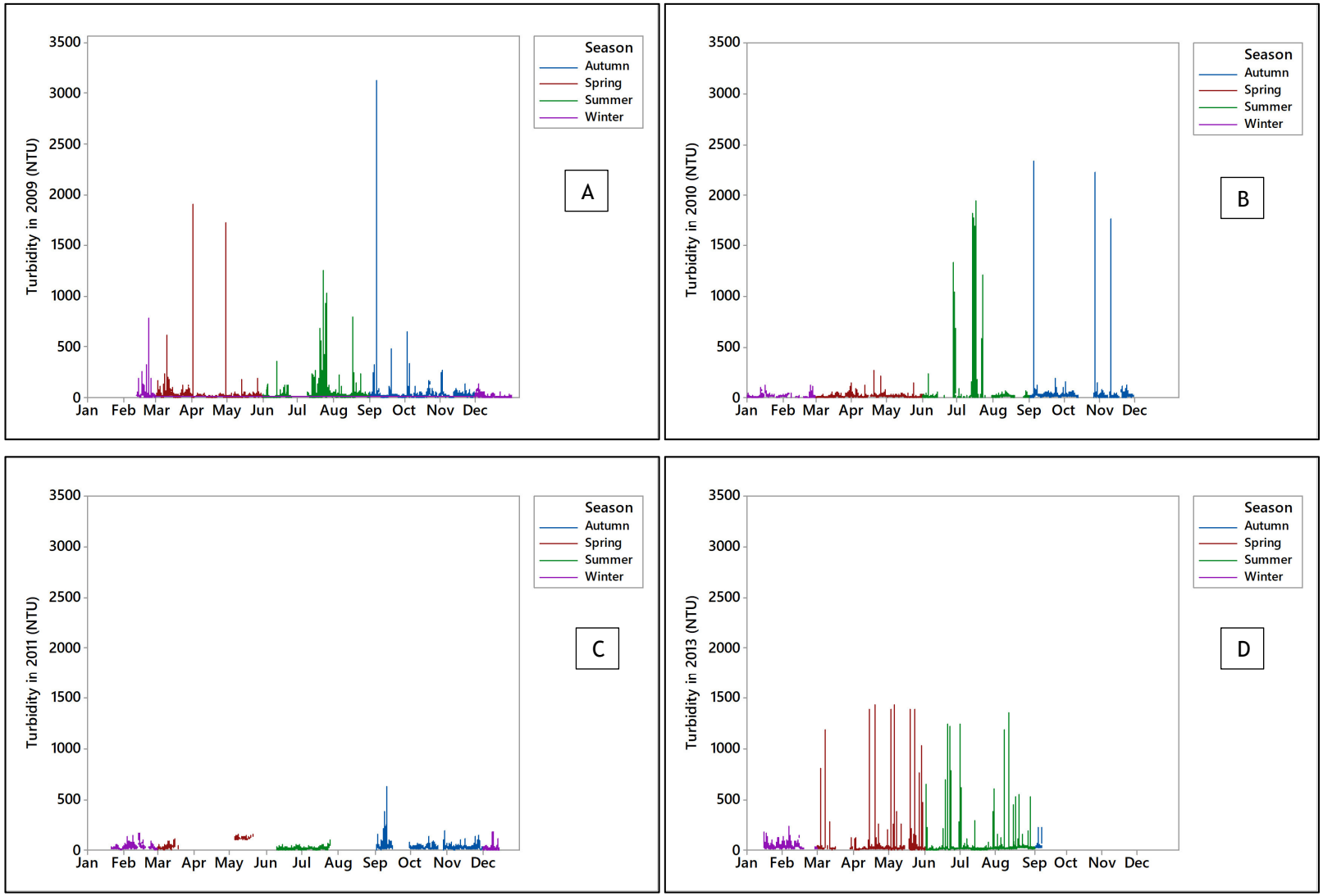


**Figure 3-27:** Turbidity in 2009 (A); 2010 (B); 2011 (C); 2013 (D); data from SEPA buoy (see Table 2-1 for details)

**Table 3-5:** Turbidity (NTU) anomaly (%) for each season

| Season | 2010 | 2011 | 2013 |
|---|---|---|---|
| Winter | -19.6% | 118.7% | 10.1% |
| Spring | -36.7% | 560.3% | 25.9% |
| Summer | -7.9% | -17.3% | -70.7% |
| Autumn | -5.6% | 41.9% | 35.0% |

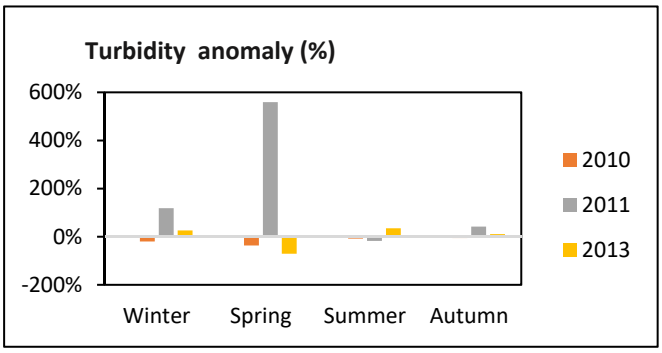


**Figure 3-28:** Turbidity anomaly (%) from 2009 to 2010, 2010 to 2011, and 2011 to 2013

In 2010, in contrast, the highest Chlorophyll-a was found in separate periods in early autumn, late spring, and summer. In addition, there was an unusual increase in Chlorophyll-a during mid-winter in 2010. In 2011 and 2013, the highest Chlorophyll-a was found in late spring, summer and late autumn (Figure 3-29). The amount of Chlorophyll-a varied every year from 2009-2013, and the highest values in each year occurred between spring, summer, autumn (Table 3-6; Figure 3-30) when the weather and water temperatures increase. This is supported by a positive correlation coefficient between WT and Chlorophyll-a (Table 3-8), which implies that increased WT seems to raise the amount of Chlorophyll-a in the estuary. Although increased Chlorophyll-a is associated with WT, DO, and turbidity, it is poorly correlated to river flow ($R$ = 0.039 ($p<0.001$) in 2009 and -0.119 ($p<0.001$) in 2011 (Table 3-7). The correlation relationships suggest that the amount of Chlorophyll-a in the Ythan has stronger relationships with WT, DO, and turbidity than with pH and river flow. Likewise, river flow also has strong relationships with WT, pH, DO, and turbidity but not Chlorophyll-a (Table 3-7). The autocorrelation between these variables makes it difficult to identify causal links directly from statistical analysis.

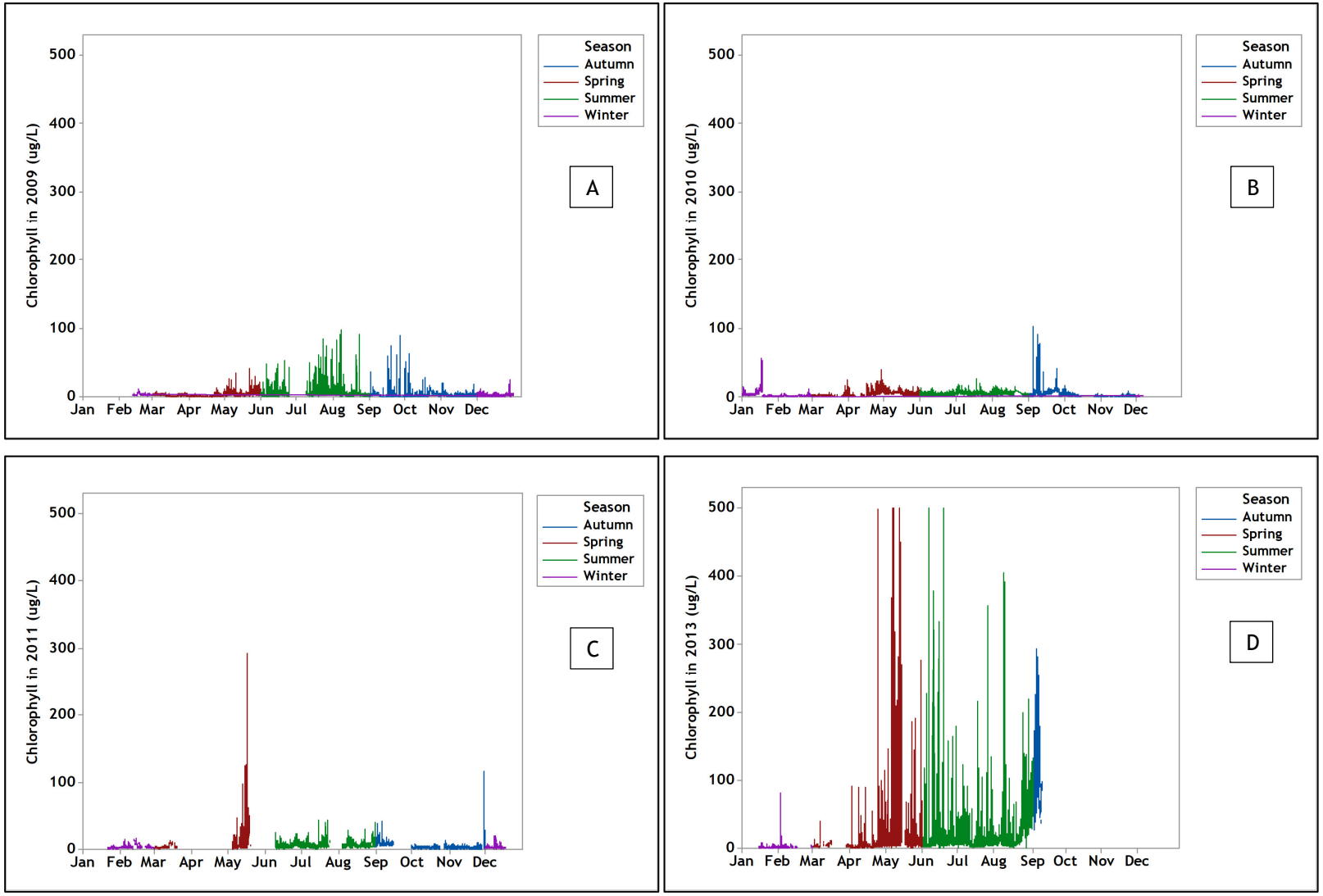


**Figure 3-29:** Chlorophyll-a in 2009 (A); 2010 (B); 2011 (C); 2013 (D); data from SEPA buoy (see Table 2-1 for details)

**Table 3-6:** Chlorophyll-a (mg/L) anomaly (%) for each season

| Season | 2010 | 2011 | 2013 |
|---|---|---|---|
| Winter | -17.2% | 41.7% | -55.9% |
| Spring | 22.2% | 172.7% | 107.8% |
| Summer | -14.3% | 35.4% | 189.2% |
| Autumn | 20.0% | 22.2% | 2643.2% |

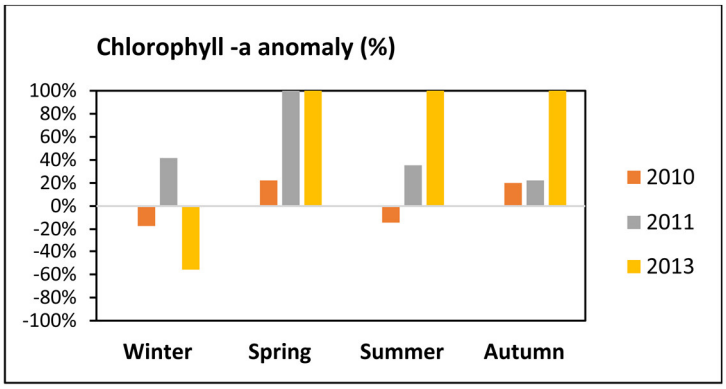


**Figure 3-30:** Chlorophyll-a anomaly (%) from 2009 to 2010, 2010 to 2011, and 2011 to 2013

**Table 3-7:** Correlation coefficients between river flow and water quality variables

| Variable | | 2009 | 2011 |
|---|---|---|---|
| River flow/ temperature | *R* | -.475 | -.760 |
| | p-value | .000 | .000 |
| | N | 28965 | 11289 |
| River flow/ pH | *R* | -.500 | -.700 |
| | p-value | .000 | .000 |
| | N | 8213 | 8106 |
| River flow/ DO | *R* | -.330 | -.600 |
| | p-value | .000 | .000 |
| | N | 30958 | 10237 |
| River flow/ turbidity | *R* | .144 | -.040 |
| | p-value | .000 | .000 |
| | N | 27741 | 9962 |
| River flow/ Chlorophyll-a | *R* | .039 | -.119 |
| | p-value | .000 | .000 |
| | N | 29615 | 11289 |

**Table 3-8:** Correlation coefficients between chlorophyll and water quality variables

| Variable | | 2009 | 2010 | 2011 | 2013 |
|---|---|---|---|---|---|
| WT/ Chlorophyll-a | *R* | .189 | .241 | .152 | .201 |
| | p-value | .000 | .000 | .000 | .000 |
| | N | 28965 | 28898 | 11289 | 9596 |
| Turbidity/ Chlorophyll-a | *R* | .233 | .165 | .404 | .025 |
| | p-value | .000 | .000 | .000 | .015 |
| | N | 27741 | 23848 | 9962 | 9596 |
| pH/ Chlorophyll-a | *R* | -.567 | .073 | .096 | .035 |
| | p-value | .000 | .000 | .000 | .000 |
| | N | 8213 | 32539 | 8106 | 9594 |
| DO/ Chlorophyll-a | *R* | -.116 | -.198 | -.118 | -.201 |
| | p-value | .000 | .000 | .000 | .000 |
| | N | 35,040 | 29615 | 10237 | 9584 |

### 3.8.6 Interaction of Chlorophyll-a, tidal cycle, and river flow

The previous results suggest significant seasonal patterns in water quality data in the Ythan, and associations between these variables and river flow further implies that event-scale variability may be significant. Further results derived from seasonal and event scale analysis, which provides understanding of potential casual links, of the influence of river flow and tides on the amount of Chlorophyll-a measured at the SEPA buoy and its transport behaviour in the estuary are described as follows:

#### 3.8.6.1 Seasonal scale

- ***Winter to spring***

The amount of Chlorophyll-a gradually declines from winter to spring, which corresponds to falling trends of river flow. The lowest amount of Chlorophyll-a was found during mid-spring when river flow was the lowest. However, the amount of Chlorophyll-a usually increased when high river flow events occurred (Figure 3-31A).

- ***Summer to early autumn***

During summer-autumn periods of low river flow, Chlorophyll-a concentrations increased rapidly. However, although the river flow was low in general in this part of the year, there were some moderate river flow peaks which resulting from weather events. Interestingly, moderate river flows at this time of year also corresponded with locally high amounts of chlorophyll, reflecting its abundance during the summer period of high biological productivity. Thus, high amounts of Chlorophyll-a in summer to early autumn were found during both normal low flows and during moderate river flow events (Figure 3-31B).

- ***Mid-autumn to winter***

The interaction between river flow and the amount of Chlorophyll-a during this period was the same as in winter to spring, although there was an overall declining trend in the Chlorophyll-a concentration. This suggests that river flow plays a more important role in controlling the amount of Chlorophyll-a at this time of year, when biological production is low (Figure 3-31C).

In both late winter to mid-spring and mid-autumn to mid-winter periods, Chlorophyll-a concentrations are positively correlated with river flow. However, during late spring to early autumn high amounts of Chlorophyll-a could be found during either high or low river discharge. Overall, these results suggest that the amount of river flow influences the amount of Chlorophyll-a in the water column.

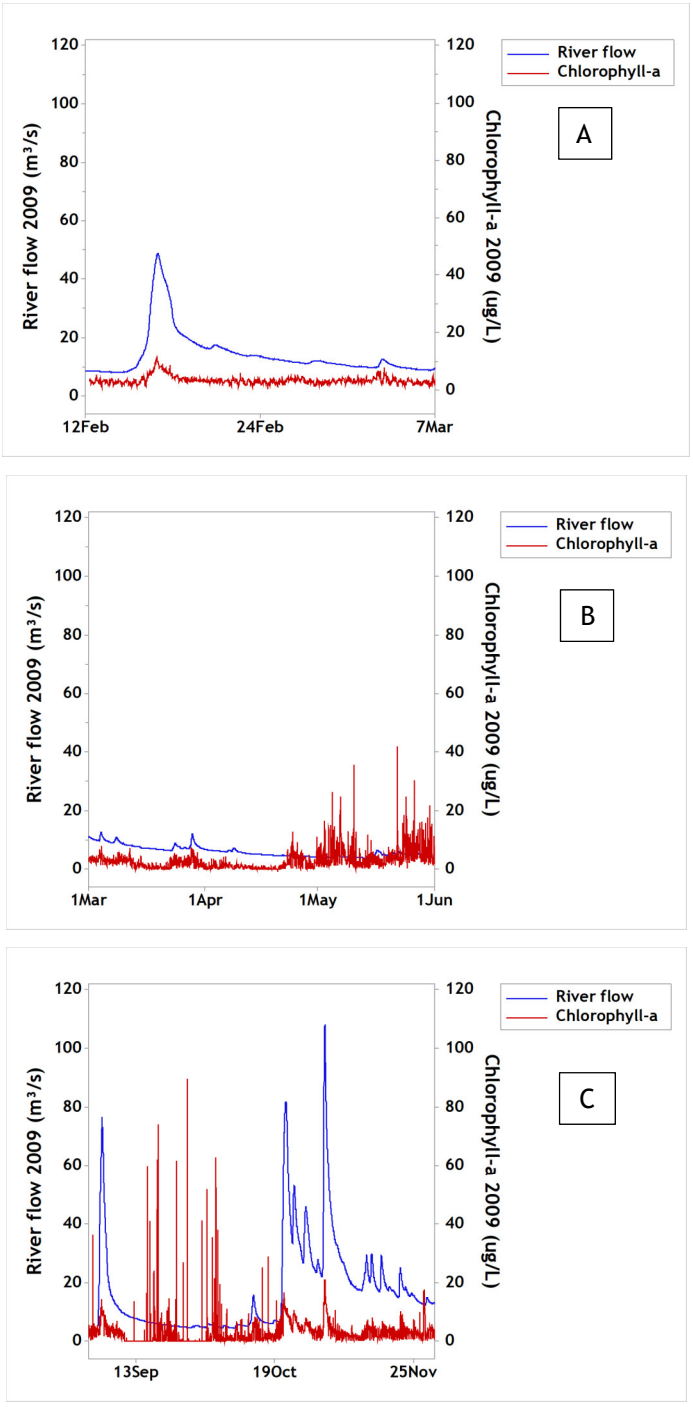


**Figure 3-31:** High amount of chlorophyll-a found during high river flow in winter, 2009 (A); High amount of chlorophyll-a during high river flow in early spring and low river flow in late spring, 2009 (B); High amount of chlorophyll-a found during periods of high river flow in autumn, 2009 (C).

#### 3.8.6.2 Event scale

- ***Moderate chlorophyll-a coincides with high flow in winter***

During this period, chlorophyll-a concentrations were relatively low (< 7 µg/L) and were negatively related to tide level. Higher chlorophyll-a concentrations were usually found during low tide and lower values during high tide, for instance as shown in Figure 3-32A.

- ***High chlorophyll-a coincides with low flow in late spring***

During low flow in late spring to summer chlorophyll-a concentrations increased dramatically. In addition, interaction between the amount of chlorophyll-a and the tidal cycle was different from the pattern found in winter high flow. In late spring, the highest chlorophyll-a concentrations were found at high tide whereas low amounts of chlorophyll-a occurred at low tide levels (Figure 3-32B).

- ***High chlorophyll-a coincides with low flow in summer (dry summer)***

During dry summer periods, both the concentrations of chlorophyll-a and the relationship between these and the tidal cycle were similar to in late spring (Figure 3-32C).

- ***High chlorophyll-a coincides with high flow in summer (summer rainfalls)***

During summer rainfall events, which led to increased river flow, the amount of chlorophyll-a kept rising. However, a short period of moderate river flow led to changed relationships between chlorophyll-a concentrations and the tidal cycle. The relationships were the same as in winter in that high chlorophyll-a was found during high tide and vice versa (Figure 3-33A).

- ***High chlorophyll-a coincides with high flow in autumn***

During autumn high flows, the amount of chlorophyll-a and the interaction between chlorophyll-a levels and the tidal cycle were close to the patterns found during high flow events in both winter and summer. Although the concentrations of chlorophyll-a were higher than in winter, they remained lower than in summer, and did not exceed 12 µg/L. In addition, the chlorophyll-a concentrations clearly followed the river flow (Figure 3-33B).

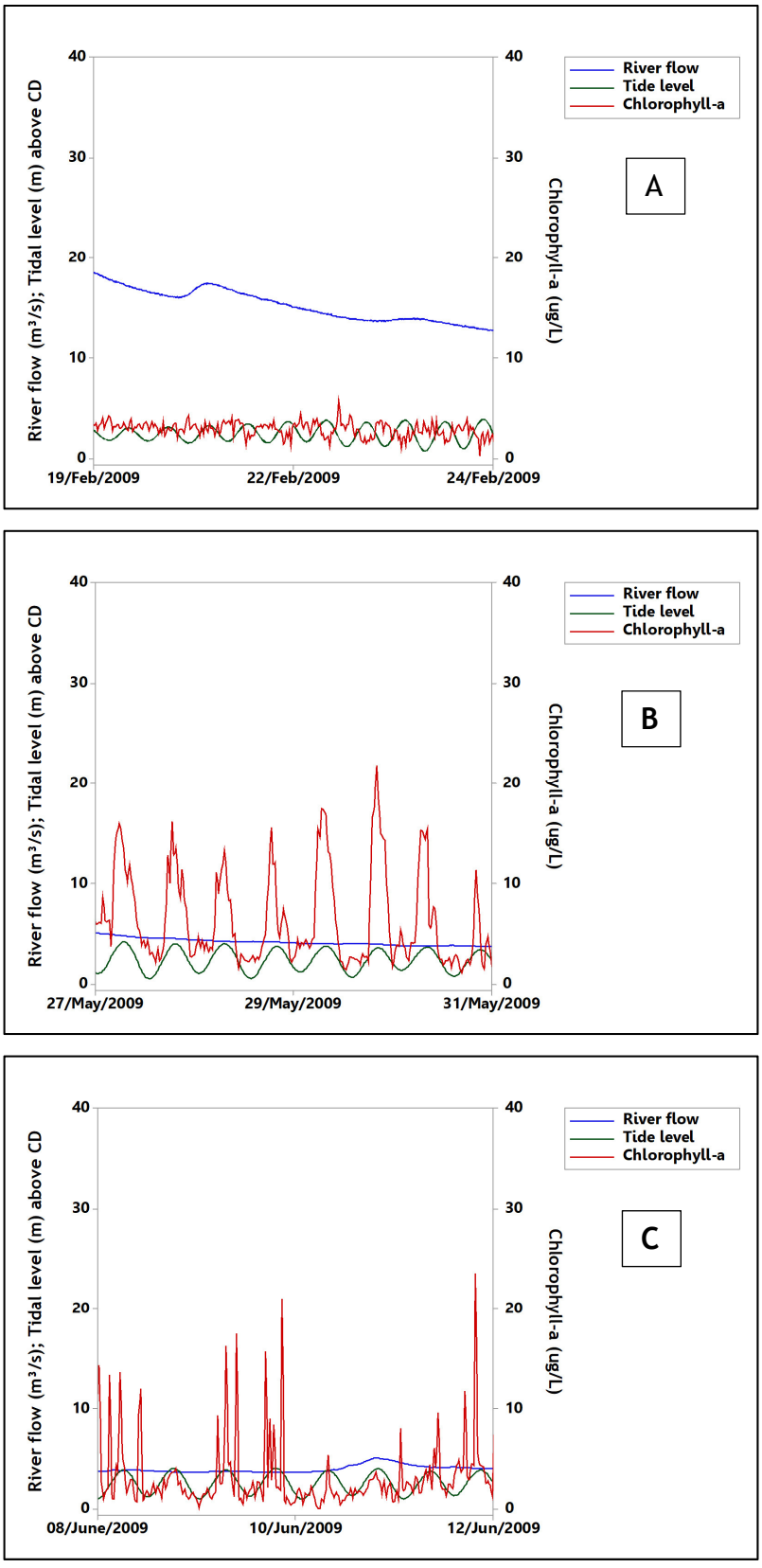


**Figure 3-32:** Moderate chlorophyll concentrations during low tide and low concentrations during high tide in winter high flow (A); High chlorophyll levels during high tide and low concentrations during low tide in spring low flow (B); High chlorophyll concentrations during high tide and low concentrations during low tide in summer dry (low flow) (C).

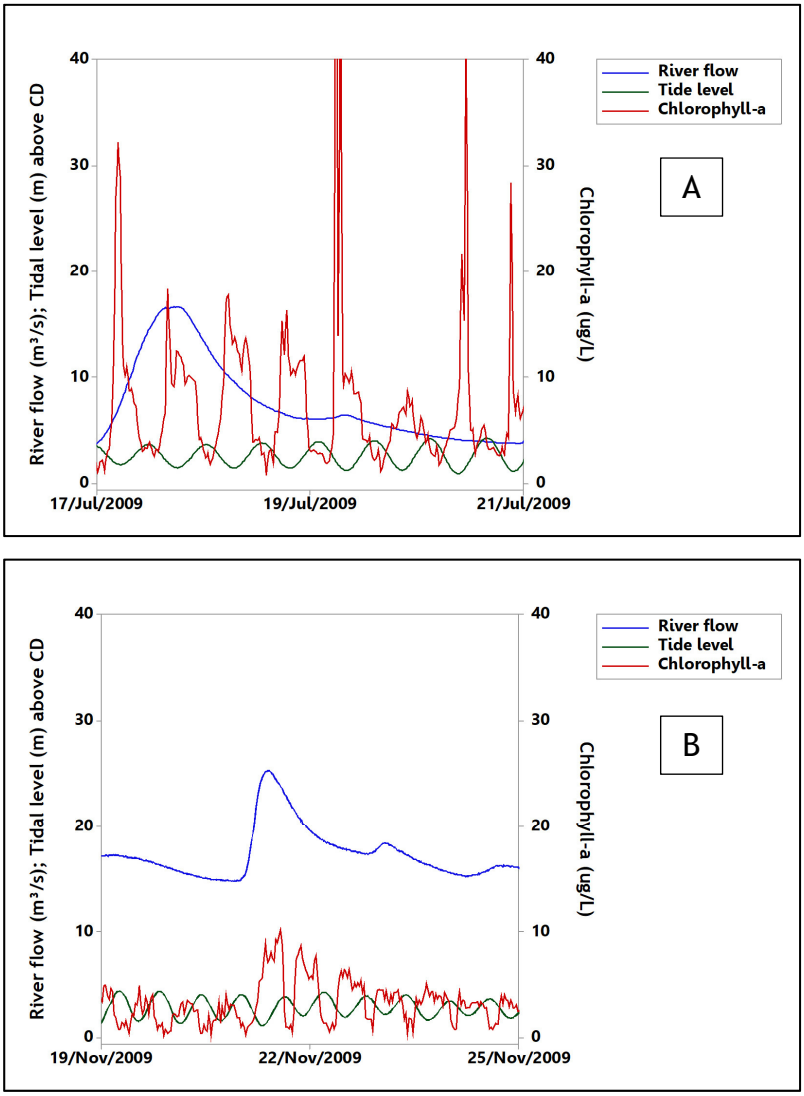


**Figure 3-33:** High chlorophyll concentrations low tide and low values during high tide in a summer rainfall period (A); High chlorophyll concentrations during high tide and low values during low tide in autumn high flow (B).

## 3.9 Summary

Study of the Ythan catchment provides understanding that the physical and social characteristics of the catchment influence increase in nutrients in the Ythan estuary. With low average tidal range and low river flow along with the bar-built characteristics, the Ythan estuary seems to have flow energy. Consequently, the estuary undergoes low rates of modification, which can be seen from the very small amount of morphological change. Sediment grain size and sorting on mudflats varies by location as it is influenced by different sediment sources and hydrodynamic processes. Coarser sediments with lower organic matter dominate

the lower region of the estuary where marine processes have influence, whereas extensive mudflats in the upper and central regions far from the mouth are mainly composed of finer sediments with higher organic matter concentrations. In addition to low rates of lateral movement, vertical deposition rates in the estuary are also low. Lachendro (2016) reported deposition rates in the central region of 0.5 to 1 mm/year, and 5 to 10 mm/year close to the tributary mouth in the upper estuary. Coarser sediments are also found in the upper estuary resulting from river input rather than tidal influences. Although algae seem to develop preferentially on mudflats composed of finer sediment with higher organic matter, some areas of coarser sediments with lower organic matter also support algal growth, in particular in the lower estuary.

Analysis of the hydrology and water quality data also provides insight into the relationships between river flow and the water quality parameters measured at the SEPA buoy, including water temperature, pH, dissolved oxygen, turbidity, and chlorophyll-a. Water temperature is strongly negatively associated with river discharge. The river discharge also influences pH values in the estuary. During low river flow sea water can intrude further and in greater volumes into the estuary, resulting in higher pH values. High fresh water input leads to reduced pH. In addition, high river flow has the potential to keep more dissolved oxygen in the water column than low river flow. High river flow implies high flow energy that can disturb bed sediments and cause erosion of mudflat and marsh edges, which causes turbidity in the water column. The concentration of chlorophyll-a always changes in response to river flow changes. However, there is an exception during summer when algal blooms are at their greatest extent and high amounts of chlorophyll-a can be found regardless of the amount of river flow.

In addition to river flow, chlorophyll-a concentrations are associated with water temperature, dissolved oxygen, and turbidity. Apart from the control from river flow, tide levels also influence chlorophyll-a concentrations by mobilising it within the estuary. High river flow is likely to transport chlorophyll-a down the estuary during low tide, compared to high tide conditions when the amount of chlorophyll-a is lower due to being diluted. Low river flow, which brings less chlorophyll-a from the upper estuary to the lower estuary during low tide, is expected to have similar movement of chlorophyll-a as high flow although at lower concentrations, but interestingly high chlorophyll-a concentrations can be found during high tide

when river flow is low. This evidence suggests that there could be high amounts of chlorophyll-a in the lower part of the estuary or in the nearshore that are flooded back to the upper and central parts of the estuary during flood tide.

The interaction between river flow and the tidal cycle with the amount of chlorophyll-a provides an initial understanding of how river flow is highly likely to control the amount of nutrients in the estuary, whilst the tide is highly likely to control the movement of nutrients around the estuary. To expand on this analysis, modelling hydrodynamics, nutrient concentrations, and pathways is applied in chapter 6.

# Chapter 4: Utilisation of remote sensing for supporting hydrodynamic modelling and understanding algal bloom behaviour

This chapter describes the use of remote sensing data to support hydrodynamic modelling, specifically for the model input and validation. The chapter also presents calculations of NDVI and NDWI for model validation, used in Chapter 5. In addition, analysis of NDVI changes, is presented to comprehend macro algal growth behaviour from which hydrodynamics and nutrient dynamics in the Ythan estuary can be inferred.

## 4.1 Remote sensing for supporting hydrodynamic modelling

Satellite/aircraft-derived remote sensing provides information about the Earth without requiring direct access to the target areas. This results in a decrease in associated costs, and through analysing previously collected images the ability to analyse data from the past, and has thus been used to support hydrodynamic modelling studies (Klemas, 2010, Mastin and Fosness, 2009, Robinson, 2004). Remote sensing can provide data input required for hydrodynamic models such as the extent of water bodies, sea surface winds, tides, sea surface elevation, waves, current patterns, coastal circulation, and river flow (Klemas, 2010, Mastin and Fosness, 2009, Robinson, 2004). These data can be quantified from two main types of remote sensing, passive and active. For instance, sea surface wind speed and direction can be observed by scatterometer, an active microwave radar sensor designed for wind velocity vector retrieval over the ocean (Collins et al., 2012, Ebuchi et al., 2002). Sea surface elevation, tidal level, and waves can be measured by active satellite altimetry and active optical airborne LiDAR (Hwang et al., 2000, Woolf and Gommenginger, 2008). Both of these methods measure heights taken from the time of a radar pulse travelling from the satellite antenna to the surface and back to the satellite receiver (Vignudelli et al., 2011). River flow can be quantified from a combination of active and passive sensors, as used by Sichangi et al. (2016), Sun et al. (2010), and Tarpanelli et al. (2013) in which river stage derived from satellite altimeter was used together with river width extracted from passive remote sensing data to estimate river flow from hydrological models.

Passive remote sensing uses instruments which can detect natural energy emitted or reflected by target objects, most of which are in visible and/or infrared spectra (Lillesand et al., 1994, Richards, 1999). Satellites such as Landsat, ASTER, QuickBird, and Worldview are categorised as passive remote sensing satellites (Lillesand et al., 1994, Richards, 1999, Richards and Jia, 2006). Active remote sensing, on the other hand, uses instruments which generate their own source of energy to illuminate target objects. The instruments then measure the radiation which is reflected or backscattered from the targets. The recorded time between transmitted and backscattered pulses coupled with the speed of the transmitted signal are used to determine travelled distance (Lillesand et al., 1994, Richards, 1999, Richards and Jia, 2006). The majority of active remote sensing operates in the microwave wavelength; however, it can also be used in visible and near infrared wavelength regions. Active remote sensing includes Radar (Radio Detection and Ranging), LiDAR (Light Detection and Ranging), and Sonar (Sound Navigation and Ranging) (Lillesand et al., 1994, Richards, 1999, Richards and Jia, 2006). Radar transmits a microwave signal in a series of pulses from an antenna towards a target and detects the backscattered radiation. Similarly, LiDAR uses light in the form of laser to measure the backscattered or reflected light from the objects (Liu, 2008). Sonar emits pulses of sound into the water. If an object is in the path of the sound pulse, the sound bounces off the object and returns an echo to the sonar transducer (Lurton, 2002). There are two main types of sonar including single beam and multibeam echo sounders. Single beam echo sounders are traditional sonar while multibeam echo sounders emits sound waves generated through a wide angular lateral aperture transducer (fan-shaped coverage) (Lurton, 2002).

In addition to being used for model input, remote sensing data are widely used in validation and calibration for hydrodynamic modelling studies. For instance, Pietroniro et al. (2001) used data from the Landsat, SPOT, and RADARSAT satellites to create initial conditions for model runs and validation parameters to observe flood conditions. Da Silva et al. (2010) used ENVISAT satellite altimeter data to generate a time series of water level data in the Amazon basin to validate modelled water level. Additionally, remote sensing data have been used for flood extent validation, with results revealing comparable accuracy between the remotely sensed data and other flood extent indicators (Paiva et al., 2013).

Since using remote sensing data to aid model validation has provided promising results, as shown above, so using such data for model input and validation is a viable approach for this study. Using these data reduces the time and cost of field data collection, which can be a complicated process for studying hydrodynamics and nutrient concentration, and overcomes the lack of measured field data when simulating scenarios in the past.

For this study, LiDAR DEM and single beam echo sounder are utilised for model input. They are used to create a bottom elevation data set suitable to act as a model input. The methods for acquiring the data were explained previously in 2.3.7.10. As for model validation, WV-2 images, CASI data, and Landsat-8 images are utilised to create algal bloom location maps, which are compared to nutrient concentrations and pathways derived from the model, to investigate a link between algal bloom areas and nutrient concentrations and to assess the reliability of the model. In addition, WV-2 images and Landsat-8 images are used to identify inundated areas and so to validate wet-dry areas quantified from the model. The rational for selection of these methods as well as the procedure to obtain locations of algal blooms and inundated areas are explained in 4.2-4.4.

## 4.2 Remote sensing for monitoring algal bloom

Remote sensing is a cost-effective powerful tool to support studies of eutrophication and nutrient management in the next section. in estuaries (Keith, 2014, Klemas, 2012, Mantas et al., 2013). It can be used for monitoring eutrophication status and its severity through estimating bloom magnitude and duration through its proxy, chlorophyll-a (Hu, 2009, Keith, 2014, Klemas, 2012, Mantas et al., 2013, Van der Wal et al., 2014, Stumpf, 2001, Tiit, 2004). In addition, remote sensing can be used to determine biomass, another critical bloom index to detect trends in bloom size and significance (Hu et al., 2017, Xing et al., 2015, Van der Wal et al., 2010). The wide range of multi-spectral sensors that are now available with high temporal repetition rates makes possible studies of spatio-temporal variation of eutrophication over estuarine and coastal systems (Klemas, 2012, Mantas et al., 2013, Van der Wal et al., 2010). Medium to low spatial resolution images with high spectral resolution, such as Aqua MODIS 250, SeaWIFS, and MERIS, are mainly useful for monitoring bloom formation and so predicting bloom location on a broad scale (Gower, 2004, Gower et al., 2004,

McClain et al., 2006). Higher spatial resolution sensors, either from satellites or airborne platforms, are usually required to accurately map eutrophication and its effects in small estuaries (Kabbara et al., 2008, Klemas, 2012, Roelfsema et al., 2006). To assess eutrophication, apart from using the standard NDVI index (Xing et al., 2015), algorithms have been developed to estimate chlorophyll-a, such as the MODIS global chlorophyll-a concentration estimation algorithm (OC3M), OC4.V4 algorithm for the SeaWIFS sensor, and MERIS for Case 2 Waters, all of which have been widely implement for ocean waters (Moore et al., 2009, O'Reilly et al., 1998, Ruddick et al., 2008, Seguro et al., 2015). In addition, there are the Floating Algae Index (FAI) developed by Hu (2009) and the Scaled Algae Index (SAI) developed by Keesing et al. (2011) as substitutes for NDVI, which are sensitive to atmospheric conditions. However, those algorithms are for retrieving chlorophyll-a from floating macroalgae from low spatial resolution images.

For small estuaries, where algal blooms occur on exposed intertidal mudflats, NDVI is most widely used as a proxy for benthic chlorophyll-a (Benyoucef et al., 2014, Brito et al., 2013, Liu et al., 2009, Hu and He, 2008, Van der Wal et al., 2010) since it has low sensitivity to sediment background effects compared to other vegetation indices (Barillé et al., 2011). This study aims to differentiate algal blooms from intertidal sediment so that the bloom areas can be linked to modelled nutrient concentrations and pathways. Therefore, NDVI is chosen in this study, derived from WV-2, CASI, and Landsat-8 images, due to its simplicity and tolerance to influence by sediment. Additionally, NDVI is also used to investigate algal growth behaviour through the spatio-temporal variation of NDVI, which could reveal links between algal blooms, hydrodynamics, nutrient concentrations and pathways.

## 4.3 Identification of algal mat location using NDVI

### 4.3.1 Pre-processing

#### 4.3.1.1 Geo-metric correction and transformation of projection

The 2015 and 2016 WV-2 images were pre-processed using the ENVI software package version 5.1, which is mainly used for pre-processing and image analysis in this study. The pre-processing steps were performed at first to ensure that all images are ready for further analysis (Aiazzi et al., 2007). Pre-processing begins

with geometric-correction of the WV-2 images. Although the WV-2 images were provided at level 2A, which means that the following corrections had already been applied, radiometric, sensor, and geometric, the images still require geometric-corrections as the images were captured at different off nadir angles. This difference of pointing direction results in offsets between the two datasets, inserting errors into multi-temporal data analysis unless corrected. To remove the overlapped areas and make two images able to be used together for multi-temporal image analysis, Image-to-Image registration, which matches the coordinate systems of a reference image to the uncorrected image, was applied (Baird and Milne, 1981, Murai, 1993, Richards, 1999, Richards and Jia, 2006). The 2015 image, collected at average off nadir angle of 9° which therefore has little horizontal plane distortion, was used as a reference image for the 2016 data, which was collected at a higher average off nadir angle of 20°.

The two images were co-registered using 10 control points selected from the reference image. The projection and datum used is the Universal Transverse Mercator (UTM) Zone 30 and the World Geodetic System datum (WGS84). Then, the dataset was resampled using the Nearest Neighbour method with a Root Mean Square Error (RMSE) of the results less than 0.05 m. The Image-to-Image geo-correction method was operated as described in Richards (1999), which explains the use of mapping functions for image correction. In addition, the CASI data, which have a different coordinate system (OSGB 1936), were transformed to the same coordinate system as the WV-2 images using the Nearest Neighbour resampling technique in Raster Projection module in the ArcGIS software package.

#### 4.3.1.2 Atmospheric correction

To remove influence of atmospheric effects in the image pixels, WV-2 and Landsat-8 images, which were delivered as radiometrically corrected image pixels, were converted to top of atmosphere spectral radiance using equation 4-1 (Updike and Comp, 2010) for each band of WV-2 images, and equation 4-2 (USGS, 2016) for each band of Landsat-8 images. The CASI data were provided as radiometrically corrected radiance pixels and so no conversion of DN to radiance was required.

$$L_{\lambda Pixel,Band} = \frac{K_{\text{Band}} \cdot Q_{Pixel,Band}}{\Delta\lambda_{Band}} \qquad \textit{Equation 4 - 1}$$

where $L_{\lambda Pixel,Band}$ are top of atmosphere spectral radiance image pixels ($W.m^{-2}.sr^{-1}.\mu m^{-1}$), $K_{Band}$ is the absolute radiometric calibration factor ($W.m^{-2}.sr^{-1}.count^{-1}$) for a given band as provided in the metadata file (.IMD), $Q_{Pixel,Band}$ are radiometrically corrected image pixels (counts), and $\Delta\lambda_{Band}$ is the effective bandwidth (μm) for a given band.

$$L_\lambda = M_L . Q_{cal} + A_L \qquad \textit{Equation 4 - 2}$$

where $L_\lambda$ is top of atmosphere spectral radiance ($W.m^{-2}.sr^{-1}.\mu m^{-1}$), $M_L$ is the band-specific multiplicative rescaling factor from the metadata file (RADIANCE_MULT_BAND_x, where x is the band number), $Q_{cal}$ is the quantized and calibrated standard product pixel values (DN), and $A_L$ is the band-specific additive rescaling factor from the metadata file (RADIANCE_ADD_BAND_x, where x is the band number).

The radiance WV-2, CASI, and Landsat-8 images were then processed using FLAASH (Fast Line of sight Atmospheric Analysis of Spectral Hypercubes), available in ENVI software, integrating the MODTRAN4 radiative transfer codes by Matthew et al. (2000). The FLAASH module retrieves sensor's gain and offset, as well as geometric information from metadata of those images. For the Ythan estuary, the middle latitude winter and summer atmospheric models were used, with a maritime aerosol model with an initial visibility of 80 km. After performing FLAASH, the influence of the atmosphere was removed and the images present top of atmosphere spectral reflectance values.

#### 4.3.1.3 Image pan-sharpening

WV-2 data and Landsat-8 have high resolution panchromatic bands (0.5 m) and (15 m) and lower resolution multispectral bands (1.88 m) and (30 m), respectively. For this study it would be ideal to use multispectral information at the higher resolution, so ENVI was used again to increase the resolution of the multispectral bands using the panchromatic band, so that algal mats can be identified and delineated with the highest possible accuracy. This technique is called pan-sharpening, and involves merging the low spatial resolution multispectral image to the higher resolution panchromatic image to get a new multispectral image

with the high resolution of the panchromatic image, in the region where the two images fully overlap (Candra, 2013, Kim et al., 2011, Yuhendra and Kuze, 2011).

The Gram-Schmidt pan-sharpening (GS) method, invented by Laben and Brower (2000) and patented by Eastman Kodak (Laben and Brower, 2000) was used to produce a new pan-sharpened image as it produces better sharpening images with lower colour distortion than any other methods (Aiazzi et al., 2007, Carle et al., 2014, Laben and Brower, 2000, Maurer, 2013). The GS method is based on an algorithm for vector orthogonalisation, which will take in non-orthogonal vectors and rotate them until they are orthogonal. In the case of satellite images, each image band corresponds to a one dimensional vector (Laben and Brower, 2000).

The GS process starts from a low spatial resolution panchromatic band being simulated by computing a weighted average of the multispectral bands. Then, the low spatial resolution multispectral bands are decorrelated using the Gram-Schmidt orthogonalisation algorithm, treating each band as a one-dimensional vector. The simulated low spatial resolution panchromatic band is then used as the first vector, which is not rotated or transformed in Gram-Schmidt transformation process but replaced by the high spatial resolution panchromatic band. Finally, all image bands are back transformed into the higher resolution space (Laben and Brower, 2000). As the CASI images supplied by SEPA have a high multispectral spatial resolution (1m), and no higher resolution panchromatic band, no pan-sharpening is required. The pre-processing steps are illustrated in Figure 4-1.

In addition, in order for all images to be used for multi-temporal analysis, it is necessary that all the images have the same spatial resolution. Since Landsat-8 and CASI data have lower spatial resolution (15 m and 1 m) than the pansharpened WV-2 image (0.5 m) after image sharpening, the Landsat-8 and CASI data were resampled to 0.5 m so that they have the same pixel size as WV-2 images. The resampling process was performed using the Map tool and the Layer Stacking tool in the ENVI software using the cubic convolution method before the resampled data are exported to analyse the variation in ArcGIS.

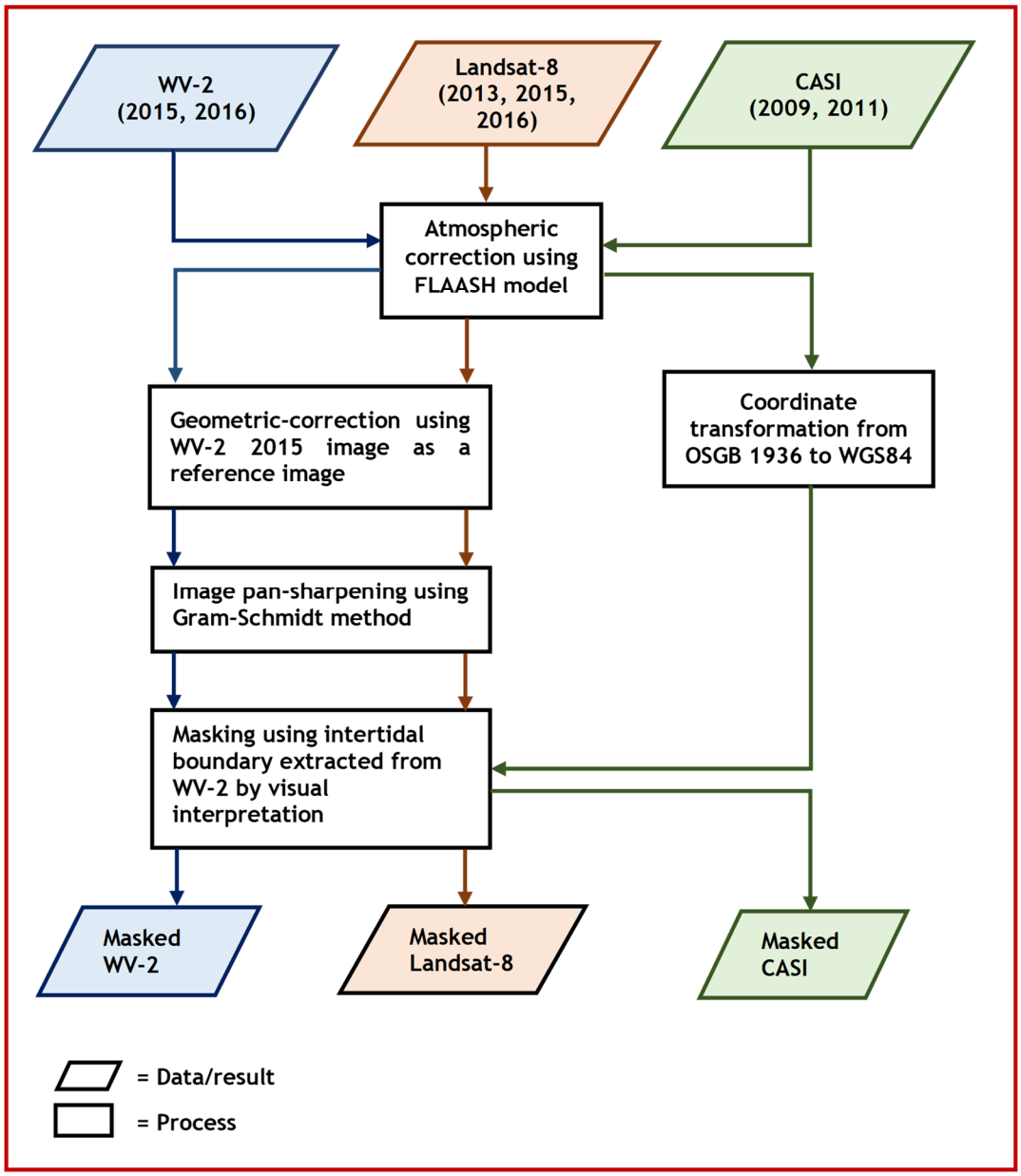


Figure 4-1: Pre-processing steps before image analysis

### 4.3.2 Identifying algal mat locations from NDVI

After the pre-processing stages described above, all of the images were analysed to initially identify areas where algal mats develop using NDVI. NDVI is an effective tool to identify healthy and vigorous live vegetation as well as for estimating green biomass (Buchhorn et al., 2016, DeFries and Townshend, 1994, Hayes and Sader, 2001, Huang et al., 2014, Pettorelli et al., 2005, Tucker et al., 1985, Zhang et al., 2009). It has been used to help to understand vegetation dynamics and distribution for many land cover studies (Buchhorn et al., 2016, DeFries and Townshend, 1994, Hayes and Sader, 2001, Huang et al., 2014, Pettorelli et al., 2005, Tucker et al.,

1985, Zhang et al., 2009). NDVI was first used by Rouse Jr et al. (1974), and is calculated from the difference between the near infrared band (NIR) and the red band divided by the sum of the spectral reflectances of the NIR and red bands (Equation 4-3) (Lillesand et al., 1994). Those two bands are used as they have strong and contrasting spectral responses to live green vegetation. Strong and healthy green plants produce high reflectance in the NIR band, while absorbing strongly in red band. Conversely, unhealthy plants have weak absorption in the red band and lower reflectance in the NIR band (Figure 4-2).

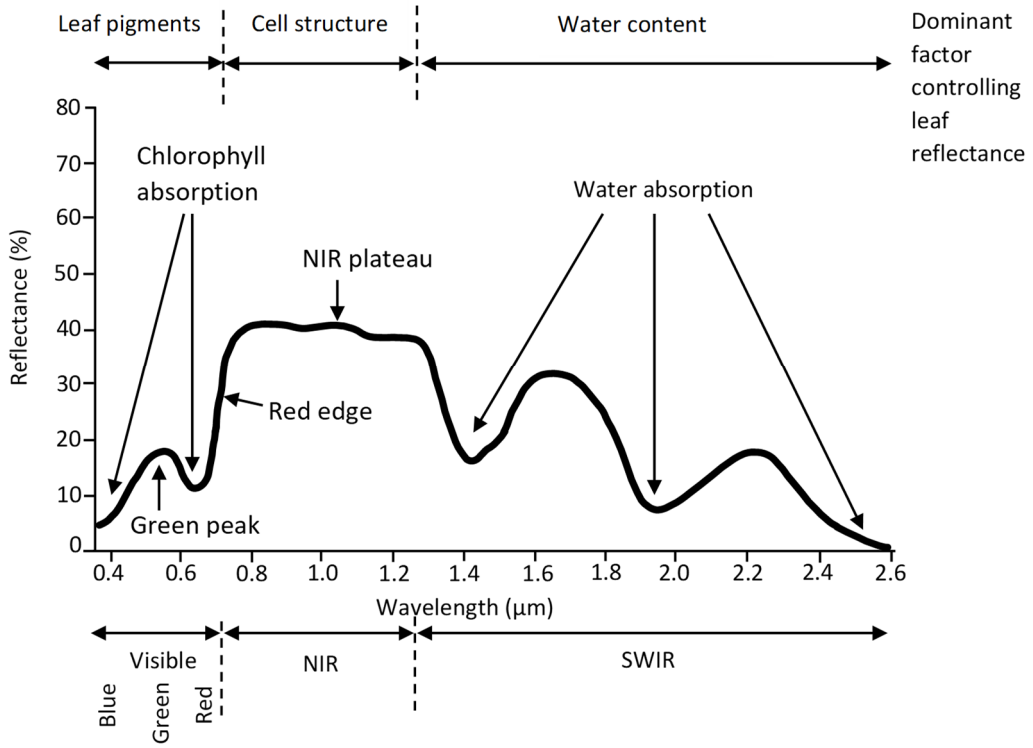


**Figure 4-2:** Electromagnetic spectral responses of vegetation. Modified from Keyworth et al. (2009).

NDVI values range from -1 to 1, with zero taken as the threshold for distinguishing vegetated and non-vegetated areas (Lillesand et al., 1994). Values close to 1 correspond to higher biomass of live green vegetation whilst values below 0 mean that no live green vegetation is present (Lillesand et al., 1994). For this study, NDVI values greater than 0.1 are used as a threshold to differentiate microalgal *(Microphytobentos: MPB)* from sediment (Benyoucef et al., 2014, Kazemipour et al., 2012), and 0.3 is a threshold to differentiate macro algae from MPB (Benyoucef et al., 2014, Kazemipour et al., 2012).

$$NDVI = \frac{(NIR - R)}{(NIR + R)}$$ *Equation 4 - 3*

where NIR is the reflectance of chlorophyll-a from NIR (band 2 in WV-2; band 16 in CASI; band 5 in Landsat-8) and R is the red band (band 5 in WV-2; band 10 in CASI; band 4 in Landsat-8)

The variation in NDVI is also calculated to understand how NDVI values at the same location vary from year to year, and from season to season. The NDVI variation is derived from the standard deviation of NDVI values at the corresponding pixels from the different image dates. The variation is calculated as Equation 4-4 using the Raster Calculator in Spatial Analyst Tools in ArcGIS.

$$SD = \sqrt{\frac{\sum(NDVI(ij) - \overline{NDVI(ij)})^2}{n - 1}}$$ *Equation 4 - 4*

Where $NDVI(ij)$ is the NDVI value at the $(i)$ pixel on image $(j)$, the mean $NDVI(ij)$ is calculated from all images and n is the number of images.

After calculating the NDVI from WV-2, CASI, and Landsat-8 images using the ENVI software package, the inter-seasonal NDVI maps for 2015 reveal that the coverage of MPB and macroalgae in autumn larger than spring and the higher NDVI (NDVI>0.3) is mostly found in autumn (Figure 4-3). Likewise, the inter-seasonal NDVI maps for 2016 reveal that the coverage of MPB and macroalgae in autumn is the largest, followed by spring and winter (Figure 4-4). MPB and macroalgae are only found in winter on exposed mudflats at Foveran Burn (Figure 4-4A) while in spring and autumn they occupy exposed mudflats along the main channel and at the tributaries (Figure 4-4B, C). These suggest the exposed mudflat at Foveran Burn has favourable conditions for macroalgal growth regardless of seasonal changes. Along the upstream part of the main channel, in contrast, there is instability of conditions favourable for growth as macroalgae were not present in spring but were during autumn. On the extensive mudflats in the central region, the NDVI values are lower than 0.1 in winter, which means there is no algal growth during winter (Figure 4-4A). However, NDVI values become higher (mostly 0.1-0.3) in both spring and autumn, reflecting spring growth of MPB in this area (Figure 4-4B, C).

The inter-annual NDVI in the same season shows consistency of algal type in spring, although the coverage of each type may vary (Figure 4-5). On the contrary, algal types found in summer for each location are significantly different year by year, in particular, on the extensive mudflats and exposed mudflats at Tarty Burn and Burn of Forvie (Figure 4-6). This suggests variation of factors support algal growth during summer. During this period, MPB and macroalgae can develop with different intensities in those areas and the pattern of development is less obviously related to the topography of the estuary. However, the exposed mudflats at Foveran Burn and along the main channel remain favourite locations for micro- and macro-algal growth during summer. In autumn (Figure 4-7), there is consistency of MPB and macroalgal development in the lower region, particularly along the main channel and on the exposed mudflats at Foveran Burn. In contrast, MPB on the extensive mudflats in the central region and macroalgae on the exposed mudflats at Burn of Forvie and Tarty Burn develop with different densities and patterns year by year.

Inter-annual variation of NDVI in the same season (Figure 4-8) reveals that autumn has the lowest variation across the estuary compared with spring and summer. However, the exposed mudflats at Forveran Burn where variation is slightly higher is an exception. Areas with low variation of the NDVI suggest stability of MPB and macroalgal growth. Where there is medium to high variation of NDVI, this suggests instability of algal growth. For instance, pure mudflats can develop MPB and then macroalgae, and areas with MPB can become macroalgal, and vice versa. High stability of algal growth in each area implies high stability of favourable conditions for algal growth.

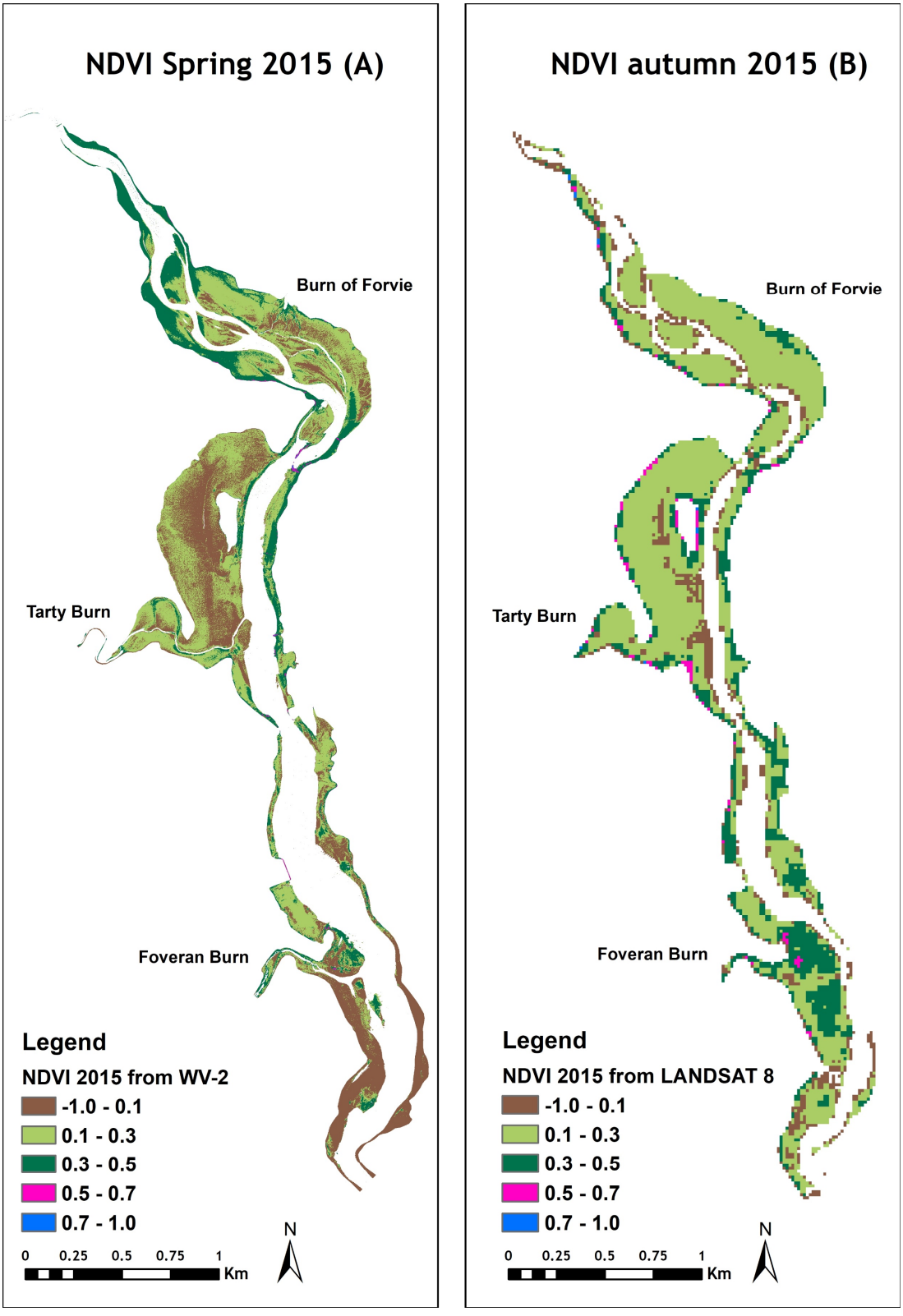


**Figure 4-3:** NDVI maps at different times. (A) Spring (WV-2; 20 April 2015; (B) Autumn (Landsat-8; 30 September 2015).

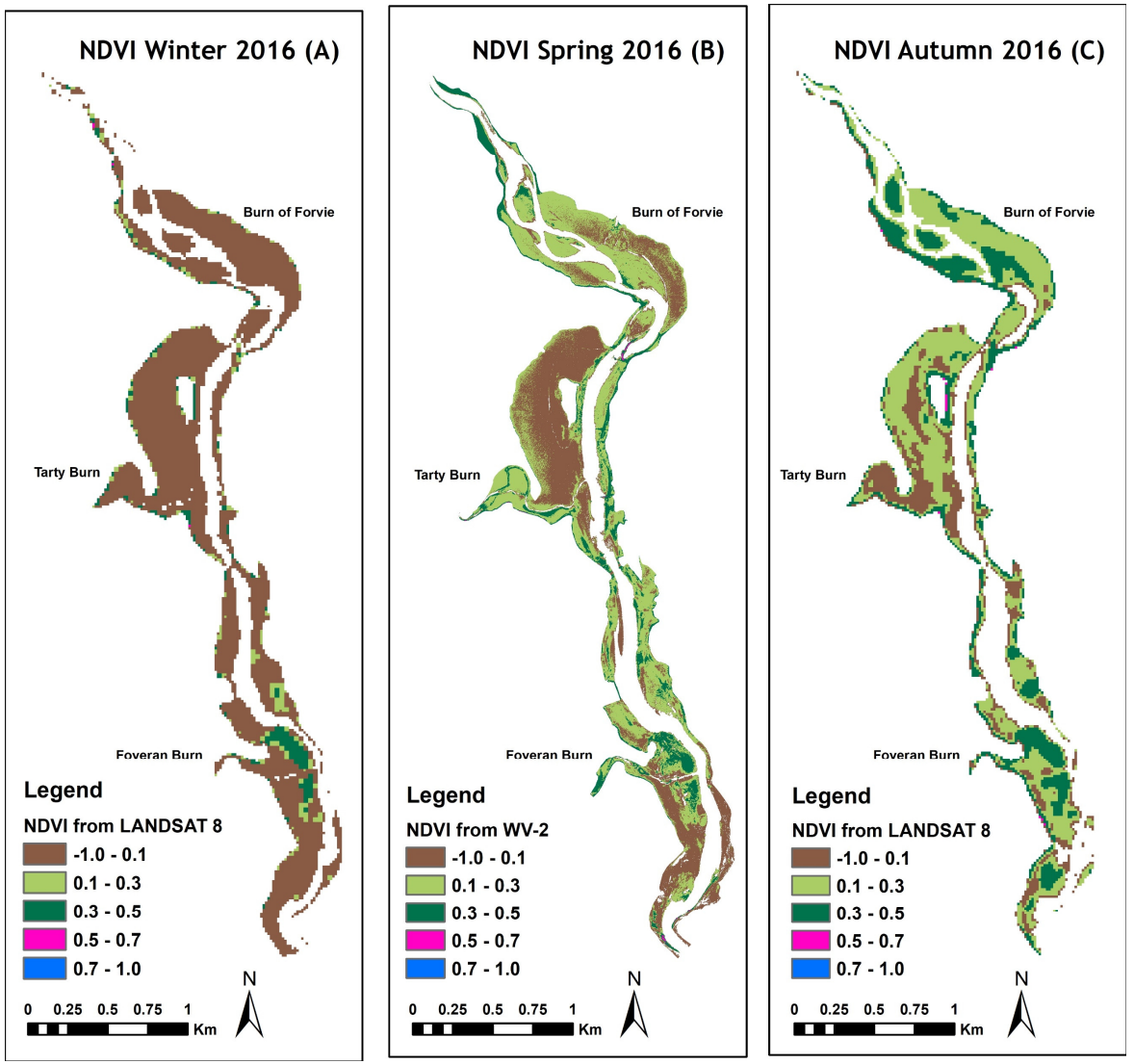


**Figure 4-4:** NDVI maps at different times. (A) Winter (Landsat-8; 28 February 2016); (B) Spring (WV-2; 9 May 2016); (C) Autumn (Landsat-8; 09 October 2016).

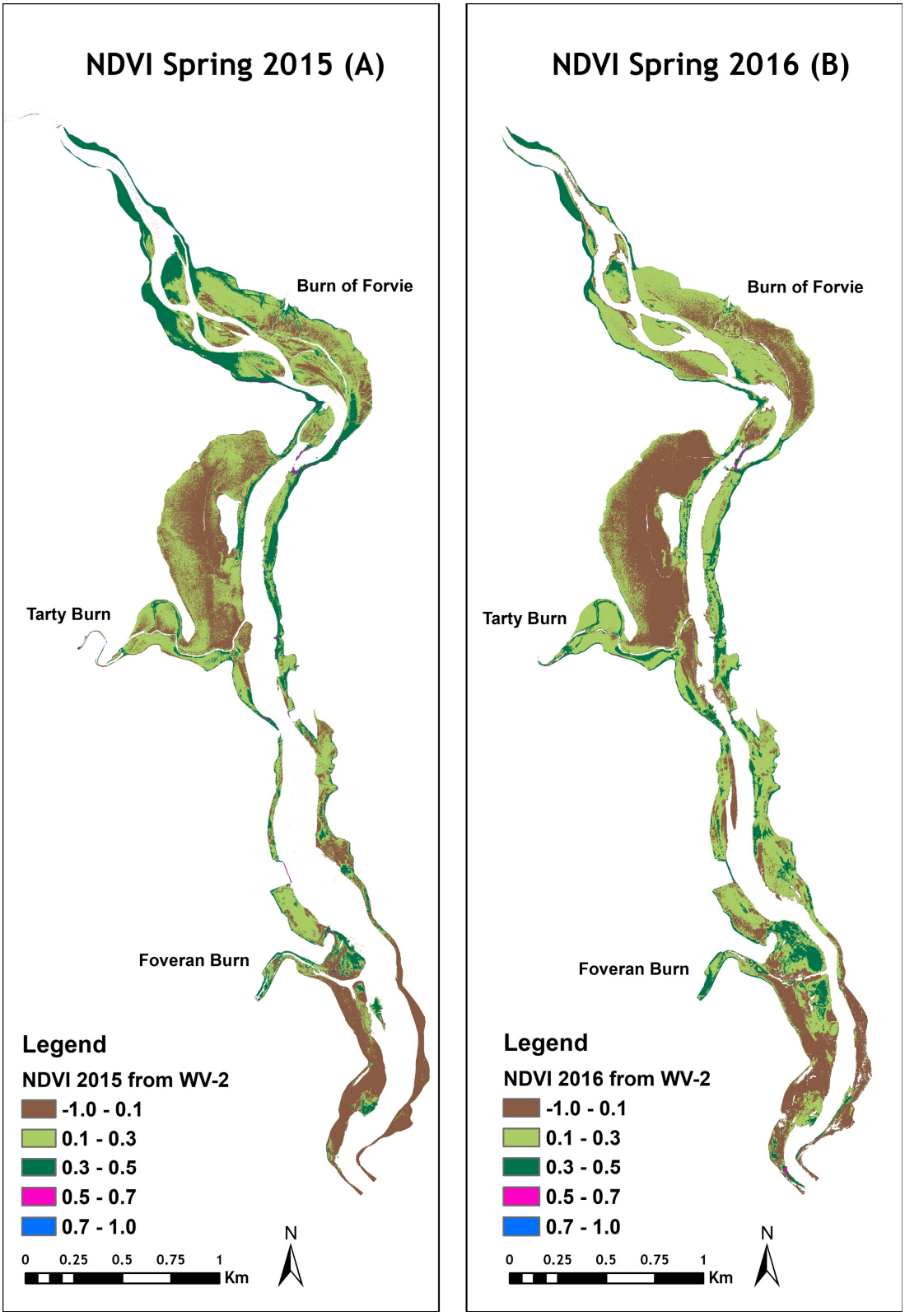


**Figure 4-5:** NDVI maps at different times. (A) Spring (WV-2; 20 April 2015; (B) Spring (WV-2; 09 May 2016).

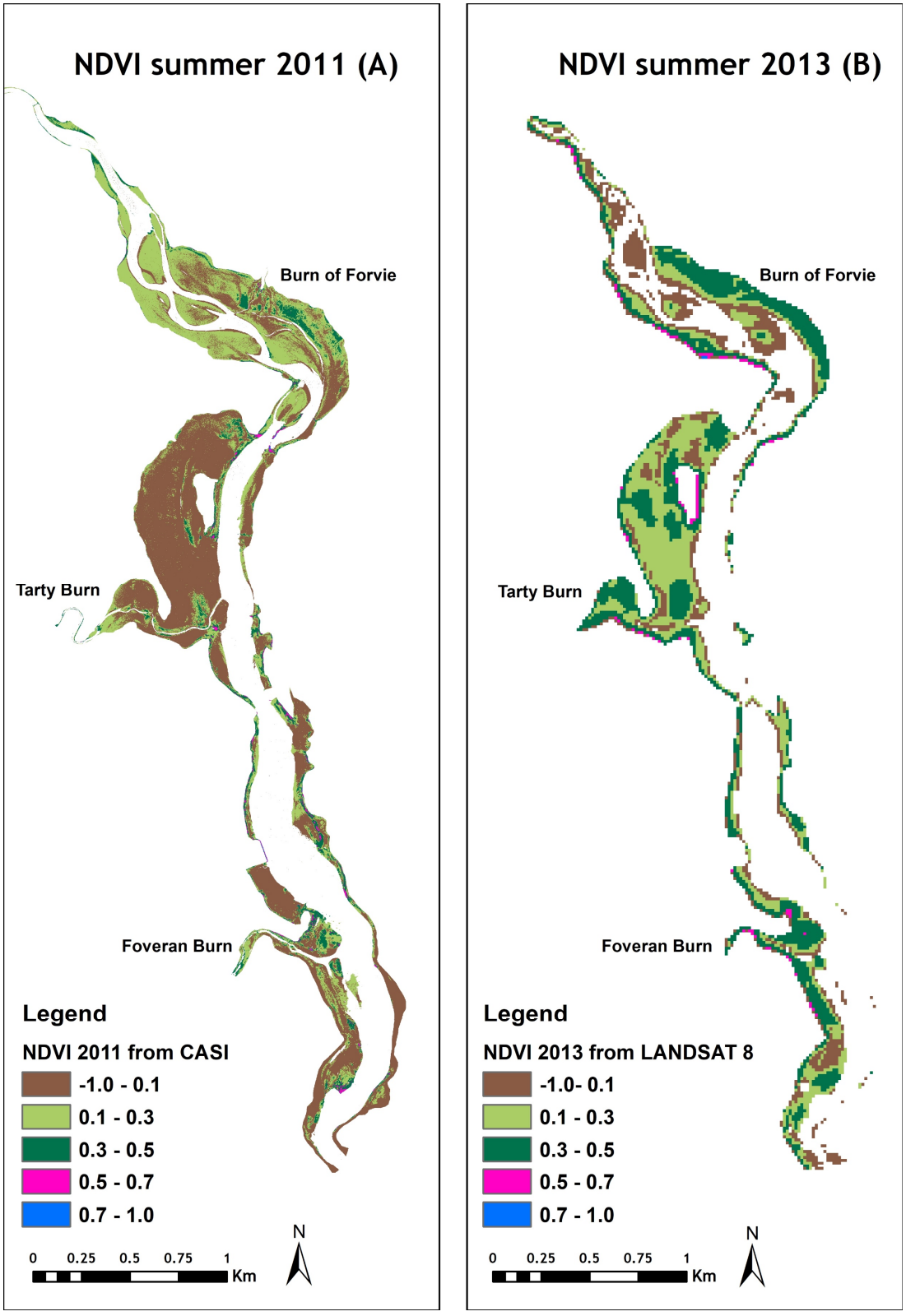


**Figure 4-6:** NDVI maps at different times. (A) Summer (CASI; 14 July 2011; (B) Summer (Landsat-8; 30 August 2013).

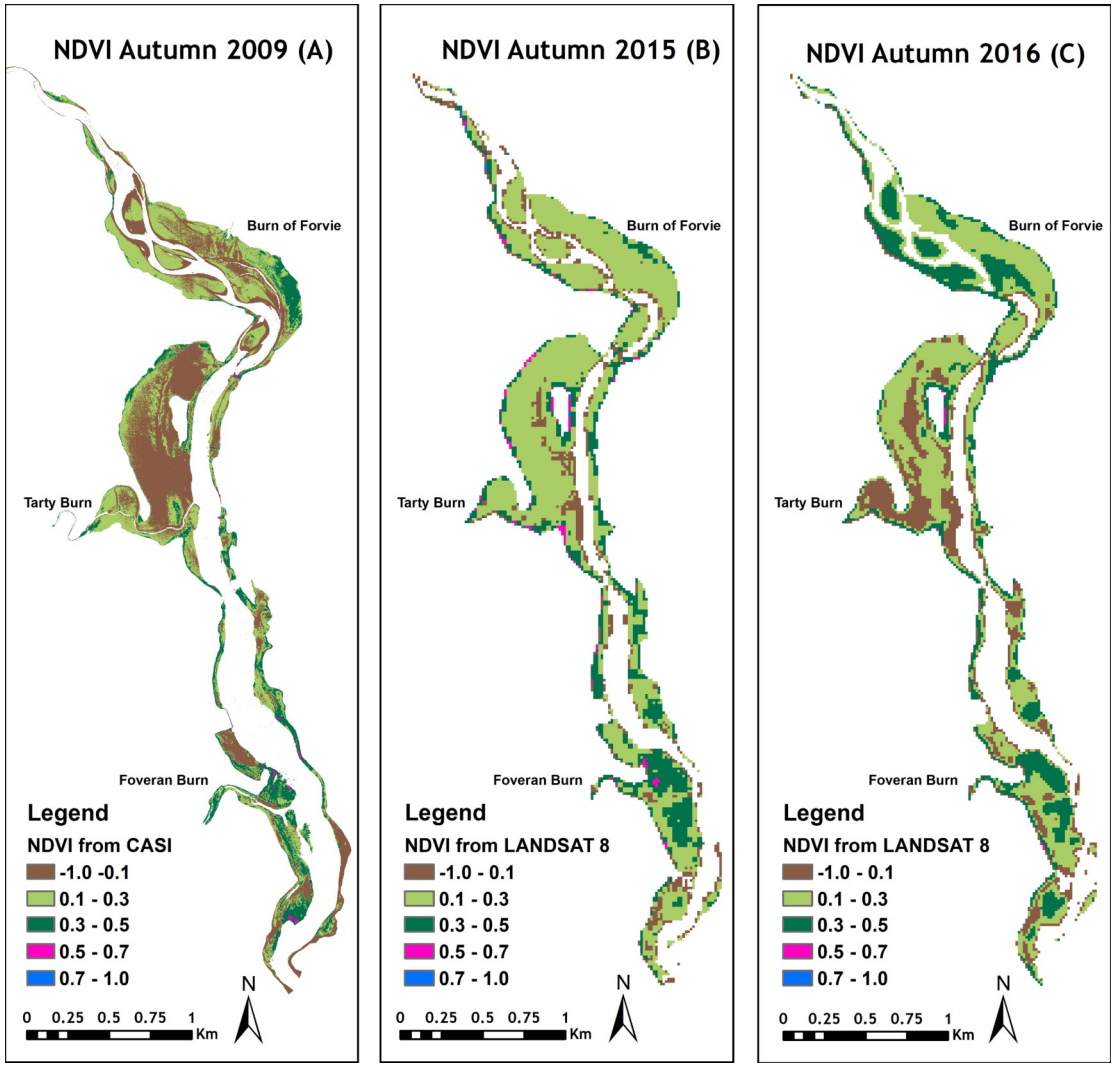


**Figure 4-7:** NDVI maps at different times. (A) Summer (CASI; 11 September 2009; (B) Autumn (Landsat-8; 30 September 2015); (C) Autumn (Landsat-8; 09 October 2016)

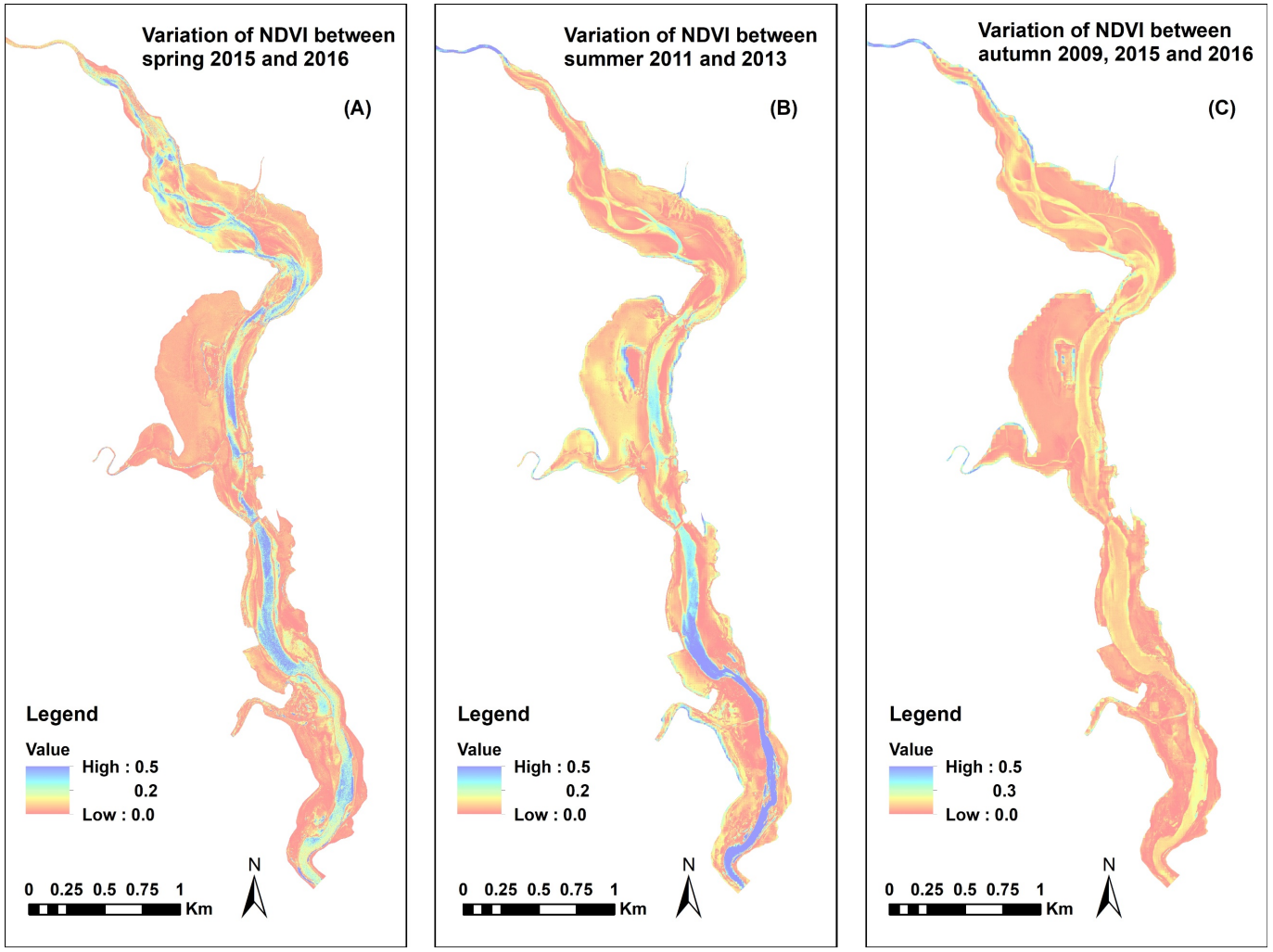


**Figure 4-8:** variation of NDVI between spring 2015 and 2016 (A); summer 2011 and 2013 (B); and autumn 2009, 2015, and 2016 (C)

These NDVI data are then used to assess whether the algal mats develop in accordance with the nutrient concentrations modelled for the same seasons as the NDVI data. Chapter 5 describes how NDVI data is used to help validate the model results.

### 4.3.3 Investigation of the relationship between NDVI and biomass patch data

Although remote sensing data provide information from a distance and need less on-site observation, the results derived from the image analysis still require assessment to assess their quality. NDVI maps obtained from the image analysis thus need assessment. However, no field measured NDVI data collected at the same time the images were taken are available. Biomass data, from samples collected by SEPA, are used to validate the NDVI results retrieved from the CASI. Biomass is selected for NDVI validation as many studies have shown that NDVI derived from remote sensing data is highly correlated with green biomass (Bindu et al., 2018, Prabhakara et al., 2015, Wang et al., 2016, Wehlage et al., 2016). For instance, Wehlage et al. (2016) studied the relationship between NDVI from satellite images including MODIS and SPOT 4 and 5 and above-ground biomass, as well as NDVI from field spectrometry during two growing seasons in the Alberta prairies, USA. They show that NDVI is positively related to the log of green biomass especially during mid-summer, which provides the strongest correlation *[$R^2$ = 0.97]*. Wang et al. (2016) also studied relationships between NDVI and productivity of prairie grassland in the growing season (May to October, 2014). Their findings confirm that NDVI, which is strongly related to biomass, is associated with the variety of plants at the study site. They also note that growing stage and the demand for water of plant influence the strength of the relationship.

The biomass used in this study is calculated from 28 algal patches found on intertidal mudflats in 2009 and 9 algal patches in 2011. According to Gray (pers comm 2018) biomass was calculated from the size of each algal patch multiplied by the average wet weight of the algal patch. Additionally, the average wet weight was calculated from the actual weight of the sample from the 0.25 $m^2$ quadrat, which was recorded twice and then the weight multiplied by 4. The biomass of each algal patch was stored as a GIS shapefile polygon, which were used as a clipping mask to extract NDVI calculated from the CASI images. NDVI values which are inside each clipping mask then were extracted and observed their normal

distribution. The workflow of extracting NDVI using the biomass file is shown in Figure 4-9.

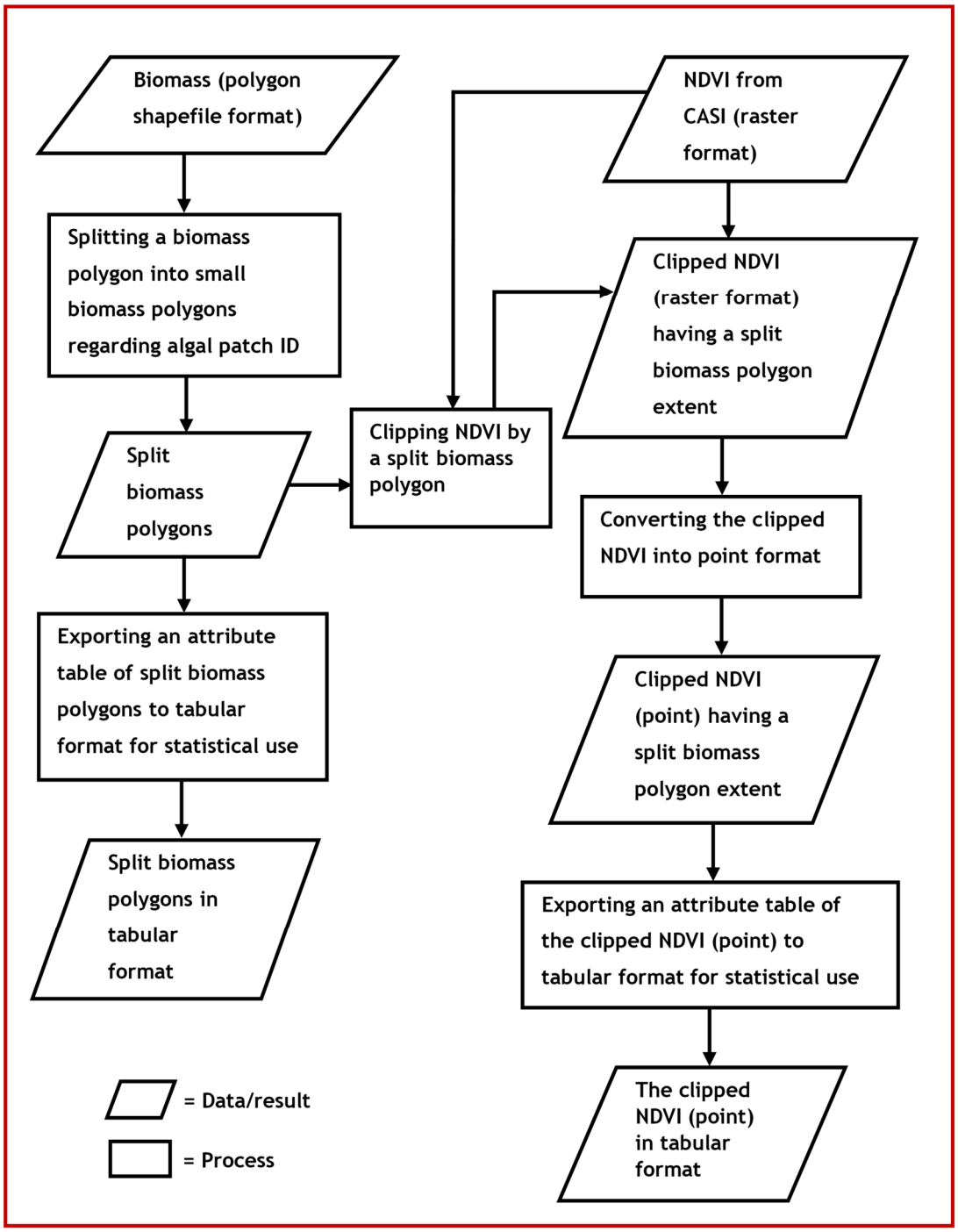


**Figure 4-9:** The work flow of extracting NDVI using biomass file carried out in ArcGIS Model builder

The extracted median NDVI values and measured biomass were fitted using linear regression models within Minitab software to study their relationships. The sign of the coefficient is negative on September 11, 2009, which indicates a negative

relationship between median NDVI and biomass. It can be explained as biomass increases, median NDVI decreases. This relationship is possibly due to different times of collection of the data: biomass samples were obtained during the summer period when algae were mature, but the CASI data were acquired on September 11, 2009 when biomass was affected by some algae dying and the early growth stage of other algae types that grow in the area during autumn. The model equation implies that the median NDVI decreases by 0.000060 $gC/m^2$ for every 1 unit increase in biomass. (Table 4-1; Figure 4-10A). On July 14, 2011, the sign of the coefficient is positive, due to collecting biomass samples and acquiring CASI data at the same algal growth stage. At zero biomass, the median NDVI is 0.369 and for each 1 $gC/m^2$ increase in biomass, the median NDVI increases on average by 0.000118 (Table 4-2; Figure 4-10B). The model for 2009 explains 23% of the variation in the median NDVI 2009, and 46% in 2011.

Although the model $R^2$ values are low, both 2009 and 2011 have significant p-values (0.028 and 0.044, respectively) and so are statistically significant. Plots of model residuals versus fit for both 2009 and 2011 show that the residuals are randomly distributed (Figure 4-11). These results suggest that the NDVI data can be reliably be used to validate modelled nutrient concentrations in chapter 5.

**Table 4-1:** The regression model summary of median NDVI and biomass in 2009 from 28 samples.

| **Model 2009** | **S** | **R-sq** | **R-sq (adj)** | |
|---|---|---|---|---|
| | 0.048 | 22.95% | 18.89% | |
| **Term** | **Coef** | **SE Coef** | **T-Value** | **P-Value** |
| Constant | 0.0967 | 0.0149 | 6.50 | 0.000 |
| Biomass | -0.000060 | 0.000025 | -2.38 | <0.028 |
| **Regression Equation** | Median NDVI 2009 = 0.0967 – 0.000060 Biomass | | | <0.028 |

**Table 4-2:** The regression model summary of median NDVI and biomass in 2011 from 9 samples.

| **Model 2011** | **S** | **R-sq** | **R-sq (adj)** | |
|---|---|---|---|---|
| | 0.034 | 46.08% | 38.38% | |
| **Term** | **Coef** | **SE Coef** | **T-Value** | **P-Value** |
| Constant | 0.3692 | 0.0210 | 17.59 | 0.000 |
| Biomass | 0.000118 | 0.000048 | 2.45 | <0.044 |
| **Regression Equation** | Median NDVI 2011 = 0.3692 + 0.000118 Biomass | | | <0.044 |

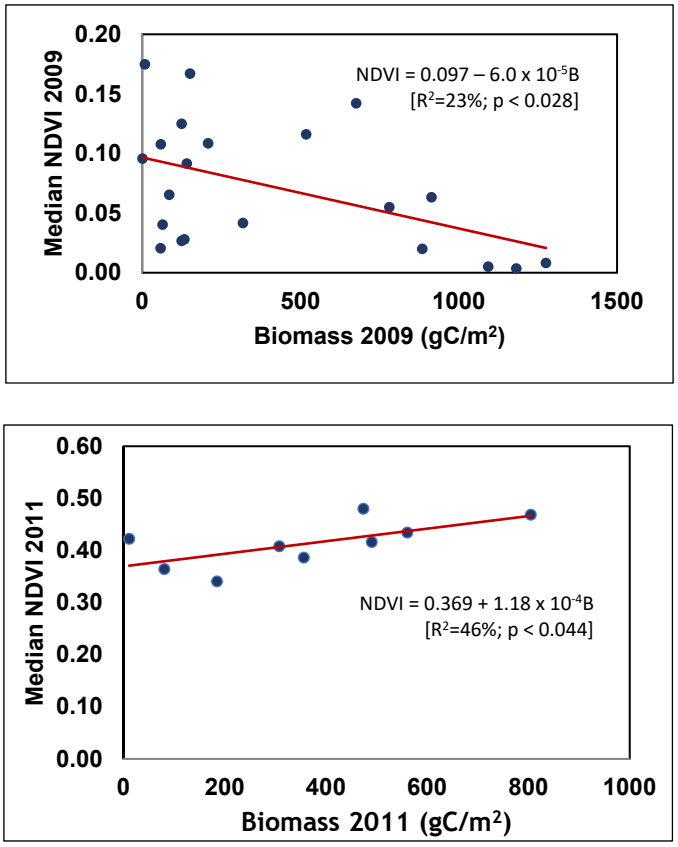


**Figure 4-10:** Relationships between median NDVI and measured biomass in: (A) 2009; and (B) 2011. Lines are linear regression relationships.

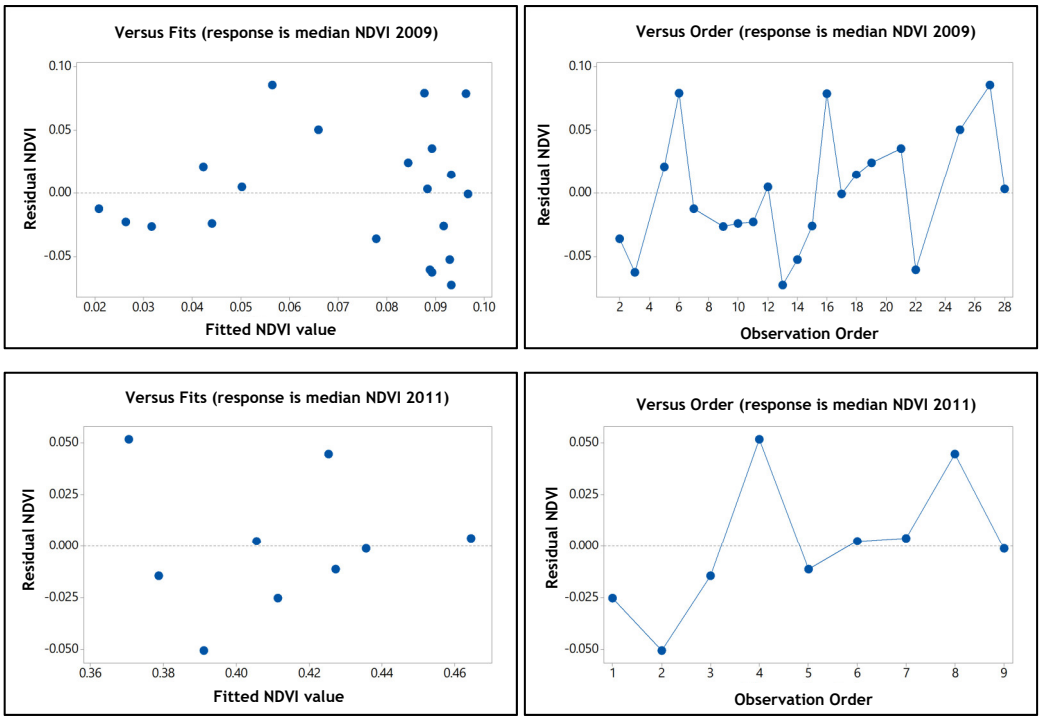


**Figure 4-11:** The plot of residual versus fit and the plot of residual versus order in 2009 and 2011.

### 4.3.4 Using vector algal mat maps from SEPA for assessing NDVI maps

Apart from using the regression relationships above to study the relationship between NDVI derived from CASI data and algal biomass, the reliability of the NDVI results can also be examined qualitatively. The method compares NDVI maps with vector algal mat maps, which are in a field-based GIS shape file format created in 2009 and 2011. The comparison between the NDVI and vector algal mat maps is based on a raster format. The comparison starts with extracting areas where algal mats develop from pure mudflats on the NDVI maps from 2009 and 2011. The NDVI threshold used to define algal mats is values greater than 0.1. This threshold is selected based on studies by Benyoucef et al. (2014) and Kazemipour et al. (2012), which corresponds to the locations of algal blooms which were found during the site visit. Once algal mats are defined, these areas are compared with the vector algal mat maps once converted into raster format. The raster calculator tool in ArcGIS is used to find corresponding areas between algal mats from NDVI and vector algal mat maps, as well as identifying overestimated and underestimated algal mats. The work flow of the comparison method is shown in Figure 4-12.

The results in Figure 4-13 show that in 2009, 44% of the total area of algal mats from NDVI correspond to algal mats from SEPA, but 56% of the total area of algal mats from NDVI were not identified as such in the field and so are overestimated algal mats. In addition, 54% of total area of algal mats mapped in the field by SEPA are not classified as algal mats by NDVI analysis (Table 4-3). In 2011, the total area of algal mats from NDVI is much greater than from SEPA with only 13% of the total area of algal mats identified from NDVI corresponding to SEPA's field mapping. Also, 10% of the total area of algal mats from SEPA maps are not recognised as algal mats by NDVI analysis (Table 4-3). Although the correspondence between algal mat locations identified from NDVI analysis and from SEPA maps are low in both years, most of the NDVI-based areas of algal mats that do correspond are completely within the areas of algal mats identified by SEPA. These suggest that NDVI still gives promising results, even though there are some overestimations and underestimations. These results suggest that some caution is needed in interpreting NDVI maps, although how much of the discrepancy is due to mis-identification in the field mapping and how much is from the NDVI classification is unable to be determined. Taking account of this uncertainty, NDVI maps are

used along with vector algal mat maps for validation of nutrient concentration predictions in Chapter 5.

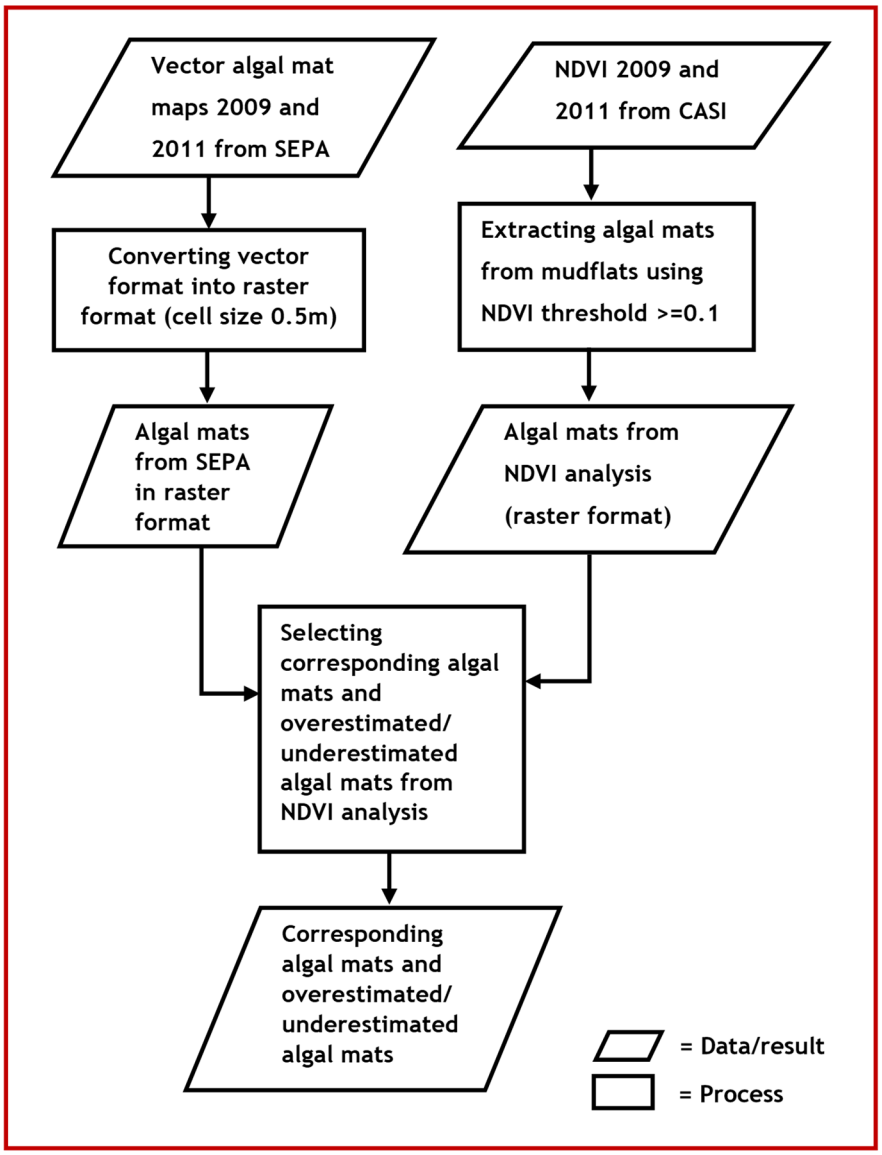


**Figure 4-12:** Work flow of the comparison method carried out in ArcGIS

**Table 4-3:** Percentage of algal mats from NDVI 2009 and 2011 compared to algal mats mapped in the field by SEPA

| No. | Description | Algal mats from NDVI 2009 | Algal mats from SEPA 2009 | Algal mats from NDVI 2011 | Algal mats from SEPA 2011 |
|---|---|---|---|---|---|
| 1. | Total algal mats | 0.48 $km^2$ | 0.45 $km^2$ | 0.70 $km^2$ | 0.10 $km^2$ |
| 2. | Corresponding algal mats | 0.21 $km^2$ (44%) | | 0.09 $km^2$ (13%) | |
| 3. | Overestimated algal mats | 0.27 $km^2$ (56%) | | 0.61 $km^2$ (87%) | |
| 4. | Underestimated algal mats | 0.24 $km^2$ (54%) | | 0.01 $km^2$ (10%) | |

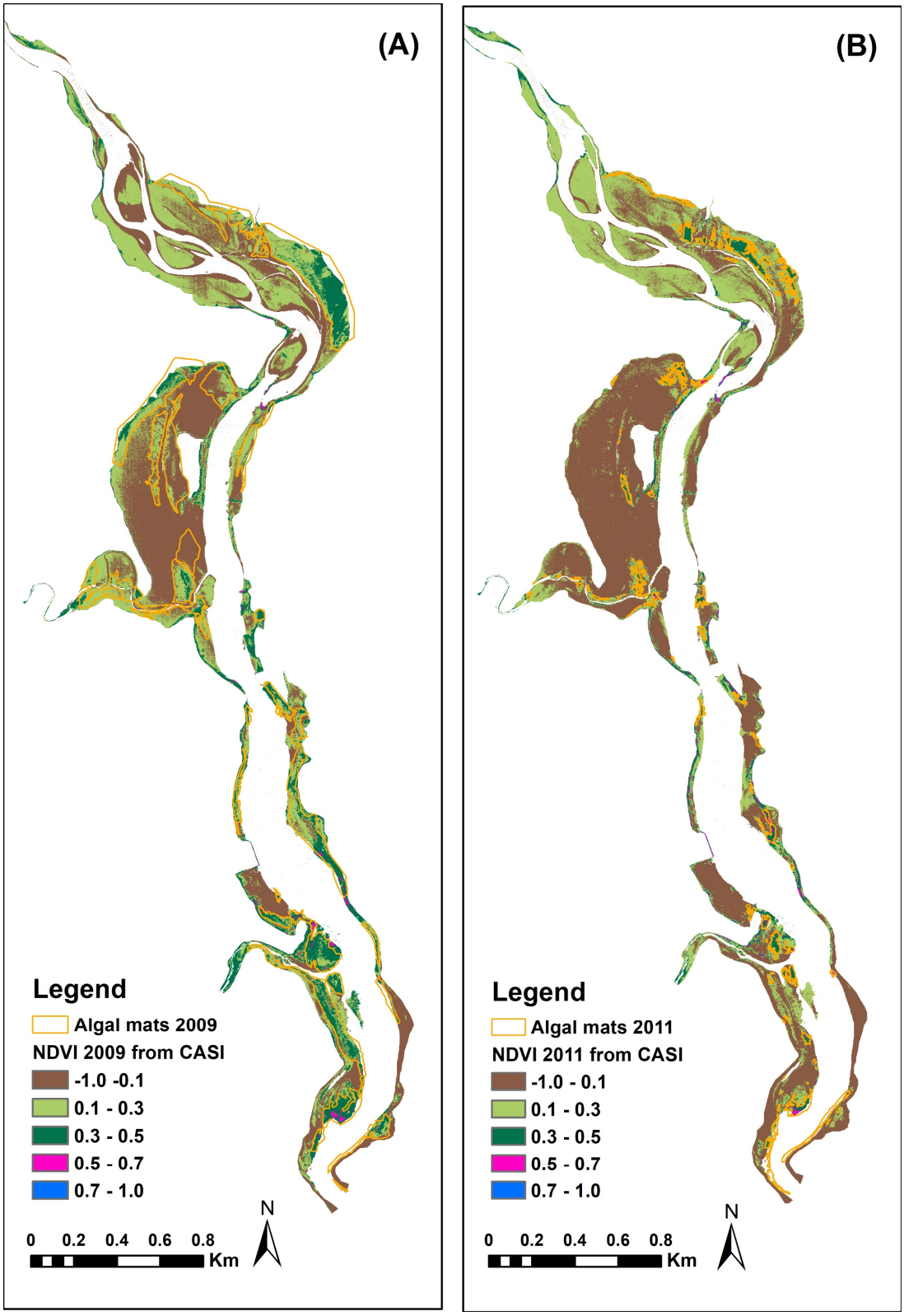


**Figure 4-13:** NDVI in September 2009 comparing to SEPA algal mat vector 2009 (A); NDVI in October 2011 comparing to SEPA algal mat vector 2011 (B)

## 4.4 Identification of wet - dry area using image ratio

The WV-2 image acquired at 11:30 am on 20 April 2015 and the Landsat-8 image acquired at 11:10 am on 30 September 2015 during low tide were used to differentiate the river channel from mudflats, the results of which are used to validate the delimitation of flooded and dry areas by the model. The WV-2 and Landsat-8 images are utilised as they were captured at a known specific time and hence, they can be used to compare with the modelled water depths simulated at the same time. In addition, the very high spatial resolution (0.5m) of the pan-sharpened WV-2 image and 15m the pansharpened Landsat-8 image enable ease of comparison between the model results and the identified wet - dry areas from the images. Although there are two WV-2 and four Landsat-8 images available for this study (see Chapter 2.2), the images taken only in 2015 were used for this purpose. This limitation results from unavailability of modelling parameters such as river flow and tidal level data in 2013 and 2016. As a result, there are no simulated hydrodynamics for these years. As for the CASI data, they are excluded as they are collected from several flight paths, each of which has its own time record and has smaller coverage compared to WV-2 and Landsat-8.

Extracting inundated areas and exposed mudflats can be achieved by many methods from remotely sensed data including: classification and band ratio techniques using multiple bands, density slices and edge detection methods using a single band, as well as digitization through visual interpretation. Among these methods, image ratio of infrared wavelength regions, which exhibits strong absorption of the water spectrum, and the visible wavelength region, which shows highest reflectance of the water spectrum (Frazier and Page, 2000, Manavalan et al., 1993, Ryu et al., 2002), is one of the most effective methods used to separate water and land (Santra and Mitra, 2016, White and El Asmar, 1999). For instance, Alesheikh et al. (2007) used band ratio between band 5 (Shortwave infrared band) and band 2 (green band) of Landsat-5 image, which is an algorithm for separating water from land from Landsat imagery within the ERMapper software, to detect coastline change. In addition to using two bands in a simple ratio, the Normalized Difference Water Index (NDWI) formula, originally published by McFeeters (1996), has also been widely used to extract water content (Santra and Mitra, 2016). In addition, a different NDWI, introduced by Gao (1996), has been applied in many studies to indicate the change in the water content. For this study, the NDWI of

McFeeters (1996) was applied. The NDWI is computed by difference between the green band and the NIR band, divided by the sum of spectral reflectance of these two bands (Equation 4-5; (McFeeters, 1996). The NDWI formula produces a new image (values from -1 to +1) in which the positive values are water areas whilst the negative values are non-water areas. Although Xu (2006) pointed out that the NDWI formula overestimates water areas due to a including built-up areas which also have low reflectance in the NIR band, this is not a problem in the Ythan case as there are no built-up areas. For the WV-2 image, it is found that the NIR band 2 (band8) of WV-2 image has the lowest spectral response to water while the green band (band 3) of WV-2 has the highest spectral response. Thus, those two bands were selected to calculate NDWI on ENVI software platform using Equation 4-5.

$$NDWI = \frac{(Green - NIR2)}{(Green + NIR2)} \qquad \textit{Equation 4-5}$$

where Green refers to the green band (WV-2 band 3, Landsat-8 band3) and NIR2 refers to the NIR band2 (WV-2 band 8, Landsat-8 band 5).

The ratio image (Figure 4-14A, 4-15A) reveals water content in bright tone whilst darker tone represents non-water content. The river channel derived from NDWI is also compared to water channel derived from the original WV-2 and Landsat-8 images by visual interpretation to examine whether the boundary of the water channel seen from the original image corresponds to the ratio images. The results show that the boundary of the ratio images and the water channel derived from visual interpretation match closely (99.4%, 96.4%) (Table 4-4, 4-5). Figure 4-14B shows that 0.62% mismatch areas are mostly found in the upper region of the estuary where the main channel is very shallow, which can cause misinterpretation. Figure 4-15B shows larger mismatched areas (3.6%), which are found along the main channel across the estuary, which could be caused by a larger pixel size (15m). The high percentage of matching water areas between NDWI and visual interpretation supports using NDWI to differentiate channels. Thus, the extracted water channels from the WV-2 and Landsat-8 images, which reveal wet-dry areas occurring at the time the images were taken, were used as references to compare with the modelled water depths simulated at the same time the images acquired, which is detailed in Chapter 5.

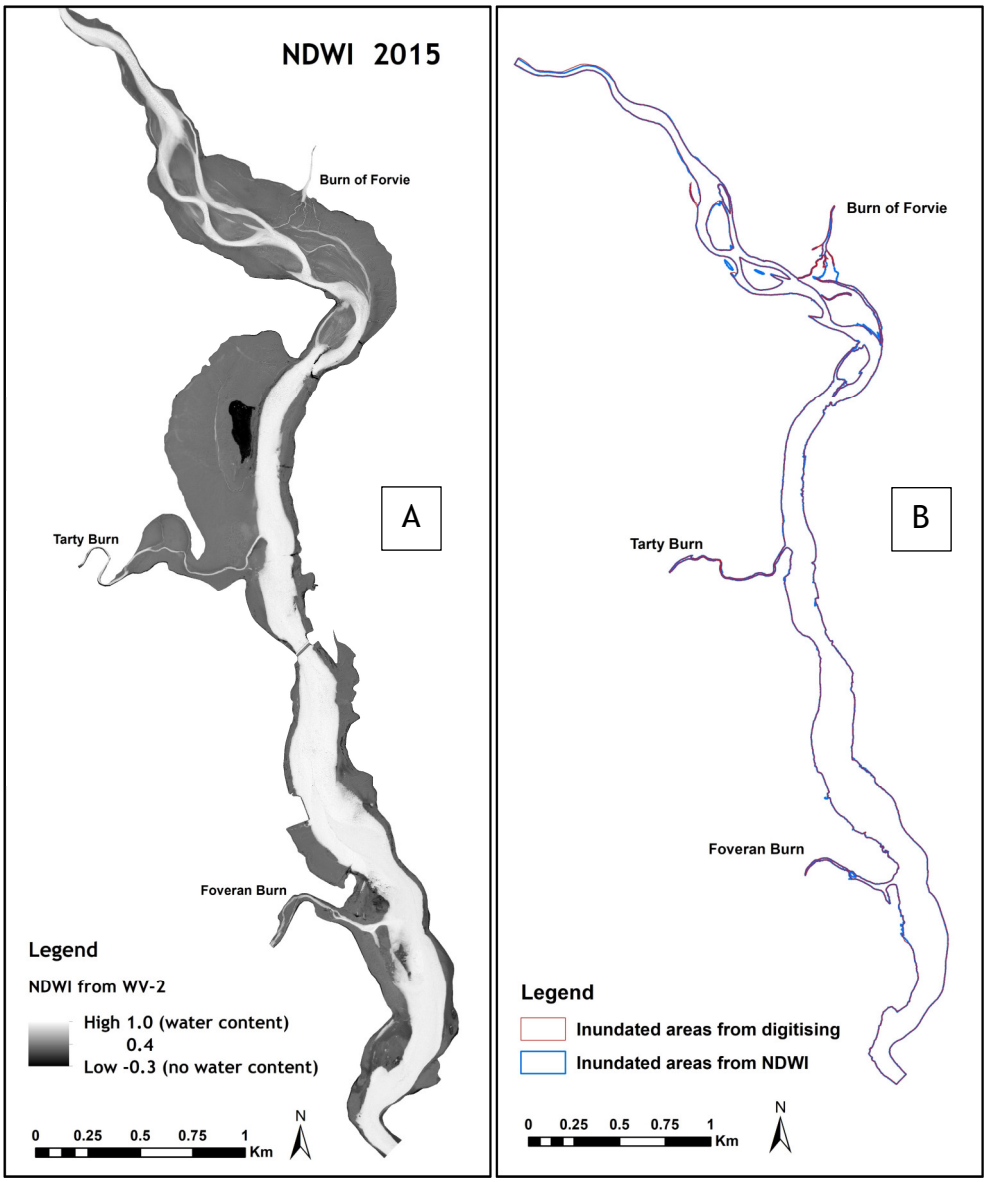


**Figure 4-14:** (A) NDWI derived from WV-2 image acquired during low tide at 11:30 am on 20 April 2015; (B) Inundated areas from NDWI derived from WV-2 overlaid by inundated areas from visual interpretation.

**Table 4-4:** Percent of matched and mismatched inundated area derived from visual interpretation compared with NDWI from WV-2

| Method | Inundated area (water content) ($km^2$) | Matched area (%) | Mismatched area (%) |
|---|---|---|---|
| Visual interpretation | 0.90 | 99.38 | 0.62% |
| NDWI | 0.89 | | |

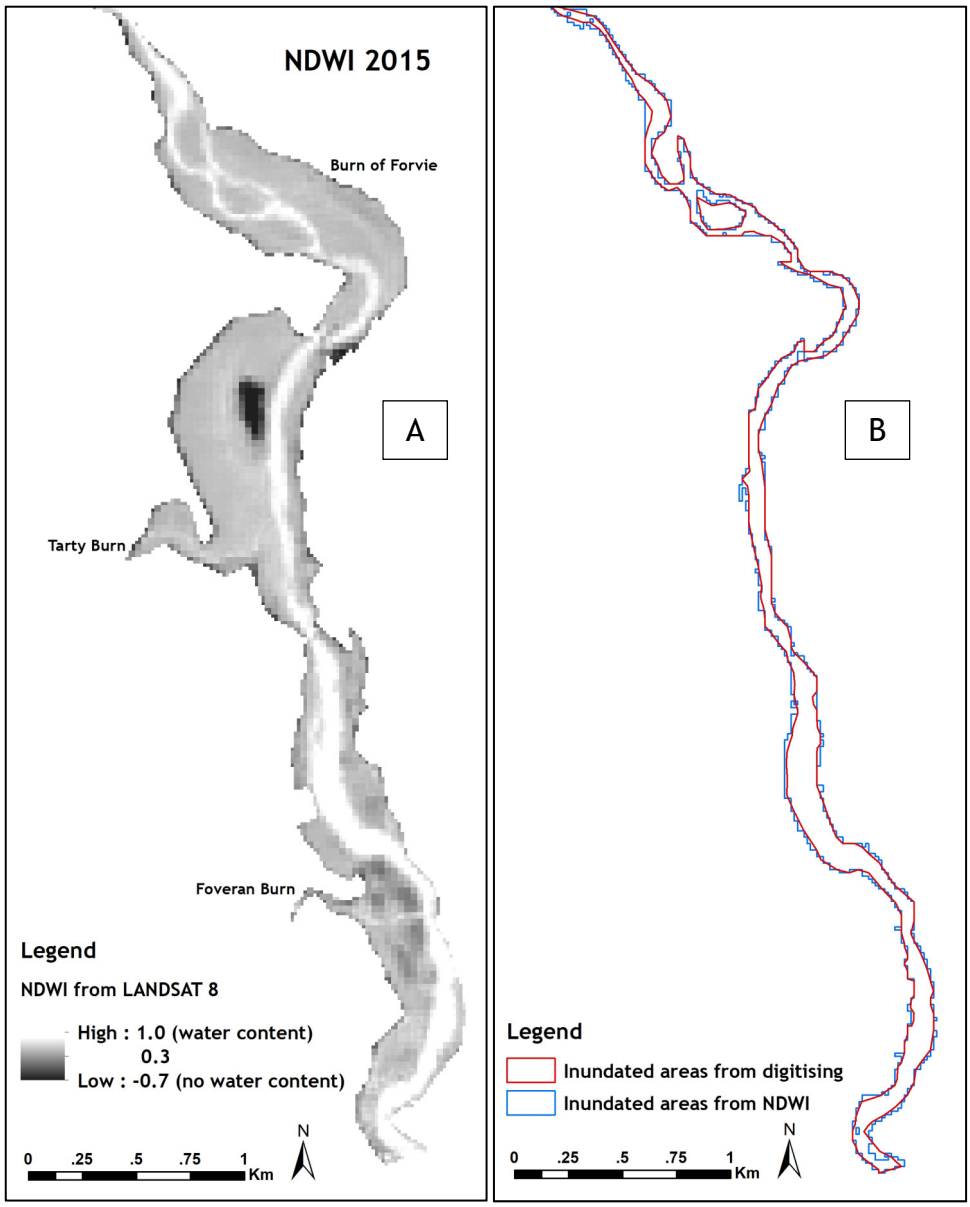


**Figure 4-15:** (A) NDWI derived from Landsat-8 image acquired during low tide at 11:10 am on 30 September 2015; (B) Inundated areas from the NDWI derived from Landsat-8 overlaid by inundated areas from visual interpretation.

**Table 4-5:** Percent of matched and mismatched inundated area derived from visual interpretation compared with NDWI from Landsat-8

| Method | Inundated area (water content) ($km^2$) | Matched area (%) | Mismatched area (%) |
|---|---|---|---|
| Visual interpretation | 0.54 | 96.43% | 3.57% |
| NDWI | 0.56 | | |

## 4.5 Summary

This chapter focuses on how to calculate NDVI and NDWI maps from WV-2, CASI, and Landsat-8 images for model validation. The aims of using remote sensing data as a tool for validating model results are to help reduce cost and time of field data measurements as well as to examine potential of using the data for model validation. NDVI, a proxy for algal bloom density, is used for studying their relationships to modelled nutrient concentrations and to comprehend behaviour of algal development. Studying inter-season NDVI through the time reveals that algal coverage in winter is the lowest followed by spring and autumn, which is the highest. This reflects the growing season of algae in the Ythan estuary. MPB and macroalgae can be generally found on the exposed mudflats along the main channel and on exposed mudflats at the tributaries in spring and autumn. However, they can be found in winter as well but only on exposed mudflat at Foveran Burn. This suggests the exposed mudflat at Foveran Burn has greater stability of favourable conditions for micro and macroalgal growth regardless of season compared with other areas. Inter-annual NDVI for the same seasons reveal consistency of algal types that develop at each location in the estuary during spring and autumn. However, this consistency is not found during summer particularly on extensive mudflats in the central region and on the exposed mudflats at Burn of Forvie and Tarty Burn, which suggests that a variety of factors support algal growth during summer in these areas.

Inter-annual variation of NDVI in the same season reveals that autumn has the lowest variation across the estuary followed by spring and summer, which has the highest variation. Low variation suggests high stability of favourable conditions for algal growth during autumn and as such stability of MPB or macroalgal growth in the areas. Whilst medium to high variation implies low stability of favourable condition during spring to summer in the estuary resulting in instability of their development in the areas.

To assess the validity of using NDVI maps to infer algal density, this study investigates the relationship between NDVI retrieved from remote sensing data and biomass and algal mat maps derived from SEPA's field mapping and sampling. The relationship shows that NDVI and biomass can be both positively and negatively related, depending on the timing of the field sampling relative to the

remote sensing data collection. Where both data sets are collected at the same time, a positive relationship between NDVI and algal biomass is found. Although the strength of the relationship between NDVI and biomass is low, the residuals are independent, and the p-values of the linear regression models are statistically significant. Comparing NDVI with algal mat maps also shows promising results although there are some overestimations and underestimations of algae from NDVI.

To identify wetted and dry areas, the NDWI index is used, created from WV-2 and Landsat-8 data. As there was no field data collection when the image was taken, the inundated areas derived from the NDWI map were validated with the water areas extracted from the same WV-2 image by visual interpretation. The comparison shows a good agreement between flood-dry area from the NDWI and from visual interpretation. In summary, although not without some uncertainties, remote sensing provides useful information on algal growth location and behaviour as well as it illustrates boundary of flood-dry areas, all of which can be used to help validation of model nutrient concentration and modelled flooded-dry areas in Chapter 5.

# Chapter 5: Delft3D model setup, model parameter testing, and assessment

This chapter explains the model setup, which includes file preparation and parameter settings for Delft3-FLOW and Delft3D-PART. The results from sensitivity testing are also presented, revealing optimal settings for physical and numerical parameters (bottom roughness, horizontal eddy viscosity, and horizontal diffusivity) for scenario simulation of hydrodynamics, nutrient concentration, and pathways for the Ythan estuary model domain in Chapter 6. The chapter also presents an assessment of the applied physical and numerical parameters as well as validating model predictions using data from measured water depth and image processing techniques (NDWI and NDVI).

## 5.1 Delft3D-FLOW module set up and parameter settings

The input files needed for hydrodynamic simulations were created by FLOW GUI and other utility programmes in Delft3D GUI so that they were in the required proper format. The input files are comprised of the curvilinear grid file (name.grd), grid enclosure file (name.enc), bathymetry or depth (name.dep), open boundaries (name.bnd), flow boundary conditions (time-series) (name.bct), and observation points (name.obs), all of which were used along with a master input file (MDF-file) containing other necessary physical and numerical parameters for the model test run. The file preparation and the physical and numerical parameters that were not set to default values are described as follows.

### 5.1.1 Grid

The high resolution orthogonal curvilinear grid, which can be fitted along the estuary channel boundary, was the grid type used in this study. The curvilinear grid was generated using the RGFGRID utility programme, which is in the main Delft3D GUI. RGFGRID can directly read shape file format input data, thus the estuarine boundary shape file format extracted from a pan-sharpened WV-2 image using digitising function in ArcGIS 10.1 was used as a background file to create the refined orthogonal curvilinear grid file. 8,640 refined curvilinear grid cells, with a smallest cell size 1.2 x 0.6 m were created to represent the study area in the model domain (Figure 5-1). As the grid is curvilinear it is generally orthogonal to, and is fitted as closely as possible to, the boundary of the estuary in order to

minimise error in the finite difference operators, the grid spacing varies over the model domain (Deltares, 2014). The study focuses only on one domain, which is the main estuary. The four tributaries where river flow data are not available were excluded from the model domain. As the tributaries are small, about 5 m in width and very shallow, the impact on estuary hydrodynamics from omitting these tributaries is assumed to be negligible.

### 5.1.2 Bathymetry

The bottom elevation used for the model is the new bottom elevation obtained from integrating the terrestrial LiDAR DEM with single beam echo sounder data from the boat survey. To fit the new bottom elevation to the orthogonal curvilinear grids in the model domain, the new bottom elevation dataset was converted into XYZ format and imported into the QUICKIN utility programme. For construction of the bathymetry, the data measured at sampling points were assigned to the grid cells by using the interpolation function in QUICKIN. Deep areas are dark red through to the highest areas relative to MSL represented by dark blue (Figure 5-1).

### 5.1.3 Open boundary

Two open boundaries, which are a fresh water boundary in the River Ythan and a sea boundary, were defined at top and bottom of the model domain (Figure 5-1). The freshwater boundary condition was a 15-minute interval time series of fresh water discharge from the Ellon gauging station. The sea boundary condition was a 15-minute interval time series of tide level at Aberdeen port. In addition, the study used constituent data including daily mean freshwater and sea surface temperature and daily mean salinity of fresh and sea water. The temperature and salinity of freshwater were measured at Ellon gauge station whilst temperature and salinity of sea surface water derived from global ocean reanalysis (Copernicus Programme). The 15-minute interval time series of water surface temperature and salinity at the sea and fresh water boundaries were modelled from the daily mean temperature and salinity based on the gradient of water density (Deltares, 2014). The locations of the open boundaries were as far away as possible, given the available bathymetric data, from the areas of interest in the estuary to reduce errors resulting from the boundary conditions. The boundary conditions for the model test simulation are summarised in Table 5-1.

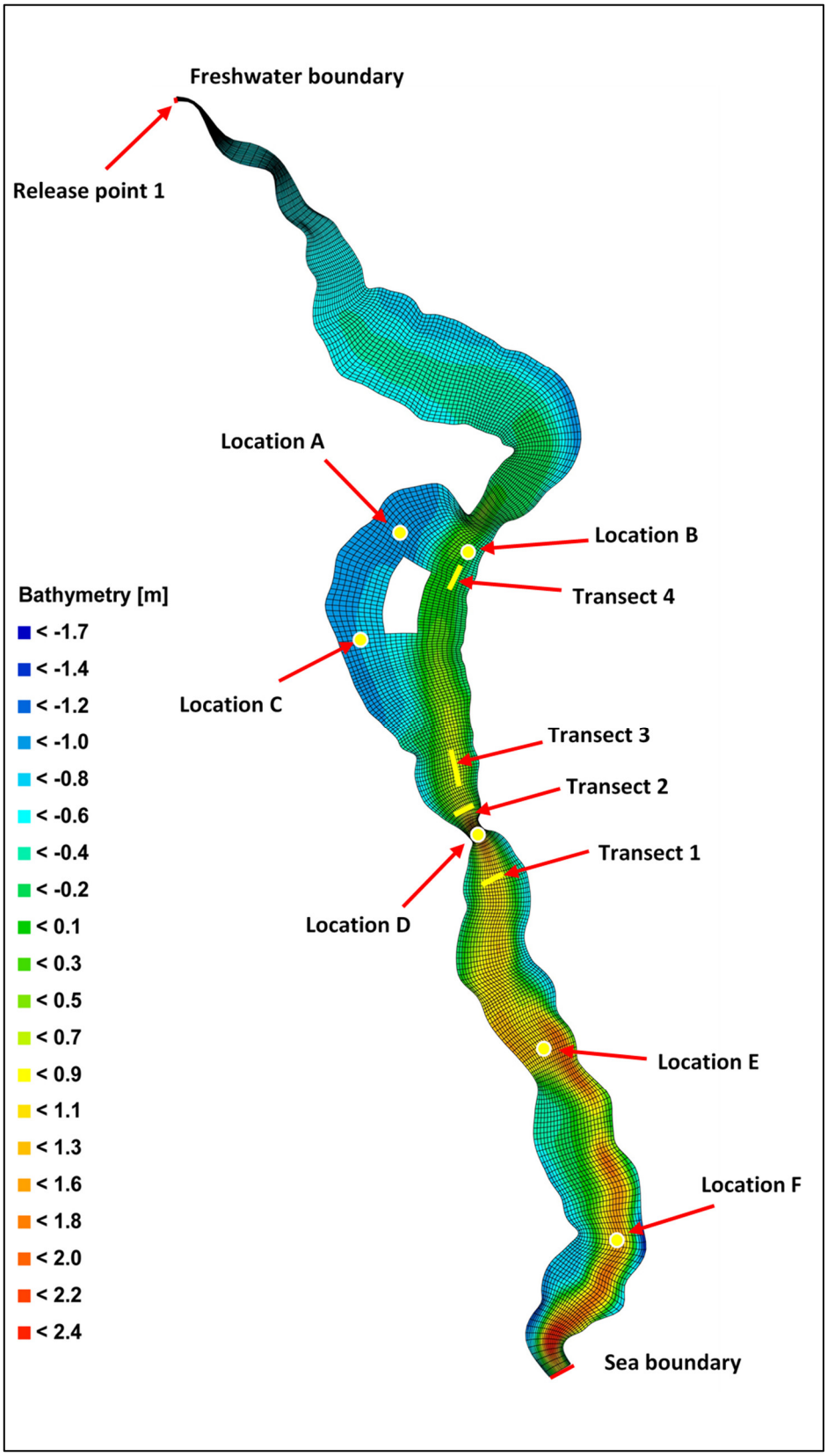


**Figure 5-1:** Grid cells and bathymetry (relative to mean sea level) representing the Ythan estuary in the model domain; a small island is represented by the white area. Open boundaries, locations to observe the model results, and boat survey transects used for model validation are shown. Note that depth in Delft3D is defined positive downward.

**Table 5-1:** Boundary conditions for the model test run and sensitivity testing

| No. | Open boundary | Type of open boundary | Boundary condition | Data used |
|---|---|---|---|---|
| 1 | Fresh water boundary | Total discharge | Time-series | River flow |
| | | | | River temperature |
| 2 | Sea boundary | Water level | Time-series | Tidal level |
| | | | | Interpolated sea surface temperature |
| | | | | Interpolated salinity |

### 5.1.4 Time step

The time step, which controls the computation time, accuracy and stability of the model, is set as 0.1 minutes. This time step was selected based on the Courant number, which is a celerity relation between the time step, and the smallest grid size in the model domain.

### 5.1.5 Initial conditions

No measured water level data are available during the modelled period. The study uses modelled water levels derived from the first cold start test run. A cold start is when the model is initialized for the first time and the model is run until an equilibrium stage is reached (Oc.nps.edu, 2003). The time needed for equilibrium to be reached in a run is called spinning-up time (Webb, 2001). For this study, the cold start test run was run for a two-week period until reaching an equilibrium condition, as the initial uniform water level in the model domain. There is no time standard for this spinning-up time and it is noted that time to reach an equilibrium condition can vary from model to model depending on the complexity of the model domain, the quality of the assumed initial and boundary conditions, as well as with the purpose of the run (Webb, 2001). For example, modelling in shallow water requires spinning-up time for a few days or weeks whilst modelling of the upper ocean can require spinning-up times of a year or longer in the deep ocean (Webb, 2001). The other initial properties of water, salinity and temperature, were set based on average measured salinity and temperature obtained from the SEPA measuring buoy during the specified modelled period. Restart files derived from the cold start run were also used for the warm start, a restart of a model by using saved files from a recent run with the same model settings, to reduce the model spin-up time for each model run.

### 5.1.6 Point locations to examine model results

Six locations were defined, covering the length of the entire estuary, from which modelled hydrodynamic conditions were output for point-based assessment of model performance, in addition to spatial maps covering the entire model domain. Locations A and B were selected based on abundance of algal growth, whereas locations C to F in the main channel were selected based on the gradient and width of the main channel. Location D was the deepest followed by F, E, and C which was the shallowest.

### 5.1.7 Bottom roughness

The bottom roughness, or the bed resistance, causes the total energy losses in the flow and combines several sources of resistance such as the friction of the fluid against the bed and the banks, channel bends, irregularities of the cross section, as well as resistance caused by the fluid characteristics (viscosity) and flow features (Chanson, 2004, Machiels et al., 2009). In Delft3D-FLOW, the bottom roughness can be computed in several ways (Deltares, 2014) as explained in 2.3.7.7. Roughness can be defined as a uniform value across the model domain, or may be space-varying (Deltares, 2014). For the model test run, a uniform and constant value of the Chézy coefficient was used. The Chézy coefficient was used as it is the simplest form of the available roughness measures and has been shown to be widely applicable for modelling river channel velocities (Huthoff and Augustijn, 2004a, Huthoff and Augustijn, 2004b, Yen, 2002). The Chézy coefficient value of 30 $m^{0.5}/s$, which was recommended by Deltares (2014), was used initially. However, the optimal value of the Chézy coefficient for the Ythan estuary model domain was explored during sensitivity testing, which is discussed in 5.3.1.

### 5.1.8 Eddy viscosity

Eddy viscosity (or turbulent exchange coefficient) is a concept used in turbulence theory, which assumes that turbulence in the fluid consists of small eddies that continuously form and dissipate and in which momentum transfer proportional to velocity gradients (Fletcher, 1991). Most turbulence models use the effective eddy viscosity to model the net rate of transfer of momentum in the fluid (Claussen, 1988, Fletcher, 1991, Larson et al., 2003). In Delft3D-FLOW, the eddy viscosity is used to solve the advection-diffusion equation for mass transport as explained in

2.3.7.2 (Deltares, 2014). It can be assigned either as a uniform number or space varying. For the model test run, the horizontal eddy viscosity was assigned a uniform value of 0.01 $m^2/s$ for the whole estuary. As the estuary shape and channel profile are narrow and irregular, resulting in increased fluid friction, a low eddy viscosity was used to increase mass transport. In addition to reducing fluid friction induced by the boundary, this value was selected to avoid exaggerated values of water depth and depth averaged velocity in a model domain that has a small average grid size (Williams et al., 2013). The sensitivity of model results to varying horizontal eddy viscosity is presented and discussed in sensitivity test section 5.3.2.

### 5.1.9 Eddy diffusivity

As with eddy viscosity, the eddy diffusivity, or turbulent diffusion, is difficult to determine experimentally and models usually use an optimised value (Dmowska and Holton, 1994). The eddy diffusivity represents the rate of mixing of a conservative property in the fluid, which in turbulent flow is caused by eddy motion (Dmowska and Holton, 1994). Tracer concentration, which was simulated using the Delft3D-PART module, illustrates the effect of eddy diffusivity. For the model test run, a horizontal eddy diffusivity value of 200 $m^2/s$ was used to control the rate at which mixed fluids/ particles spread due to eddy motion in the horizontal plane. The value was calculated from the equation described in MacCready (1999) which includes the effects of changing tidal amplitude and tidal velocity on mixing, a substantial effect for a tide dominated estuary (Mccarthy, 1993) such as the Ythan estuary. Sensitivity testing to define the optimum eddy diffusivity for the model domain is presented and discussed in 5.3.3.

## 5.2 Delft3D-PART module set up and parameter setting

The Delft3D-PART module uses the results from hydrodynamic simulations in the Delft3D-FLOW module as inputs to simulate transport by means of a particle tracking method. The module simulates the positions of particles using advection (transport by water flow) and diffusion/ dispersion (a random component). The capability of the module was used to simulate the possible pathways as well as the concentration of nutrients transported in the estuary. There are two sub-modules available in the main module, which are the Tracer module and the Oil spill module; only the Tracer module was used in this study. The files needed for

running the Tracer module are a master definition part (*.mdp) file, corresponding files (*.inp), and a hydrodynamic file (*.hyd). The master definition part and the corresponding files contain other necessary numerical and physical parameters and they are created by PART GUI. The hydrodynamic file, which contains information about the hydrodynamic scenario and the associated hydrodynamic files (flows, volumes and grid) from previous running of the FLOW module, is created by the coupling module.

One-time (instantaneous) release of tracer, representing nutrients dissolved in the water at particular points, was used in this study. Thus, the Instantaneous Release function was implemented, in which a scenario name, the instantaneous release location, the initial radius of the release and the number of particles to be released were specified. For the model test run, the tracer was released from the upstream fresh water boundary of the model domain to represent the main nutrient source to the estuary. The same locations for examining the results of hydrodynamic modelling in Delft3D-FLOW were used to observe tracer concentration and pathway behaviours.

Since this study considered nutrients as conservative substances, the decay rate and sediment/erosion parameters were excluded from this study. The physical process parameters including wind speed and wind direction during specific times were defined according to weather data gathered from the closest weather station, at Aberdeen Airport (20 km south of Newburgh). In addition, parameters controlling horizontal dispersion and vertical dispersion coefficients were set as 0.07 $m^2/s$, and 0.7 $m^2/s$, respectively. These parameter values are set as default values for this study. The formulation used to compute horizontal dispersion can be found in Chapter 2.3.7.4. The time step for tracing was the same as that in the hydrodynamic modelling. After all of the necessary files and parameters for the Delft3D-FLOW and Delft3D-PART were created and set, they were transferred to the Ubuntu platform for the model test run and sensitivity testing, results from which are discussed in the next section. The simulation results obtained from the model were then exported to Delft3D Window GUI for visualisation using the QUICKPLOT utility programme.

## 5.3 Model parameter testing

Bed roughness, horizontal eddy viscosity, and horizontal eddy diffusivity parameters, adjustment of all of which effects modelled hydrodynamics (Friedrichs and Wright, 1997, MacCready, 1999, Panigrahi and Khatua, 2015), were adjusted independently using the One-factor-at-a-time (OFAT) approach. The effects of changing these parameter values were assessed using the flooded-dry areas derived from NDWI, so determining their optimal values for this model domain.

**Table 5-2:** Parameter values for the simulation first run

| Simulation | Parameter | Value | Units |
|---|---|---|---|
| Hydrodynamics | Time step | 0.1 | minute |
| Hydrodynamics | Bottom roughness (Chézy, $C$) | uniform 30 | $m^{0.5}/s$ |
| Hydrodynamics | Horizontal eddy viscosity ($v_H$) | uniform 0.01 | $m^2/s$ |
| Hydrodynamics | Horizontal eddy diffusivity ($D_H$) | uniform 200 | $m^2/s$ |
| Nutrient transport | Horizontal dispersion coefficients $a$ and $b$ | uniform 0.07 and 0.7 | $m^2/s$ |

### 5.3.1 Bed roughness testing

Although the Chézy coefficient is a simple form of roughness representation in hydraulic models (Yen, 2002), the values of this coefficient value can vary widely. An initial value of 30 $m^{0.5}/s$, recommended by Deltares (2014), was used across the model domain. Further model runs used uniform values of 45 $m^{0.5}/s$, and 65 $m^{0.5}/s$, respectively (Table 5-3). The C value of 65 $m^{0.5}/s$ produced the greatest damping, reflecting higher friction, at every location (Figure 5-2). In addition, the reduction of damping with low roughness values is greater at spring tides than at neap tides, causing increases in modelled spring tide water depths (Figure 5-3). The increase of bed roughness coefficient produces increased modelled water depths, in particular during spring tides, and also increased modelled depth averaged velocities and bed shear stresses (Figure 5-4, 5-5). The C value of 30 $m^{0.5}/s$ is the most appropriate value for this study based on the damped water level oscillations that it produces.

**Table 5-3:** Chézy, C values tested for sensitivity with constant eddy viscosity and diffusivity

| Chézy, $C$ value ($m^{0.5}/s$) | Eddy viscosity ($m^2/s$) | Horizontal eddy diffusivity ($m^2/s$) |
|---|---|---|
| uniform 30 | uniform 0.01 | uniform 200 |
| uniform 45 | uniform 0.01 | uniform 200 |
| uniform 65 | uniform 0.01 | uniform 200 |

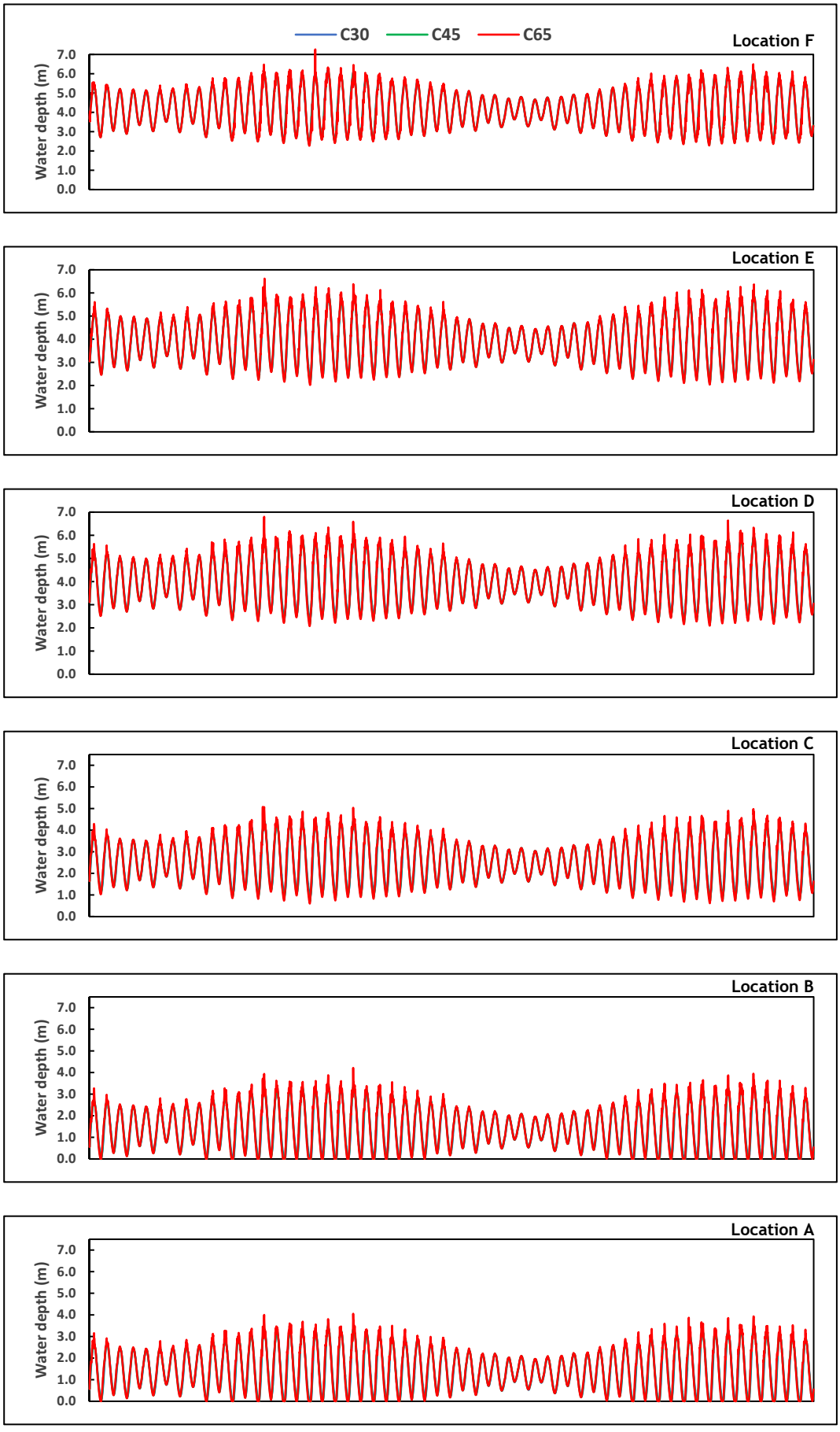


**Figure 5-2:** Water depth from the model using Chézy coefficient values of 30 $m^{0.5}/s$ (blue line), 45 $m^{0.5}/s$ (green) and 65 $m^{0.5}/s$ (red) at locations F to A on 01-30 April 2009.

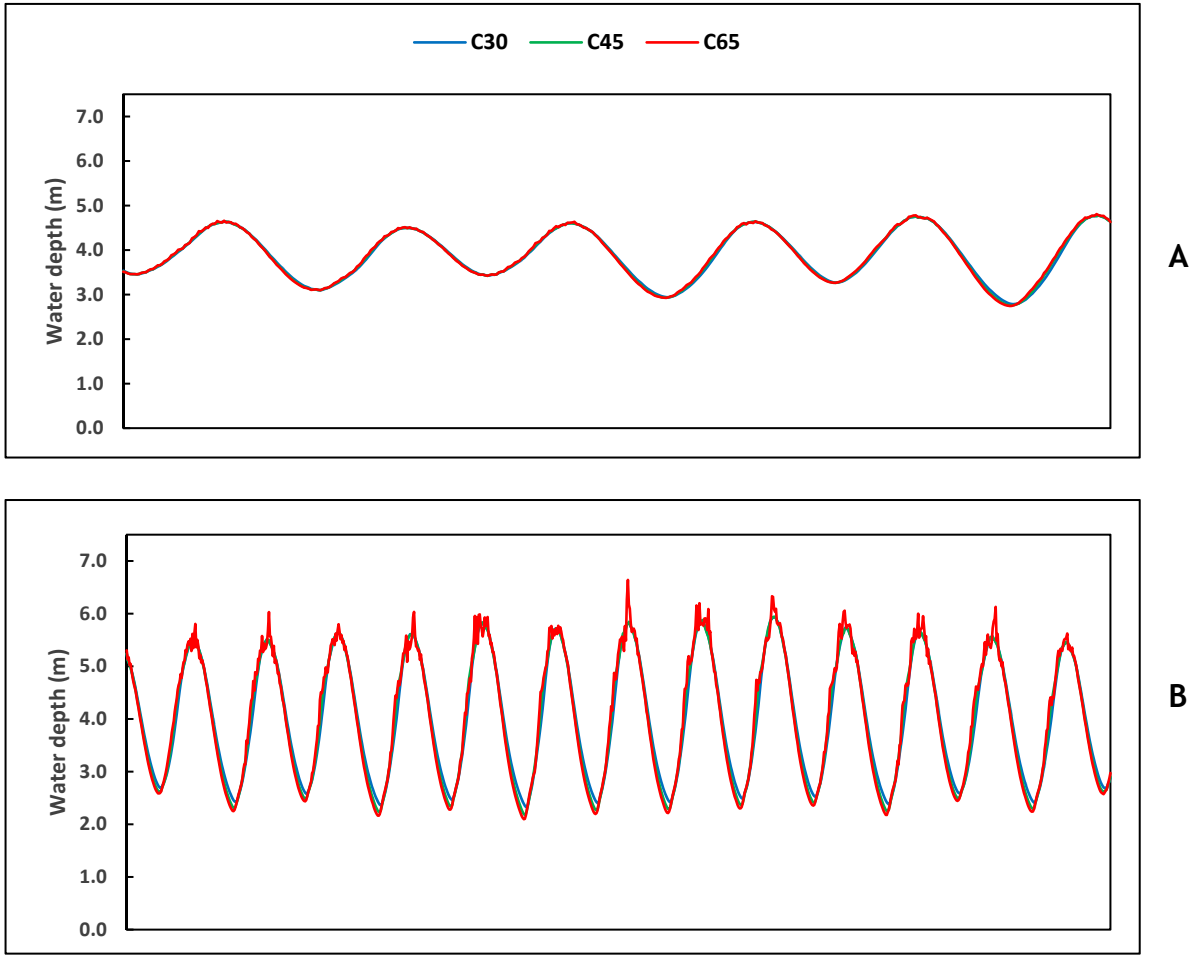


**Figure 5-3:** Water depth from the model using Chézy coefficient values of 30 $m^{0.5}/s$ (blue), 45 $m^{0.5}/s$ (green) and 65 $m^{0.5}/s$ (red) during (A) neap (17-22 Apr 2009) and (B) spring tides (23-29 Apr 2009) at location D.

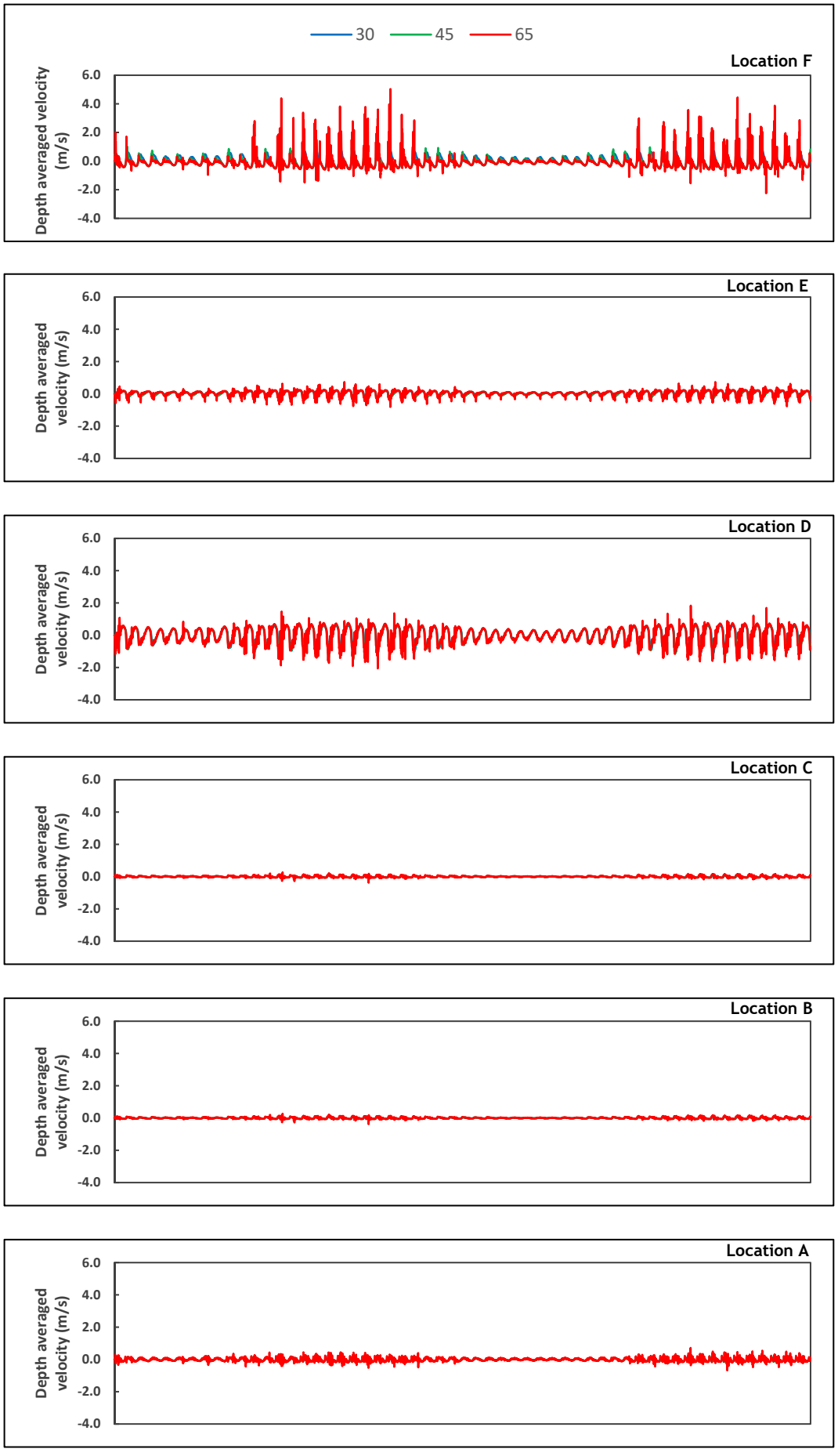


**Figure 5-4:** Depth averaged velocity from the model using Chézy coefficient values of 30 $m^{0.5}/s$ (blue line), 45 $m^{0.5}/s$ (green) and 65 $m^{0.5}/s$ (red) at locations F to A (landward) on 01-30 April 2009.

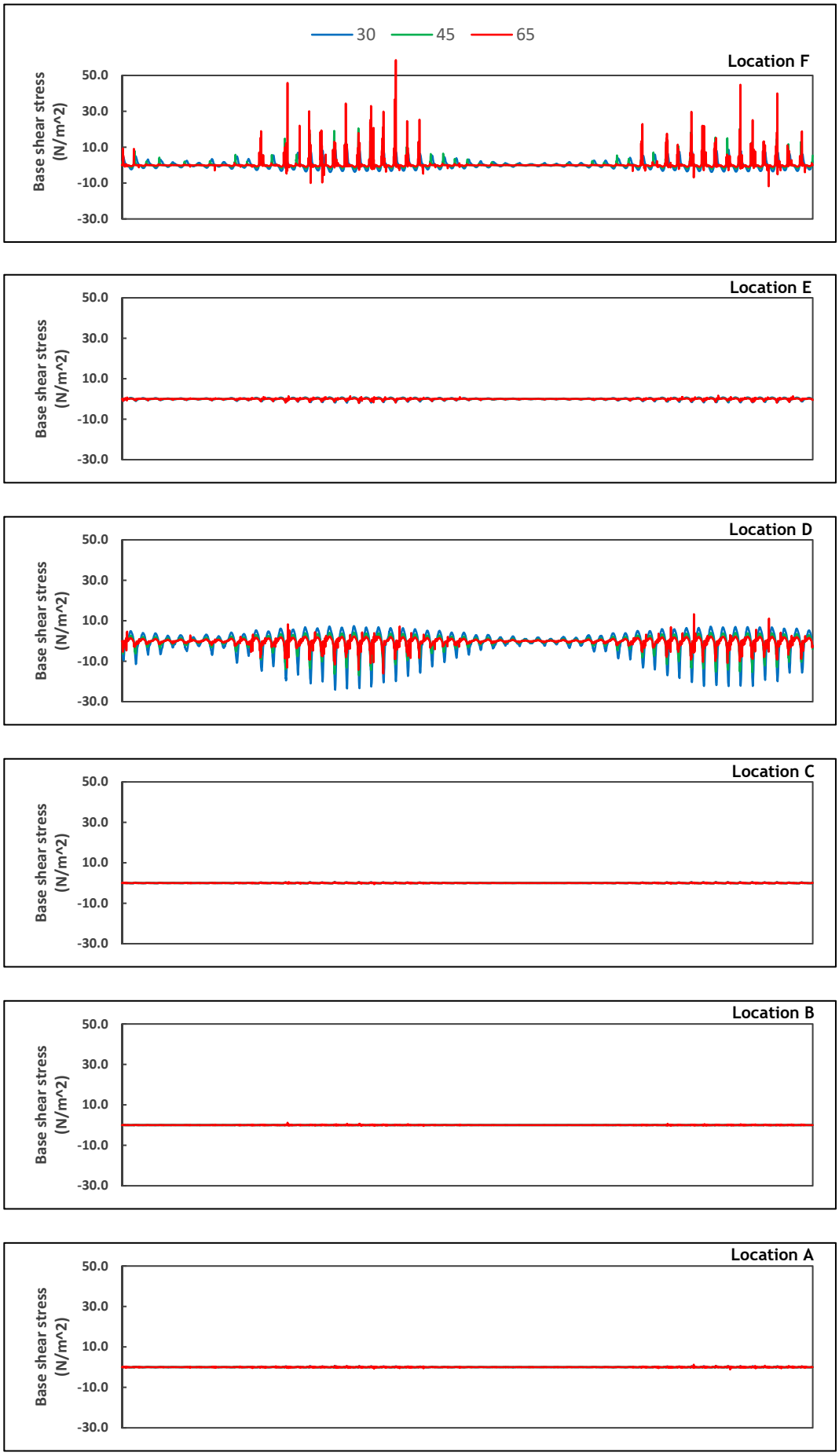


**Figure 5-5:** Bed shear stress from the model using Chézy coefficient values of 30 $m^{0.5}/s$ (blue line), 45 $m^{0.5}/s$ (green) and 65 $m^{0.5}/s$ (red) at locations F to A (landward). Positive shear stress is directed landwards and negative values are seaward (01-30 April 2009).

### 5.3.2 Horizontal eddy viscosity testing

The uniform values of 0.01, 1, and 10 $m^2/s$ were tested while keeping the roughness coefficient constant at 30 $m^{0.5}/s$ (Table 5-4).

**Table 5-4:** Eddy viscosity values tested for sensitivity with constant Chézy, $C$ and eddy diffusivity

| Eddy viscosity ($m^2/s$) | Chézy, $C$ value ($m^{0.5}/s$) | Horizontal eddy diffusivity ($m^2/s$) |
|---|---|---|
| uniform 0.01 | uniform 30 | uniform 200 |
| uniform 1.00 | uniform 30 | uniform 200 |
| uniform 10.00 | uniform 30 | uniform 200 |

This variation produces very small changes in depth averaged velocity, bed shear stress, and water depth at all locations except for the location that is close to sea boundary where variations in depth averaged velocity and bed shear stress are observed (Figures 5-6, 5-7, 5-8). It also has been found that spring tides do not magnify the response of those flow properties to different horizontal eddy viscosities although spring tides produce higher depth averaged velocity, bed shear stress, and water depth than neap tides at all locations. However, distance from sea boundary strongly affects these results. Although the variation of uniform eddy viscosity appears to have no significant effect on flow velocity, bed shear stress, and water level, the horizontal eddy viscosity is taken as 0.01 $m^2/s$ subsequently in this study to aviod possible overestimation of depth and underestimation of velocity in a very small grid size (Williams et al., 2013) in this model domain.

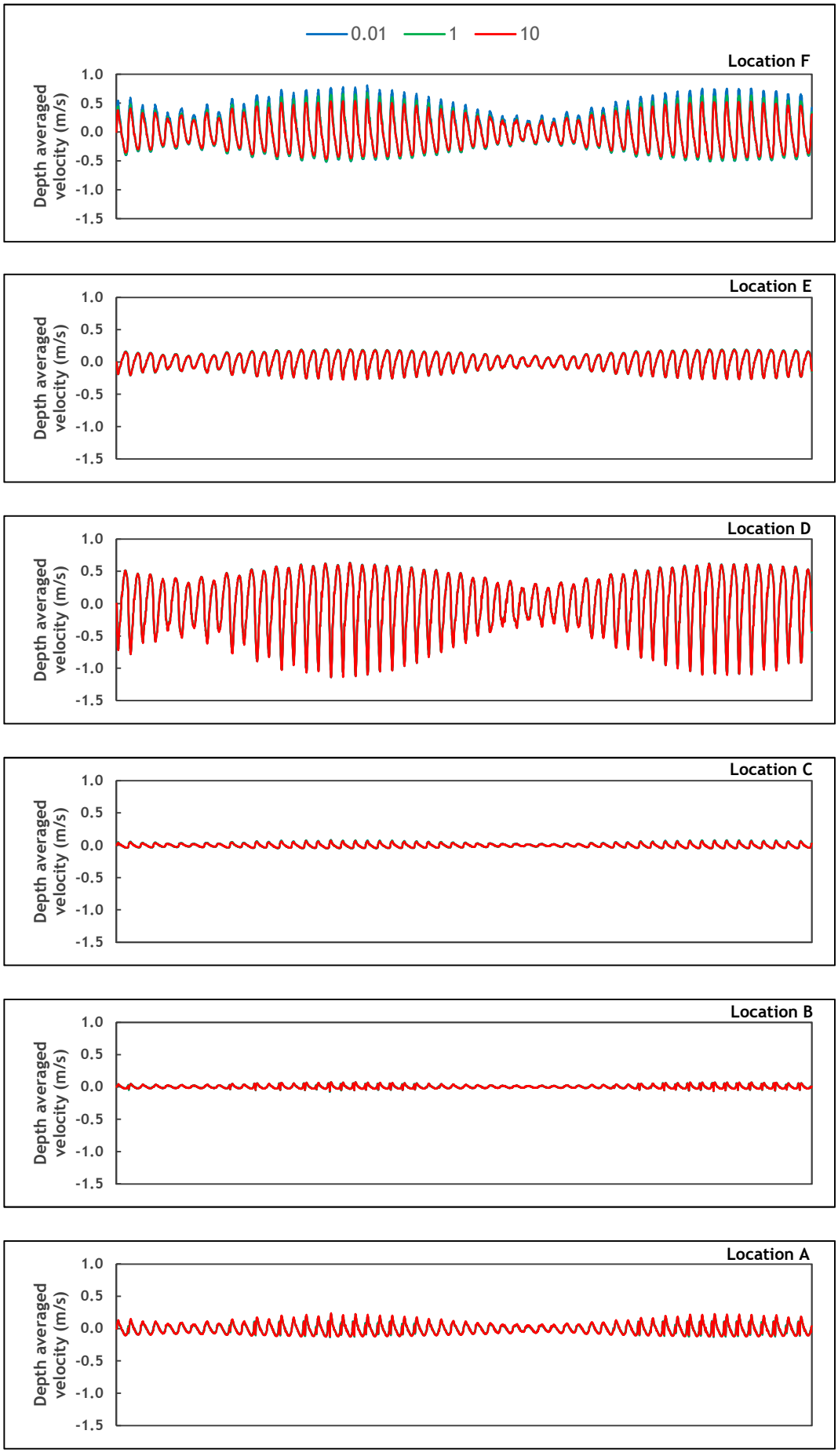


**Figure 5-6:** Depth averaged velocity with different horizontal eddy viscosities (0.01 $m^2/s$, blue; 1 $m^2/s$, green; 10 $m^2/s$, red); positive velocity values are in the upstream direction and negative values downstream (01-30 Apr 2009).

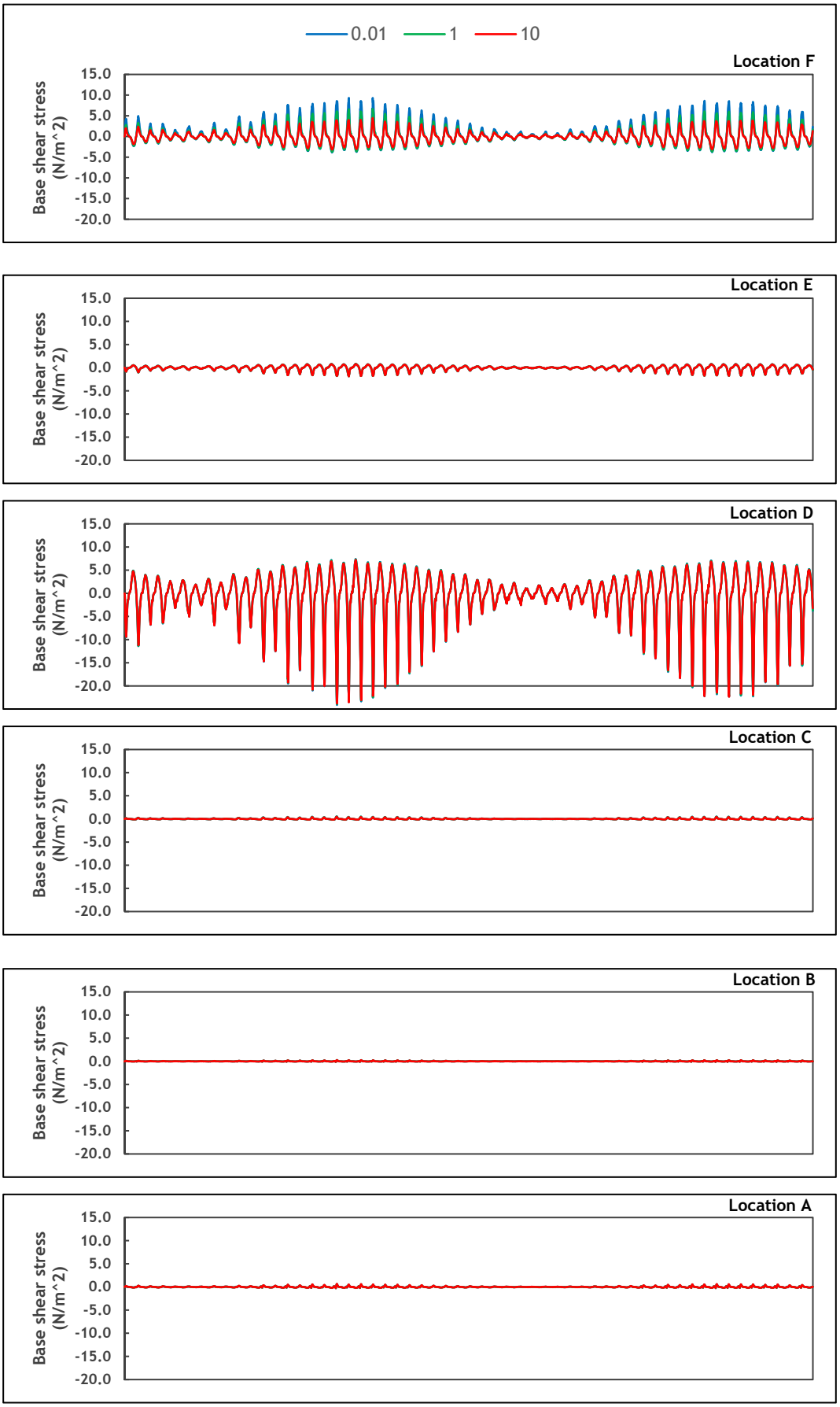


**Figure 5-7:** Bed shear stress from the model using different horizontal eddy viscosities (0.01m$^2$/s, blue; 1m$^2$/s, green; 10m$^2$/s, red); positive values are in the upstream direction and negative values downstream (01-30 Apr 2009).

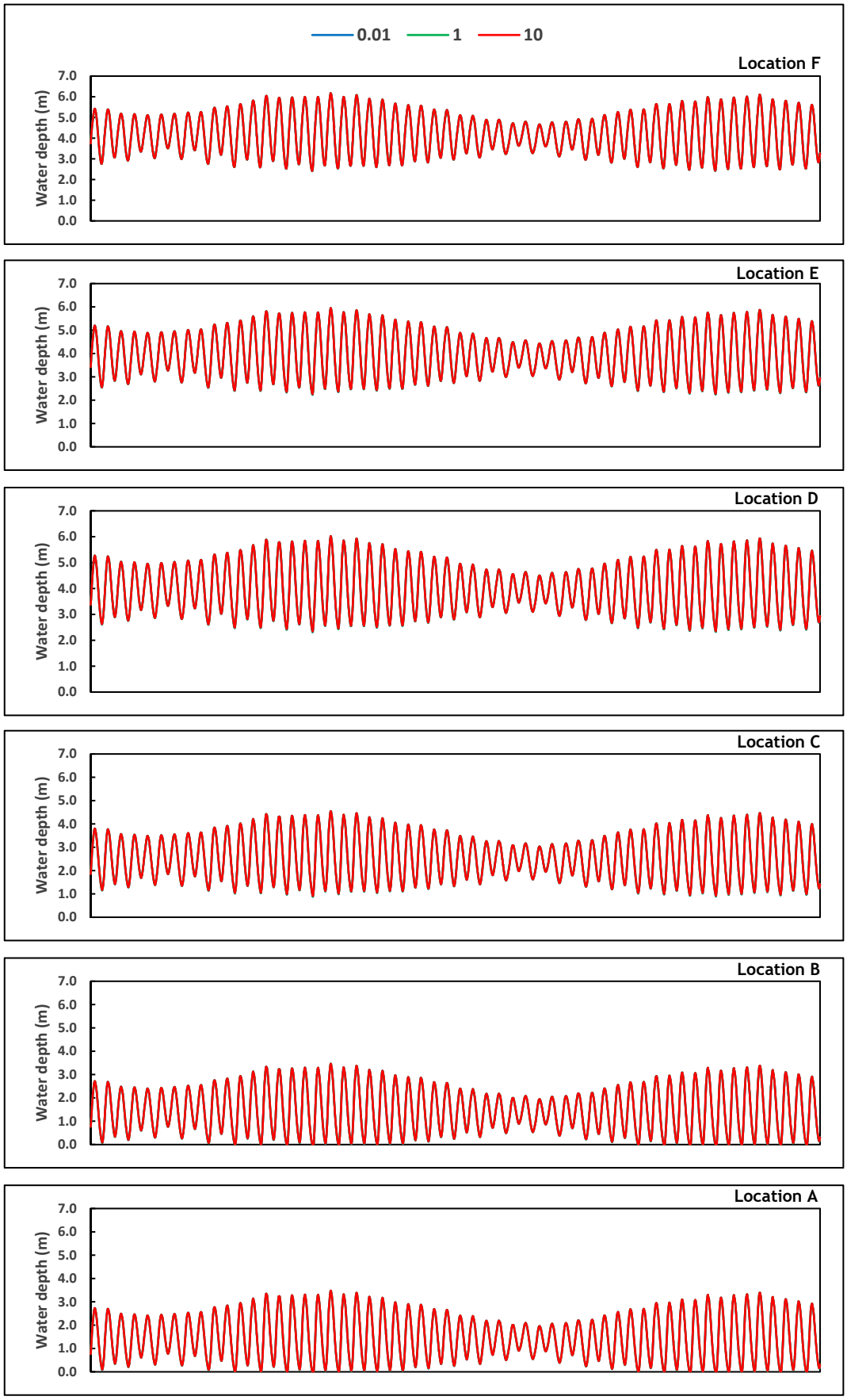


**Figure 5-8:** Water depth from the model using different horizontal eddy viscosities (0.01m$^2$/s, blue; 1m$^2$/s, green; 10m$^2$/s, red) for 01-30 April 2009.

### 5.3.3 Horizontal eddy diffusivity testing

Uniform values of 100, 200, and 400 $m^2/s$ were tested using constant values for both eddy viscosity and Chézy roughness (Table 5-5). The results show that changing values of horizontal eddy diffusivity do not affect water depth with no significant difference of modelled water depths at any of the test locations (Figure 5-9). Depth averaged velocity and bed shear stress also show no significant differences using different eddy diffusivity values, although high horizontal eddy diffusivity does lead to slightly higher bed shear stresses (Figure 5-10, 5-11).

Lower values of horizontal eddy diffusivity produce higher levels of temperature and salinity in the model domain (Figure 5-12: A-B). Lower values of eddy diffusivity slow mixing processes and slow the movement of seawater up the estuary during high tide, which results in the observed higher salinity and temperature values. Conversely, higher eddy diffusivity values allow rapid movement and mixing of seawater leading to low salinity and water temperature in the estuary. Although, a value of 100 $m^2/s$ produced average salinity value that is realistic (33 ppt during flood and 27 ppt during ebb tides) compared with the unlikely result from using a value of 400 $m^2/s$ (30 ppt during flood and 18 ppt during ebb tides), the lower eddy diffusivity produces unrealistic high surface water temperatures during the ebb. The value of 100 $m^2/s$ produced high surface water temperatures (greater than 15°C) during low tide when fresh water entering the estuary should keep temperatures relatively low thanks to low air temperatures in autumn 2009 (min 9°C and max 10°C; www.weatheronline.co.uk) (Figure 5-12B). Therefore, the value of 200 $m^2/s$ which derived from MacCready (1999) and produced the realistic average salinity of 32 ppt during flood tide and 25 ppt during ebb tide and the average surface water temperature of 11°C during flood tide and 8°C during ebb tide, is used as the uniform horizontal eddy diffusivity value for this model domain as it produced the most qualitatively sensible results.

**Table 5-5:** Eddy diffusivity tested for sensitivity with constant Chézy, $C$ and eddy viscosity

| Horizontal eddy diffusivity ($m^2/s$) | Eddy viscosity ($m^2/s$) | Chézy, $C$ value ($m^{0.5}/s$) |
|---|---|---|
| uniform 100 | uniform 0.01 | uniform 30 |
| uniform 200 | uniform 0.01 | uniform 30 |
| uniform 400 | uniform 0.01 | uniform 30 |

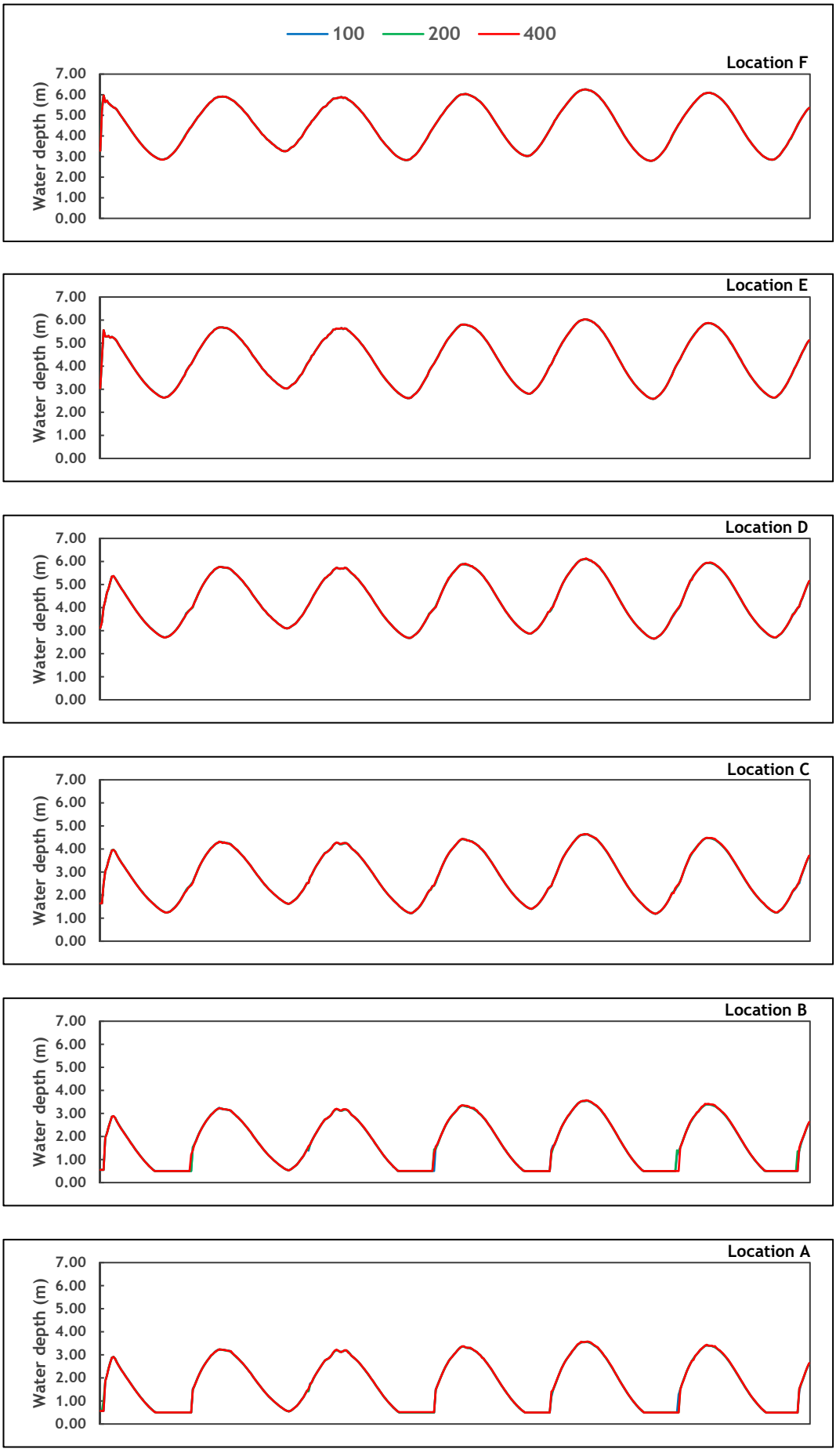


**Figure 5-9:** Water depth with different eddy diffusivities (100 $m^2/s$, blue; 200 $m^2/s$, green; 400 $m^2/s$, red) modelled for 1-3 Nov 2009.

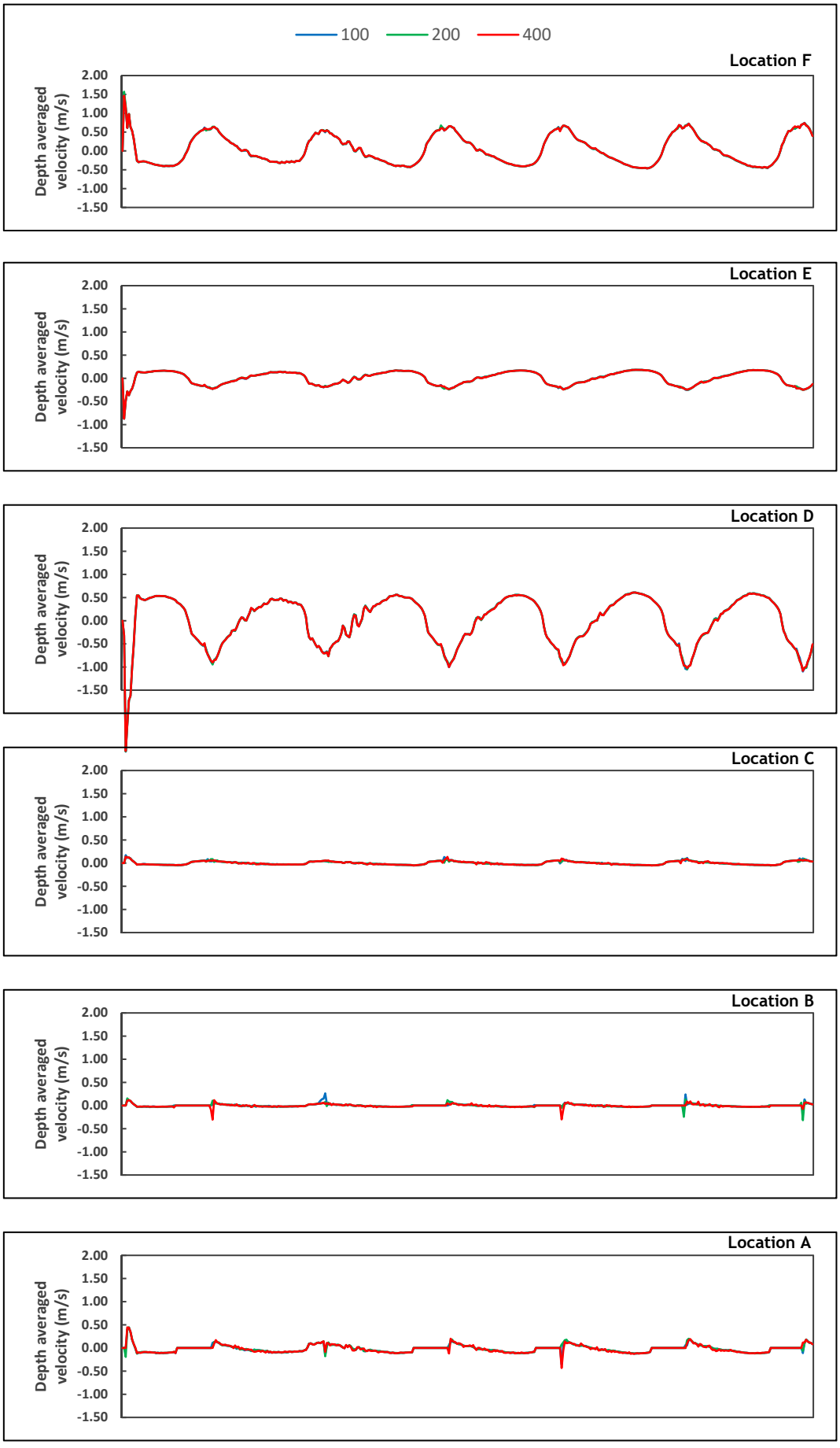


**Figure 5-10:** Depth-averaged velocity from the model using different horizontal eddy diffusivities (100 $m^2/s$, blue; 200 $m^2/s$, green; 400 $m^2/s$, red) modelled for 1-3 Nov 2009.

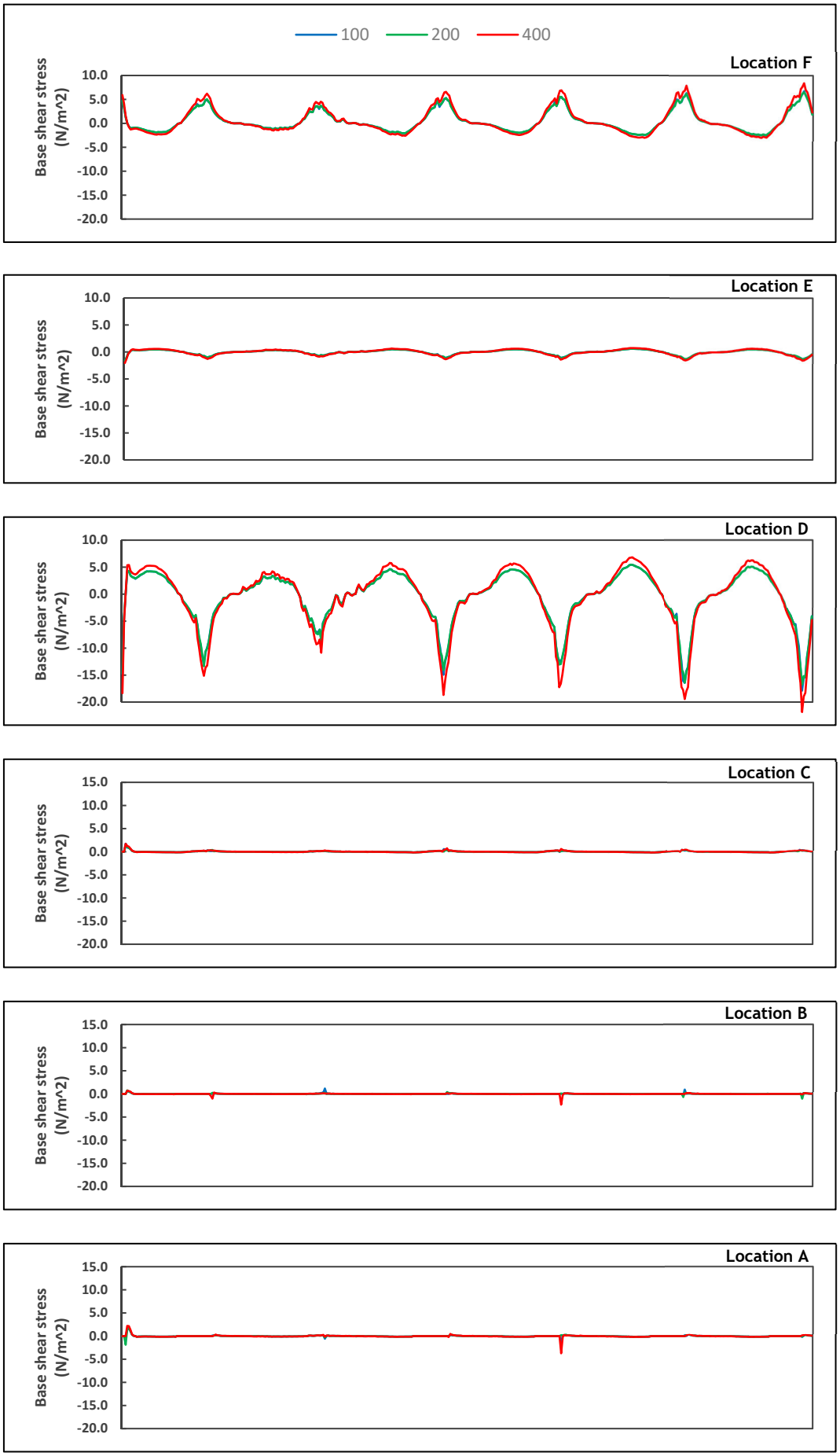


**Figure 5-11:** Bed shear stress from the model using different horizontal eddy diffusivities (100 $m^2/s$, blue; 200 $m^2/s$, green; 400 $m^2/s$, red) modelled for 1-3 Nov 2009.

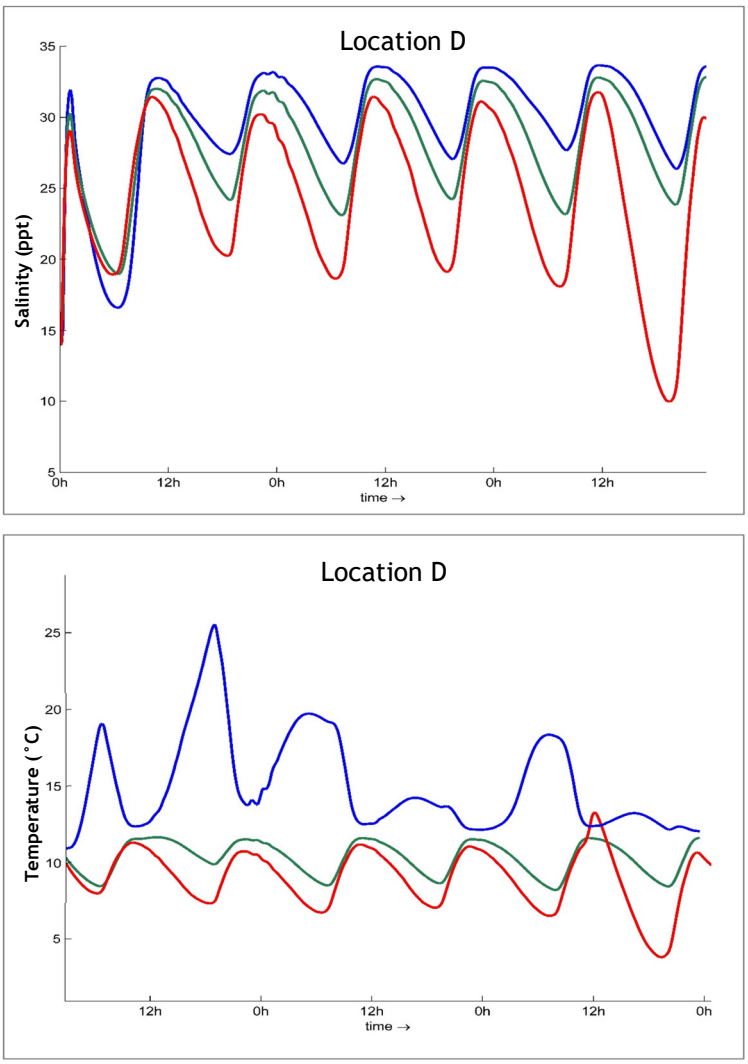


**Figure 5-12:** Salinity (A) and water surface temperature (B) from the model at location D using different horizontal eddy diffusivities: 100 $m^2/s$ blue, 200 $m^2/s$ green, 400 $m^2/s$ red, modelled for 1-3 Nov 2009. The lower value horizontal eddy diffusivity produced higher salinity and water surface temperature.

## 5.4 Model assessment

Following sensitivity testing, model parameter settings that are the same as those used in the first model run ($C$ = 30 $m^{0.5}/s$, $\nu_H$ = 0.01 $m^2/s$, and $D_H$ = 200 $m^2/s$) were selected as producing valid predictions across the model domain. However, before applying those parameter values for full period hydrodynamic simulations of the Ythan estuary, the reliability of these parameters is assessed using both measured water depth data and pseudo-water depths derived from NDWI. As measured water depth data is limited, this section relies mainly on the NDWI from WV-2 and Landsat-8 as a proxy of water-inundated areas to select suitable parameter settings and to assess model predictions. The results are explained as follows;

### 5.4.1 Water depth

Overall, modelled water depths are in good agreement with measured water depths, although there are some areas of mis-matches which may be caused by tidal currents generated by wind along channel centre for measurements that took place during flood tide (Figure 5-26: A-B). The modelled water depths are lower than observed close to high tide in the main channel (Figure 5-26: C-D), which might also be caused by hydrodynamic or wind forcing. The RMSE residuals between measured and modelled water depths range from 0.15-0.17 m. The patterns of the residuals suggest that the model requires improvement in the main channel where wind forcing could have the most significant effect.

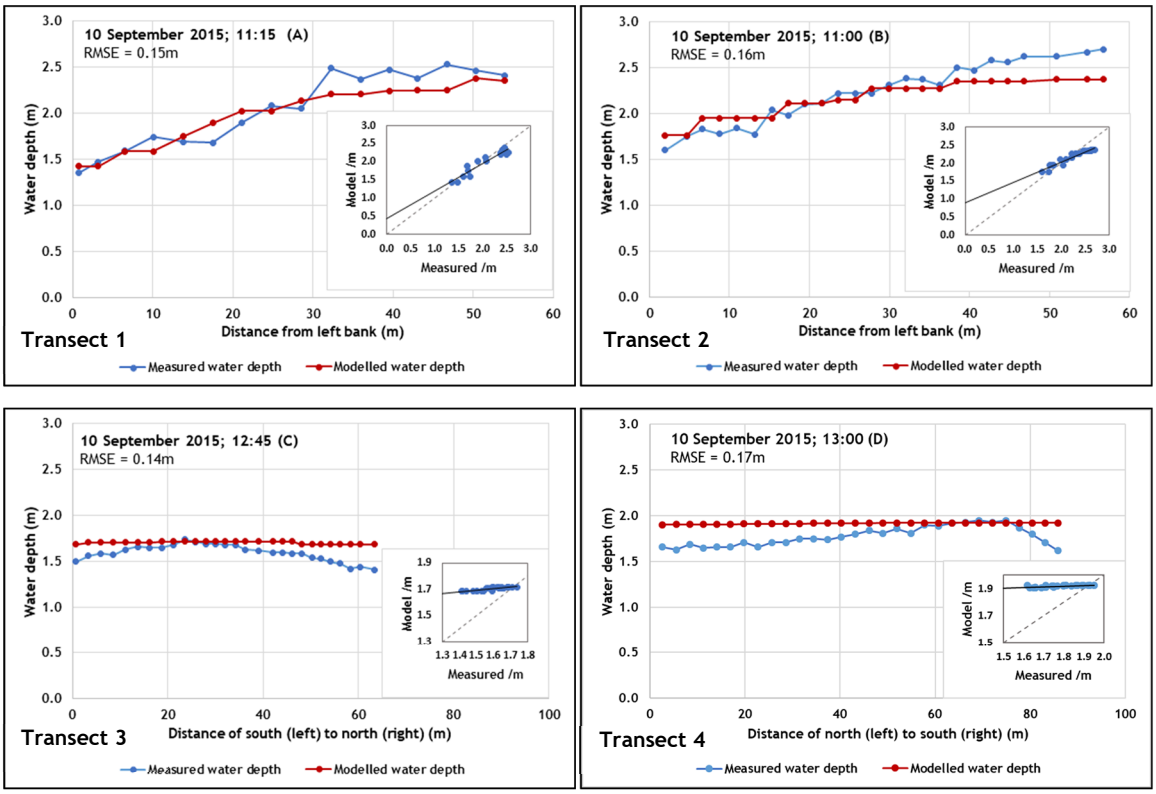


**Figure 5-13:** Comparison of modelled and measured water depths at 11:00 (A) and 11:15 (B) on 17 November 2014, and at 12:45 (C) and 13:00 (D) on 10 September (for transect locations see Figure 5-1); the model parameters used are $C$ =30 $m^{0.5}/s$, $V_H$ = 0.01$m^2/s$, and $D_H$ = 200 $m^2/s$.

### 5.4.2 Flooded-dry areas

WV-2 and Landsat-8 were the only images suitable for analysis of wetted areas as the other available satellite data were captured during high water, when it is not possible to do a time-stamped analysis of flooded and dry area. The results from WV-2 and Landsat-8 data reveal that modelled inundation areas generally

agree with the flooded - dry areas derived from the image ratio technique applied to the WV-2 and Landsat-8 images. Using a Chézy C value of 30 $m^{0.5}/s$ provides the best agreement between modelled water-inundated areas and those inferred from WV-2 at 78.9% (Table 5-6). Likewise, C = 30 $m^{0.5}/s$ produces the highest agreement with inundation inferred form Landsat-8 at 69.2% (Table 5-8). As C = 30 $m^{0.5}/s$ produces the best matches with both remote sensing data sets, this value was used to model inundation with a range of eddy viscosities ($v_H$). Parameter settings of C = 30 $m^{0.5}/s$ and $v_H$ = 0.01 $m^2/s$ produce the highest percentage of agreement in inundated areas between the model and remote sensing, 79% using WV-2. Changing $v_H$ to 1 $m^2/s$ produces the lowest percentage match of 75.2% (Table 5-7). Using Landsat-8, $v_H$ = 0.01 $m^2/s$ also provides the highest match (69.2%) (Table 5-9).

Although there is a good agreement between the modelled results and the ratio image, the agreement is not so good in the upper region of the estuary where the model fails to predict deep water in the main river channel (Figures 5-13 to 5-24). The failure of prediction can be explained by the DEM in this region poorly representing the bottom elevation of the main river channel. This error is due to permanent water in the channel preventing terrestrial LiDAR from identifying the bed, and the inaccessibility of this part of the estuary during the boat bathymetry survey. Model results in the upper part of the estuary (North of the red line on Figure 5-27) cannot be considered reliable. However, the reach between the upstream boundary of the model domain and the red line acts as a numerical buffer so that any instabilities that may be introduce by upstream model boundary conditions have been removed by the red line. As the parameter setting of $C$ = 30 $m^{1/2}/s$ and $v_H$ = 0.01 $m^2/s$ produced the most satisfactory results, this setting was used for full hydrodynamic simulations to understand hydrodynamic patterns in the Ythan estuary in Chapter 6.

**Table 5-6:** Percentage of flooded/dry areas and match/ mis-match areas between the modelled water inundation compared with NDWI image derived from WV-2 (Figure 5-14, 5-15, 5-16, 5-17). The inundation is modelled for a range of Chézy *C* values, with constant eddy viscosity (0.01 $m^2/s$) for the same date/time at which the WV-2 image was acquired [11:30am on 20 April 2015]. The simulations were performed during low flow period and low tide (river flow was 3.5 $m^3/s$ and tide level was 2.7 m above ACD (Admiralty Chart Datum).

| Chézy *C* value ($m^{0.5}/s$) | Eddy viscosity ($m^2/s$) | Area type | % of area inundated | | % Match | % mis-match | |
|---|---|---|---|---|---|---|---|
| | | | Model | NDWI image | | Model flooded /NDWI dry | Model dry /NDWI flooded |
| 25 | 0.01 | Flooded | 39.0 | 49.1 | 29.8 | 9.1 | |
| | | Dry | 61.0 | 50.9 | 48.7 | | 12.4 |
| 30 | 0.01 | Flooded | 43.1 | 49.1 | 32.2 | 11.0 | |
| | | Dry | 56.9 | 50.9 | 46.7 | | 10.1 |
| 45 | 0.01 | Flooded | 53.3 | 49.1 | 34.7 | 18.7 | |
| | | Dry | 46.7 | 50.9 | 39.0 | | 7.6 |
| 65 | 0.01 | Flooded | 80.4 | 49.1 | 42.0 | 38.5 | |
| | | Dry | 19.6 | 50.9 | 19.2 | | 0.3 |

**Table 5-7:** Percentage of flooded/dry areas and match/mis-match areas between the modelled water inundation compared with NDWI image derived from WV-2 (Figure 5-15, 5-18, 5-19). The inundation is modelled for a range of eddy viscosity, with constant Chézy *C* values (30 $m^{0.5}/s$) for the same date/time at which the WV-2 image was acquired [11:30am on 20 April 2015]. The simulations were performed during low flow period and low tide (river flow was 3.5 $m^3/s$ and tide level was 2.7 m above ACD).

| Chézy *C* value ($m^{0.5}/s$) | Eddy viscosity ($m^2/s$) | Area type | % of area inundated | | % Match | % mis-match | |
|---|---|---|---|---|---|---|---|
| | | | Model | NDWI image | | Model flooded /NDWI dry | Model dry /NDWI flooded |
| 30 | 0.01 | Flooded | 43.1 | 49.1 | 32.2 | 11.0 | |
| | | Dry | 56.9 | 50.9 | 46.7 | | 10.1 |
| 30 | 1 | Flooded | 47.9 | 57.7 | 32.6 | 15.2 | |
| | | Dry | 52.1 | 42.3 | 42.6 | | 9.6 |
| 30 | 10 | Flooded | 52.3 | 57.7 | 32.7 | 15.0 | |
| | | Dry | 47.7 | 42.3 | 42.7 | | 9.6 |

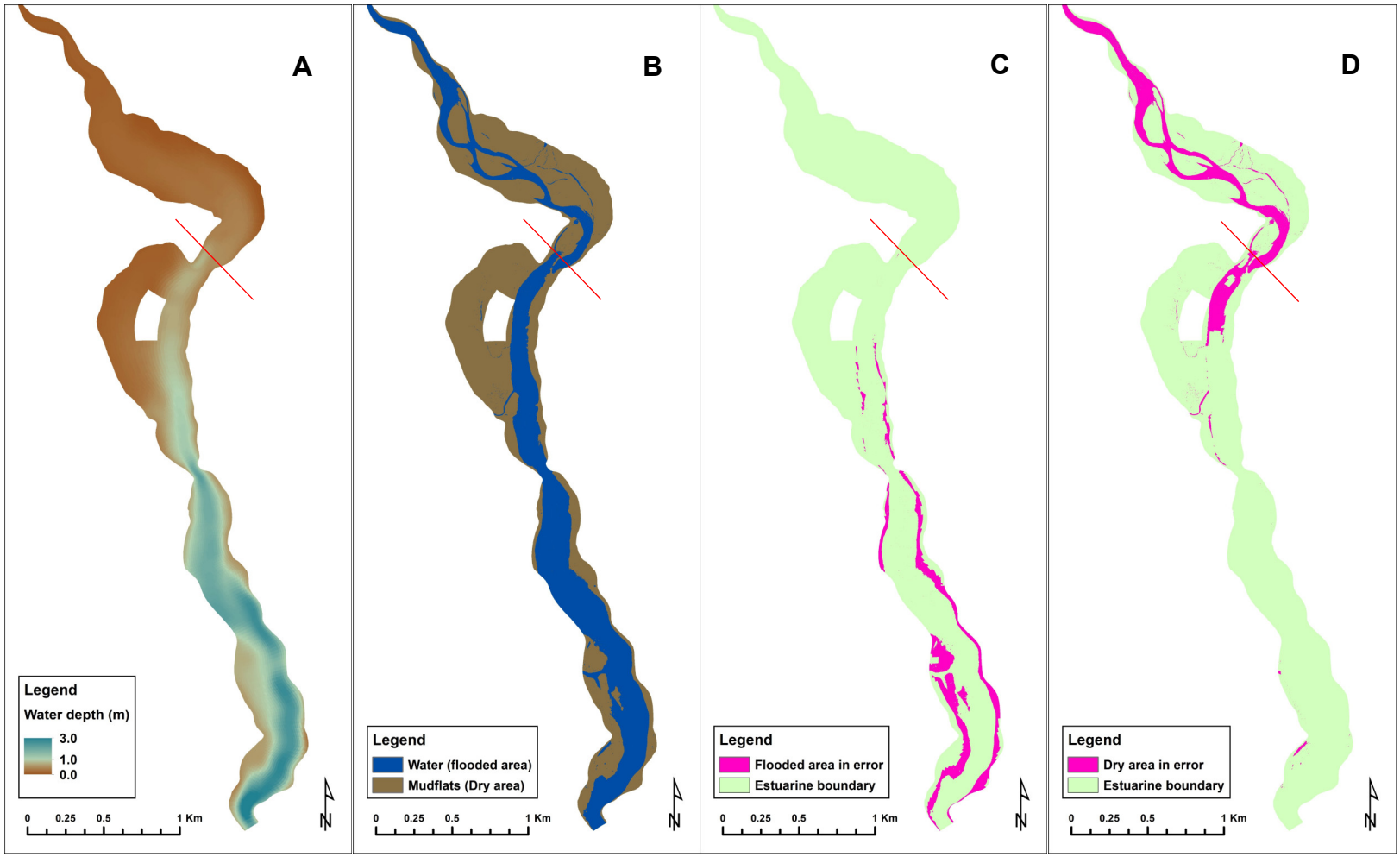


**Figure 5-14:** (A) modelled water depth, (B) NDWI image, (C) flooded area in error, and (D) dry area in error derived from Chézy value of 25 $m^{0.5}/s$ with eddy viscosity of 0.01 $m^2/s$.

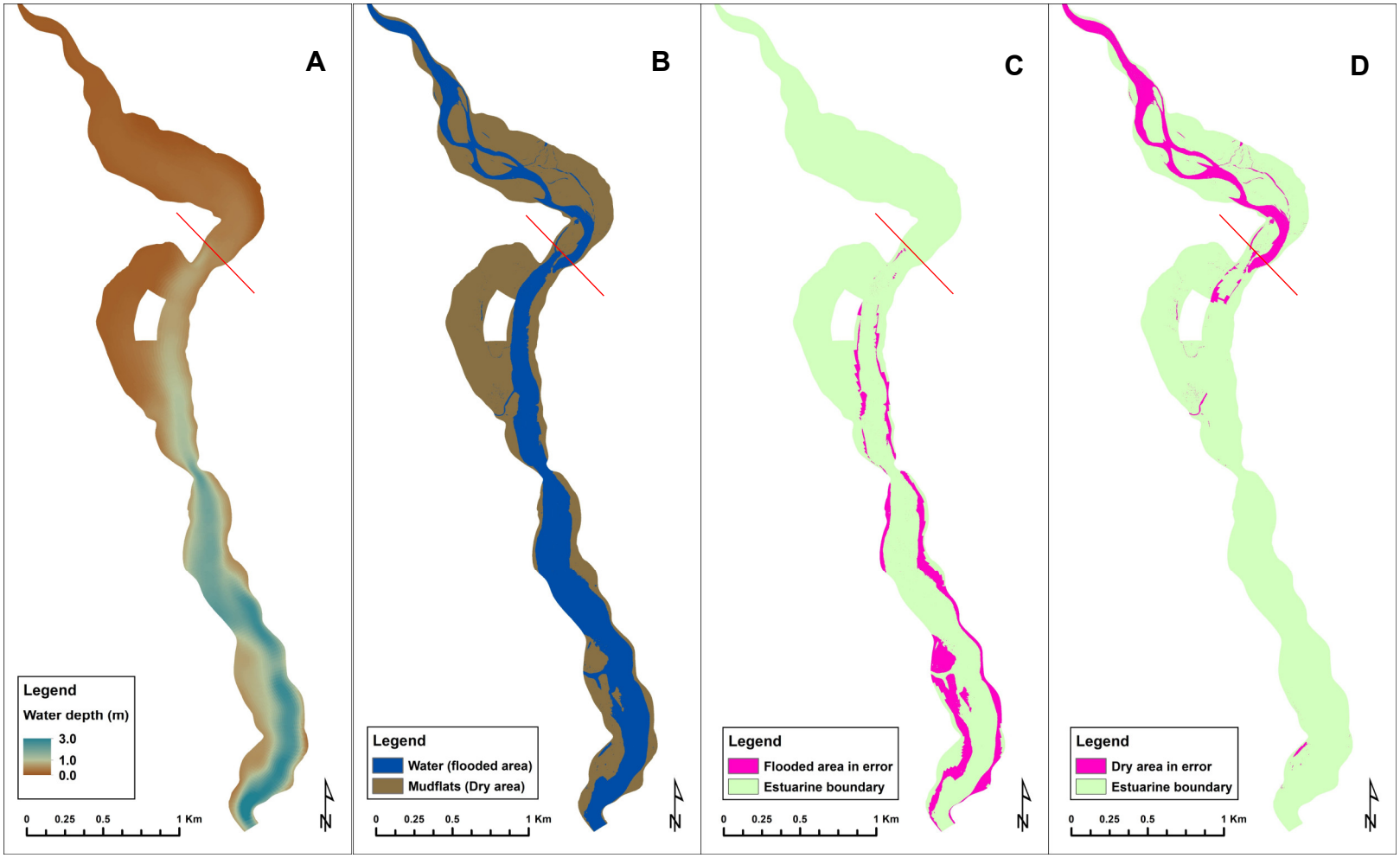


**Figure 5-15:** (A) modelled water depth, (B) NDWI image, (C) flooded area in error, and (D) dry area in error derived from Chézy value of 30 $m^{0.5}/s$ with eddy viscosity of 0.01 $m^2/s$.

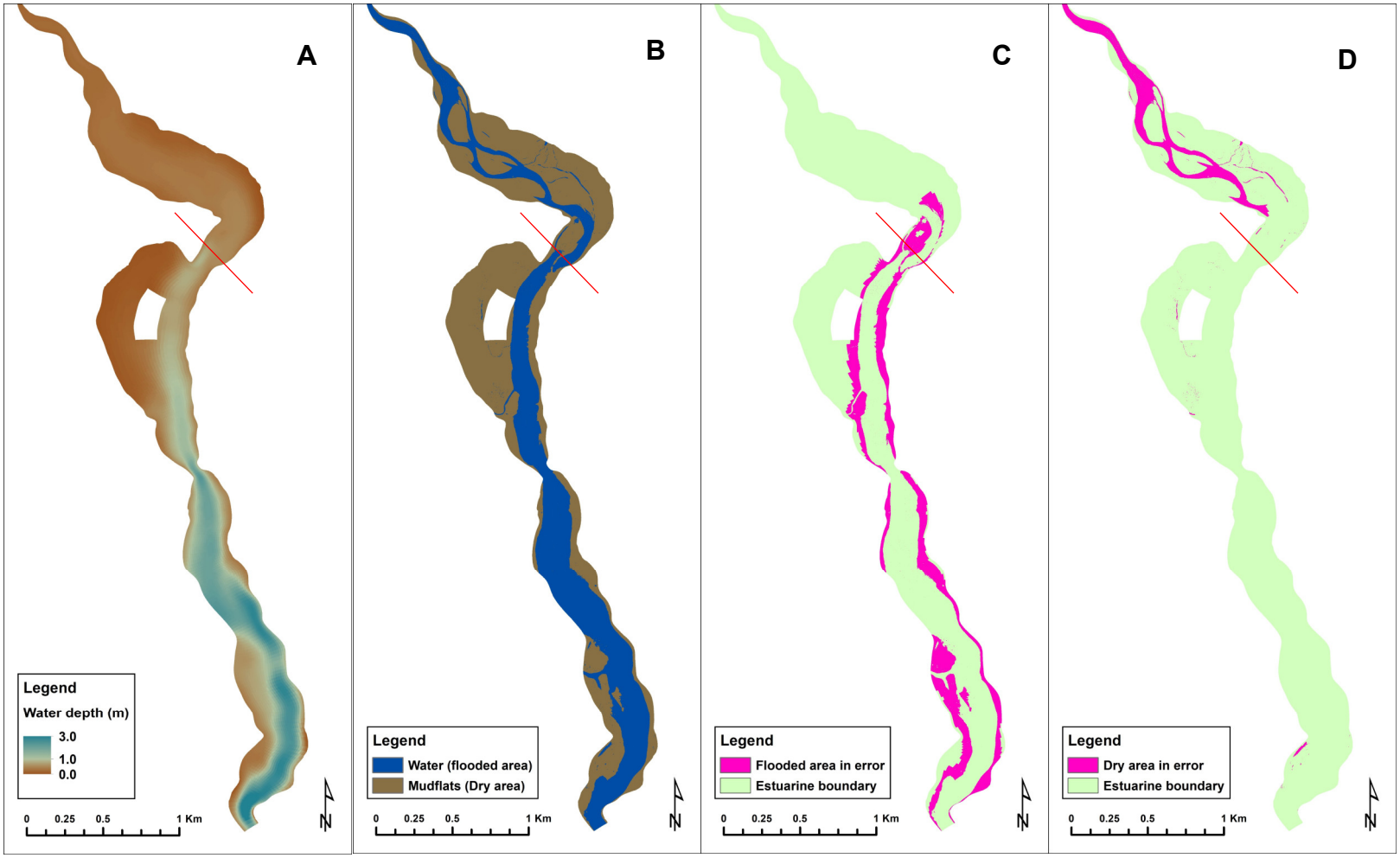


**Figure 5-16:** (A) modelled water depth, (B) NDWI image, (C) flooded area in error, and (D) dry area in error derived from Chézy value of 45 $m^{0.5}/s$ with eddy viscosity of 0.01 $m^2/s$.

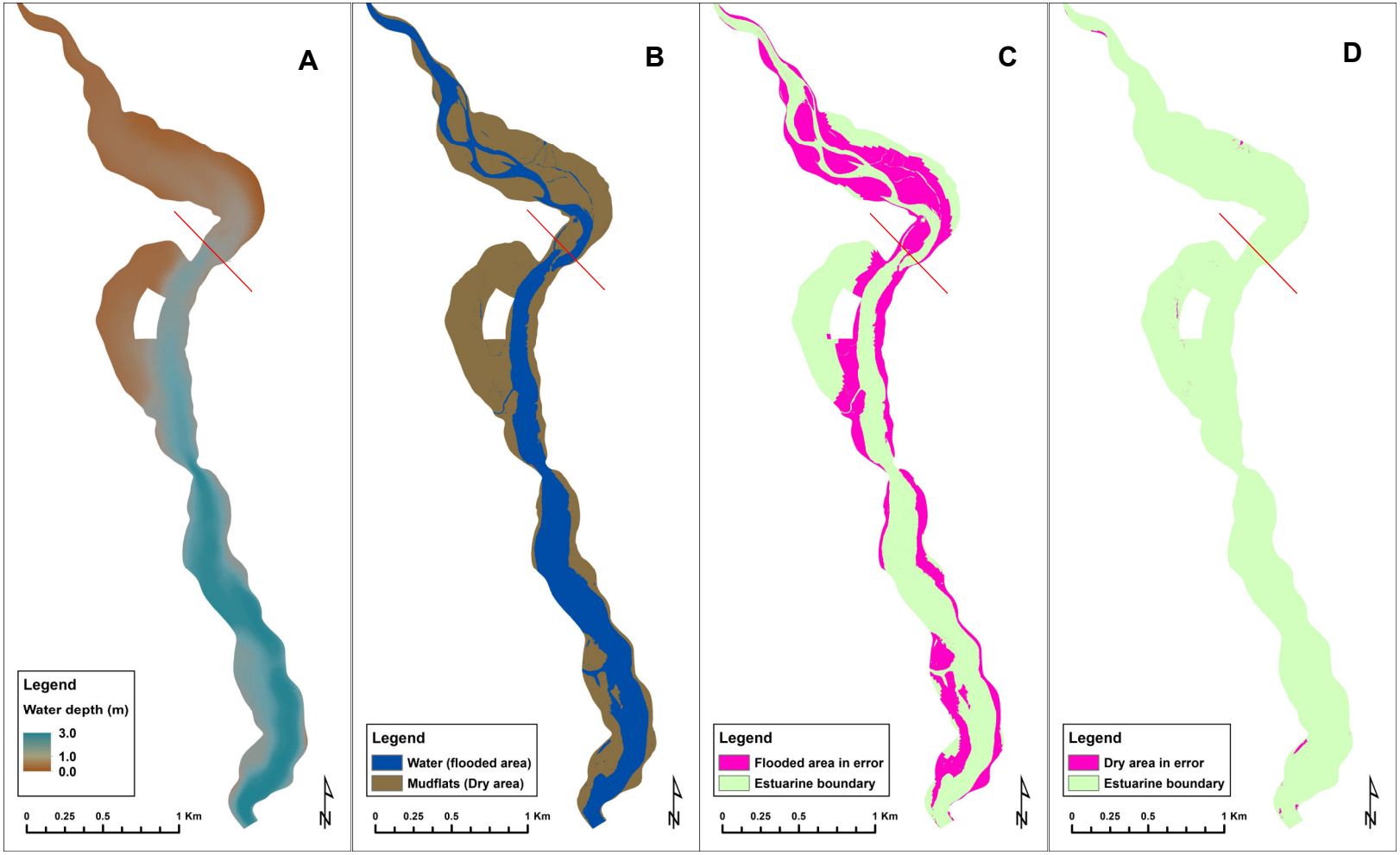


**Figure 5-17:** (A) modelled water depth, (B) NDWI image, (C) flooded area in error, and (D) dry area in error derived from Chézy value of 65 $m^{0.5}/s$ with eddy viscosity of 0.01 $m^2/s$.

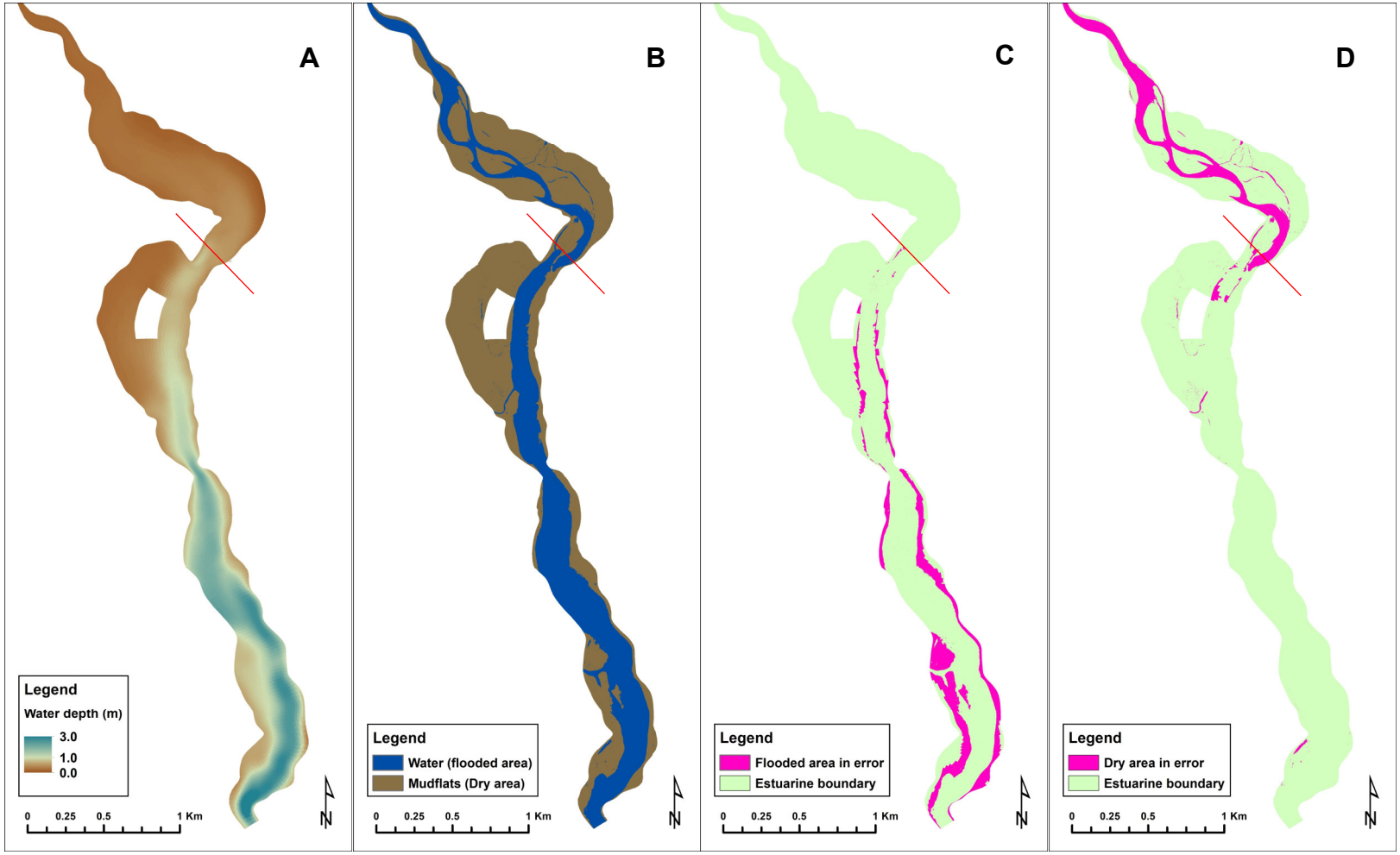


**Figure 5-18:** (A) modelled water depth, (B) NDWI image, (C) flooded area in error, and (D) dry area in error derived from Chézy value of 30 $m^{0.5}/s$ with eddy viscosity of 1 $m^2/s$.

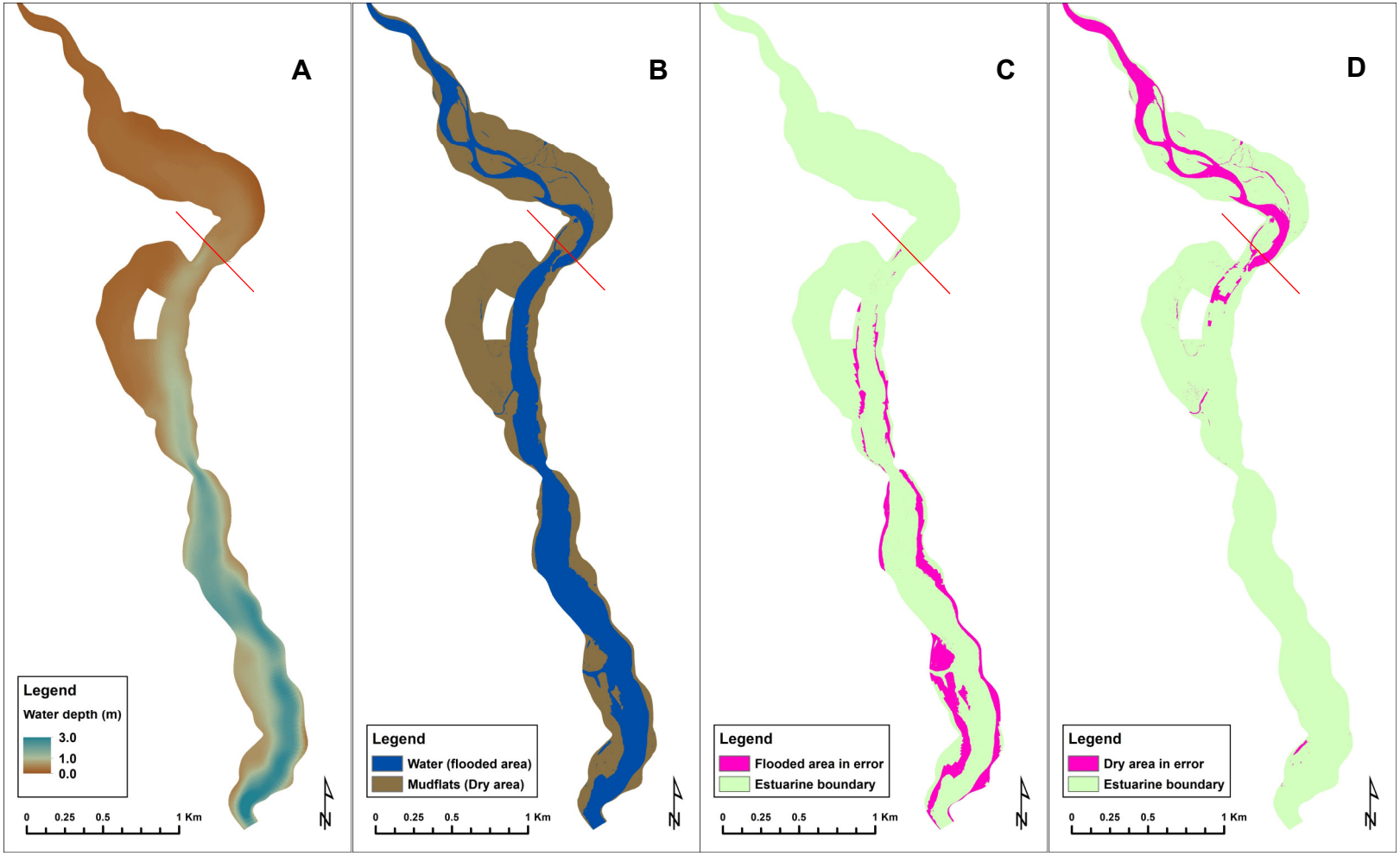


**Figure 5-19:** (A) modelled water depth, (B) NDWI image, (C) flooded area in error, and (D) dry area in error derived from Chézy value of 30 $m^{0.5}/s$ with eddy viscosity of 10 $m^2/s$.

**Table 5-6:** Percentage of flooded/dry areas and match/mis-match areas between the modelled water inundation compared with NDWI image derived from Landsat-8 (Figure 5-20, 5-21, 5-22, 5-23). The inundation is modelled for a range of Chézy *C* values, with constant eddy viscosity (0.01 $m^2/s$) for the same date/time at which the Landsat-8 image was acquired [11:10am on 30 September 2015]. The simulations were performed at river flow of 4.03 $m^3/s$ and tide level of 2.03 m above ACD.

| Chézy *C* value ($m^{0.5}/s$) | Eddy viscosity ($m^2/s$) | Area type | % of area inundated | | % Match | % mis-match | |
|---|---|---|---|---|---|---|---|
| | | | Model | NDWI image | | Model flooded /NDWI dry | Model dry/ NDWI flooded |
| 25 | 0.01 | Flooded | 37.8 | 30.0 | 18.7 | 19.2 | |
| | | Dry | 62.2 | 70.0 | 47.1 | | 15.0 |
| 30 | 0.01 | Flooded | 39.8 | 30.0 | 19.5 | 20.3 | |
| | | Dry | 60.2 | 70.0 | 49.7 | | 10.5 |
| 45 | 0.01 | Flooded | 45.1 | 30.0 | 20.5 | 24.6 | |
| | | Dry | 54.9 | 70.0 | 45.4 | | 9.5 |
| 65 | 0.01 | Flooded | 47.7 | 30.0 | 20.7 | 27.0 | |
| | | Dry | 52.3 | 70.0 | 43.0 | | 9.3 |

**Table 5-7:** Percentage of flooded/dry areas and match/mis-match areas between the modelled water inundation compared with NDWI image derived from Landsat-8 (Figure 5-21, 5-24, 5-25). The inundation is modelled for a range of eddy viscosity, with constant Chézy *C* values (30 $m^{0.5}/s$) for the same date/time at which the Landsat-8 image was acquired [11:10am on 30 September 2015]. The simulations were performed at river flow of 4.03 $m^3/s$ and tide level of 2.03 refer to ACD.

| Chézy *C* value ($m^{0.5}/s$) | Eddy viscosity ($m^2/s$) | Area type | % of area inundated | | % Match | % mis-match | |
|---|---|---|---|---|---|---|---|
| | | | Model | NDWI image | | Model flooded /NDWI dry | Model dry /NDWI flooded |
| 30 | 0.01 | Flooded | 39.8 | 30.0 | 19.5 | 20.3 | |
| | | Dry | 60.2 | 70.0 | 49.7 | | 10.5 |
| 30 | 1 | Flooded | 41.3 | 30.0 | 20.0 | 21.3 | |
| | | Dry | 58.7 | 70.0 | 48.7 | | 10.0 |
| 30 | 10 | Flooded | 40.7 | 30.0 | 19.8 | 21.0 | |
| | | Dry | 59.3 | 70.0 | 49.0 | | 10.2 |

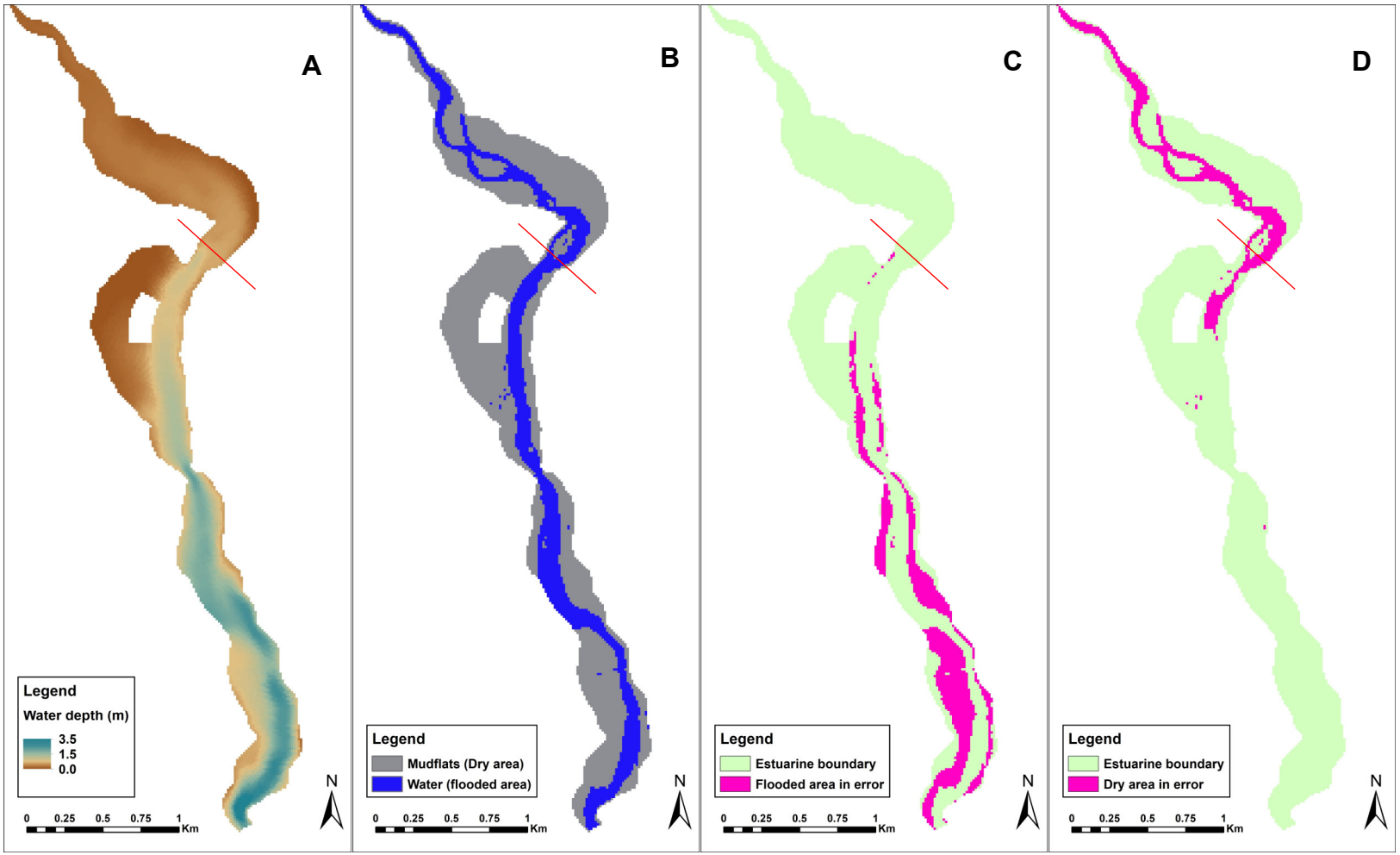


**Figure 5-20:** (A) modelled water depth, (B) NDWI image, (C) flooded area in error, and (D) dry area in error derived from Chézy value of 25 $m^{0.5}/s$ with eddy viscosity of 0.01 $m^2/s$.

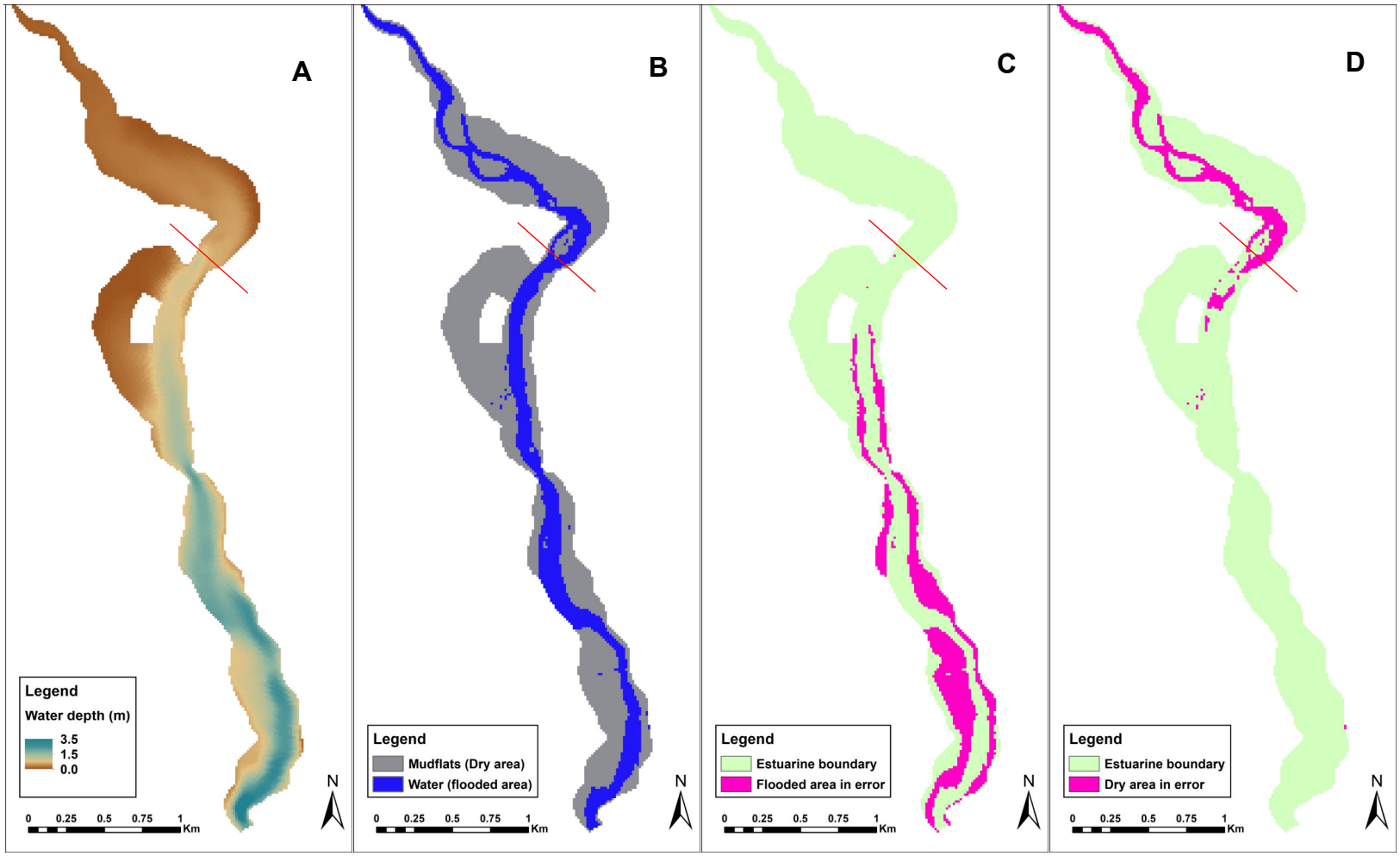


**FFigure 5-22:** (A) modelled water depth, (B) NDWI image, (C) flooded area in error, and (D) dry area in error derived from Chézy value of 30 $m^{0.5}/s$ wwith eddy viscosity of 0.01 $m^2/s$.

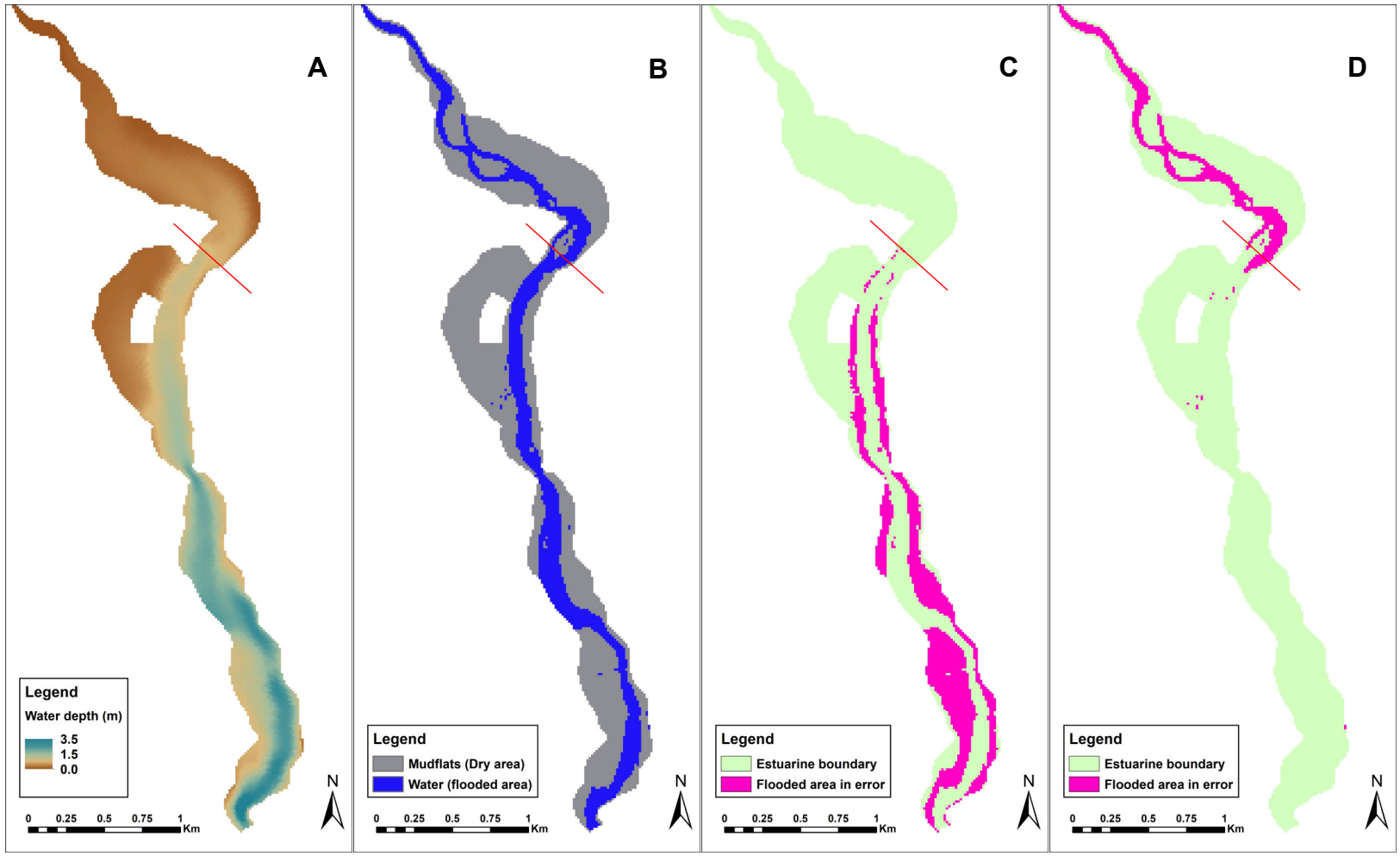


**Figure 5-23:** (A) modelled water depth, (B) NDWI image, (C) flooded area in error, and (D) dry area in error derived from Chézy value of 45 $m^{0.5}/s$ with eddy viscosity of 0.01 $m^2/s$.

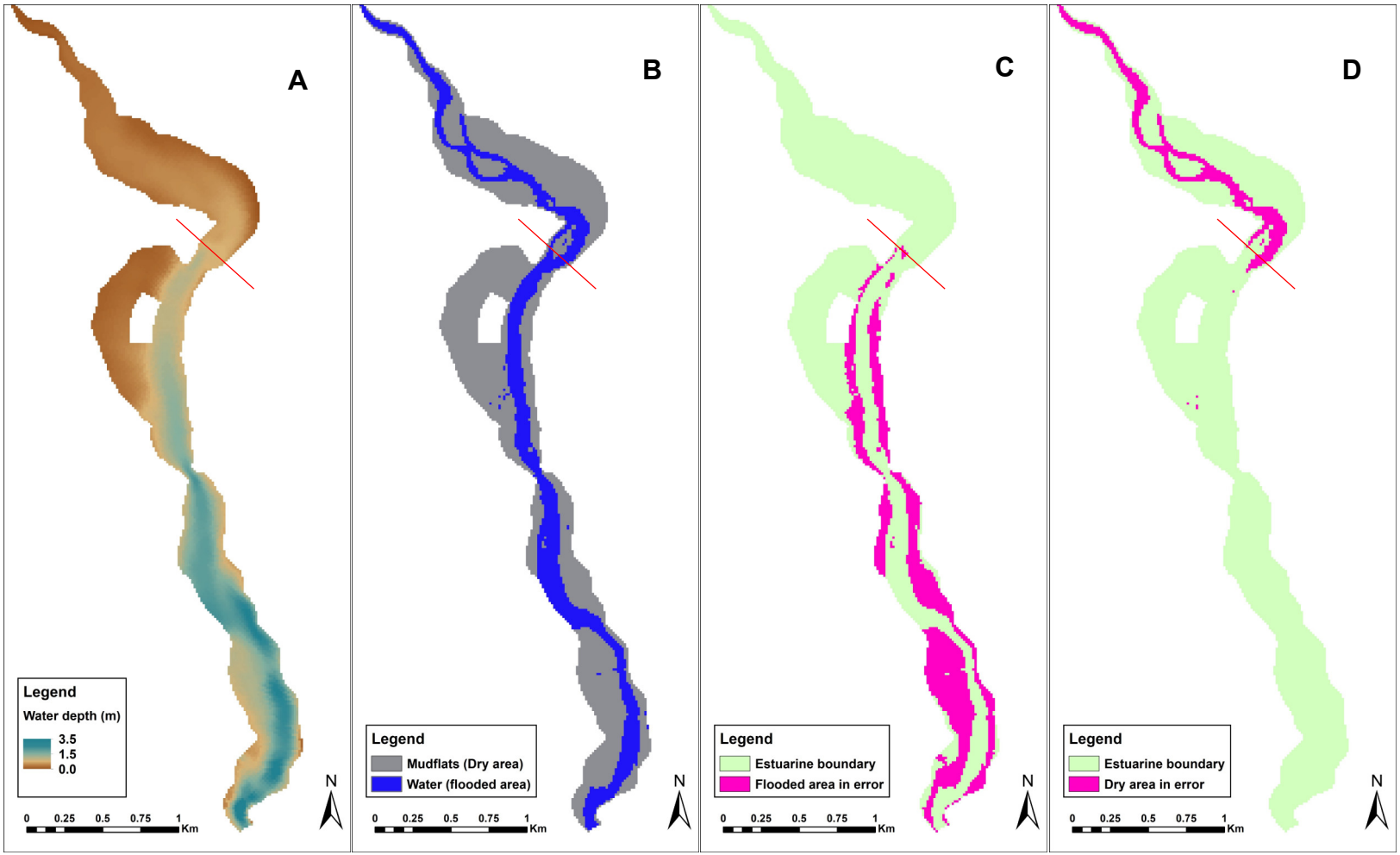


**Figure 5-24:** (A) modelled water depth, (B) NDWI image, (C) flooded area in error, and (D) dry area in error derived from Chézy value of 65 $m^{0.5}/s$ with eddy viscosity of 0.01 $m^2/s$.

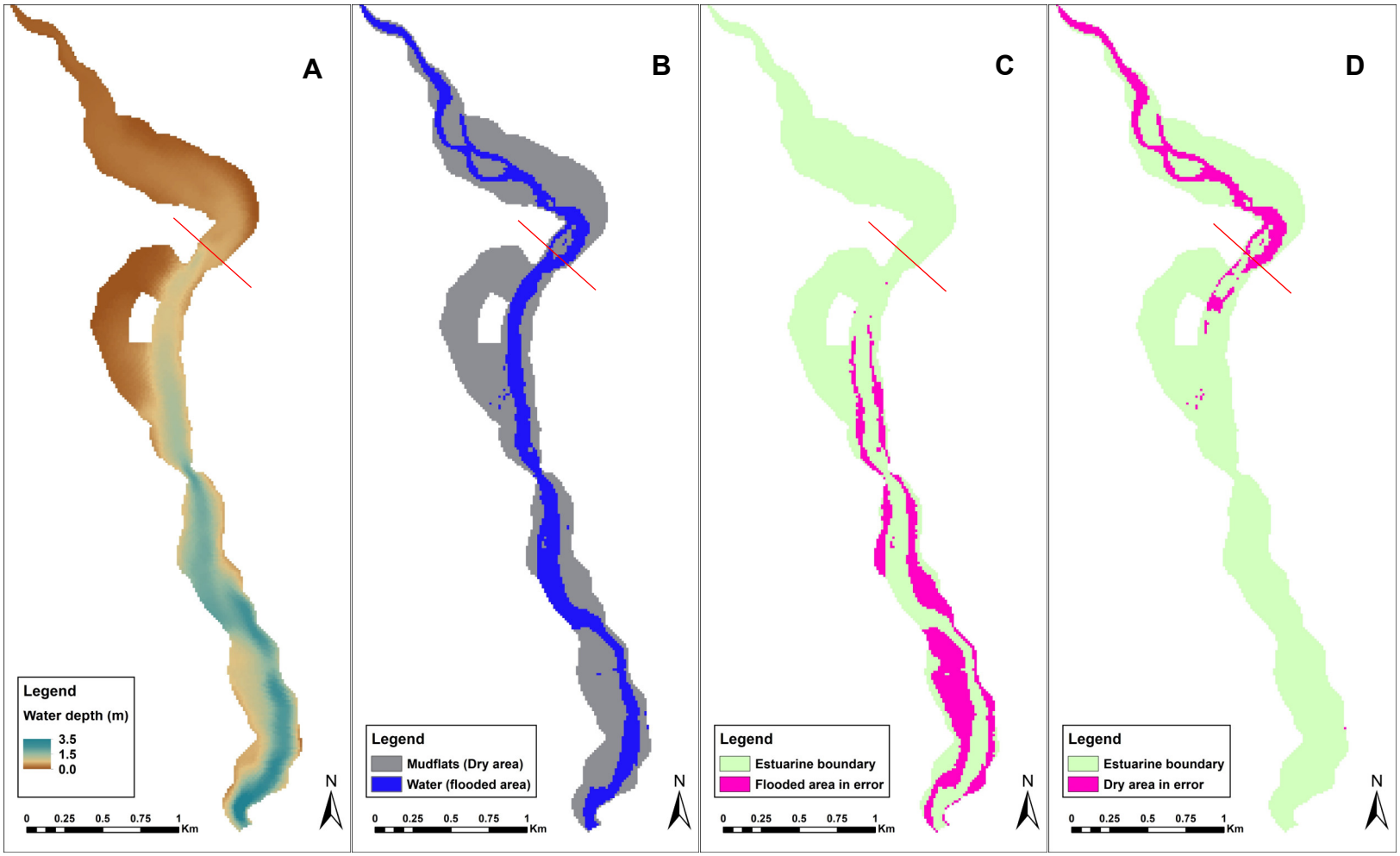


**Figure 5-25:** (A) modelled water depth, (B) NDWI image, (C) flooded area in error, and (D) dry area in error derived from Chézy value of 30 $m^{0.5}/s$ with eddy viscosity of 1 $m^2/s$.

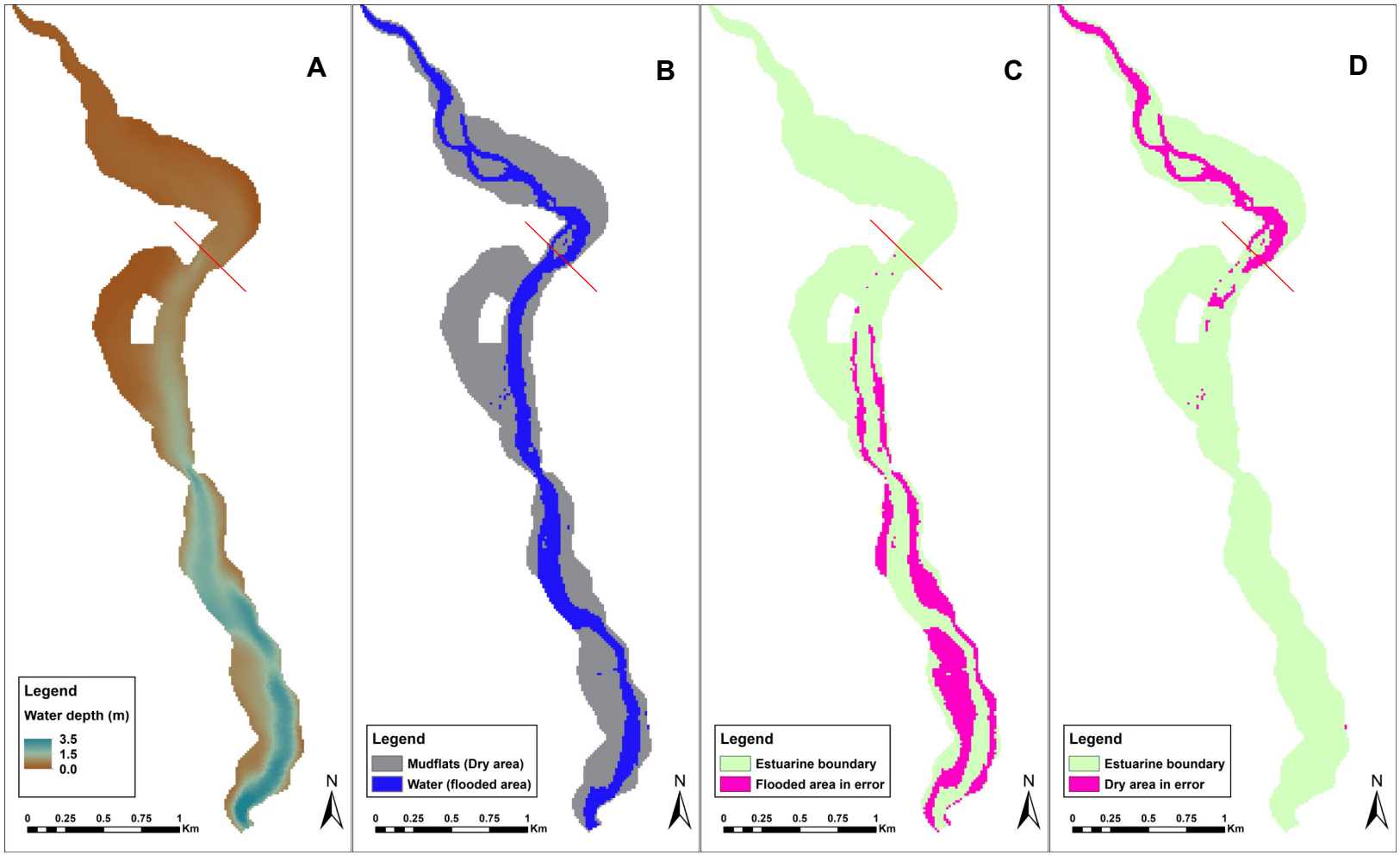


**Figure 5-26:** (A) modelled water depth, (B) NDWI image, (C) flooded area in error, and (D) dry area in error derived from Chézy value of 30 $m^{0.5}/s$ with eddy viscosity of 10 $m^2/s$.

### 5.4.3 Nutrient concentrations using NDVI and substrate classification

Association between the modelled nutrient concentrations in 2009 and 2015 which were categorised into five zones (Figure 5-26) and the extracted NDVI in corresponding years was investigated using boxplots. The extracted NDVI values were positive skewed, except for the NDVI of the level 5 (very high concentration) zone in early autumn 2009, which is close to normally distributed. The median NDVI during late spring and early autumn rises in accordance with nutrient concentrations (Figure 5-27). In autumn 2009, high median NDVI is found in the highest two nutrient concentration zones (4 and 5) whilst median NDVI in zones 1-3 are lower. The ranges of NDVI in zones 2 and 3 are slightly different from those in the level 1 (lowest nutrient concentration) zone where the variation is higher (Figure 5-27A). This high variation of NDVI could result from the large extent of mature algal mats in the lower estuary (Figure 4-12B).

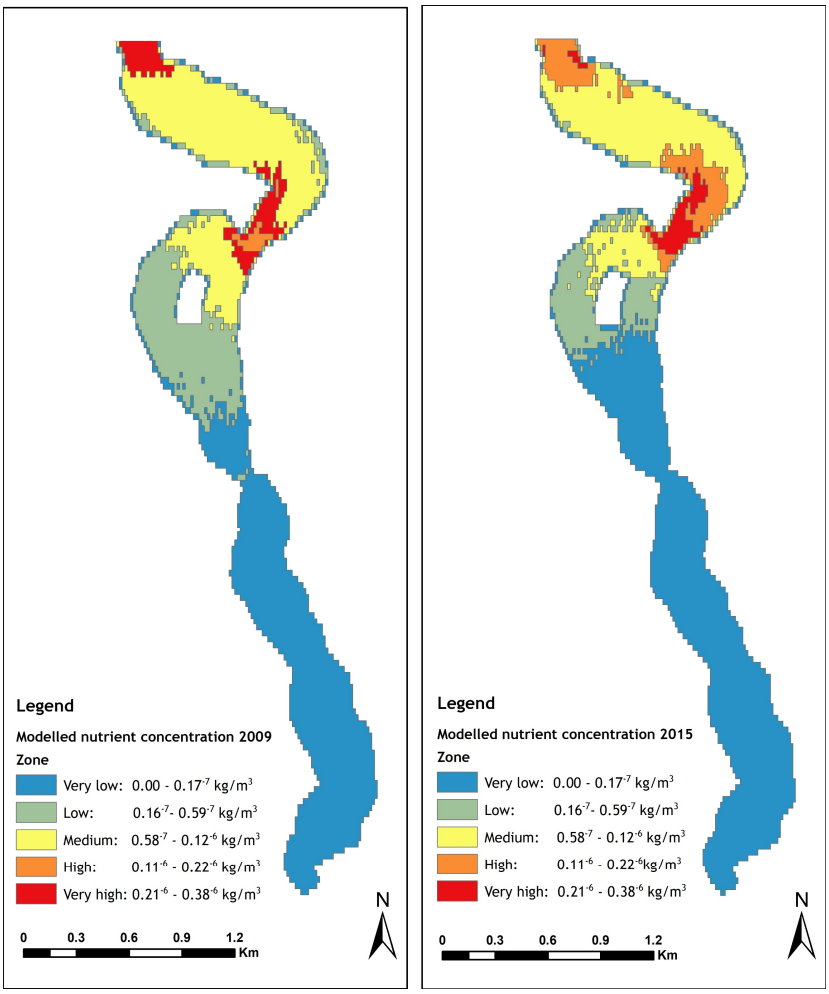


**Figure 5-26:** Modelled nutrient concentrations during slack tide derived from one-time release of 1 kg tracer at fresh water boundary, modelled at 12:00 pm on 11 September 2009 and 01:40 am 20 April 2015.

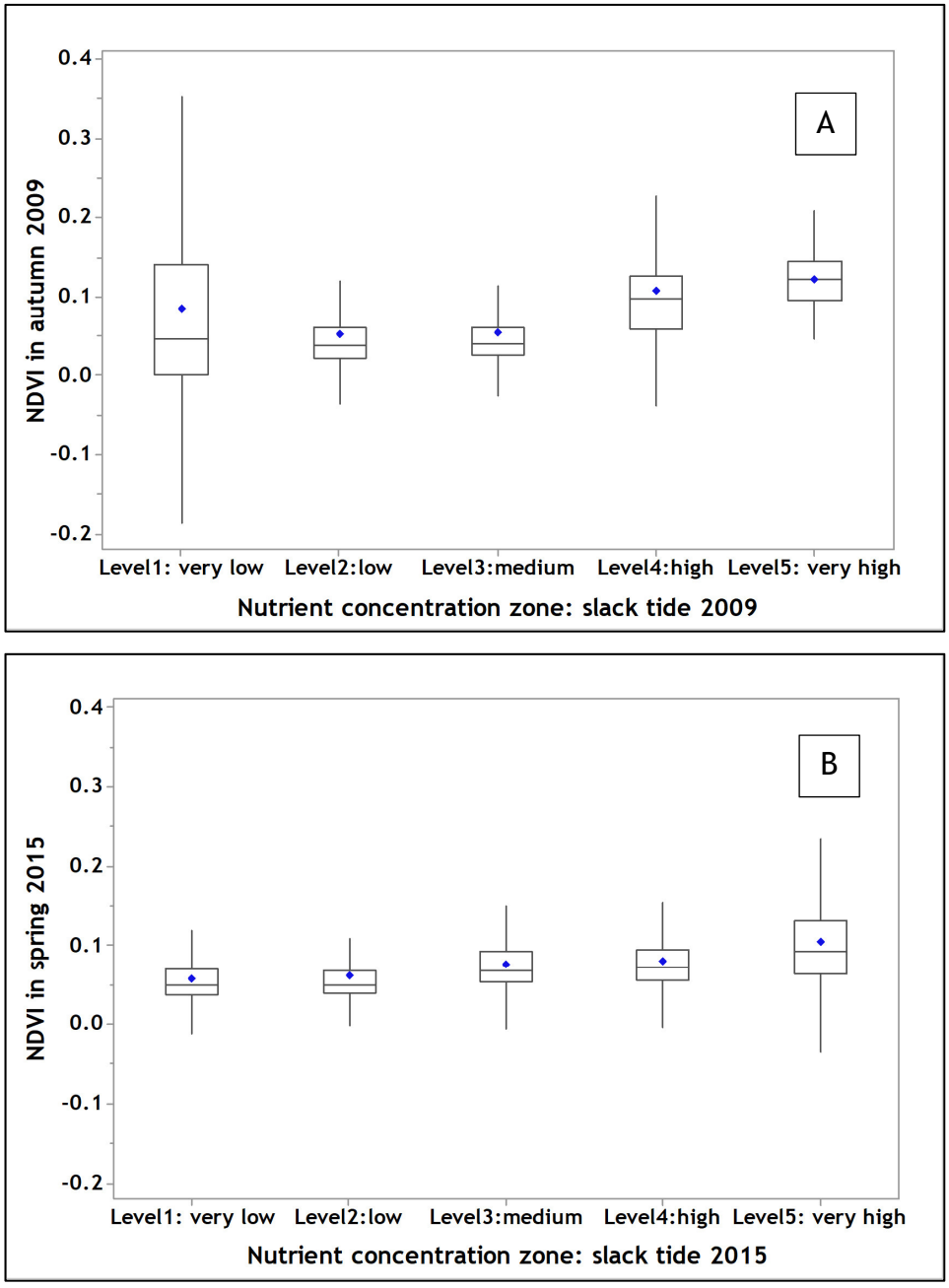


**Figure 5-28:** Boxplots of NDVI in each of the nutrient concentration zones modelled at 12:00 pm on 11 September 2009 (A) and 01:40 am 20 April 2015 (B)

In late spring, overall median NDVI is generally lower than autumn, except in the nutrient level 3 zone where NDVI is slightly higher than autumn. In addition, high variation of NDVI is found in level 5 in the late spring unlike in the autumn (Figure 5-27B). These behaviours could be explained by the growing season of algae in the Ythan estuary, which normally starts in late spring when days become longer and temperature rises (Edwards et al., 2003, Taylor, 1999). In this period, the algae are immature and produce much lower chlorophyll than in summer and early

autumn (Edwards et al., 2003, Taylor, 1999). The high variation of NDVI and the NDVI maximum values, especially in level 5 and 4 zones in both spring and autumn, reflect the association of very high nutrient supply to this area with algal growth.

There are significant correlations between NDVI and nutrient concentration zones (Table 5-10). In late spring, moderately significant relationships are found in the very low [$R = 0.35$, $p<0.001$] and very high [$R = 0.32$, $p<0.001$] nutrient zones, whereas the other nutrient concentration zones show weaker relationships. In autumn, however, a significant relationship [$R= 0.39$, $p<0.001$] is found in the medium nutrient concentration zone. Moreover, there is a negative relationship in the very low nutrient concentration zone, which reflects the very low nutrient supply to this area of macroalgal growth, i.e. macroalgae can be found with nutrient concentrations that are seasonally low (Table 5-10).

The NDVI data, which can be used to classify substrates on mudflat according to Benyoucef et al. (2014),Brito et al. (2013), Liu et al. (2009), Hu and He (2008), and Van der Wal et al. (2010) were also analysed coupled with the modelled nutrient concentration zones using the Zonal statistics function in Spatial Statistics tools, ArcGIS to understand types of substrate found in each of the nutrient concentration zones. This study considers NDVI values between -1.0 - 0.1 as mudflats, NDVI values between 0.1 - 0.3 as benthic micro algae or *Microphytobenthos* (MPB), and NDVI values greater than 0.3 as macroalgae as seen in Benyoucef et al. (2014) and Kazemipour et al. (2012). The results show that in autumn, macro algae are dominantly found in the very high, high, medium and very low nutrient concentration zones whilst mudflats occupy most of the low concentration zone. On the contrary, in late spring, mudflats with MPB are the dominant component in four of the nutrient concentration zones, with the very low nutrient concentration zone being dominated by mudflats. These results suggest that nutrient supply is likely to support algal growth in early spring rather than autumn, when the algal demand for nutrients seems lower (Harrison and Hurd, 2001, Hurd et al., 2014). In addition, low nutrient supply from the water column during slack tide can also help algae to develop on mudflats.

**Table 5-8:** Correlation coefficients between NDVI and nutrient concentration zones during slack tide in early autumn and late spring

| *Nutrient concentration zone* | | *NDVI early autumn (2009)* | *NDVI late spring (2015)* |
|---|---|---|---|
| Level 1: very low | *R* | -.13 | .35 |
| | p-value | .000 | .000 |
| | N | 793,565 | 287,773 |
| Level 2: low | *R* | .02 | .18 |
| | p-value | .000 | .000 |
| | N | 232,571 | 1,048,575 |
| Level 3: medium | *R* | .39 | .17 |
| | p-value | .000 | .000 |
| | N | 35,921 | 1,048,575 |
| Level 4: high | *R* | .27 | .10 |
| | p-value | .000 | .000 |
| | N | 6,663 | 406,070 |
| Level 5: very high | *R* | .19 | .32 |
| | p-value | .000 | .000 |
| | N | 1,103 | 80,301 |

**Table 5-9:** Majority substrate types found in different nutrient concentration zones during slack tide in 2009 (autumn) and 2015 (spring)

| Nutrient concentration zone (early autumn in 2009) | Majority of substrate in 2009 | Area of Majority of substrate ($m^2$) | Area of Majority of substrate (%) |
|---|---|---|---|
| Very high | Macro algae | 38,907 | 30% |
| High | Macro algae | 4,714 | 24% |
| Medium | Macro algae | 383,967 | 65% |
| Low | Mudflats | 323,010 | 77% |
| Very low | Macro algae | 522,435 | 56% |
| Nutrient concentration zone (late spring in 2015) | Majority of substrate in 2015 | Area of Majority of substrate ($m^2$) | Area of Majority of substrate (%) |
| Very high | Mudflats with MPB | 33,071 | 53% |
| High | Mudflats with MPB | 95,424 | 61% |
| Medium | Mudflats with MPB | 384,286 | 81% |
| Low | Mudflats with MPB | 204,870 | 81% |
| Very low | Mudflats | 452,890 | 41% |

## 5.5 Summary

Two modules of the Delft3D package, Delft3D-Flow and Delft3D-PART were set up for simulations of hydrodynamics, and nutrient concentrations and pathways. To run the model, the necessary files including grid, bathymetry, open boundary,

initial conditions, and observation points were created. The significant physical numerical parameters which were not set to default values, bottom roughness, horizontal eddy viscosity, and horizontal eddy diffusivity, were tested to find the optimal values for the model domain. The tests are based on the One-factor-at-a-time (OFAT) approach, in which one selected parameter is varied while keeping all other parameters fixed. The results from the tests suggest that assigning higher bottom roughness value to the model causes reduced damping of tidal oscillations, particularly during spring tides, whereas lower value produces smoother oscillations. In addition, change of bottom roughness coefficient to a higher value increases modelled depth, average velocity and bed shear stress.

Unlike bottom roughness, changing the horizontal eddy viscosity does not introduce significant changes in water depth, depth average velocity or shear stress along main channel. However, close to the sea open boundary (520 m) the results are found to be affected. Assigning lower horizontal eddy velocity produces the highest depth average velocity, sheer stress, and water depth in areas within a short distance of seaward open boundary. Changing the horizontal eddy diffusivity also does not affect water depth, depth average velocity and bed shear stress except in these areas close to the open boundaries where are sensitive to high horizontal eddy diffusivity. The concentrations of nutrients are reduced by increased horizontal eddy diffusivity, lowering this diffusivity produces higher concentrations throughout the model domain. The simulation results derived from assigning the optimum parameter values were validated to assess overall model performance. The first assessment compared modelled with independently measured water depths collected from an echo sounder. The model performance is good, particularly in shallower areas (the water depth is less than 2 m). In the deeper areas, where tidal currents have the greatest effects, the model performance could be further improved by considering adding wind-wave effects to the hydrodynamic model.

The modelled water depths were also validated by using flooded-dry areas extracted from the WV-2 and Landsat-8 images. The model exhibits good performance in predicting delimitation of flooded and dry areas in the central and lower regions of the estuary, although the model fails to predict the deep narrow stream lines in the upper estuary due to the lack of bathymetric data from the main channel. The modelled nutrient concentrations also show good

correspondence with the NDVI derived from CASI and WV-2 images. Median NDVI and the variation of NDVI within each nutrient concentration zone reflect the growth stage of algae within the growing season and the concentration of nutrients which supports algae growth. High variation of NDVI in the highest nutrient concentration zone in spring suggests that nutrients support algal growth in early spring, rather than autumn when demanding of nutrient is lower.

The model, after adjustment of default parameters to optimise performance, provides reliable predictions of hydrodynamics and nutrient concentrations. The ratio image and NDVI are effective aids for model validation, as well as providing directly useful information of algae growth behaviour in response to nutrient concentrations.

# Chapter 6: Modelling hydrodynamics, nutrient concentrations and pathways in the River Ythan

This chapter presents the results of applying the model described in Chapter 5 to the study site, the Ythan estuary. Optimum model parameter settings derived from Chapter 5 are used to simulate hydrodynamics, nutrient concentrations and pathways during high and low river flow events. The different river flow events were the focus of the simulations as the river is the main source of nutrients entering the estuary and river flow is likely to control the amount and, along with tidal conditions, the movement of nutrients in the estuary (Gillibrand and Balls, 1998). High river flow, which in winter and early spring is likely to carry large quantities of nutrients to the estuary (Lyons et al., 1993) before the main algae blooming period in mid-spring to summer (Balls et al., 1995, Edwards et al., 2003, Maier et al., 2009, Raffaelli, 1999), is the main focus. As a comparison, a summer low flow event, which is expected to transport lesser nutrient quantities (Gillibrand and Balls, 1998) , is also investigated. River flow and tidal data collected during corresponding periods were used to simulate hydrodynamic conditions in the estuary. The hydrodynamic simulations help to comprehend seasonal variation of hydrodynamic patterns and inter-annual variation (Duarte et al., 2002, Duarte and Vieira, 2009) is also considered. The simulated hydrodynamics from modelling high- and low-flow conditions are then used to model inter-seasonal and inter-annual patterns of nutrient concentration and nutrient pathways. From modelling these case study events to predict nutrient concentrations and pathways, the extent to which patterns of algal mat locations in the Ythan estuary can be explained by hydrodynamic factors is considered.

## 6.1 Modelling of hydrodynamics, nutrient concentrations and pathways

### 6.1.1 Hydrodynamic simulation

The modelling focuses on hydrodynamics in 2009 as in this year the estuary was severely affected by algal blooms (Gov.scot, 2011). However, events in 2011 and 2015 are also simulated to understand inter-annual hydrodynamic variations which can explain consistency of algal growth patterns in this estuary. The choice of simulation scenarios in Table 6-1 is based on association of river discharge with the amount of chlorophyll, a proxy for nutrient concentrations and movement.

As high river flow (winter, early spring, and autumn) is associated with high chlorophyll concentration in the estuary, it is important to understand the hydrodynamics, nutrient concentrations and pathways during these conditions and to compare these results with low flow periods (mid spring to summer) when nutrient concentrations are lower. Furthermore, scenarios were created under different tidal conditions in order to understand the impact of spring and neap tides, on hydrodynamic conditions in this tide dominated estuary. In particular, simulating these different tidal conditions allows assessment of whether spring tides can increase fluid energy during high river flow when compared to the same high river flows during neap tides. The results of the hydrodynamic simulation include water depth, depth average velocity and bed shear stress. Modelling periods, open boundary types, and boundary conditions are listed in Table 6-1.

**Table 6-1:** Summary of modelling periods and boundary conditions for the 8 hydrodynamic simulations

| No. | Open boundary | Open boundary type | Boundary condition | Data used | Date/ season | Flow event | Tidal condition |
|---|---|---|---|---|---|---|---|
| 1. | Fresh boundary, Sea boundary | Total discharge, Water level | Time series 15-minute interval | River flow, Sea level | Winter 2009 | High flow | Spring tide |
| 2. | Fresh boundary, Sea boundary | Total discharge, Water level | Time series 15-minute interval | River flow, Sea level | Mid spring 2009 | Low flow | Spring tide |
| 3. | Fresh boundary, Sea boundary | Total discharge, Water level | Time series 15-minute interval | River flow, Sea level | Autumn 2009 | High flow | Spring tide |
| 4. | Fresh boundary, Sea boundary | Total discharge, Water level | Time series 15-minute interval | River flow, Sea level | Winter 2009 | High flow | Neap tide |
| 5. | Fresh boundary, Sea boundary | Total discharge, Water level | Time series 15-minute interval | River flow, Sea level | Mid spring 2009 | Low flow | Neap tide |
| 6. | Fresh boundary, Sea boundary | Total discharge, Water level | Time series 15-minute interval | River flow, Sea level | Autumn 2009 | High flow | Neap tide |
| 7. | Fresh boundary, Sea boundary | Total discharge, Water level | Time series 15-minute interval | River flow, Sea level | Early Spring 2011 | High flow | Spring tide |
| 8. | Fresh boundary, Sea boundary | Total discharge, Water level | Time series 15-minute interval | River flow, Sea level | Summer 2015 | Low flow | Spring tide |

Following the sensitivity analysis in Chapter 5.3, the physical and numerical parameters for the hydrodynamic simulations are set in Table 6-2.

**Table 6-2:** Physical and numerical parameters for the hydrodynamic simulations

| Parameter | Value | Units |
|---|---|---|
| Time step | 0.1 | minute |
| Bottom roughness (Chézy, $C$) | uniform 30 | $m^{0.5}/s$ |
| Horizontal eddy viscosity ($v_H$) | uniform 0.01 | $m^2/s$ |
| Horizontal eddy diffusivity ($D_H$) | uniform 200 | $m^2/s$ |
| Threshold depth | 0.001 | m |

The initial conditions for each simulation were obtained from the restart files generated at the end (10 days) of the cold start run carried out during model testing in Chapter 5.3. Locations to examine model results including water depth, depth averaged velocity, and base shear stress are in the central region and lower region of the estuary as shown in Figure 6-1. These are the same locations used in Chapter 5 (Figure 5-1); however, locations A, B, D, and E are the focus in this chapter. These locations were chosen based on proximity to areas where macroalgal mats usually develop and the gradient of the bed. Although only a small number of locations are used, results at these defined locations, along with maps covering the whole of the model domain, can represent the behaviour of hydrodynamic parameters in areas with macroalgal blooms, shallow water and deep water in the main channel. Location A represents areas of high density where macro algal mat development. Locations B and D, respectively located in the shallowest and the deepest regions of the main channel, show behaviours at different water depths and bed gradients. Location E, which is closest to the sea boundary, presents the effects of this sea boundary on hydrodynamics and nutrient concentrations. In addition, this location shows how hydrodynamic and nutrient concentration behaviours algal development in the estuary mouth region. Sample of fresh water discharge and tide level data for simulation no.1 can be seen as Figure 6-2.

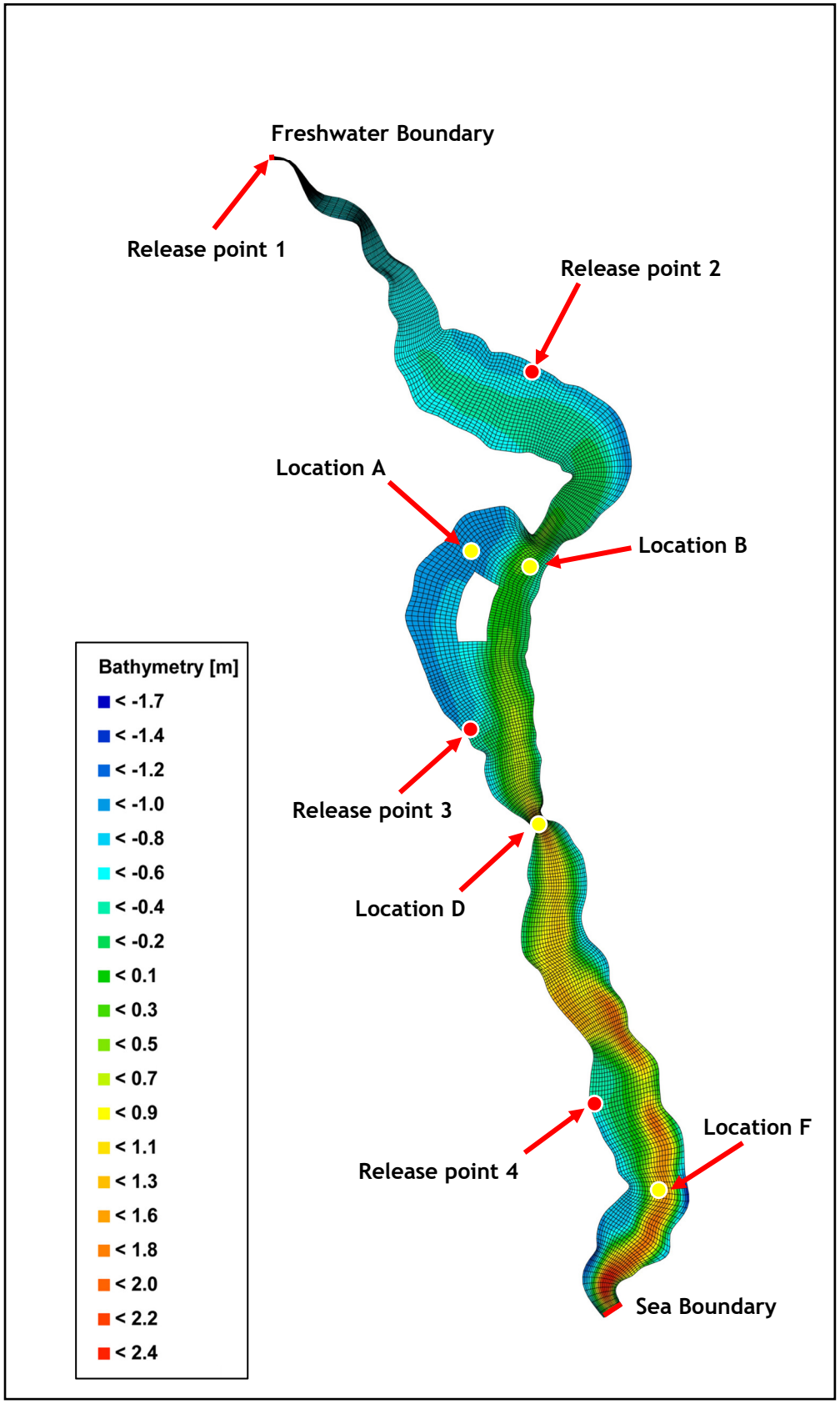


**Figure 6-1:** Bathymetry, open boundaries, tracer release points, and locations for model results

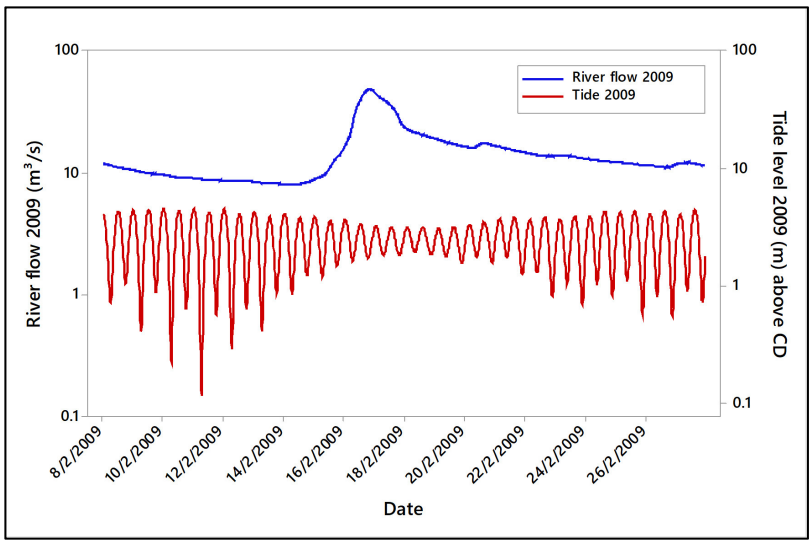


**Figure 6-2:** Fresh water discharge and tide level data for simulation no.1 (winter 2009)

### 6.1.2 Nutrient concentration and pathway simulation

The conservative tracer simulation is used to model patterns of nutrient concentration and transport pathways during both high and low river flow events. Four tracer release points were used: release point 1 at the upstream fresh water boundary (River Ythan input), and release points 2-4 located at the 3 tributaries to the estuary (Figure 6-1). These release points are used to create realistic scenarios for the locations of nutrient input. There are two main groups of scenarios for the tracer simulation. In the first group, tracer is released from a single point during both the flood tide and the ebb tide. In the second group of scenarios, the tracer is released from all 4 release points simultaneously at one time on each flood tide and ebb tide. The tracer input is not scaled to the magnitude of flow or nutrient in the input and 1 kg of conservative tracer, instantaneously released from the specified release point, is used as the input for all simulations. The two scenarios were created to help understand nutrient behaviour when it is released from different locations and from different numbers of release points at different points on the tidal cycle (Table 6-3). Each of the simulations shows the combined influence of fresh water input and tidal conditions on the spatial pattern of tracer (nutrient) concentrations as well as transport pathways. The physical and numerical parameters for modelling nutrient concentration and pathways are given in Table 6-4. It is noted that wind speed and wind direction data gathered from Aberdeen Airport (20 km south of

Newburgh) were assigned to the corresponding simulation periods listed in Table 6-4. Additionally, the estuary shape and bed topography were also considered in interpreting the modelled nutrient concentrations and pathways, through their influence on hydrodynamics. Note that this study has tried a limited range of nutrient input scenarios, and all form up to four-point sources, with no consideration of diffuse inputs.

**Table 6-3:** List of tracer simulations

| Scenario group | Simulation ID | Tracer (kg) | Date/ season | Flow event | Tidal condition | Number of release points | Release point no. |
|---|---|---|---|---|---|---|---|
| 1 | 1-T1-1 | 1 | 8-12 Feb 2009 winter | High flow | Flood tide | 1 | 1 |
| | 1-T1-2 | 1 | 8-12 Feb 2009 winter | High flow | Ebb tide | 1 | 1 |
| | 1-T2-1 | 1 | 1-4 Apr 2009 Mid spring | Low flow | Flood tide | 1 | 1 |
| | 1-T2-2 | 1 | 1-4 Apr 2009 Mid spring | Low flow | Ebb tide | 1 | 1 |
| | 1-T3-1 | 1 | 1-4 Nov 2009 autumn | High flow | Flood tide | 1 | 1 |
| | 1-T3-2 | 1 | 1-4 Nov 2009 autumn | High flow | Ebb tide | 1 | 1 |
| | 1-T4-1 | 1 | 8-12 Feb 2009 winter | High flow | Flood tide | 1 | 2 |
| | 1-T4-2 | 1 | 8-12 Feb 2009 winter | High flow | Ebb tide | 1 | 2 |
| | 1-T5-1 | 1 | 8-12 Feb 2009 winter | High flow | Flood tide | 1 | 3 |
| | 1-T5-2 | 1 | 8-12 Feb 2009 winter | High flow | Ebb tide | 1 | 3 |
| | 1-T6-1 | 1 | 8-12 Feb 2009 winter | High flow | Flood tide | 1 | 4 |
| | 1-T6-2 | 1 | 8-12 Feb 2009 winter | High flow | Ebb tide | 1 | 4 |
| 2 | 2-T1-1 | 1 | 8-12 Feb 2009 winter | High flow | Flood tide | 4 | 1, 2, 3, 4 |
| | 2-T1-2 | 1 | 8-12 Feb 2009 winter | High flow | Ebb tide | 4 | 1, 2, 3, 4 |

**Table 6-4:** The physical and numerical parameters for modelling nutrient concentration and pathways

| Parameter | Value | Units |
|---|---|---|
| Horizontal dispersion coefficients $a$ and $b$ | 0.07 and 0.7 | $m^2/s$ |
| Water density | 1000.00 | $kg/m^3$ |

## 6.2 Modelling results

### 6.2.1 Modelled hydrodynamics during high and low flow events

#### 6.2.1.1 Water depth

Water depths in high flows are greater throughout the estuary than during lower flows (Figure 6-3). Depths at locations D and F and throughout the lower region of the main channel are greater than at locations A and B in the central regions regardless of river flow, which reflects the gradient and topography of the bed (Figure 6-4). Water depths at all locations in the different river flow conditions typical of winter, spring, and autumn vary little at spring tide. However, during neap tide with high (autumn) flows water depths are generally greater than is typical in winter and spring at all locations as a result of higher river inflow coinciding with lower tide levels (Figure 6-4).

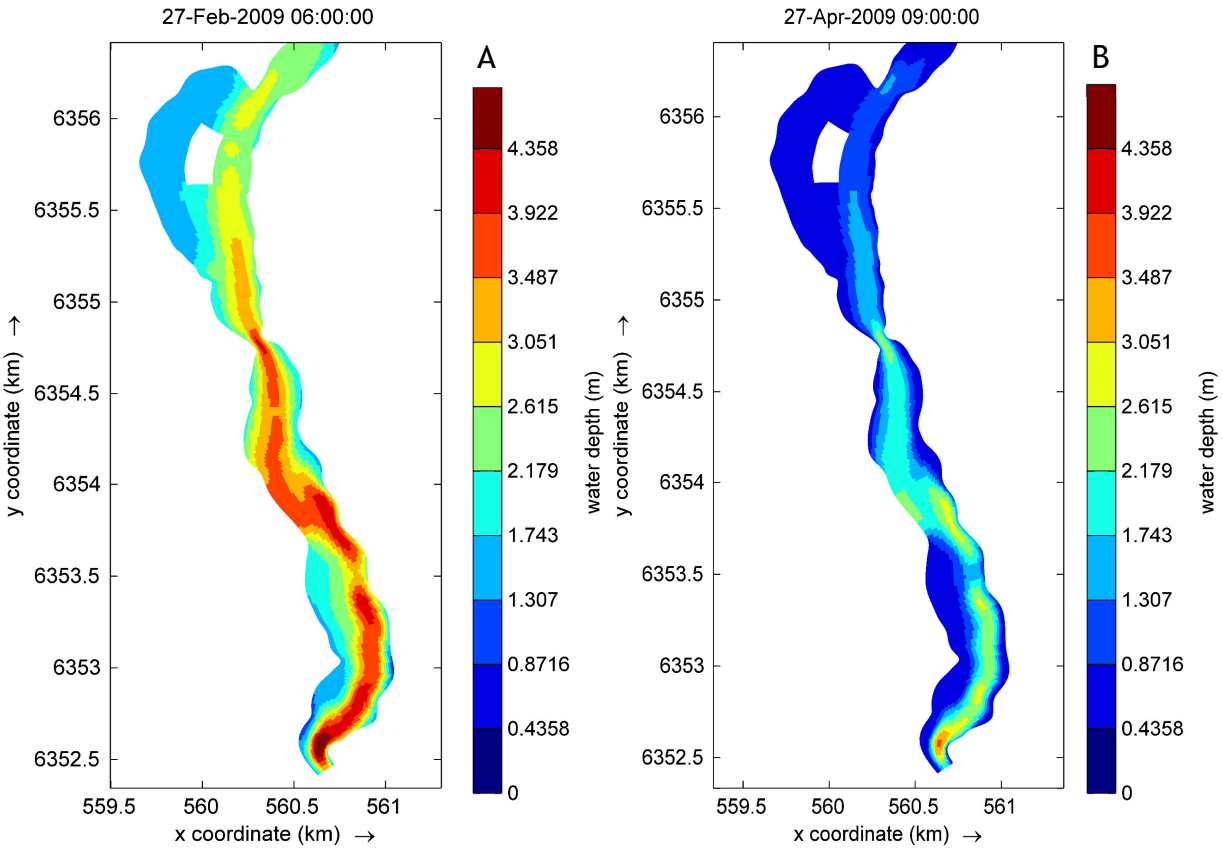


**Figure 6-3:** The overall spatial pattern of water depths at high tide during (A) high flow (winter in 2009) and (B) low flow (mid spring in 2009) during spring tide. The upper area was discarded as the model results were unreliable as a result of uncertainty in main channel elevation.

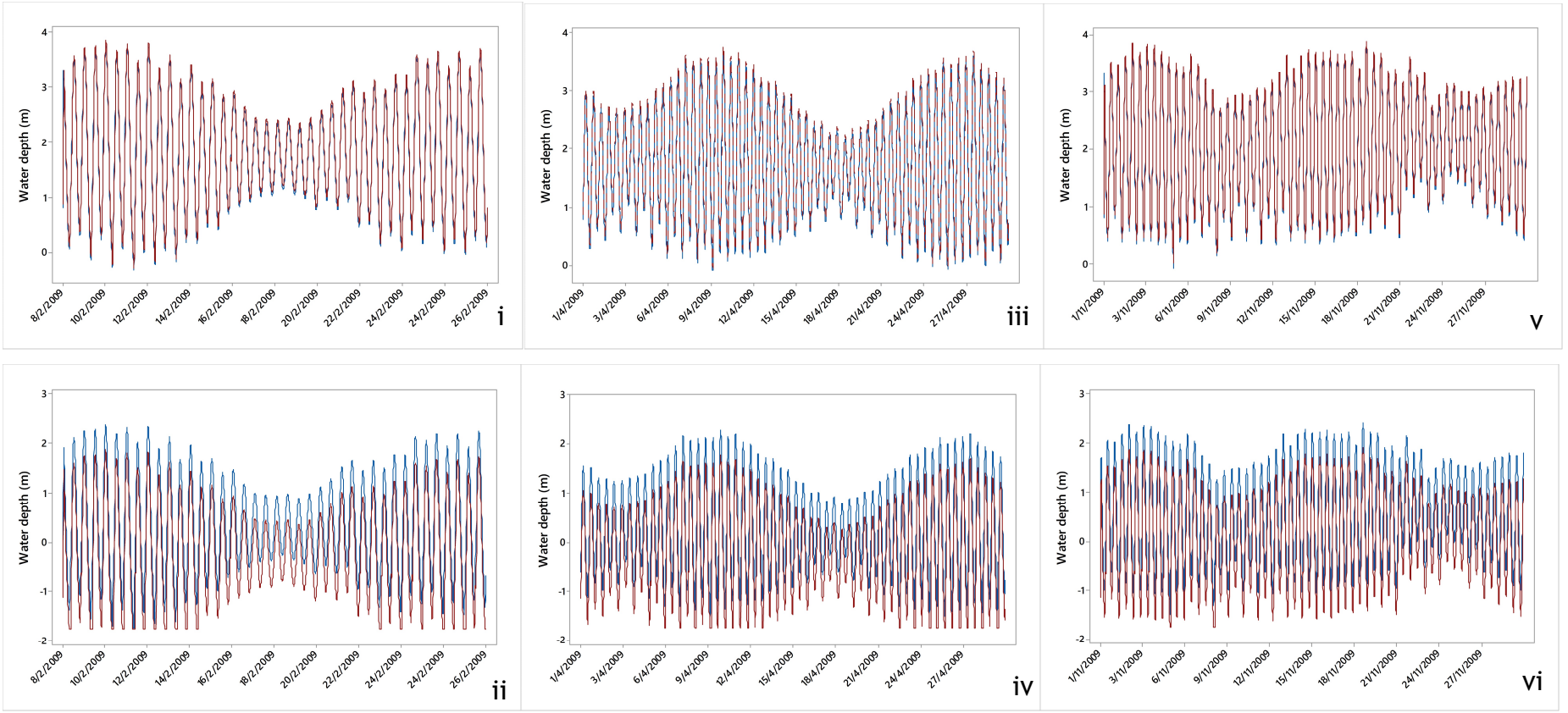


**Figure 6-4:** Water depth (m) above CD under three flow conditions: high winter flow, February 2009, (i, ii); low flow in late spring, April 2009 (iii, iv); high flow in autumn, November 2009, (v, vi). Location F (blue) and D (red) (i); Location B (blue) and A (red) (ii); Location F (blue) and D (red) (iii); Location B (blue) and A (red) (iv); Location F (blue) and D (red) (v); Location B (blue) and A (red) (vi)

#### 6.2.1.2 Depth averaged velocity

The spatial patterns of velocity in the estuary are very similar in both high and low river flow events, whether coinciding with spring or neap tides. The modelled velocity is higher across all of the estuary during flood tide than in the ebb whilst the velocity during slack tide is the lowest (Figures 6-5, 6-6). The velocity in the areas of greatest algal development (mudflats in the central region of the estuary) remains very low throughout the tidal cycle. In addition, the velocities in winter and autumn are almost equivalent throughout the estuary (Figure 6-5). However, the magnitude of velocity shows some significant differences resulting from both river flow and tidal conditions as follows;

(A) The velocities during low flow events are slightly lower than during high flow events (0.08 m/s for low flow and 0.09 m/s for high flow during slack tide and 0.50 m/s for low flow and 0.55 m/s for high flow during ebb tide), except during flood tide conditions when these velocities are nearly the same (≈ 0.64 m/s for both high and low flow in the main channel and 0.32 m/s for both high and low flow at the extensive mudflats in the central estuary) (Figure 6-5: A-B). These patterns reflect the dominance of tide level over river flow in controlling velocities.

(B) The velocities during neap tides are lower than during spring tides across all of the estuary. For instance, when low river flow coincides with neap tide, the velocities at the extensive mudflats in the central estuary are not greater than 0.08 m/s whilst during spring tide, these go up to 0.32 m/s (Figure 6-5B; Figure 6-6B). When high flow coincides with spring tide, the velocities at the same locations are not greater than 0.32 m/s, being below 0.25 m/s during neap tide (Figures 6-5A, 6-5C, 6-6A, 6-6C). The lowest velocities are, as expected, during slack water when low river flow coincides with neap tide (0.02 m/s - 0.04 m/s).

Velocities during high and low flow events in 2011 and 2015 are also examined to understand different combinations of flow and tide level in different years. For the modelled events in 2011, velocities are lower than for the 2009 events as the 2011 events had lower river flow (Figure 6-7). Similarly, velocities modelled for 2015 are slightly higher than in 2009 (Figure 6-8). The variations of velocities from year to year under different river flow levels are small, and velocity remains low over the extensive mudflats in the central region of the estuary.

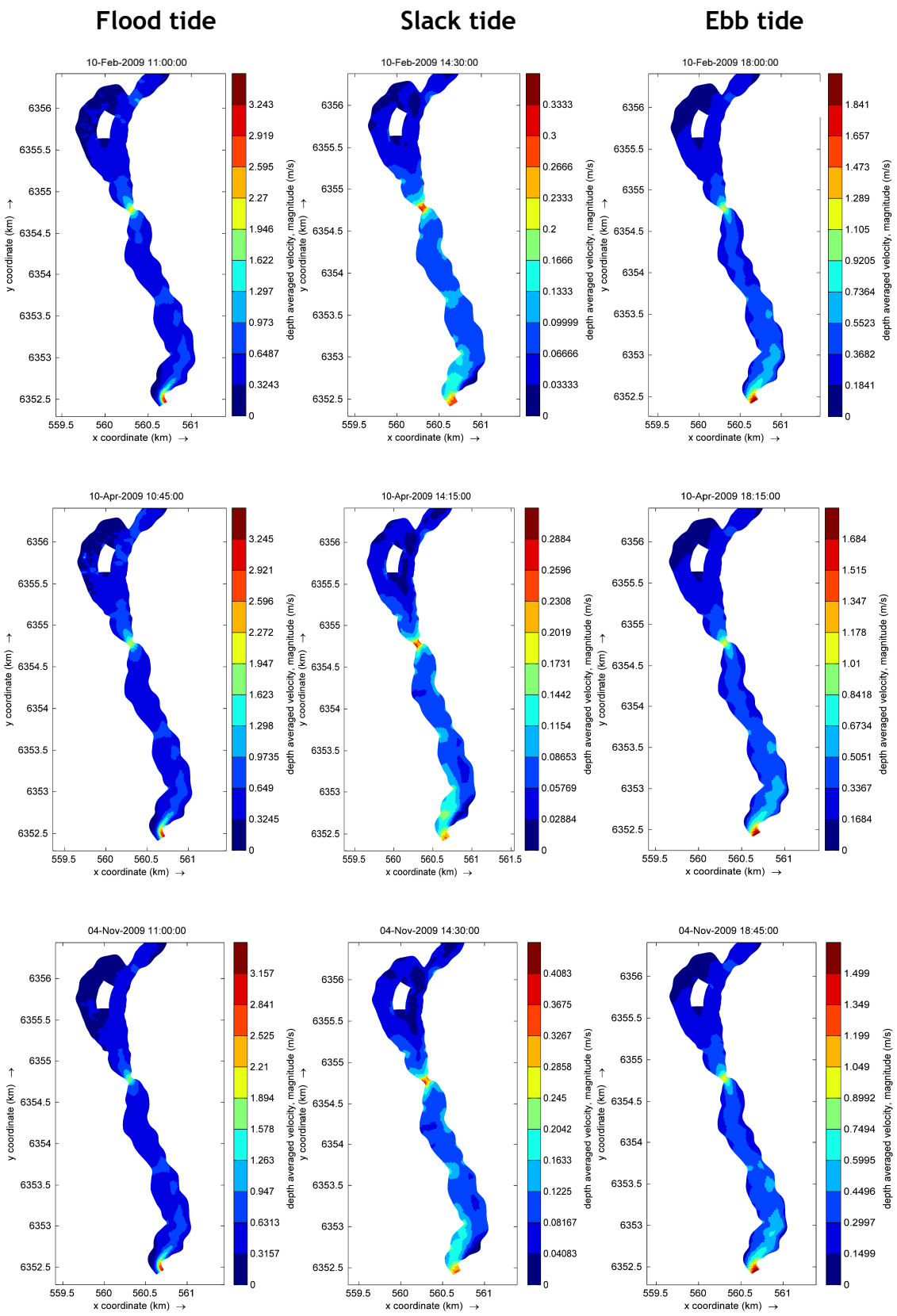


**Figure 6-5:** Depth average velocity during spring tide in (A) winter (high flow event), (B) spring (low flow event, and (C) autumn (high flow event) in 2009. The peak discharge in late winter (48.60 $m^3/s$), mid-spring (7.27 $m^3/s$), and late autumn (101.13 $m^3/s$). It is noted that flood tide is approximately 1.0 hours before highest water, slack tide is approximately 3.0 hours after the highest water, and ebb tide is approximately 3.0 hours after slack water. The upper area was discarded as the model results were unreliable as a result of uncertainty in main channel elevation.

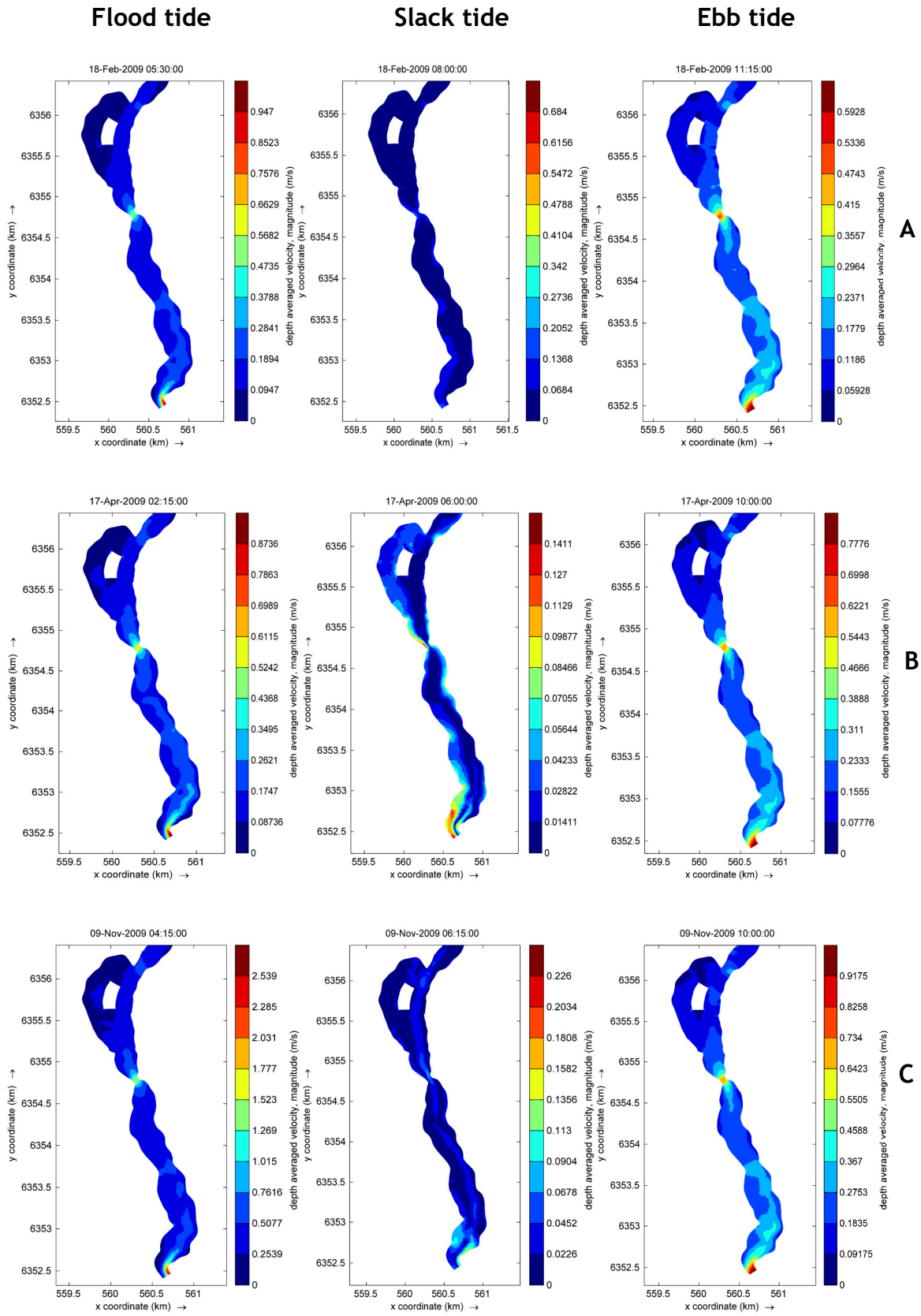


**Figure 6-6:** Depth average velocity during neap tide in (A) late winter (high flow event), (B) mid-spring (low flow event), and (C) late autumn (high flow event) in 2009. It is noted that flood tide is approximately 1.0 hours before highest water, slack tide is approximately 3.0 hours after the highest water, and ebb tide is approximately 3.0 hours after slack water. The upper area was discarded as the model results were unreliable as a result of uncertainty in main channel elevation.

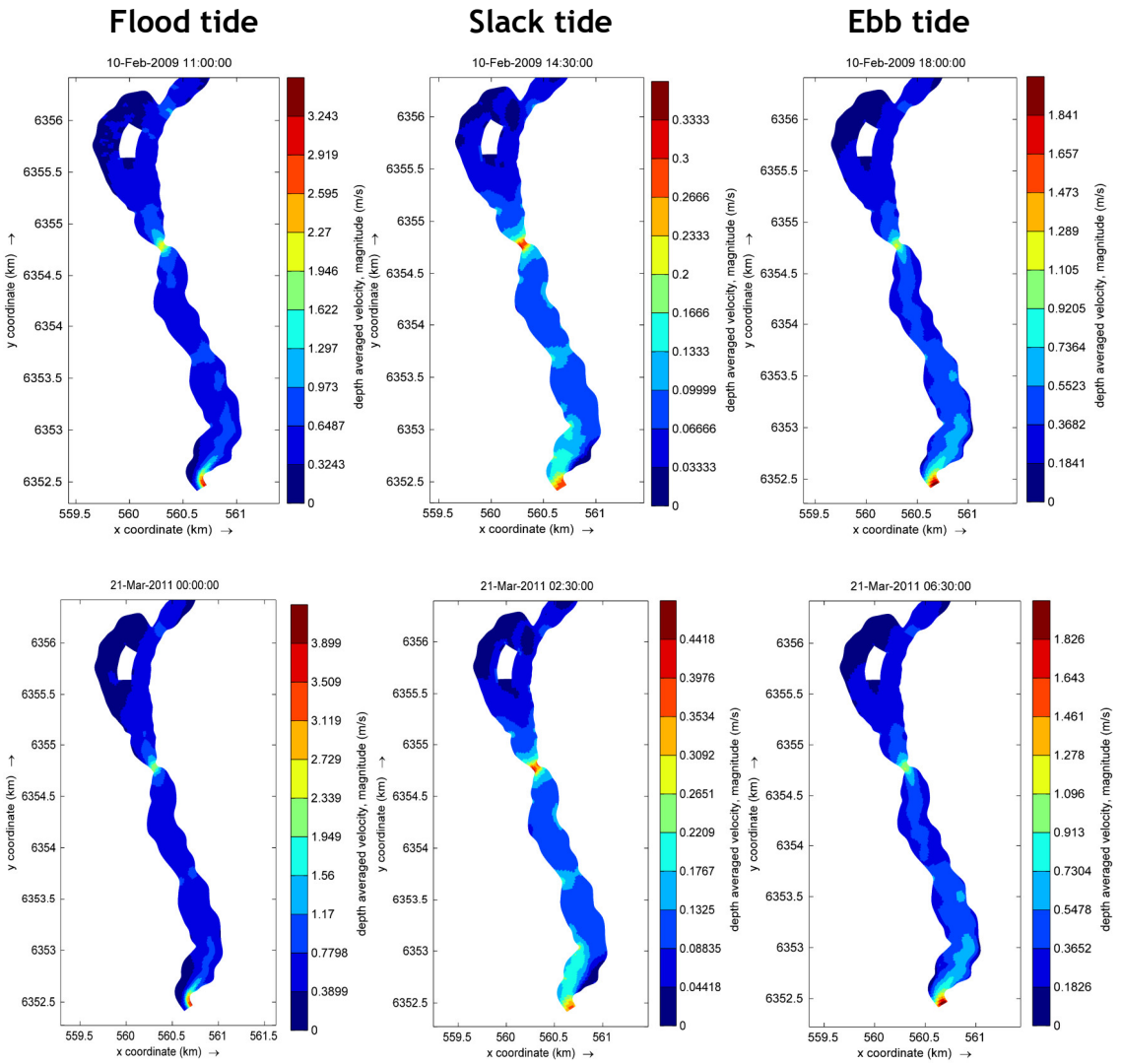


**Figure 6-7:** Depth average velocity in winter (high flow event) in 2009 (A) and 2011 (B). The peak discharge in late winter 2009 (48.60$m^3/s$), and early spring 2011 (29.81$m^3/s$). It is noted that flood tide is approximately 1.0 hours before highest water, slack tide is approximately 3.0 hours after the highest water, and ebb tide is approximately 3.0 hours after slack water.

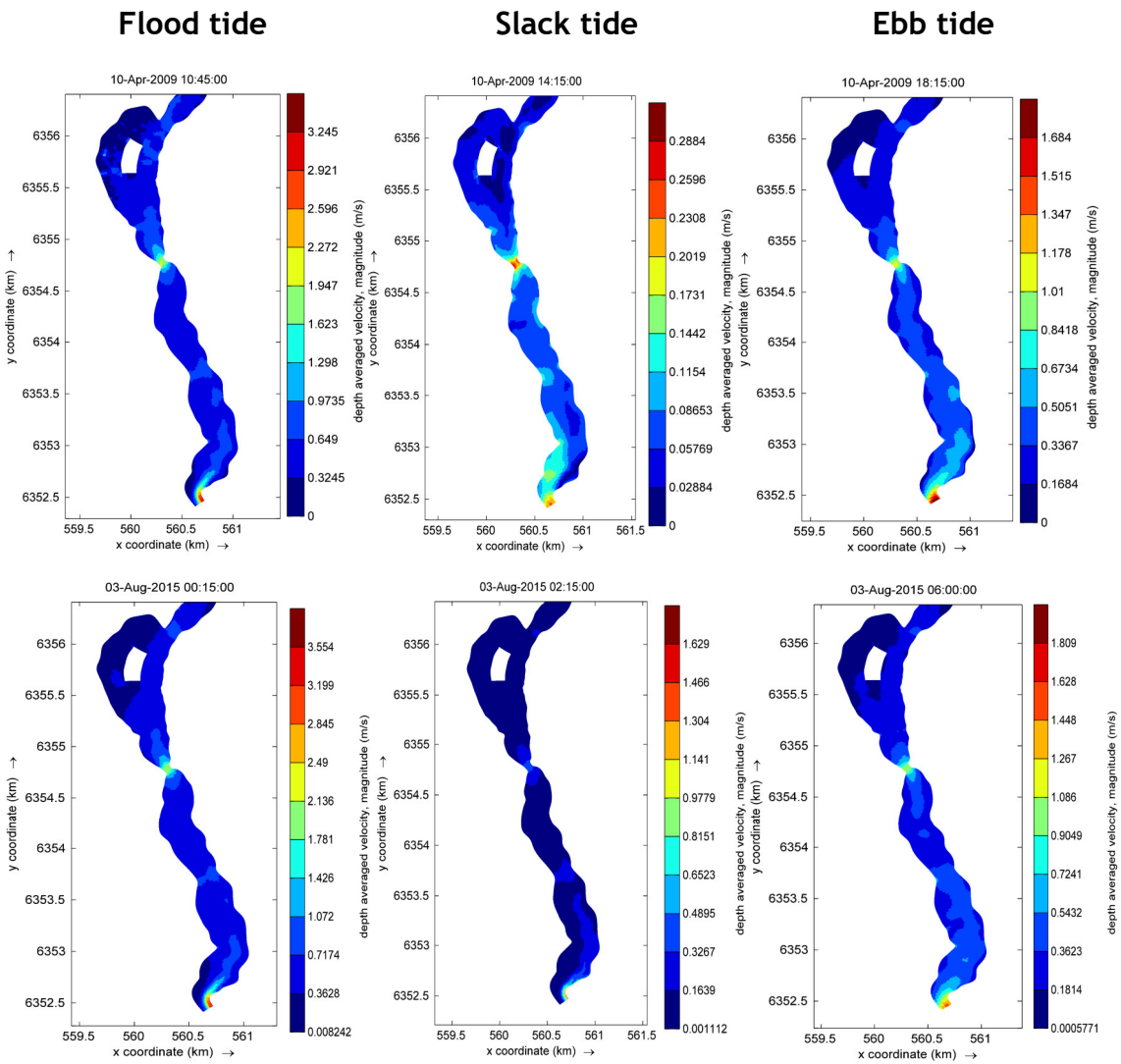


**Figure 6-8:** Depth average velocity in spring/summer (low flow event) in 2009 (A) and 2015 (B). The peak discharge in spring 2009 (7.27m$^3$/s) and summer 2015 (17.56 m$^3$/s). It is noted that flood tide is approximately 1.0 hours before highest water, slack tide is approximately 3.0 hours after the highest water, and ebb tide is approximately 3.0 hours after slack water.

#### 6.2.1.3 Bed shear stress

The modelled bed shear stress indicates the sediment transport capacity of water movement in the estuary, and thus the potential for entraining (high stress) or depositing (low stress) sediment. Four locations, two located in the central region of the estuary and two in the lower region, were used to investigate modelled bed shear stress (Figure 6-1). The locations in the central region are in areas where extensive algal development occurs, while the locations in the lower region were chosen to examine the influence of the sea boundary on water movement.

At all locations, the bed shear stress corresponds closely to the depth averaged velocity. During both high and low flow events, the shear stresses at locations D and F located in the lower region are greater than those at locations A and B in the central region. The overall shear stress in the estuary is low (90% of values are below 1.25 $N/m^2$), especially in the central region, which results in deposition of sediment in this region. In addition, high flow events only cause moderate increases in shear stress. However, regardless of the amount of river flow, the shear stresses during spring tide are always much higher than on neap tide (Figure 6-9).

The modelled shear stresses, along with the depth-averaged velocities discussed above, show that the river discharge is not the main control of water movement, and the effects of the tidal cycle and spring and neap tides are significant. The estuary has the lowest energy during low river flow coinciding with neap tide.

In addition, although tidal forcing is expected to produce more water movement in the lower region of the estuary which is closer to the sea boundary, the results show low velocities and stresses in the lower region. In contrast, higher energy flow is confined to an area near the mouth and in narrow areas of deeper water in the main channel in both the lower (location D) and central regions (location B; the narrow point between the central and upper regions).

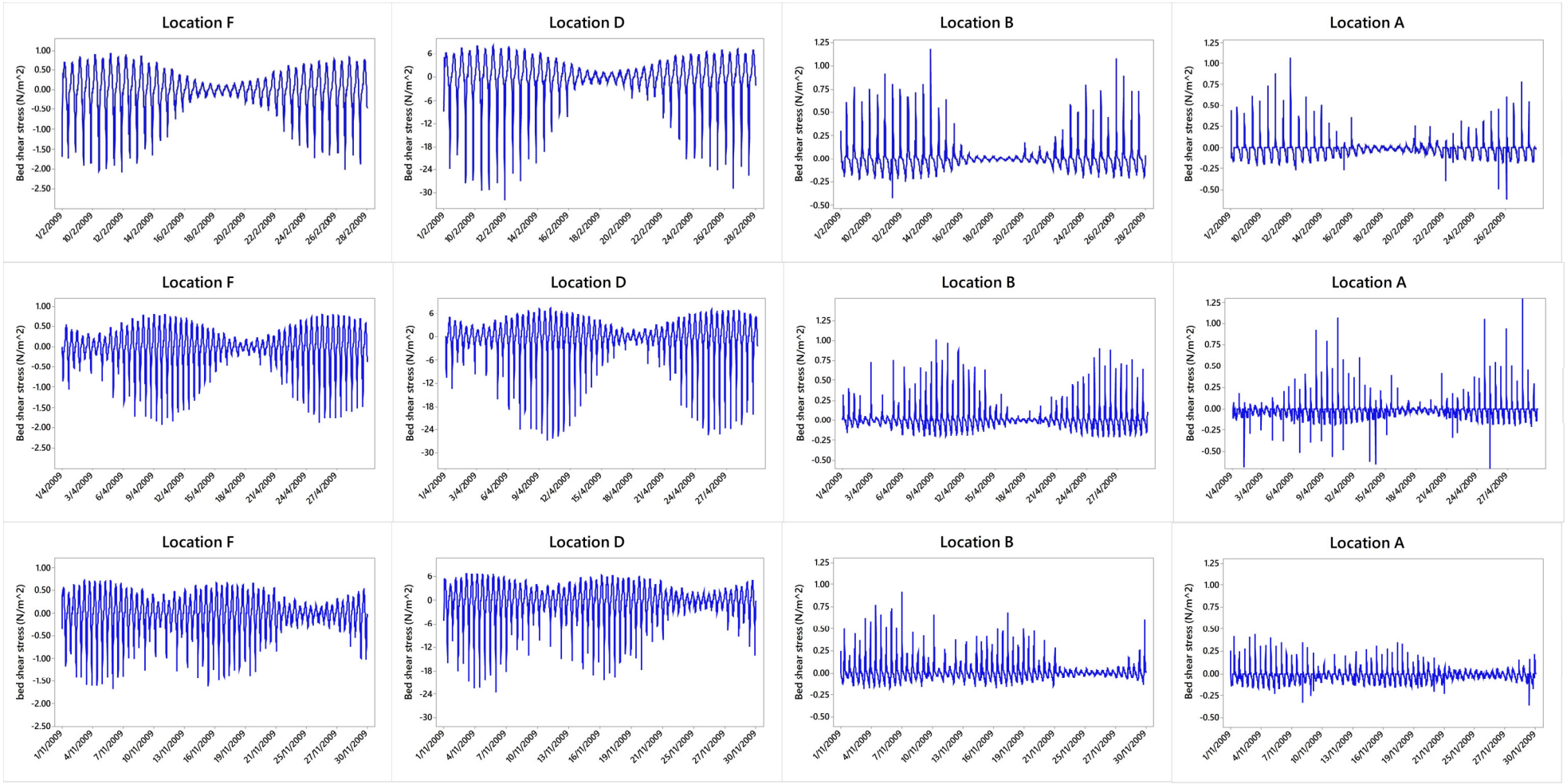


**Figure 6-9:** Bed shear stress at locations F and D in the lower region and locations B and A in the central region during: (i) high flow event in February 2009 (ii) low flow event in April 2009; (iii) high flow event in November 2009. A positive shear stress means landward and negative means seaward.

### 6.2.2 Modelled nutrient concentrations and pathways during high and low flow events

#### 6.2.2.1 First group scenarios (group A)

**1) Tracer introduced on flood tide**

The simulation of tracer input from release point 1 during flood tide in a high flow event (winter and autumn 2009) shows high nutrient concentrations in the main channel (locations B and D) where depth averaged velocity and bed shear stress are both high (Figures 6-10, 6-11). The highest concentration is at location B (0.53 mg/m$^3$) which is closest to the release point (1.8 km) followed by location D (0.29 mg/m$^3$). Although location A, which is located in area of extensive algal growth, is closer to release point 1 (2.8 km) compared with location D (4.8 km), low nutrient concentration is predicted for this location (0.12 mg/m$^3$). At location F, the concentration is the lowest due to distance from release point 1 (6 km). Tracer is found at all locations for approximately 4 days after injection. When releasing tracer during flood tide and in a low flow event (spring 2009), nutrient concentrations are much lower throughout the estuary than in the high flow event; however, the spatial and temporal patterns of tracer concentration are the same in both the low and high flow events (Figure 6-12).

When tracer is introduced from release point 2, patterns of concentration are similar to those when tracer is input at release point 1. Location B, which is located within the distance of 1 km from the release point still shows the highest concentrations (1.7 mg/m$^3$) during the first tidal cycle. While location A shows the lowest concentration (0.3 mg/m$^3$), despite also being close to release point 2 (1.28 km). However, the overall concentrations at all observation points are higher than in the simulation from release point 1 (Figure 6-13). The simulation from release point 3 also produces higher concentrations compared to point 1. This simulation produces the same overall patterns of concentration as the previous two simulations, but in this case location A, which is nearest to the release point (1.12 km), has higher concentrations (1.98 mg/m$^3$) than when the tracer was input at the previous two release points. Although location A concentrations are higher in this case, concentrations from location B (1.4 km from the release point) are still the highest overall (2.1 mg/m$^3$) followed by location D (0.87 mg/m$^3$) (0.72 km from the release point) (Figure 6-14).

The simulation from release point 4 produces a similar pattern of concentration to that from release point 3. Overall concentrations are also higher compared to the first simulation. Significantly, the highest concentration is not found at location F, which is closest to (0.67 km) the release point, but at location B (1.5 mg/$m^3$) followed by locations A, D, and F (Figure 6-15).

**2) Tracer introduced on ebb tide**

Introducing tracer from release point 1 during the ebb tide produces modelled nutrient concentrations at all locations that are lower than in the flood tide simulation. The concentrations at location B are the highest (0.38 mg/$m^3$) followed by locations D, F, and A (Figure 6-16). Similarly, results from release point 2 show higher concentrations at locations A, B, D, F than when the tracer is released on the flood tide (Figure 6-17). Tracer input from release points 3 and 4, shows very high concentrations at locations D and F. Location D is closest to release point 3 (0.72 km) and has the maximum modelled concentration (4.2 mg/$m^3$), which decreases to 1.2 mg/$m^3$ at location F located 2.5 km further down the estuary (Figure 6-18). For release from point 4, only location F, the nearest to the release point (0.67 km), shows a high peak concentration (1.82 mg/$m^3$) (Figure 6-19).

### 6.2.2.2 Second group scenarios (group B)

The results of simulating tracer introduced from the 4 release points at one time show that patterns of concentration are not significantly different from the first group scenario. Locations B (3.21 mg/$m^3$) and D (2.81 mg/$m^3$) are still the primary locations where the tracer aggregates, followed by locations A (2.08 mg/$m^3$) and F (1.22 mg/$m^3$). However, concentrations during flood tide in this scenario at all observation points are greater than those in the first group scenarios, especially at location A. Likewise, in comparison to the first scenario simulations, the highest concentrations are found during the first tidal cycle and gradually decreases during the following tides (Figure 6-20). The study also simulated the tracer released from 4 release points during ebb tide. The concentrations during ebb tide are, as expected, greater than those modelled in the flood tide simulation. The highest concentrations are found at locations D (4.30 mg/$m^3$), B (3.40 mg/$m^3$), F (1.80 mg/$m^3$) and A (1.90 mg/$m^3$), respectively (Figure 6-21).

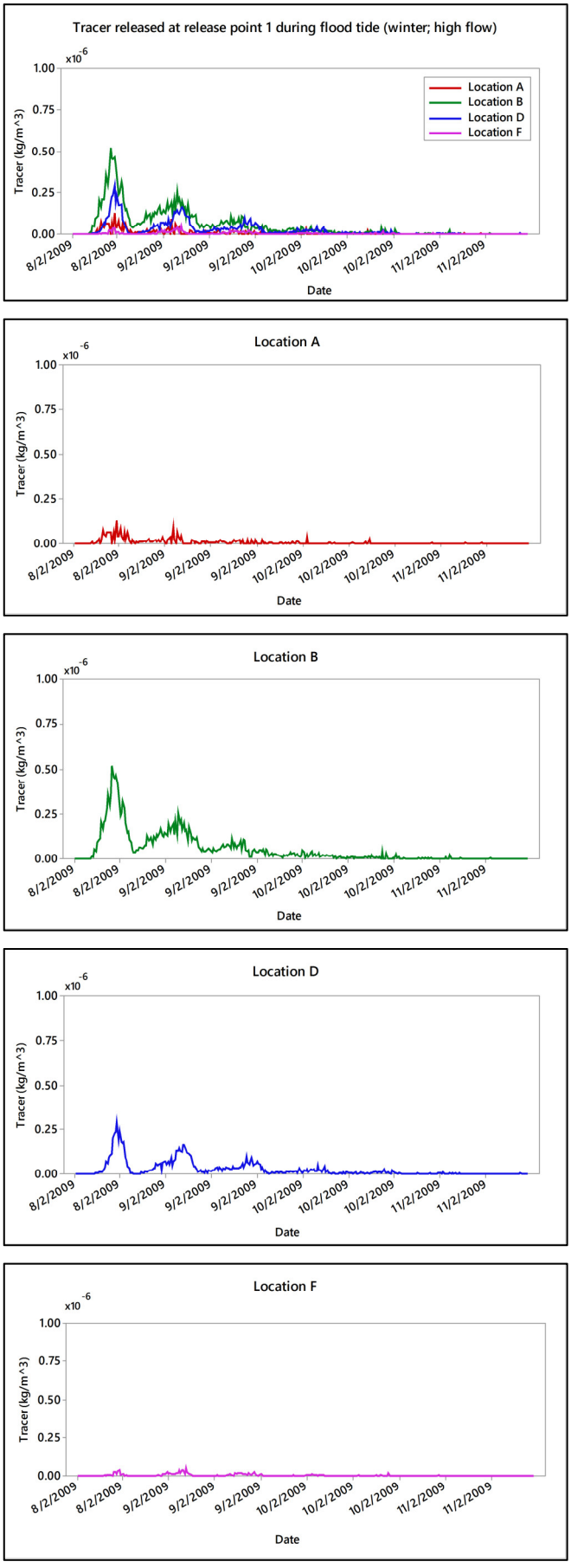


**Figure 6-10:** Modelled tracer concentration between 8-11 February 2009 (winter; high flow) from release point 1. Tracer introduced at release point 1 during flood tide.

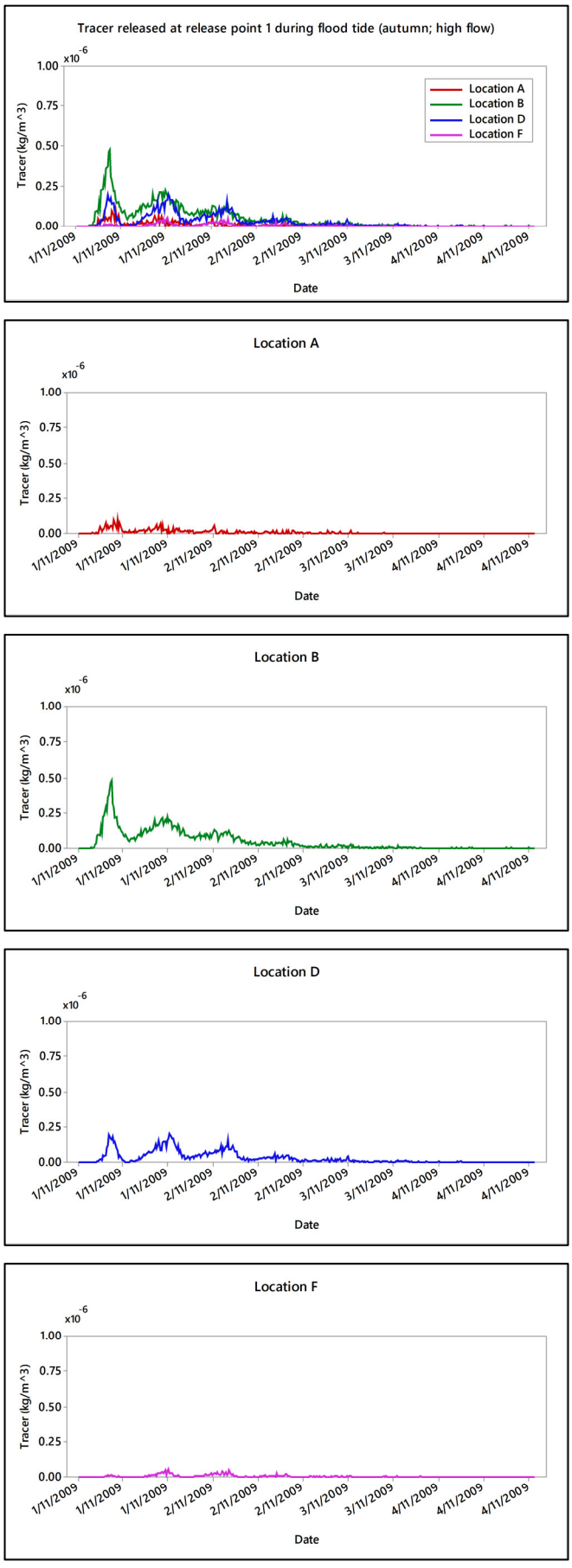


**Figure 6-11:** Modelled tracer concentration between 1-4 November 2009 (autumn; high flow) from release point 1. Tracer introduced at release point 1 during flood tide.

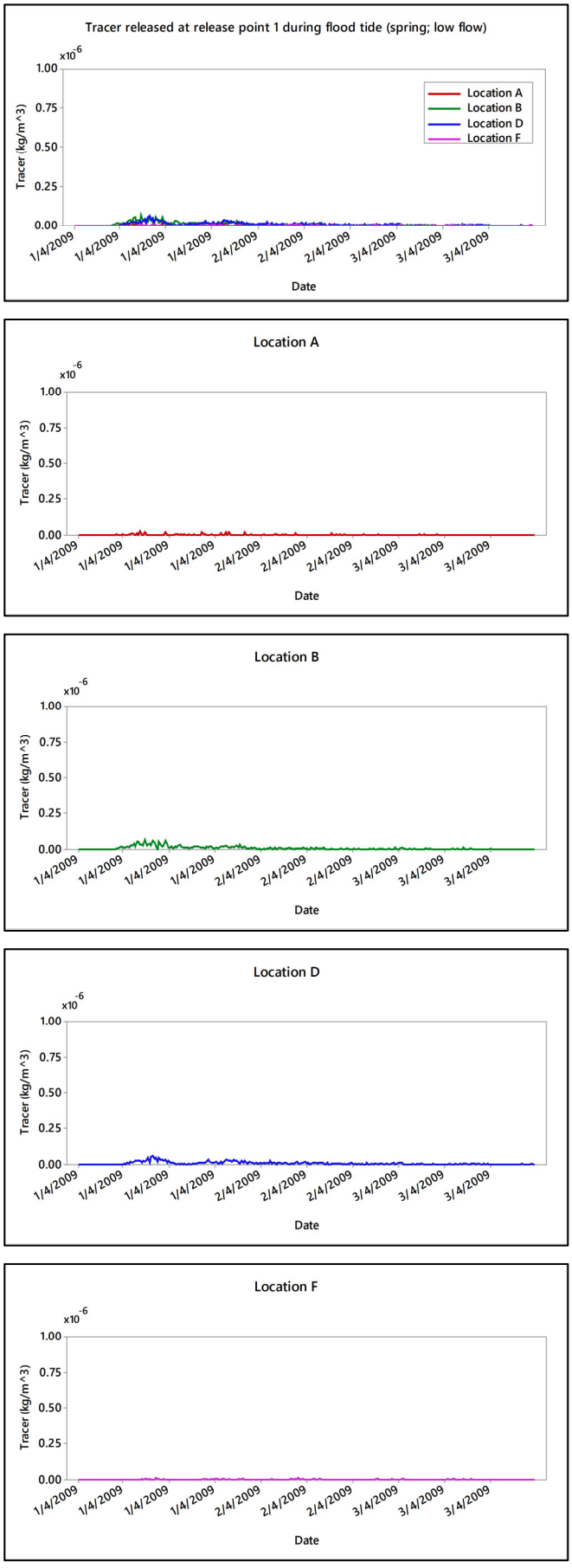


**Figure 6-12:** Modelled tracer concentration between 1-4 April 2009 (spring; low flow) from release point 1. Tracer introduced at release point 1 during flood tide.

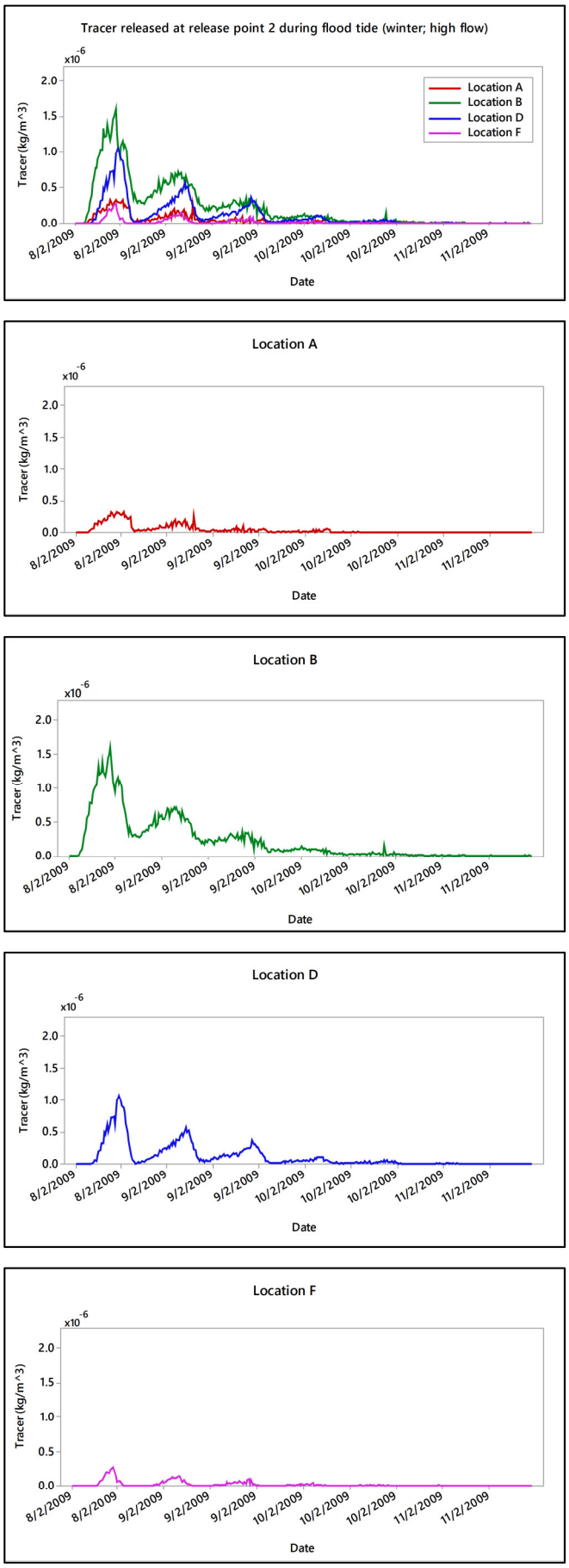


**Figure 6-13:** Modelled tracer concentrations between 8-12 February 2009 (winter; high flow) from release point 2. Tracer introduced at release point 2 during flood tide during flood tide.

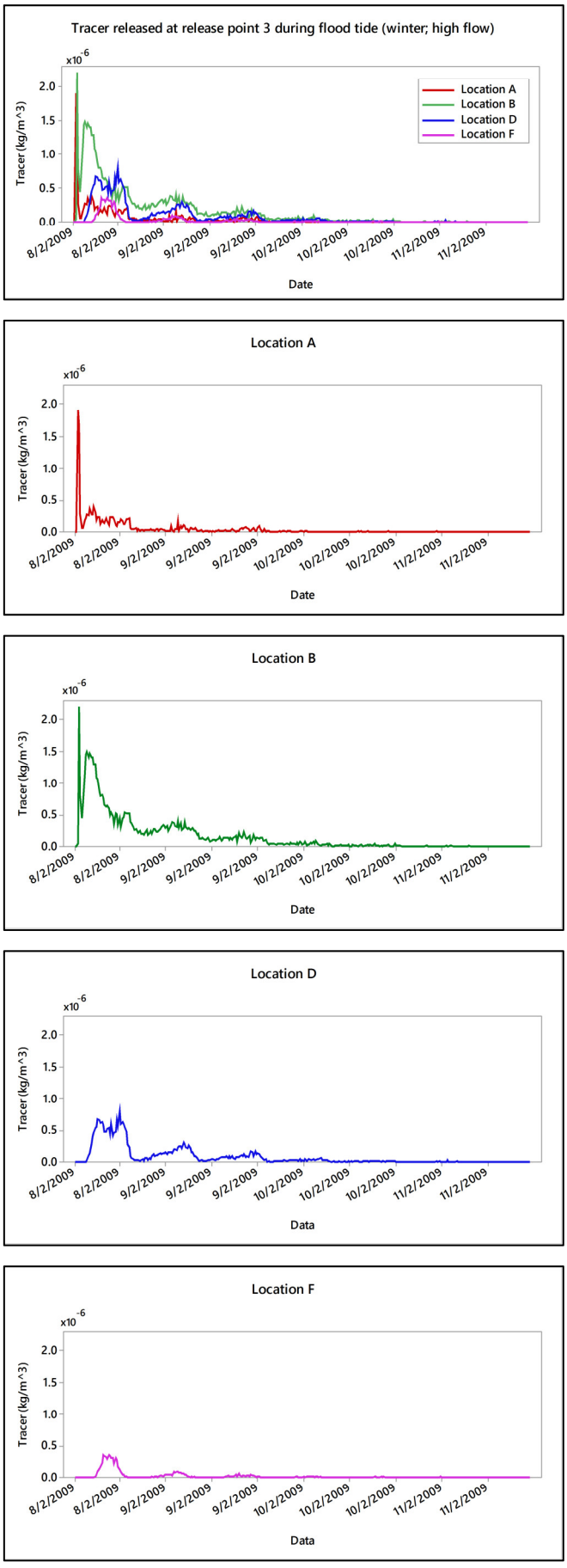


**Figure 6-14:** Modelled tracer concentrations between 8-12 February 2009 (winter; high flow) from release point 3. Tracer introduced at release point 3 during flood tide.

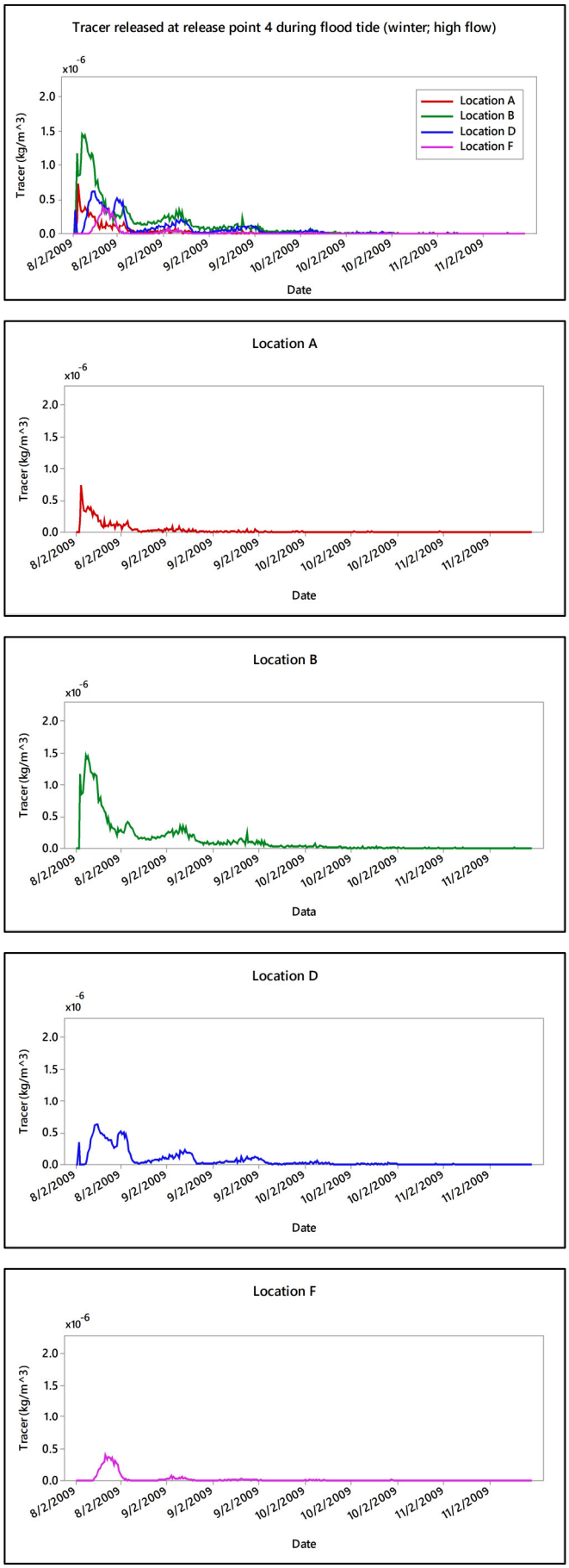


**Figure 6-15:** Modelled tracer concentrations between 8-12 February 2009 (winter; high flow) from release point 4. Tracer introduced at release point 4 during flood tide.

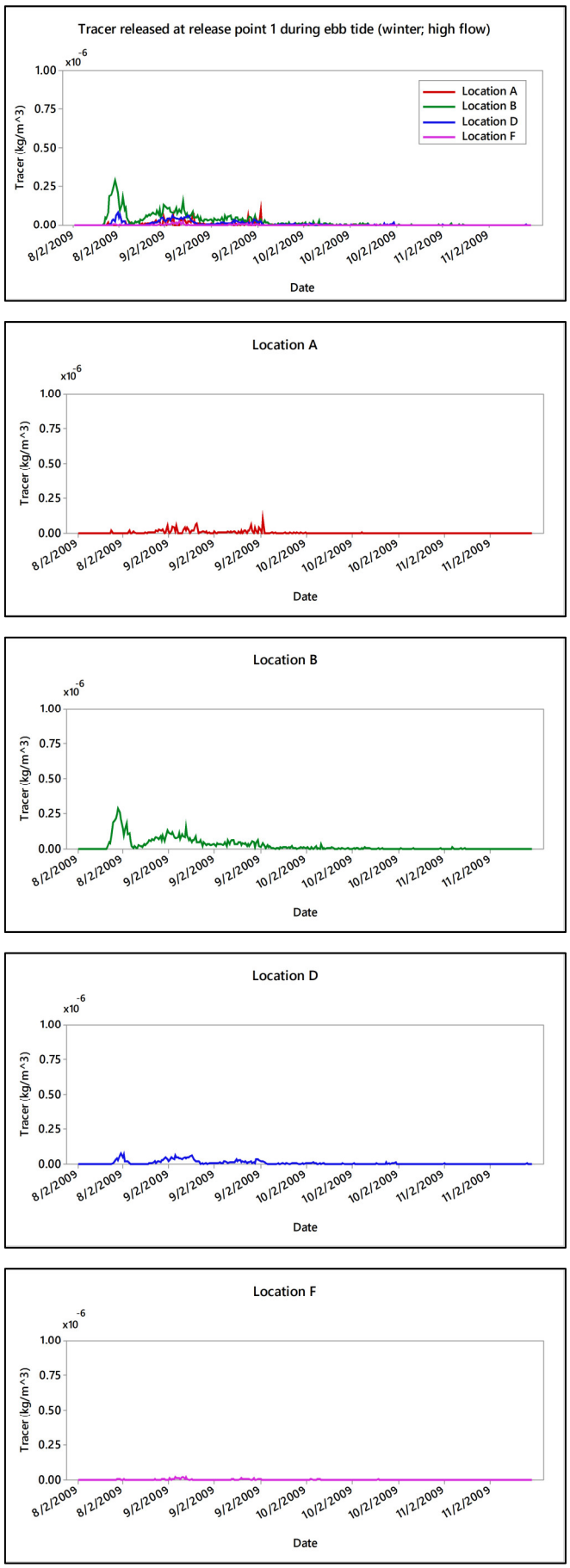


**Figure 6-16:** Modelled tracer concentration between 8-11 February (winter; high flow) from release point 1. Tracer introduced at release point 1 during ebb tide.

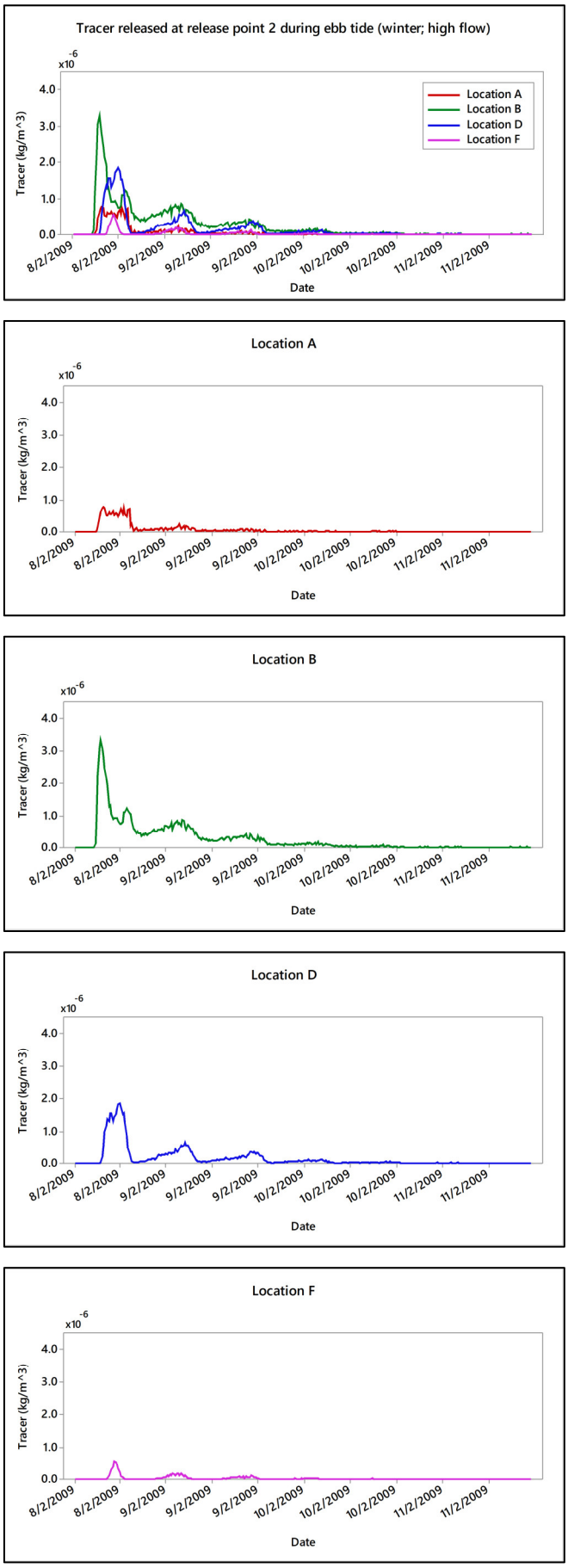


**Figure 6-17:** Modelled tracer concentration between 8-11 February (winter; high flow) from release point 2. Tracer introduced at release point 2 during ebb tide.

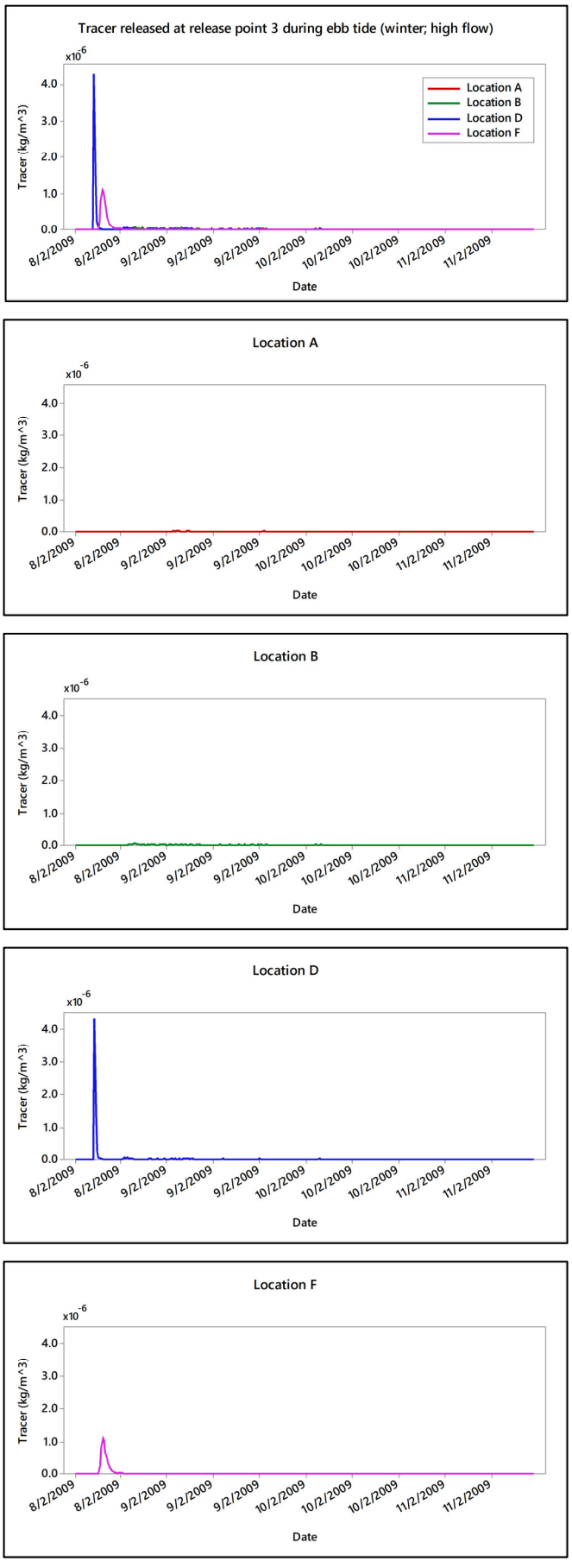


**Figure 6-18:** Modelled tracer concentration between 8-11 February (winter; high flow) from release point 3. Tracer introduced at release point 3 during ebb tide.

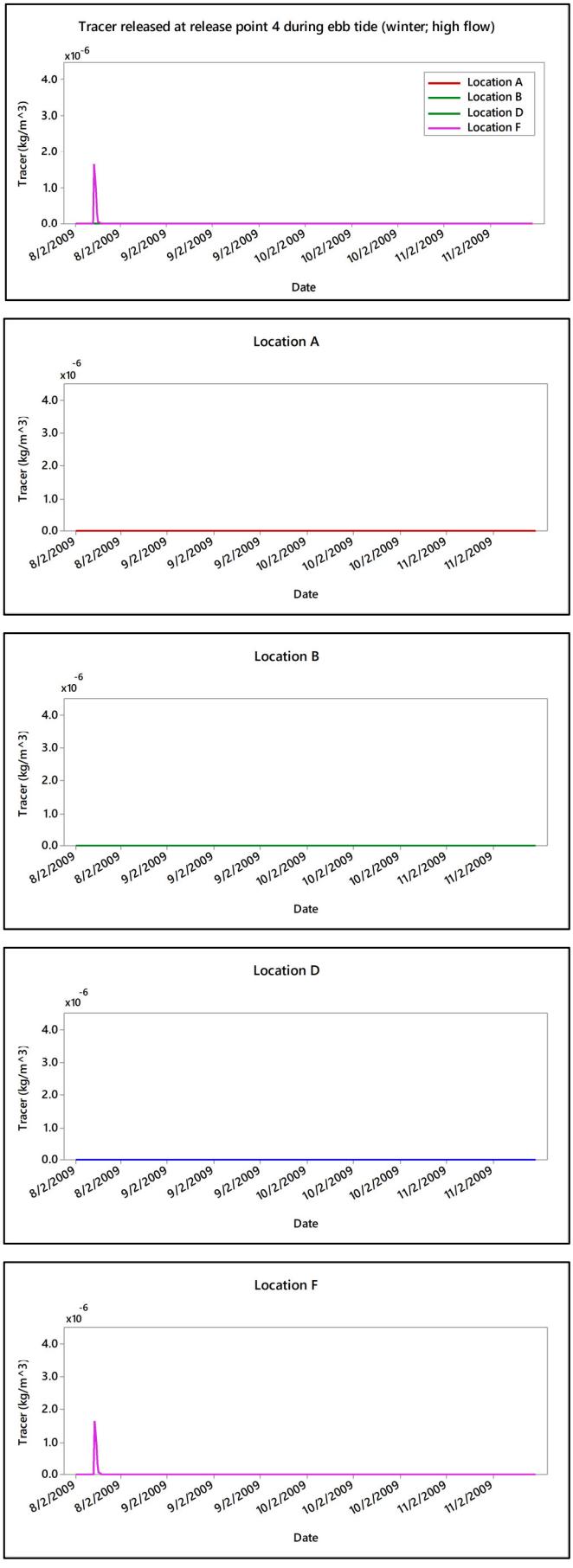


**Figure 6-19:** Modelled tracer concentration between 8-11 February (winter; high flow) from release point 4. Tracer introduced at release point 4 during ebb tide.

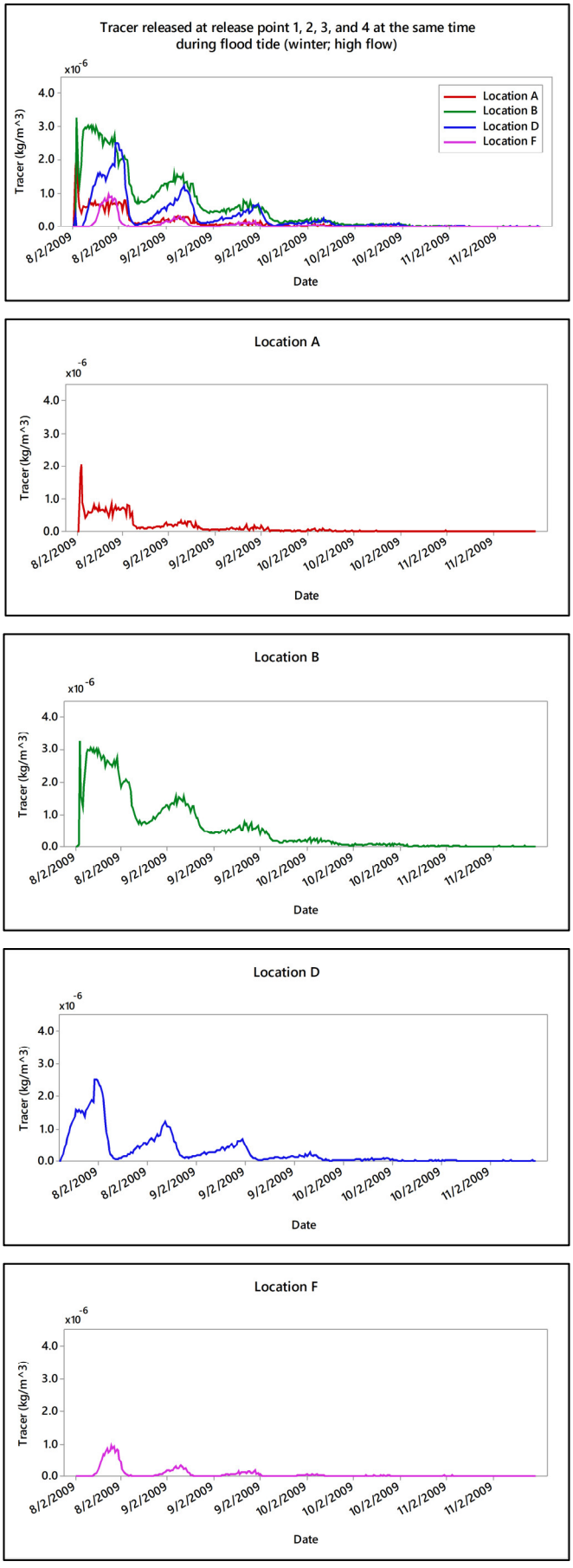


**Figure 6-20:** Modelled tracer concentrations between 8-12 February 2009 (winter; high flow) from all 4 release points. Tracer introduced from all 4 release points during flood tide.

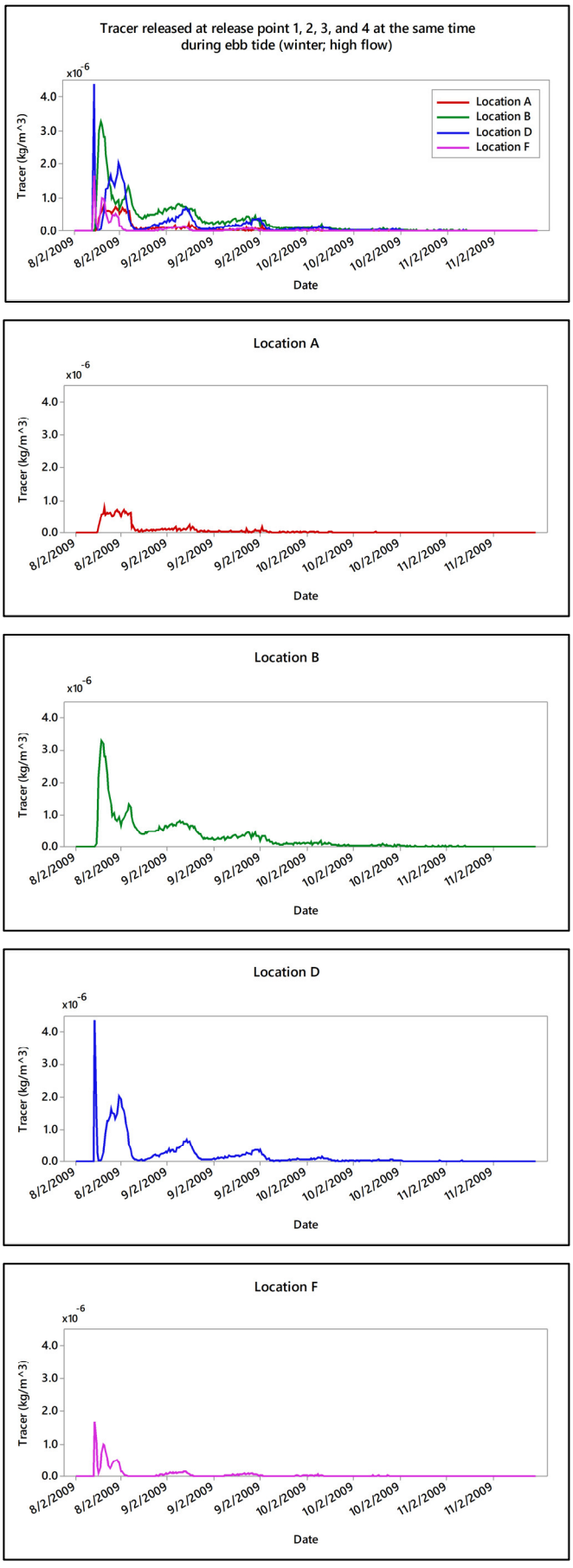


**Figure 6-21:** Modelled tracer concentrations between 8-12 February 2009 (winter; high flow) from all 4 release points. Tracer introduced from all 4 release points during ebb tide.

#### 6.2.2.3 Tracer pathway results:

The tracer pathways are entirely consistent with the tracer concentration simulations at all locations. Some snap shots of tracer pathways were extracted to help understand the tracer movement in the estuary. Note that the excerpts presented here are from high flow event simulations only. All simulations including low flow events are available in video format attached to this thesis. During winter high flow, 2009, most of the tracer released from release point 1 during the flood tide moved slowly and congregated in the upper region. As a result of the flood tide, only a small amount of the tracer moved further down to the central region. During slack tide, small amounts of the tracer could be detected in the lower region but not in the mouth region. Although the tracer was found in the central and lower regions during this period, tracer concentrations in those regions are low. As for the ebb tide, the tracer could be transported down to the estuary mouth, although concentrations were lower than during the flood tide or slack water, as a result of dispersion (Figure 6-22). In addition, the tracer pathway during autumn high flow 2009 is comparable to that in winter. During the low flow event, the tracer pathway simulation starting from the release point 1 during flood tide shows the same patterns as the high flow event, although the tracer concentration is lower.

The tracer pathways from release point 1 during flood and ebb tide are equivalent, but the pathways from release points 2, 3, and 4 are in the opposite direction up the estuary. From release point 2, the tracer moves in a northerly direction and congregates in high concentrations in the upper region of the estuary during the flood tide. The tracer then moves downstream in a southerly direction during the ebb tide, which results in high tracer concentrations at location B during the first tidal cycle (Figure 6-23). Likewise, the tracer from release point 3 moves north during the flood tide simulation and south during the ebb tide. The tracer released from this point generally moves towards the area of extensive algal growth in the central region during the flood tide (Figure 6-24). Tracer from release point 4 also moves north during flood tide and south during the ebb tide, eventually accumulating at the mouth especially towards the left side of the river where algal blooms occur (Figure 6-25).

The tracer pathways show that the tidal cycle and location of the release point play important roles in determining these pathways, but the planform shape and bed profile of the estuary also affect nutrient movement and concentration. An extensive mudflat in the central region of the estuary, which is far from and is at higher elevation than the main channel, has low nutrient concentrations particularly when the nutrients are released during ebb tides. However, when nutrients are released from Tarty Burn (release point 3) and Forveran Burn (release point 4) during high tide, this area has high nutrient concentrations as it lies on a main transport path. The high elevation of the mudflats causes flow velocity dissipation resulting in slow dispersion of the tracer and, consequently, longer nutrient retention in this area. The shape of the edge of the mudflats and a small island in the centre of the mudflats also help to define nutrient pathways and cause slow nutrient movement into the main channel. Additionally, this area is located close to the bottle neck in the upper region (location B) which always exhibits high nutrient concentrations, and so these mudflats receive some nutrients released from release point at Burn of Forvie as a result of water from the main channel moving across the mudflats.

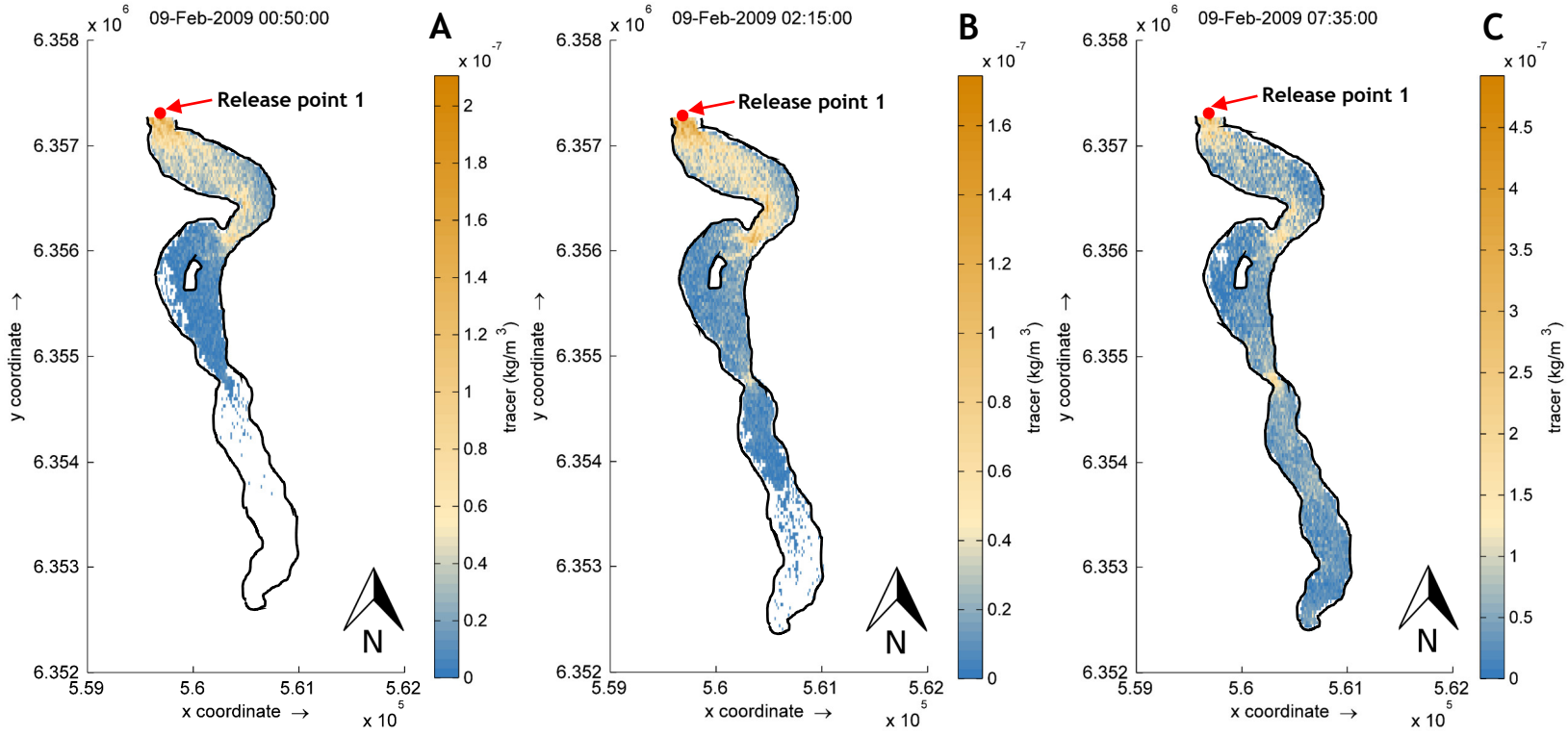


**Figure 6-22:** Modelled tracer pathway, tracer introduced from release point 1 during flood tide (a), slack tide (b), and ebb tide (c) in winter 2009 (tracer moves in south direction).

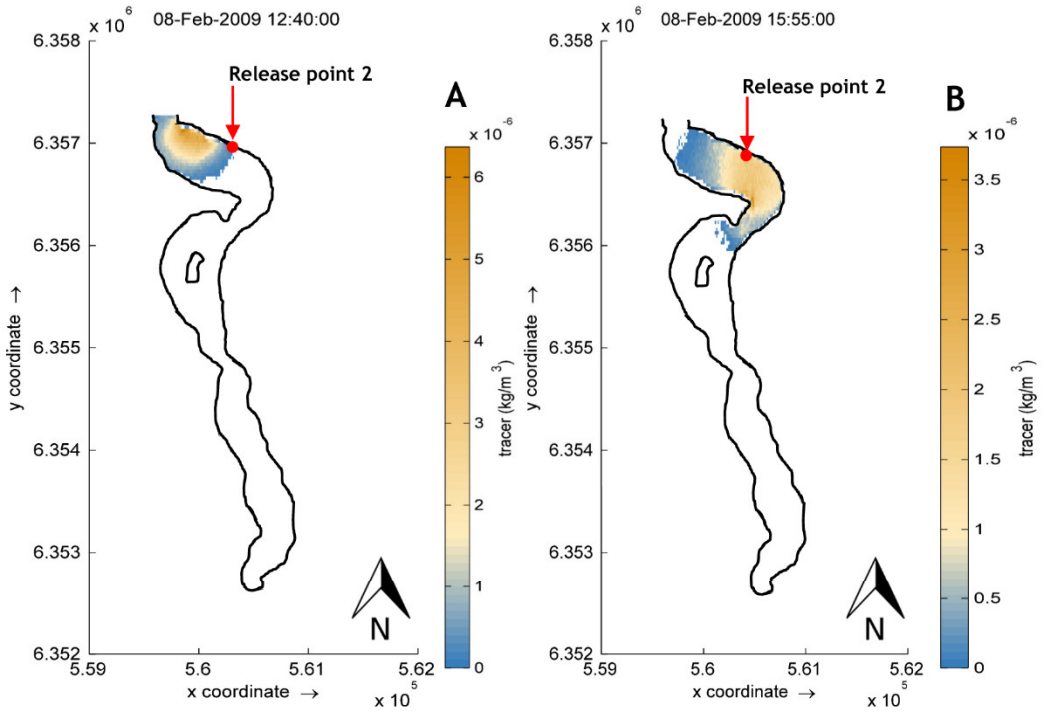


**Figure 6-23:** Modelled tracer pathway, tracer introduced from release point 2 simulated during flood tide (tracer moves in north direction) (A) and ebb tide (tracer moves in south direction) (B).

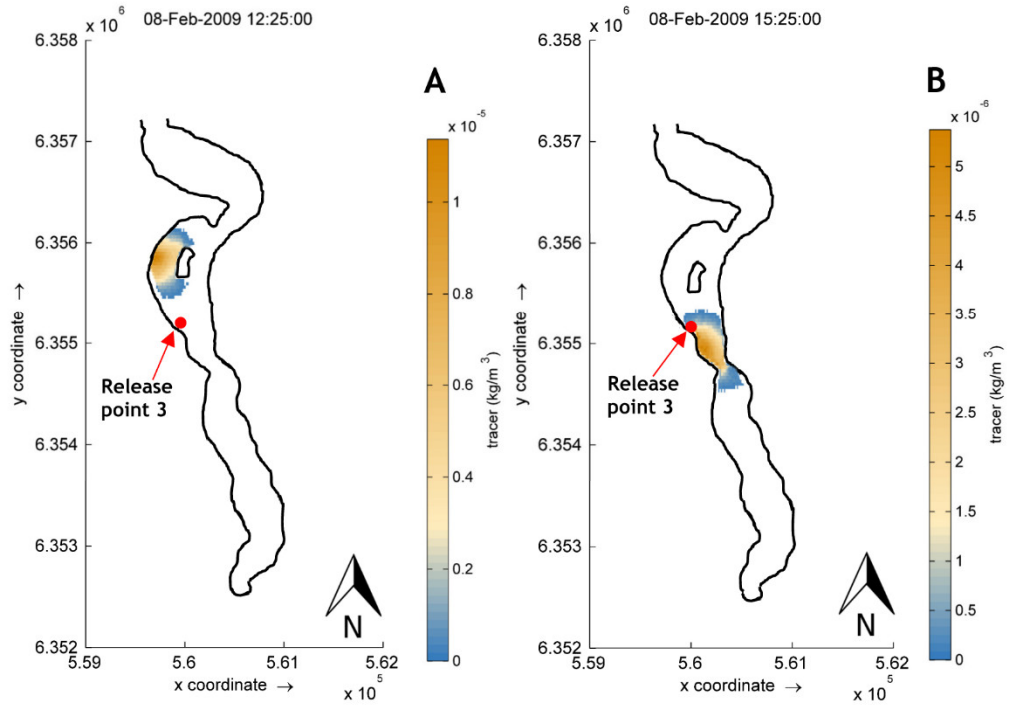


**Figure 6-24:** Modelled tracer pathway, tracer introduced from release point 3 simulated during flood tide (tracer moves in north direction) (A) and ebb tide (tracer moves in south direction) (B).

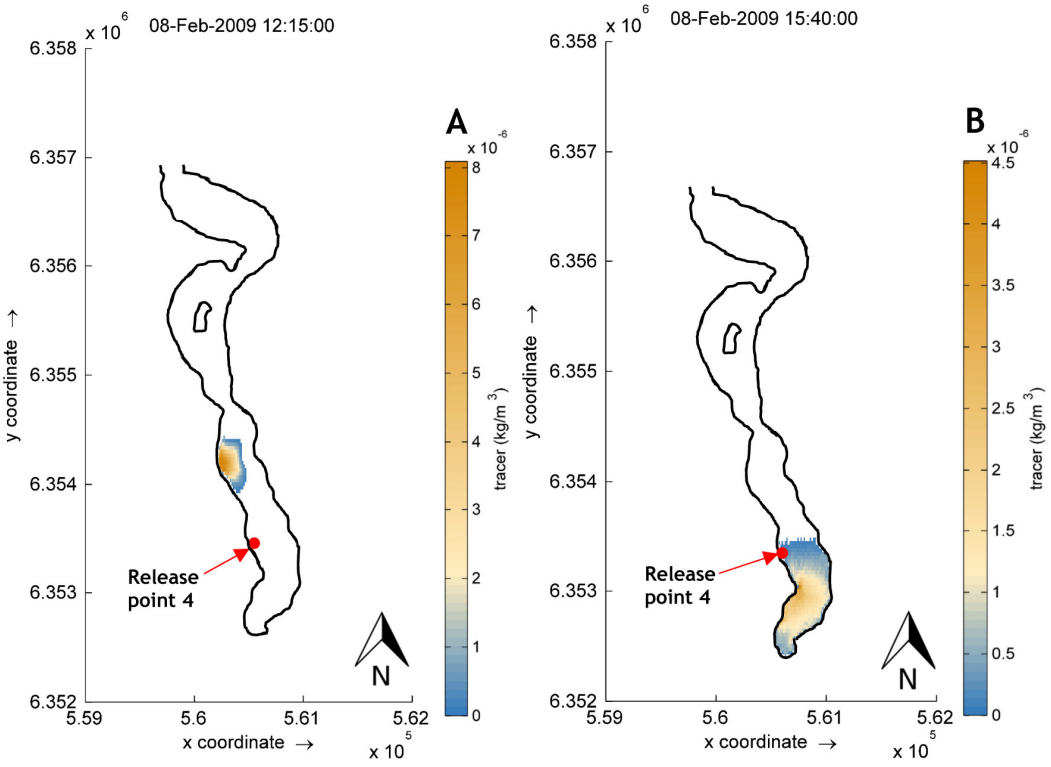


**Figure 6-25:** Modelled tracer pathway, tracer introduced from release point 4 during flood tide (tracer moves in north direction) (A) and ebb tide (tracer moves in south direction) (B).

## 6.3 Summary

Modelling nutrient concentrations and pathways in the Ythan during high and low flow events provides increased understanding of hydrodynamic influences on nutrient transport in the estuary. The overall velocity in the estuary is low. The velocities in the extensive mudflats in the central region of the estuary are not greater than 0.08 m/s during neap tide and 0.32 m/s during spring tide. The velocities in the same tidal conditions in the lower region are up to 0.65 m/s and 0.97 m/s in the main channel, the highest velocities being found close to mouth of the estuary. The tidal cycle and tidal range play more important roles in changing velocity in this estuary. Flood tide conditions provide the fastest water movement and Spring tides provides higher velocities than neap tides. As expected, the movement of water in the estuary is least during neap tide slack water and is greatest on spring flood tide. The river discharge has less impact on velocity than the tidal cycle, but when high river flow coincides with the ebb of spring tides the velocity is increased. Furthermore, the river discharge influences

the water depth in the main channel during low tide. Moreover, the river discharge does control the nutrient concentration in parts of the estuary. High river flow produces high nutrient concentrations compared to low flow events, and high nutrient concentrations are usually found during low tide. Not only does the tide influence velocity and hence water movement in the estuary, it also controls the direction of transport of nutrients released from the headwaters and tributaries. Nutrients are usually flooded into the upper region and then dispersed further down to the central region during slack water and eventually transported to the lower region during the ebb. This pattern of movement results in high nutrient concentrations at mudflats in the upper and central regions, mudflats near the estuary mouth, and mudflats along the estuary which are prone to algal growth.

The mudflats in the upper region of the estuary are always supplied by nutrients released from the headwaters and the Burn of Forvie tributary during flood and ebb tides. However, this tributary has greater impact since its channel flows through the mudflats. The mudflats near the estuary mouth directly receive high nutrient concentrations released from the Foveran Burn and small amount of nutrients from other tributaries during low tide. As a result, accumulation of nutrients near to the mouth is high. Unlike the mudflat in the upper region and the mudflats near the estuary mouth, the extensive mudflat at the Sleek of Tarty, where extensive algal development occurs, receives nutrients released from a tributary at the Tarty Burn during flood tide. Whilst, during the ebb, this area receives only a small amount of nutrients released from a tributary at the Burn of Fovie and the headwaters.

# Chapter 7: Discussion

This chapter is a combined discussion of results from Chapters 3-6, and is focused on model performance, the potential of using remote sensing data to support model validation, the influence of hydrodynamic characteristics on water quality, and the influence of the combination of hydrodynamics, nutrient concentrations and pathways on algal growth in the Ythan estuary. The discussion assesses the implications of the research findings and evaluates the strengths and weaknesses of the research strategy.

## 7.1 Using Delft3D model for modelling hydrodynamics, nutrient concentrations and pathways

### 7.1.1 Model performance

(a) *Hydrodynamics:* As this study contains the first use of Delft3D, or any other hydrodynamic model, in the Ythan estuary, there are no other model results available for cross-comparison and evaluation of model performance. Thus, validation of the model performance in the present study was mainly based on matching areas between the ratio images (NDWI) as a proxy for the flooded-dry areas produced from the model. This is a potentially valuable validation technique as it uses readily available data, but one that requires further testing.

Results from this study gave a match between modelled flooded - dry areas with the WV-2 ratio image of 78%, and with a Landsat-8 ratio image of 69%. The agreement in terms of the water surface boundary and hence elevation suggests satisfactory predictions of velocity by the model, as water surface elevation drives the energy slope, which in turn controls velocities. However, there are no field velocity measurements to confirm this inference, and although the model is considered to exhibit satisfactory performance in terms of hydrodynamics, further validation is required.

Comparing the modelled water depth with measured data, the model reproduces water depth with mean residuals of 0.15 m - 0.17 m. Although the residuals are not low, as a percentage of depth in this estuary, they are

considered reasonable. The agreement between the two datasets is found in areas of shallow (< 2.5 m) water near the river bank. As for the main channel, the model performance in reproducing depths is less satisfactory. One possible explanation for this mis-match in the main channel is wind speed of 13 km/h (gentle breeze) during the boat survey. This wind speed according to the Beaufort scale (Beer, 1983) could generate large wavelets which could be high from 0.5 m to 1.0 m, and surface waves were observed during the survey.

An additional explanation for the mis-match is vertical turbulence caused by rough longitudinal bedforms in the main channel (Mashayek et al., 2017). The effect of vertical turbulence on currents and waves was also found by Luijendijk (2001) in the western Wadden Sea, The Netherlands. Luijendijk (2001) found large residuals between the currents produced by the Delft3D model without specifying wind and wave parameters, and the measurements, particularly over gully bed topography in a basin with a rough bed and has water depth, ranging from 1 m - 25 m during flood tide (Luijendijk, 2001). The basin also experiences strong winds even though there is a large sand bar at the entrance (Luijendijk, 2001). Winds in this basin seems to work with high tidal energy and rough bottom bed resulting in vertical turbulences causing the large residuals of the modelled and the measured currents.

The Ythan estuary also has an incised main channel, similar to the gully bed topography of Luijendijk (2001), particularly in the longitudinal profile of the main channel and has tidal energy and wind influences although these are likely to be dissipated to some extent by the Sands of Forvie at the estuary. Hence, significant vertical turbulence that affects water depths, in a similar way to the Marsdiep basin, is considered possible in this situation. This further suggests that wind and wave parameters should be included in the model, particularly when there is rough bottom topography, high tidal energy (tide-dominated estuary), and wind effects. Adding wind and waves parameters in the Ythan estuary model domain could improve residual between modelled water level and measured water level in the main channel. However, this was not possible here as the measured water depths collected during the boat survey are not independent from the bed

elevation determination. Consequently, further independent field measurements for water depths would be required to assess the possible effects from winds and waves and to adjust model parameters accordingly.

(b) *Nutrient concentrations and transport:* This study uses the association between modelled nutrient concentrations and NDVI as indirect validation tool. The NDVI, which reflects the density of biomass, is used here as a proxy for the amount of nutrient concentrations. Since the modelled nutrient concentrations show positive association with median NDVI, this proxy is considered to be applicable to the Ythan. The modelled nutrient pathways provide understanding of nutrient movement and their reliability was inferred from the credibility of modelled nutrient concentrations when compared with known values.

Additionally, the modelled pathways show spatial association with NDVI maps. Correlations between modelled nutrient concentrations and NDVI showed that the model reproduces nutrient concentrations with a significance level of 0.01. However, although the relationships are significant, the $R^2$ values are relatively low (-13% to 39% in early autumn 2009 and 10% to 15% in late spring 2015). One possible explanation for this is that the nutrient concentrations were modelled using a single nutrient release point in the main river channel at the upstream open boundary. Modelling nutrient concentration using simultaneous nutrient releases from other tributaries could improve the relationship between the two parameters. In addition, modelling the release of nutrients from the other tributaries at different times in the tidal cycle could provide more comprehension of how nutrients mobilise during different conditions. To constrain this additional modelling, further information is required on the nutrient loadings in the different tributaries. In the absence of concentration data, such additional modelling is beyond the scope of this project but could form the basis for future work.

(c) *Bathymetry:* In addition to validation and calibration of the model, the quality of model inputs such as bathymetry and open boundary inputs have significant influences on model performance (Bates and De Roo, 2000, Legleiter et al., 2011). Accurate bathymetric data is a primary control on

the quality of model predictions (Bates and De Roo, 2000, Legleiter et al., 2011). Small errors (c. 0.1m) in the bed elevations in critical locations could affect model predictions. In particular the depth average velocity, bed shear stress and water depths can be affected by the input bathymetry (Breemen, 2008). For this study, according to cross validation the bathymetric data derived from interpolated bottom elevation are considered acceptable although the need for new bathymetric data in the upper part of the estuary where the channel is deep would be valuable and improve obvious mis-matches in the model output. In addition, further field validation of the bathymetric data for the whole estuary would improve confidence in model results.

### 7.1.2 Sensitivity testing

The default bottom roughness (C) of 65 $m^{0.5}/s$ recommended by Deltares (2014) has been successfully applied in several studies, for instance, Breemen (2008) imposed C ranges from 50 $m^{0.5}/s$ - 80 $m^{0.5}/s$ in Selangor estuary, Malaysia and Luijendijk (2001) prescribed a C value of 65 $m^{0.5}/s$ at the Marsdiep basin, the Netherlands. Varying the C value for the Ythan led to greater sensitivity in the results for water level, depth averaged velocity and bed shear stress than did varying viscosity and diffusivity coefficients with reasonable ranges. In addition, increasing C leads to increases in both flow velocity and water level in the estuary. In contrast, using the lower C value of 30 $m^{0.5}/s$ produced the most promising values and spatial patterns of water depth, depth averaged velocity, and bed shear stress in the Ythan model domain.

Considering the physical characteristics of the estuaries where high C values have successfully been used, those estuaries are largely composed of shallow mudflats and a main channel similar to the Ythan. However, those estuaries all have deeper main estuary channels than the Ythan, where the rough and locally steep main channel reaches the maximum depth of 4.85 m and is 1.08 m at its shallowest. For instance, the Selangor estuary, Malaysia has an average main channel depth of 10 m and has a relatively smooth and flat bed (Breemen, 2008) and at the ferry transect of the Marsdiep basin (4 km in width) the maximum depth is 27 m (Buijsman, 2007, Leote et al., 2016). These studies suggest that using C values from 50 - 80 $m^{0.5}/s$ is suitable for situations with a deep (>10m) channel, compared

with the Ythan where a shallow and rough main channel leads to mismatches between modelled and measured water depths unless C is reduced significantly. Although reducing the C roughness value appears to contradict the expectation that an increase in bottom roughness will cause energy dissipation resulting in decreased flow velocity (Breemen, 2008), imposing lower C value in the Ythan could reduce the effect of vertical turbulence discussed above. However, in addition to varying roughness, consideration of wind-wave effects is required to reduced persistent mis-matches between modelled results and measurements.

Plum Island Sound, Massachusetts, USA, has physical characteristics more similar to those of the Ythan and it's hydrodynamics have been successfully modelled (Fagherazzi et al. (2014) using C values of 45 $m^{0.5}/s$, 40 $m^{0.5}/s$, and 35 $m^{0.5}/s$ for the main channel, tidal creeks and salt marshes, respectively. Plum Island Sound is a shallow tidal dominated estuary (mean depth 3 m), which contains a vast network of tidal creeks, large and small, which meander through approximately 3,500 hectares of salt marsh (Fagherazzi et al., 2014). Its average discharge (11 $m^3/s$) is small relative to the magnitude of its tidal prism ($3.0 \times 10^7$ $m^3$) (Fagherazzi et al., 2014, Vallino and Hopkinson, 1998). With a large tidal range (3.2 m) and low river discharge, Plum Island Sound is considered to be a well-mixed estuary, although some parts are partially mixed (Vallino and Hopkinson, 1998).

The success of varying C across the model domain according to the bed type suggests that variation of geometry of estuary channels, bed roughness, vegetation, and sedimentation and erosion requires using different C values (Fagherazzi et al., 2014). Even though using a uniform C value of 30 $m^{0.5}/s$ in the Ythan adequately reproduced of water depths and depth averaged velocities in this estuary, variation of C values according to bed characteristics (eg lower C on mudflats which are shallower and smoother than the main channel) is suggested as an approach for further research. In addition, varying C spatially could be coupled with field measurements to validate such additional complexity in the model, and this could reveal more spatial differentiation of flow velocity, and so improve model results.

Regarding horizontal eddy viscosity (HEV), this study found that this parameter appears to have no significant effect on modelled flow velocity and water level, except for areas close to the sea boundary, which is in contrast to Williams et al.

(2013) who state that it has strong influence on modelled cross-channel velocity. The model grids in this study, ranging in size from minimum of 1.2 m x 0.6 m to maximum of 7.0 m x 3.5 m, are larger than those created by Williams et al. (2013) who built a modelled grid with a 2 m resolution for a much steeper and topographically complex reach, and this size difference is likely to result in the contradiction in terms of HEV. As stated in Breemen (2008), the value of HEV in the computations is a function of grid size, so the value of HEV to use increases with grid size. Breemen (2008) also notes that HEV tends to have greater effects in small model domains, in which the effects of eddies are more significant. The insignificant effect from varying HEV from 1-10 $m^2/s$ in this model suggests agreement with Breemen (2008) in that detailed models with grid sizes lower than several tens of metres should have HEV ranging from 1 to 10 $m^2/s$ and for a large tidal model domains (grid sizes of hundreds of metres or more), HEV values should range from 10 to 100 $m^2/s$. Considering the sea boundary, the evidence from this study suggests that its position affects the numerical results, which corresponds to Williams et al. (2013) who state that the location of open boundaries should be sufficiently far away from target model domain to reduce error in velocity distribution.

For eddy diffusivity, a range of values from 0.1 $m^2/s$ to 1 $m^2/s$ have been widely used. For example, Van Dongeren (2009) used eddy diffusivity of 0.1 $m^2/s$ for a fine 2D model domain (grid size ranges from 0.15 – 18 m) in San Diego Bay, USA (average depth 7 m, maximum depth 18 m, and relatively flat and smooth bottom bed), whilst Breemen (2008) used eddy diffusivity of 1 $m^2/s$ for a 3D model domain (grid size ranges from 20 - 50 m) in the Selangor Estuary, Malaysia to reduce underestimation of stratification. However, the range of values is inappropriate for the Ythan model domain. On the contrary, the value of 200 $m^2/s$, which is much higher than the small values used in the other studies, produces the best model results. This value was calculated based on an equation developed for estuarine study by MacCready (1999). Considering the depth and roughness of the San Diego Bay and the Selangor Estuary compared with the Ythan, it seems the channel depth is a significant control over the appropriate eddy diffusivity values for hydrodynamic modelling. Similar to both C and eddy viscosity, eddy diffusivity is difficult to measure directly, and the appropriate value can vary with the

characteristics of the model domain. However, this value can be refined if further field measurements of nutrient pathways and concentrations are carried out.

## 7.2 Using remote sensing in model validation

Remote sensing data have been successfully used to aid model validation and to help define model input values in this study. The remotely-sensed data help to reduce the cost and time of field data measurements, and provide useful information of algal growth behaviour. However, there are some limitations to the data that need to be considered. This section discusses both the advantages and disadvantages of using remote sensing methods, as well as giving ideas to improve the quality of the results.

The study used field-based algal mat maps and biomass to assess algal mats inferred from NDVI. There is relatively poor agreement between algal mat locations inferred from NDVI and algal mat maps created by SEPA. The extent of most of the algal mats from NDVI, particularly in 2011, are overestimates of the boundaries of the mats measured in the field. Only 13% correspondence is found between the algal mat maps from the two sources. In 2009, the overestimate of algal mats is less than in 2011. This poor correspondence may be due to differences in how algal mats are identified. For example, field identification of algae uses colour and recognition of what they look like (Gray pers comm, 2018) whereas NDVI is quantified from reflectance, which depends on density and stage of the algal growth.

Previous studies suggest that biomass increases linearly over NDVI ranges between 0.0 and 0.5, as seen by Barillé et al. (2010) [$R^2$ = 0.98, p < 0.001], Méléder et al. (2003) [$R^2$ = 0.97, p<0.001], and Kwon et al. (2016) [$R^2$ = 0.34, p<0.001]. In this study, biomass is positively related with NDVI only in 2011 [$R^2$ = 0.46, p<0.05]. On the contrary, it exhibits unusual the negative relationship with NDVI in 2009 [$R^2$ = 0.23, p<0.05]. Although, both of these observed relationships are weak the residuals are independent, and the p-value of the models are less than the common alpha level of 0.05, which means the association between the median NDVI and the term is statistically significant although the explanatory power is limited (low $R^2$ values).

The negative relationship in 2009 is possibly due to the timing of SEPA field surveys being different from CASI image acquisitions. The acquisition date of CASI in autumn 2009 (11/09/2009) was one month after SEPA field surveys (10 - 13/08/2009) and this time of year could be a period of declining growth rate of algae in some parts of the estuary (Lavens and Sorgeloos, 1996), as light and chemical factors in the Ythan estuary begin to limit growth at this time of year (Raffaelli (1999); Taylor (1999). These effects may result in a negative relationship between NDVI and field biomass. In contrast, the CASI acquisition date in 2011 was during summer (14/07/2011) and before SEPA field surveys (16 -18/08/2009), so both took place during the growth period of algae in the estuary (Raffaelli, 1999, Taylor, 1999). During this period, cell density of algae increases as a function of time (Lavens and Sorgeloos, 1996). For example, growth rate of *Ulva,* which is one of the three main macro algae species in the Ythan, is up to 35% of their length per day during preferential water conditions (Pedersen and Borum, 1996). This supports the positive relationship between NDVI and biomass in the 2011 peak growth period. As average wet weight for each algal patch used for biomass calculation in 2011 was greater than 200 $g/m^2$, the weak significant positive relationship could be due to saturation of algal biomass, which begins to occur above 100 mg Chl-a/$m^2$ according to Méléder et al. (2003). In addition, having more samples from across the range of algal densities in the estuary could help to define a stronger relationship.

Using secondary data, in this case biomass and algal mat maps for validating results derived from the NDVI, requires caution. Specifically, the timing of sample collection appears to be important and it should be close to the image acquisition date as possible. This is because algae can develop as long as water conditions are suitable, each of the algal patches may not have reached their peak extent and density at the same time. Besides, biomass can vary according to algal species, season, nutrient concentrations and location (Guillaumont et al., 1993, Kwon et al., 2016). Correspondence between the field algal samples and those from NDVI could possibly be higher when biomass is collected at low Chl-a concentration (Méléder et al., 2003) and the field data are collected as close to the date of remote sensing acquisition as possible.

NDWI was quantified from both WV-2 and Landsat-8 data, and the boundaries of the inundated areas can be seen clearly on the NDWI images and are close to the

inundated areas derived from visual interpretation. This corresponds closely with studies by Baiocchi et al. (2012), Belgiu et al. (2014), and Zhou et al. (2012) who also use high resolution images and NDWI to extract coastline and water body positions and their results shift from the actual coastline derived from visual interpretation less than 1 m. For hydrodynamic model validation, NDWI demonstrates satisfactory to good agreement with the flooded-dry areas derived from modelling. However, before using NDWI to validate model results, consideration needs to be given to grid cell size of the NDWI data and of the flooded-dry areas from modelling. The grid cell size of the two datasets must be close to equal if they are to be directly comparable.

To assess use of NDVI as a proxy for nutrient concentrations, median NDVI values show a positive relation with modelled nutrient concentrations. Although there is high variation of NDVI in very low nutrient concentration areas, the model results are from nutrient concentrations derived from a single release point at the upstream end of the model domain. As nutrient concentration patterns vary with distance from the nutrient release point, using NDVI to validate nutrient concentrations derived from the three other potential release points (tributaries) could improve this agreement further. As for modelled nutrient pathways, spatial links with locations of algae inferred from NDVI maps can be seen along the estuary. The overall assessment of using NDWI and NDVI maps are useful for studying algal growth and for validation of nutrient concentrations.

### 7.3 Influence of hydrodynamics on water quality

Interactions between seasonally changing river flows and tides play a key role in creating optimal water conditions for algae growth in the Ythan estuary. During low river flow particularly in summer, salinity, water temperature, pH, DO, and turbidity tend to increase as a result of tide domination. Salinity and water temperature are the factors that limit development of *Enteromorpha spp.*, *Chaetomorpha sp.*, and *Ulva Lactuca* (Hart et al., 2003, Jahnke and White, 2003, Parida and Das, 2005, Rybak, 2018), which are the main green macroalgal found in the Ythan estuary (Raffaelli, 1999). The optimum salinity for *Enteromorpha spp.* growth is 18-22 ppt and the lower and upper limits of their salinity tolerance are 0 ppt and 45 ppt (Martins and Marques, 2002, Sousa et al., 2007). As for, *Chaetomorpha sp.*, the optimum salinity is slightly higher than *Enteromorpha spp.*

(20–30 ppt) (Tsutsui et al., 2015). The water temperature range suitable for *Chaetomorpha sp.* is 21–29°C (Deng et al., 2012). However, extreme fluctuations of the salinity and water temperature does not limit the growth and survival of *Chaetomorpha sp.* particularly in stagnant waters (Sorce et al., 2018, Tsutsui et al., 2015). The salinity range for *Ulva Lactuca* growth is <0.5 to 49 ppt (Rybak, 2018), although the ability of this species to increase productivity under low salinities is higher than with high salinities (Rybak, 2018).

With reference to the salinity and temperature ranges for green macroalgal growth, increases in salinity (average max 36.01 ppt and average min 0.41 ppt) and water temperature (average max 20.97 °C and average min 9.92°C) resulting from low river flow, seems to generate the most suitable water conditions (Rao et al., 2007, Sousa et al., 2007, Xu and Lin, 2008) for the development of green macroalgal in the Ythan estuary. The influence of salinity variations, driven by interaction between river flow and tides, on green macroalgal growth can be seen from the locations of *Enteromorpha spp.*, *Chaetomorpha sp.*, and *Ulva Lactuca* in the estuary. For instance, *Enteromorpha spp.* were found in lower estuary where seawater influence is greatest, whilst *Chaetomorpha sp.* were mostly found in calm waters over the shallow mudflats far from the main channel across the estuary. *Ulva Lactuca* were found mostly in the upper estuary and close to tributaries where seawater has less influence, and which are close to nutrient inputs. This evidence suggests the significant role of hydrodynamics and mixing on water quality, which then influences species development in the estuary.

Although nutrient levels from river inputs are low during low flow periods (Raffaelli (1999), Raffaelli et al. (1999), Taylor (1999), total nutrients in the estuary can be elevated as result of sediment resuspension during high tide (Feuillet-Girard et al., 1997, Yin and Harrison, 2000). During this period, nutrients, particularly $NH_4^+$ and P in fine sediments (Lavery and McComb, 1991, Raffaelli, 1999, Raffaelli et al., 1999) at mudflats in upper and central regions of the estuary are released and diluted to the water column (Yin and Harrison, 2000), resulting in additional nutrient availability in the water column to meet the algae growth requirement.

Considering turbidity in water column, it is likely that the Ythan, a tidal dominated estuary experiences high turbidity caused by sediment resuspension during flood – ebb tides, which blocks much of the light that would penetrate the water column.

However, low light penetration seems not to limit algal growth at the shallow mudflats across the estuary where water depths during slack water are not deeper than 1 m, as prolific algae growth can be seen in these areas both from the NDVI maps and algal maps from SEPA. On the contrary, there is no evidence of algal blooms in the main channel where the channel is deeper, flows are faster, and sediments are likely to be most mobile. This suggests light limitation and effect of flow velocity due to bottom elevations on algal growth. The evidence is consistent with chlorophyll density of *Chaetomorpha sp.* exposed to light (10.7 g $Chl.m^{-3}$) and the chlorophyll density of submerged *Chaetomorpha sp.* (2.1 - 2.8 g $Chl.m^{-3}$) studied by Krause-Jensen et al. (1996). With adequate nutrient availability, increase in salinity and water temperature, high bed elevation of intertidal mudflats, coinciding with long-light hours in summer months (Al-Qasmi et al., 2012, Rao et al., 2007, Singh and Singh, 2015, Sousa et al., 2007, Xu and Lin, 2008), conditions in the Ythan seem to promote development of algae as seen from increased chlorophyll concentration according to the buoy data, NDVI maps, and algal maps from SEPA.

In contrast with periods of low river flow, high river flow particularly in autumn and winter causes decreased salinity and water temperature in the estuary. Coinciding with short daylight hours (8-9 hours) in winter (https:// www.scotlandinfo.eu), conditions from December to February hinder algal production in the Ythan estuary. The evidence of low chlorophyll levels during high flow can also be seen in the Mondego estuary, Western Portugal. The estuary is shallow with mean tidal range of 3 m and water circulation is mostly dependent on tide and on fresh water input (Duarte et al., 2002, Martins et al., 2001) similar to the Ythan. *Enteromorpha spp.* mostly reduce in winter when river flow increases but enhance in early spring when river flow decreases (Martins et al., 2001).

However, periods of elevated chlorophyll concentration can occur in winter although the values are not as high as in summer. According to the chlorophyll concentration data from 2009-2013, the concentration during late winter in 2009 was the highest level (53 µg/L). In the same period, the river flow in the Ythan ranged only from 5-8 $m^3/s$. With supplement of longer light hours (10-11 hours) in late winter (https:// www.scotlandinfo.eu), calm weather (daily rainfall less than 10 mm according to www.metoffice.gov.uk), and low pressure on grazers during

the winter months (Buskey et al., 1997) as well as low flow velocities (approximately 0.55 m/s during the ebb according to the modelling results), water conditions over the mudflats during that time seem to have promoted high chlorophyll levels. However, when the river flow is higher than 10 $m^3/s$, the chlorophyll concentration decreased, suggesting that river flow controls chlorophyll availability during this light limited period.

These results indicate that preferential water conditions for algal growth in this estuary are controlled by river flow and tides. The river flow brings the nutrients into the estuary, so it is partly due to the amount of nutrient input and partly due to how the river flow affects the hydrodynamics of water within the estuary. This finding is in agreement with studies by Duarte et al. (2002) and Martins et al. (2001), in which hydrodynamics of fresh water and tide as well as bottom bed elevation control water quality particularly salinity, nutrients which affects algal abundances in the Mondego estuary, Western Portugal.

### 7.4 Influence of hydrodynamics on chlorophyll transport

In addition to influencing overall water conditions, the hydrodynamics in the Ythan estuary cause transport of chlorophyll and hence changes in its concentration. The river flow combined with tide conditions produce two distinct chlorophyll concentration patterns during tidal cycles which are: (1) increased chlorophyll during low tide, and decreased chlorophyll occurs during high tide; and, (2) decreased chlorophyll occurs during low tide, and increased chlorophyll occurs during high tide. As discussed earlier, shallow mudflats are likely to have less light limitation and lower effects due to velocity than the main channel, particularly during low flow. These mudflat areas, particular at Sleek of Tarty and Tarty Burn, can support algal growth even through autumn and winter. However, the amount of chlorophyll in these areas could vary according to the amount of river flow. Thus, the first pattern, which occurs during high flow possibly results from algal on these extensive mudflats providing chlorophyll that is transported back to the main channel so causing high chlorophyll concentrations during the ebb (Duarte and Vieira, 2009). In addition, tearing and erosion of macroalgae fixed to sediments as a result of increased velocity during high flow could further elevate chlorophyll concentrations in the main channel during the ebb (Vignaga et al., 2013). As for decreased chlorophyll during high tide, this could be due to export of chlorophyll to the ocean under conditions of increased flow velocity during the

ebb when river flow is high. Only a small amount of chlorophyll is then transported back up into the estuary to the measuring buoy location on the next flood tide. This is consistent with studies from Duarte et al. (2002) and Martins et al. (2001), in that increased flow velocity has ability to transport algal especially *Chaetomorpha sp.* and *Ulva sp.* to the ocean, and flood tides bring those algae and nutrients back into the estuary.

The second pattern of chlorophyll concentrations is found during decreased river flow in summer and could be caused by transport of chlorophyll from the areas of high algal density in the lower region to the central region. The high algal density in the lower region could come from aggregation of algae transported from upper and central regions during the previous tides and new algal growth during low tide on mudflats in this region. The chlorophyll concentration pattern found during low flow periods corresponds well with a higher algal extent, particularly in the lower estuary, as quantified from NDVI maps. Consumption by invertebrates in mudflats and sediment absorption during high water could both result in reduction of chlorophyll concentration during ebb conditions (Yin and Harrison, 2000). However, it is also possible that some chlorophyll is advected to high elevation areas in the central and upper regions during high tide and this is not transported back to the lower region due to the low energy of low river flow and the ebb tide (Duarte and Vieira, 2009, Martins et al., 2001). Together, these factors lead to decreased chlorophyll concentrations. The chlorophyll concentration pattern during summer rainfall and increased river flow may be due to increased water level causing transport of algae stranded on high elevation areas during previous high water back to the lower estuary. This could cause high chlorophyll concentrations during ebb tide. Chlorophyll moved from the upper and central to the lower estuary during the ebb may be transported out of the sea due to increased velocity in the main channel (Martins et al., 2001), leading to low chlorophyll concentration during the next high tide.

### 7.5 Influence of hydrodynamics on nutrient concentrations and pathways

Overall, the estuary is particularly influenced by low energy hydrodynamics. Shallow areas at Sleek of Tarty, Tarty Burn, and Foveran Burn where algae usually develop appear to experience the lowest water velocities over the whole tidal cycle regardless of river flow levels. In the main channel where water is deeper, in particular at local narrows and close to the estuary mouth, there is greater

turbulence due to increased flow velocity. Spring and neap tides control flow velocity, which usually are increased during spring tides and decreased during neap tides. Consequently during summer months, when river flow is usually low, neap tides produce the calmest conditions with long periods of stagnant water (Zhang et al., 2015). This is especially the case in the shallow areas such as Sleek of Tarty and around the tributary mouth bars at Tarty Burn and Foveran Burn.

Considering nutrient concentration, it is clearly seen that river flow level influences nutrient concentrations. In addition, nutrients released from each tributary at different parts of the tidal cycle (flood tide and ebb tide) are a key factor in elevating nutrient concentrations in areas close to the release point. Hence, nutrient concentration varies with distance from the release point while the direction of nutrient movement is controlled by the tidal cycle. The extensive mudflats in the Sleek of Tarty appear to be a main pathway for nutrients released from the tributaries at Tarty Burn and Foveran Burn during high tide. The upper part of the mudflats close to a bottle neck is a pathway for nutrients, either introduced from the River Ythan head water or the Burn of Forvie, during flood and ebb tides. Coinciding with low flow velocities in this area as previously discussed, it is likely that nutrients from the release points and from sediments accumulate in these low water velocity areas. The mudflats at Foveran Burn are also a main pathway for nutrients released from all tributaries and the main river during low tide. This implies that during summer months, especially during neap tides, nutrients released from those release points and from sediments in the mudflats may not be transported out to sea (Martins et al., 2001). As a result, these nutrients accumulate close to the estuary mouth until the subsequent flood tide. On the contrary, during winter months these nutrients are easily transported out to the ocean, especially during spring tides, by the power of the river flow coupled with the tide (Martins et al., 2001).

Releasing nutrients from all tributaries at the same time elevates modelled nutrient concentrations and, as such, introduces new pathways across the estuary. These suggest that as well as the River Ythan, the other tributaries should be taken into account. Nutrients remain available for a few days: in this case 3-4 days when released during flood tide and 1-3 days during low tide, before they disappear from the estuary. Hence, uncontrolled release of nutrients from the release points will aggravate nutrient enrichment in the estuary. Since the system receives

nutrients from sediments as well as from the water column, according to Raffaelli (1999), controlling the supply of nutrients entering the system, in particular from tributaries, could help to shorten nutrient residence time in the estuary. In addition to transporting nutrients in the water column through the estuary, hydrodynamics exert a key role in the exchange of nutrients from sediments to the water column (Yin and Harrison, 2000). Nutrients from sediments, particularly $NO_2$- and $NO_3$-, are created by nitrification after receiving $O_2$ on the flood tide and during high water (Fan et al., 2006, Feuillet-Girard et al., 1997). These $NO_2$- and $NO_3$- are then brought back to sediments during slack tide by phytoplankton and benthic organisms living in the sediments (Feuillet-Girard et al., 1997, Yin and Harrison, 2000).

Likewise, $NH_4$+ created by benthos in sediments during low tide in summer months due to high rates of decomposition (Feuillet-Girard et al., 1997, Koriyama et al., 2016) are nitrified during high water and returned to sediments during low water conditions by nutrient uptake processes of organisms living in the sediments (Yin and Harrison, 2000). As sediments act as both a source and a sink of nutrients (Feuillet-Girard et al., 1997, Yin and Harrison, 2000), nutrients seem to be recycled (Fan et al., 2006) resulting in no shortage of nutrients in the estuary. In terms of nutrient transport, since nutrients from sediments are in the water column during high water, it is possible that nutrients from sediments can either be mobilised to other areas or trapped, according to the hydrodynamic influences discussed previously.

## 7.6 Interaction of hydrodynamics, nutrient concentrations and pathways on algal growth

Nutrient concentrations and pathways driven by hydrodynamics demonstrate spatial association with locations of algal growth. Lower flow velocity areas that experience high nutrient concentrations driven by hydrodynamics, including Sleek of Tarty, Foveran Burn, Tarty Burn, and Burn of Forvie, exhibit widespread and high-density algal development. In addition, algae are present on mudflats along the main channel. Areas of deep water with high flow velocity in the main channel have no evidence of algal growth despite being a main nutrient pathway. Together, these findings suggest that flow velocity and light penetration in the water column are important factors influencing growth of algae in this estuary (Hötzel and Croome, 1994, Li et al., 2013, Maier et al., 2001, Martins et al., 2001, Sherman et

al., 1998, Zhang et al., 2015). Low inter-annual variation of NDVI and substrate types in the estuary imply consistent hydrodynamic patterns and so consistent nutrient concentration patterns in the estuary. The development of *Microphytobenthos* (MPB) is evidence of the influence of hydrodynamics on algal growth. MPB tend to develop on mudflats with low flow velocity, including at Sleek of Tarty, Tarty Burn, and Burn of Forvie. They are also found on mudflats close to the A975 road bridge and at Foveran Burn. However, densities of MPB in these mudflats are lower than in the previous three locations as a result of higher flow velocity (Underwood, 2010).

Apart from flow velocity directly influencing the growth of MPB (Zhang et al., 2015) sediment size, also driven by hydrodynamics, is an indicator of MPB (Underwood, 2010). Mudflats at Sleek of Tarty, Tarty Burn and Burn of Forvie where MPB is extensively developed are composed of medium coarse silts. In contrast, mudflats at Foveran Burn where MPB is less developed are composed of a mixture of medium coarse silt to fine sand size sediments. Although these are consistent with Underwood (2010) in that MPB biomass has a negative relationship with sediment grain size, sediment grain size seems less important than flow velocity. According to the substrate type map, at Foveran Burn MPB is not likely to develop on coarse silt sediments close to the main channel but they do develop on coarse silt sediments distant from the main channel where flow is slower. In addition, MBP is found at the bottle neck in the upper estuary only in low flow months, which further demonstrates the influence of flow velocity on the growth of MBP.

Since sediment at Forevan Burn is a mixture of coarse silt to fine sand, NDVI and hence macroalgae growth is expected to be low due to the presence of less organic matter (Underwood, 2010) and higher flow velocity compared to upper and central areas of the estuary. However, high NDVI or high macroalgal density is seen across this part of the estuary without regard to sediment type. This demonstrates that the source of nutrients in this area is not only from cohesive sediment but also from water column, these nutrients being mobilised from the upper and central regions of the estuary. In addition, flow velocities in this area is within tolerance levels for macroalgal growth, which is not higher than 1.22 m/s (Martins et al., 2001). As a result, algae are not torn and eroded, resulting in widespread and dense blooms in this area.

## 7.7 Factors control algal growth

Based on the previous discussion, some assessment of the controls over algal growth can be suggested. Flow velocity driven by interactions between river flow and tide conditions (Duarte et al., 2002, Duarte and Vieira, 2009, Martins et al., 2001) seems to play important role in controlling algal growth in this estuary. The presence of algae in low flow velocity areas demonstrates spatial association between these two parameters. This is consistent with the studies by Hötzel and Croome (1994), Li et al. (2013), Sherman et al. (1998), and Zhang et al. (2015) who found that flow velocity has relationships with stratification and algal biomass, and acknowledged low velocity as a key to control algal blooms.

Flow velocity in this estuary exhibits areas that are often lower than 0.06 m/s, which is considered the optimal flow velocity leading to an increase in algal growth (Zhang et al., 2015). For example, at Sleek of Tarty in summer months, modelled flow velocity is not higher than 0.057 m/s during spring tide and not higher than 0.042 m/s during neap tide. In the lower region of the main channel, summer low river flow leads to velocities of 0.086 m/s during spring tide and 0.070 m/s during neap tide. Although these flow velocities in the main channel are higher than over the mudflats, they remain significantly below the velocities required (1.22 m/s) to tear and erode algae (Lin and Hung, 2004, Martins et al., 2001, Traaen and Lindstrøm, 1983).

Poor flushing of nutrients due to low flow velocity is also believed to cause high abundance of algae in many estuaries (Duarte et al., 2002, Su et al., 2004, Boyle et al., 2004). However, the problem of poor flushing tends to occur in micro-tidal estuaries where the volumes of river flow and tidal flow are very low, rather than in meso- and macro-tidal estuaries where tidal range and volume are higher (Su et al., 2004).The Ythan estuary, however, is categorised as meso-tidal with tidal range between 3-4 m. This tidal characteristic seems not to prevent high phytoplankton production, and the relatively high tidal volume seems not to increase flow velocity throughout the estuary. Consequently, there is long persistence of nutrients in the estuary. This low tidal energy is due to the fact that mudflats (Maddock, 2008) and the location and orientation of John's Hole point at the estuary mouth dissipate tidal energy. Consequently, nutrients stay longer in the extensive shallow areas within the estuary. Although the main channel has higher flow velocities than the shallow areas, the evidence of macroalgae growth

close to the estuary mouth indicates long residence time of nutrients in this area. In addition, the persistence of high nutrient concentrations is particularly seen when nutrients are released during flood tide, which indicates the importance of low flow velocities in the estuary.

In the summer of 1996 there was a low coverage of algal mats in the estuary following widespread flooding within the catchment in October in 1995 (Raffaelli et al., 1998). This unusual condition is evidence that both nutrients and eroded (dead or living) algae can be transported out of the estuary as a result of high river flows. Although the concentration of nutrients entering to the estuary in the main River Ythan rarely exceeds 50 mg/l (maximum acceptable concentration; MAC) as mentioned by Edwards et al. (2003) those nutrients, coupled with nutrients replenished from sediments, may stay in the system for several days resulting in high abundance of algae.

# Chapter 8: Conclusions and recommendations

The previous discussion has assessed the implications of the research findings, evaluated the strengths and weaknesses of the approaches used, and has considered limitations of the research strategy. This chapter summarises the main results from the study as related to the research questions outlined in Chapter 1 followed by recommendations for future studies.

## 8.1 Conclusions

***Research question 1: What are the patterns of water (river and ocean) circulation in the estuary?***

Hydrodynamic modelling provides understanding of how river and ocean water interact in the Ythan estuary. Tides are the main control on the spatial patterns of velocity and movement of water, whilst seasonal changes of river flow have insignificant impact on overall spatial patterns of velocity. River flow has a secondary effect in helping to accelerate flow velocity during low tide when river flow coincides with spring tide. River flow levels also influence water depths in the main water channel during low tide. Changes of velocity are also significantly affected by spring and neap tides. Increased flow velocity during spring tides correspond closely with the shear stress, values of which are always much higher during spring than neap tides. Although the estuary is tide dominated, flow velocities away from the main channel are generally low throughout the estuary, especially in Sleek of Tarty where algae develop extensively. Summer months, when river flow is generally low, have the lowest flow velocities and the lowest fresh water influence particularly during neap tide conditions.

***Research question 2: How are nutrients transported in the estuary?***

The tidal cycle is the control over the movement of nutrients through and within the estuary. Tidal conditions lead to nutrients being mobilised back and forth from the lower region to the upper region, with down-estuary assistance from river flow during low tide conditions only. Movement of nutrients caused by hydrodynamics results in nutrient aggregation in particular areas. In addition, the river flow level controls overall nutrient concentrations in the estuary. Increases in nutrient concentration normally occur during high river flow, as a result of nutrient supply from the catchment. During flood tide, increased nutrient concentrations are

found in the Burn of Forvie area and the upper part of Sleek of Tarty close to the bottle neck in the upper region of the estuary. On the ebb tide, increased nutrient concentrations are found in the lower region, in particular around Foveran Burn and the area close to the mouth. Apart from tidal cycle and river flow conditions, tributaries have an impact on nutrient concentration in the areas surrounding their input to the estuary. The areas close to Tarty Burn, Foveran Burn, and Burn of Forvie are always affected by high nutrient concentration. However, the direction of nutrient transport depends on whether the nutrient release time from the tributary coincides with tidal cycle. Nutrients are transported throughout the estuary with high concentrations in the main channel and lower concentrations over the mudflats in Sleek of Tarty. Although Sleek of Tarty mudflats have lower nutrient concentrations than the main channel, this area is a pathway for nutrients from all tributaries.

***Research question 3: How do hydrodynamics control macroalgal growth?***

In the Ythan estuary hydrodynamics play a key role in controlling macroalgal growth. Interaction between seasonal river flow and the tide not only helps create optimal water quality (salinity and turbidity) conditions which facilitate algal growth, but also influences nutrient movements across the estuary resulting in high nutrient availability in particular areas. The abundance of nutrients coupled with low flow velocity, driven by interaction of river flow, tide and bed sediment characteristics, causes areas with long residence time of nutrient enrichment. These areas are, in particular, the shallow water at Sleek of Tarty and at tributary mouth bars. Consequently, macroalgae show persistence of development in these areas.

The results derived from this study of the Ythan estuary provide general understanding of interrelationships between volume of inflow fresh water, tidal range, and physical characteristics of the estuary such as shape, size, and bathymetry, all of which determine the hydrodynamic characteristics of the estuary. Any bar-built estuaries, which are relatively shallow (water depth less than 5 m) and have relatively low fresh water input, have a tendency to be dominated by sea water. However, tidal energy in these cases does not produce high flow velocities as a result of dissipation of energy by bathymetry and the bar at the estuary mouth. These relatively slow velocities lead to slow flushing, which increases nutrient enrichment, and so such estuaries are prone to eutrophication.

***Research question 4: Can remote sensing data and Delft3D model be used to support modelling hydrodynamics, nutrient concentrations and pathway in estuarine study effectively?***

The results of the study demonstrate advantages of using remote sensing in conjunction with modelling studies. Remote sensing can be used to produce bathymetric data which are used as inputs to a model. This approach is safe, rapid and is especially valuable in in dangerous and inaccessible estuaries. With high spatial resolution and wide coverage, remote sensing data are very valuable for validating flooded-dry areas derived from a model. In addition, a few days of repeat acquisition cycle and high spectral resolution of remote sensing data makes retrieving algae growth behaviour for model validation effortless. Multi-temporal remote sensing data also provide higher resolution data and understanding of variation of algae growth in the estuary. Remote sensing has high capability as one of the main estuarine ecological management tools for studying impacts of eutrophication and other disturbances. Remote sensing can be used alone but is especially valuable when integrated with field data and/or hydrodynamic modelling. Delft3D provides good performance in modelling hydrodynamics, nutrient concentration, and nutrient pathways and so was able in this case to provide insights into how estuarine hydrodynamics influence algal growth in this estuary.

## 8.2 Recommendation for further studies

Based on the results and limitations highlighted in the discussion chapter, recommendations for further work which could enhance scientific understanding and the management of estuaries are as follows:

- A continuous programme to generate long-term seasonal time-series of NDVI and algal types from image classification, coupled with extensive field data collections. These data will improve the quality of image classification and so would be of benefit to monitoring the ecological impact of changing environmental conditions and land management on algal growth. In addition, using the time-series NDVI and algal types data coupled with time series of water quality and meteorological data could reveal a more detailed understanding of how water quality and weather are associated with algae growth behaviour.

- Although the Ythan has the Sands of Forvie forming a barrier at its mouth, so dissipating winds and tidal energy entering the estuary, winds and waves can still strongly influence tidal flow and cause both currents and waves due to the rough bed topography of the Ythan. The currents and waves affect flow velocity and water level. Thus, adding wind-wave effects to the hydrodynamic model may improve model results particularly in terms of flow velocity and mixing, which affect estimates of nutrient residence time.
- Accurate bathymetry is crucial for hydrodynamic modelling as it directly affects flow velocity and, hence, constituent transport patterns. Obtaining further bathymetric data in particular in the upper region of the estuary, where the hydrodynamic model was unable to reproduce flow conditions in the main channel, could improve model results, and as such provide more accurate understanding of nutrient transport characteristics in the upper region. In addition, accurate bathymetry would be a database that could be used for the long-term modelling in the Ythan.

- The results of this study suggest some management strategies for the Ythan estuary.
    - Since flow velocity influences nutrient residence time, strategies for using measures to modify hydrodynamics to prevent long residence time for nutrients may be beneficial. For example, in-channel structures to enhance flow velocity in areas close to nutrient inputs such as in the tributary channels may be able to reduce residence times and also to reduce the transfer of nutrients onto the shallow mudflat areas.
    - Guidelines on the timing of release of wastewater from tributaries should be included in estuarine management in the Ythan estuary. The optimal time for release of wastewater, especially from Ellon and Foveran Burn, should correspond to the ebb tide when the introduced nutrients have high possibility of being transported out of the estuary to the ocean, rather than during flood tide and slack water conditions when they will be more likely to be retained within the estuary.

- Modelling hydrodynamics, nutrient concentrations, and nutrient pathways in conjunction with remote sensing techniques should be applied to other similar

estuaries to study estuarine hydrodynamics and associated eutrophication problems.

# List of Symbols

| Symbol | Meaning | Unit |
|---|---|---|
| $c$ | mass concentration | kg/m$^3$ |
| $C$ | Chezy coefficient | m$^{1/2}$/s |
| $CFL$ | Courant-Friedrichs-Lewy number | - |
| $Cw$ | Colebrook-White coefficient | m$^{1/2}$/s |
| $D_H, D_V$ | horizontal and vertical diffusivity coefficients | m$^2$/s |
| $D_H^{back}$ | background horizontal eddy diffusivity | m$^2$/s |
| $D_{SGS}$ | dispersion coefficient derived from the sub-grid scale turbulence model | m$^2$/s |
| $D_{x,y}$ | horizontal dispersion coefficient | m$^2$/s |
| $D_Z$ | vertical dispersion coefficient | m$^2$/s |
| $f$ | Coriolis parameter | 1/s |
| $F_x$ | turbulent momentum flux in x-direction | m/s$^2$ |
| $F_y$ | turbulent momentum flux in x-direction | m/s$^2$ |
| Fζ | turbulent momentum flux in x direction | m/s$^2$ |
| $g$ | gravitational constant | m/s$^2$ |
| $h$ | water depth | m |
| $k$ | turbulent kinetic energy | m$^2$/s$^2$ |
| $k_s$ | Nikuradse roughness length | m |
| $n$ | Manning coefficient | m$^{1/3}$/s |
| $P_x$ | gradient hydrostatic pressure in x-direction | kg/m$^2$s$^2$ |
| $P_y$ | gradient hydrostatic pressure in y-direction | kg/m$^2$s$^2$ |
| $u, v$ | flow velocities in x and y direction | m/s |

| Symbol | Meaning | Unit |
|---|---|---|
| $\overline{U}, \overline{V}$ | depth-averaged GLM velocity components | m/s |
| $U_{*b}$ | friction velocity at the bed | m/s |
| $U_{*s}$ | friction velocity at the water surface | m/s |
| $v_H, v_V$ | horizontal and vertical eddy viscosity | $m^2/s$ |
| $v_H^{back}$ | background horizontal eddy viscosity | $m^2/s$ |
| $v_{SGS}$ | computed value derived from SGS-turbulence model | $m^2/s$ |
| $z$ | vertical coordinate in physical space | - |
| $\Delta t$ | computational time step | s |
| $\Delta x$ | grid size in x direction | m |
| $\Delta y$ | grid size in y direction | m |
| $\omega$ | vertical flow velocity in sigma coordinate system | m/s |
| $\rho_0$ | reference density of water | $kg/m^3$ |
| $\zeta$ | water level above some horizontal plane of reference (datum) | m |
| $\sigma_C$ | Prandtl-Schmidt number | - |
| $\sigma$ | scaled vertical coordinate defined by $(z-\zeta)/(d+\zeta)$ (surface $\sigma$ = 0; bed level $\sigma$ = - 1) | - |

# List of References


ABERDEENSHIRE.GOV.UK. 2016. *Small Area Population Estimates and Forecasts Population Totals - Aberdeenshire Settlements* [Online]. Available: https://www.aberdeenshire.gov.uk/council-and-democracy/statistics/small-area-population-estimates-and-forecasts-1/ [Accessed 2018].

ABPMER. 2011. *The Estuary Guide* [Online]. Joint Defra/EA Flood and Coastal Erosion Risk Management R&D Programme: Department for Environment, Food, and Public Affairs, UK. Available: http://www.estuary-guide.net/guide/chapter3_estuary_setting.asp?color=h [Accessed 2018].

AIAZZI, B., BARONTI, S., SELVA, M. & ALPARONE, L. 2007. MS+Pan Image Fusion by an Enhanced Gram-Schmidt Spectral Sharpening. *New Developments and Challenges in Remote Sensing,* 45**,** 113-120.

AL-QASMI, M., RAUT, N., TALEBI, S. & AL-RAJHI, S. 2012. A Review of Effect of Light on Microalgae Growth. *Lecture Notes in Engineering and Computer Science*.

ALESHEIKH, A. A., GHORBANALI, A. & NOURI, N. 2007. Coastline Change Detection Using Remote Sensing. *International Journal of Environmental Science & Technology,* 4**,** 61-66.

ANDERSON, A. 1971. Intertidal Activity, Breeding and the Floating Habit of Hydrobia Ulvae in the Ythan Estuary. *Journal of the Marine Biological Association of the United Kingdom,* 51**,** 423-437.

ANDERSON, M. G. & BATES, P. D. 2001. *Model Validation: Perspectives in Hydrological Science*, John Wiley & Sons Ltd.

BAIOCCHI, V., BRIGANTE, R., DOMINICI, D. & RADICIONI, F. Coastline Detection using High Resolution Multispectral Satellite Images. FIG Working Week: Knowing to Manage the Territory, Protect the Environment, Evaluate the Cultural Heritage, 2012 Rome, Italy.

BAIRD, D. & MILNE, H. 1981. Energy Flow in the Ythan Estuary, Aberdeenshire, Scotland. *Estuarine, Coastal and Shelf Science,* 13**,** 455-472.

BALLS, P., MACDONALD, A., PUGH, K. & EDWARDS, A. 1995. Long-term Nutrient Enrichment of an Estuarine System: Ythan, Scotland (1958–1993). *Environmental Pollution,* 90**,** 311-321.

BAPTISTELLI, S. C. 2015. Hydrodynamic Modeling: Application of Delft3D-FLOW in Santos Bay, São Paulo State, Brazil. *In:* BAAWAIN, M., CHOUDRI, B. S., AHMED, M. & PURNAMA, A. (eds.) *Recent Progress in Desalination, Environmental and Marine Outfall Systems*. Cham: Springer International Publishing.

BARILLé, L., MOUGET, J.-L., MéLéDER, V., ROSA, P. & JESUS, B. 2011. Spectral Response of Benthic Diatoms with Different Sediment Backgrounds. *Remote Sensing of Environment,* 115**,** 1034-1042.

BARILLé, L., ROBIN, M., HARIN, N., BARGAIN, A. & LAUNEAU, P. 2010. Increase in Seagrass Distribution at Bourgneuf Bay (France) Detected by Spatial Remote Sensing. *Aquatic Botany,* 92**,** 185-194.

BATES, P. D. & DE ROO, A. 2000. A Simple Raster-Based Model for Flood Inundation Simulation. *Journal of Hydrology,* 236**,** 54-77.

BEER, T. 1983. *Environmental Oceanography,* Oxford, Pergamon Press.

BELGIU, M., DRĂGUŢ, L. & STROBL, J. 2014. Quantitative Evaluation of Variations in Rule-based Classifications of Land Cover in Urban Neighbourhoods using WorldView-2 Imagery. *ISPRS Journal of Photogrammetry and Remote Sensing,* 87**,** 205-215.

BENT, E., POSTMA, L., ROELFZEMA, A. & STIVE, R. 1991. Hydrodynamic and Dispersion Modelling of Swansea Bay. *Environmental Hydraulics,* 1**,** 865–870.

BENYOUCEF, I., BLANDIN, E., LEROUXEL, A., JESUS, B., ROSA, P., MéLéDER, V., LAUNEAU, P. & BARILLé, L. 2014. Microphytobenthos Interannual Variations in a North-European estuary (Loire estuary, France) Detected by Visible-Infrared Multispectral Remote Sensing. *Estuarine, Coastal and Shelf Science,* 136**,** 43-52.

BENZ, U. C., HOFMANN, P., WILLHAUCK, G., LINGENFELDER, I. & HEYNEN, M. 2004. Multi-Resolution, Object-Oriented Fuzzy Analysis of Remote Sensing Data for GIS-Ready Information. *ISPRS Journal of Photogrammetry and Remote Sensing,* 58**,** 239-258.

BIANCHI, T. S. & ALLISON, M. A. 2009. Large-River Delta-Front Estuaries as Natural "Recorders" of Global Environmental Change. *Proceedings of the National Academy of Sciences,* 106**,** 8085-8092.

BINDU, G., RAJAN, P., JISHNU, E. S. & AJITH JOSEPH, K. 2018. Carbon Stock Assessment of Mangroves using Remote Sensing and Geographic Information System. *The Egyptian Journal of Remote Sensing and Space Science*.

BONVIN, F., RAZMI, A. M., BARRY, D. A. & KOHN, T. 2013. Micropollutant Dynamics in Vidy Bay-a Coupled Hydrodynamic-Photolysis Model to Assess the Spatial Extent of Ecotoxicological Risk. *Environmental Science & Technology,* 47**,** 9207-9216.

BOOTHROYD, J. C. 1978. Mesotidal Inlets and Estuaries. *In:* DAVIS, R. A. (ed.) *Coastal Sedimentary Environments*. New York: Springer US.

BOYLE, K. A., KAMER, K. & FONG, P. 2004. Spatial and Temporal Patterns in Sediment and Water Column Nutrients in a Eutrophic Southern California Estuary. *Estuaries and Coasts,* 27**,** 378-388.

BREEMEN, M. 2008. *Salt Intrusion in the Selangor: Model Study with Delft3D Estuary in Malaysia*. Master Thesis, University of Twente.

BRITANNICA. 1998. *Ria* [Online]. Encyclopaedia Britannica, inc. Available: https://www.britannica.com/science/ria [Accessed 2018].

BRITO, A. C., BENYOUCEF, I., JESUS, B., BROTAS, V., GERNEZ, P., MENDES, C. R., LAUNEAU, P., DIAS, M. P. & BARILLé, L. 2013. Seasonality of

Microphytobenthos Revealed by Remote-Sensing in a South European Estuary. *Continental Shelf Research,* 66**,** 83-91.

BROWN, M. M., MULLIGAN, R. P. & MILLER, R. L. 2014. Modeling the Transport of Freshwater and Dissolved Organic Carbon in the Neuse River Estuary, NC, USA following Hurricane Irene (2011). *Estuarine, Coastal and Shelf Science,* 139**,** 148-158.

BROWN, N., GEISLER, I. & TROYER, L. 2006. RTK Rover Performance using the Master-Auxiliary Concept. *Journal of Global Positioning Systems,* 5**,** 135-144

BUCHHORN, M., RAYNOLDS, M. K. & WALKER, D. A. 2016. Influence of BRDF on NDVI and Biomass Estimations of Alaska Arctic Tundra. *Environmental Research Letters,* 11**,** 125002.

BUIJSMAN, M. C. 2007. *Ferry-Observed Variability of Currents and Bedforms in the Marsdiep Inlet*. PhD Thesis, Utrecht University.

BUSKEY, E. J., MONTAGNA, P. A., AMOS, A. F. & WHITLEDGE, T. E. 1997. Disruption of Grazer Populations as a Contributing Factor to the Initiation of the Texas Brown Tide Algal Bloom. *Limnology and Oceanography,* 42**,** 1215-1222.

CANDRA, D. S. 2013. Analysis of SPOT-6 Data Fusion using Gram-Schmidt Spectral Shapening on Rural Areas. *International Journal of Remote Sensing and Earth Sciences (IJReSES),* 10.

CARIBONI, J., GATELLI, D., LISKA, R. & SALTELLI, A. 2007. The Role of Sensitivity Analysis in Ecological Modelling. *Ecological modelling,* 203**,** 167-182.

CARLE, M. V., WANG, L. & SASSER, C. E. 2014. Mapping Freshwater Marsh Species Distributions using WorldView-2 High-Resolution Multispectral Satellite Imagery. *International journal of remote sensing,* 35**,** 4698-4716.

CHANG, K. T. 2006. *Introduction to Geographic Information Systems,* Boston, McGraw-Hill Higher Education

CHANSON, H. 2004. Introduction. *Hydraulics of Open Channel Flow (Second Edition)*. Oxford: Butterworth-Heinemann.

CHEN, Z., MULLER-KARGER, F. E. & HU, C. 2007. Remote Sensing of Water Clarity in Tampa Bay. *Remote Sensing of Environment,* 109**,** 249-259.

CHO, J., SONG, Y. & KIM, T. I. 2016. Numerical Modeling of Estuarine Circulation in the Geum River Estuary, Korea. *Procedia Engineering,* 154**,** 982-989.

CLAUSSEN, M. 1988. Models of Eddy Viscosity for Numerical Simulation of Horizontally Inhomogeneous, Neutral Surface-Layer Flow. *Boundary-Layer Meteorology,* 42**,** 337-369.

COLLINS, C., REASON, C. J. C. & HERMES, J. 2012. Scatterometer and Reanalysis Wind Products over the Western Tropical Indian Ocean. *Journal of Geophysical Research: Oceans,* 117.

COPPIN, P., JONCKHEERE, I., NACKAERTS, K., MUYS, B. & LAMBIN, E. 2004. Review Article Digital Change Detection Methods in Ecosystem Monitoring: A Review. *International Journal of Remote Sensing,* 25**,** 1565-1596.

CRACKNELL, A. 1999. Remote Sensing Techniques in Estuaries and Coastal Zones: An Update. *International Journal of Remote Sensing,* 20**,** 485-496.

DA SILVA, J. S., CALMANT, S., SEYLER, F., ROTUNNO FILHO, O. C., COCHONNEAU, G. & MANSUR, W. J. 2010. Water Levels in the Amazon Basin derived from the ERS-2 and ENVISAT Radar Altimetry Missions. *Remote Sensing of Environment,* 114**,** 2160-2181.

DALRYMPLE, R. W., ZAITLIN, B. A. & BOYD, R. 1992. Estuarine Facies Models; Conceptual Basis and Stratigraphic Implications. *Journal of Sedimentary Research,* 62**,** 1130-1146.

DAVIDSON, N. C. 2016. Estuary Types. *In:* FINLAYSON, C. M., EVERARD, M., IRVINE, K., MCINNES, R. J., MIDDLETON, B. A., VAN DAM, A. A. & DAVIDSON, N. C. (eds.) *The Wetland Book: I: Structure and Function, Management and Methods.* Dordrecht: Springer Netherlands.

DAVIES, O. A. & UGWUMBA, O. A. 2013. Tidal Influence on Nutrients Status and Phytoplankton Population of Okpoka Creek, Upper Bonny Estuary, Nigeria. *Journal of Marine Biology,* 2013**,** 16.

DE JONGE, V. N., ELLIOTT, M. & ORIVE, E. 2002. Causes, Historical Development, Effects and Future Challenges of a Common Environmental Problem: Eutrophication. *Hydrobiologia,* 475**,** 1-19.

DEFNE, Z. & GANJU, N. K. 2015. Quantifying the Residence Time and Flushing Characteristics of a Shallow, Back-Barrier Estuary: Application of Hydrodynamic and Particle Tracking Models. *Estuaries and Coasts,* 38**,** 1719-1734.

DEFNE, Z., HAAS, K. A. & FRITZ, H. M. 2011. Numerical Modeling of Tidal Currents and the Effects of Power Extraction on Estuarine Hydrodynamics along the Georgia Coast, USA. *Renewable Energy,* 36**,** 3461-3471.

DEFRIES, R. & TOWNSHEND, J. 1994. NDVI-Derived Land Cover Classifications at a Global Scale. *International Journal of Remote Sensing,* 15**,** 3567-3586.

DELTARES. 2014. Delft3D-FLOW: Simulation of Multi-Dimensional Hydrodynamic Flows and Transport Phenomena, including Sediments. Available: https://oss.deltares.nl/documents/183920/185723/Delft3D-FLOW_User_Manual.pdf [Accessed 2014].

DELTARES. 2019a. Delft3D-PART: Simulation of Mid-Field Water Quality and Oil Spills, using Particle Tracking. Available: https://content.oss.deltares.nl/delft3d/manuals/Delft3D-PART_User_Manual.pdf [Accessed 2019].

DELTARES. 2019b. Delft3D, Functional Specifications. Available: http://content.oss.deltares.nl/delft3d/manuals/Delft3D-Functional_Specifications.pdf [Accessed 2019].

DENG, Y., TANG, X., HUANG, B. & DING, L. 2012. Effect of Temperature and Irradiance on the Growth and Reproduction of the Green Macroalga, Chaetomorpha Valida (Cladophoraceae, Chlorophyta). *Journal of Applied Phycology,* 24**,** 927-933.

DIGITALGLOBE. 2010. The Benefits of the Eight Spectral Bands of Worldview-2. Available: https://dg-cms-uploads-production.s3.amazonaws.com/uploads/document/file/35/DG-8SPECTRAL-WP_0.pdf [Accessed 2013].

DMOWSKA, R. & HOLTON, J. 1994. International Geophysics Series. *In:* HARTMANN, D. L. (ed.) *International Geophysics*. Academic Press.

DOMBURG, P., EDWARDS, A. C., SINCLAIR, A. H., WRIGHT, G. G. & FERRIER, R. C. 1998. Changes in Fertilizer and Manurial Practices during 1960–1990: Implications for N and P Inputs to the Ythan Catchment, N.E. Scotland. *Nutrient Cycling in Agroecosystems,* 52**,** 19-29.

DUARTE, A. A., PINHO, J. L., PARDAL, M. A., NETO, J. M., VIEIRA, J. & SANTOS, F. S. 2002. Hydrodynamic Modelling for Mondego Estuary Water Quality Management. *In:* PARDAL, MARQUES & GRAçA (eds.) *Aquatic Ecology of the Mondego River Basin - Global Importance of Local Experience*.

DUARTE, A. A. & VIEIRA, J. 2009. Estuarine Hydrodynamic as a Key-Parameter to Control Eutrophication Processes. *WSEAS Transactions on Fluid Mechanics,* 4**,** 137-147.

EBUCHI, N., GRABER, H. C. & CARUSO, M. J. 2002. Evaluation of Wind Vectors Observed by QuikSCAT/SeaWinds using Ocean Buoy Data. *Journal of Atmospheric and Oceanic Technology,* 19**,** 2049-2062.

EDWARDS, A., SINCLAIR, A. & DOMBURG, P. 2003. Identification, Designation and Formulation of an Action Plan for a Nitrate Vulnerable Zone: a Case Study of the Ythan Catchment, NE Scotland. *European Journal of Agronomy,* 20**,** 165-172.

ELHAKEEM, A., ELSHORBAGY, W. & BLENINGER, T. 2015. Long-term Hydrodynamic Modeling of the Arabian Gulf. *Marine Pollution Bulletin,* 94**,** 19-36.

FAGHERAZZI, S., MARIOTTI, G., BANKS, A., MORGAN, E. & FULWEILER, R. 2014. The Relationships Among Hydrodynamics, Sediment Distribution, and Chlorophyll in a Mesotidal Estuary. *Estuarine, Coastal and Shelf Science,* 144**,** 54-64.

FAIRBRIDGE, R. W. 1980. The Estuary: Its Definition and Geodynamic Cycle. *In:* OLAUSSON, E. & CATO, I. (eds.) *Chemistry and Biogeochemistry of Estuaries*. Chichester: Wiley.

FAN, L., SHIEH, W., WU, W. & CHEN, C. P. 2006. Distribution of Nitrogenous Nutrients and Denitrifiers Strains in Estuarine Sediment Profiles of the Tanshui River, Northern Taiwan. *Estuarine, Coastal and Shelf Science,* 69**,** 543-553.

FERRARIN, C. & UMGIESSER, G. 2005. Hydrodynamic Modeling of a Coastal Lagoon: the Cabras Lagoon in Sardinia, Italy. *Ecological Modelling,* 188**,** 340-357.

FEUILLET-GIRARD, M., GOULEAU, D., BLANCHARD, G. & JOASSARD, L. 1997. Nutrient Fluxes on an Intertidal Mudflat in Marennes-Oléron Bay, and Influence of the Emersion Period. *Aquatic Living Resources,* 10**,** 49-58.

FLEMMING, B. W. 2011. Geology, Morphology, and Sedimentology of Estuaries and Coasts. *Treatise on Estuarine and Coastal Science*. Waltham: Academic Press.

FLETCHER, C. A. J. 1991. Computational Techniques for Fluid Dynamics 2 : Specific Techniques for Different Flow Categories. Berlin, Heidelberg: Springer Berlin Heidelberg.

FRAZIER, P. S. & PAGE, K. J. 2000. Water Body Detection and Delineation with Landsat TM Data. *Photogrammetric Engineering and Remote Sensing,* 66**,** 1461-1468.

FRENCH, J. R. 2008. Hydrodynamic Modelling of Estuarine Flood Defence Realignment as an Adaptive Management Response to Sea-Level Rise. *Journal of Coastal Research,* 24**,** 1-12.

FRIEDRICHS, C. & WRIGHT, L. 1997. Sensitivity of Bottom Stress and Bottom Roughness Estimates to Density Stratification, Eckernförde Bay, Southern Baltic Sea. *Journal of Geophysical Research: Oceans,* 102**,** 5721-5732.

GAO, B. C. 1996. NDWI - A Normalized Difference Water Index for Remote Sensing of Vegetation Liquid Water from Space. *Remote Sensing of Environment,* 58**,** 257-266.

GILLIBRAND, P. & BALLS, P. 1998. Modelling Salt Intrusion and Nitrate Concentrations in the Ythan Estuary. *Estuarine, Coastal and Shelf Science,* 47**,** 695-706.

GOULD, R. W. & ARNONE, R. A. 1997. Remote Sensing Estimates of Inherent Optical Properties in a Coastal Environment. *Remote Sensing of Environment,* 61**,** 290-301.

GOV.SCOT. 2008. NVZ Guidance for Farmers. Available: http://www.gov.scot/Topics/farmingrural/Agriculture/Environment/NVZintro/NVZGuidanceforFarmers [Accessed 2014].

GOV.SCOT. 2011. Eutrophication. Available: http://www.gov.scot/Publications/2011/03/16182005/38 [Accessed 2013].

GOV.SCOT 2015a. Moray, Aberdeenshire, Banff and Buchan NVZ. Scottish Government.

GOV.SCOT. 2015b. Revised NVZ boundaries 2015. Available: https://www2.gov.scot/Topics/farmingrural/Agriculture/Environment/NVZintro/ArchiveNVZNewsGuidance/NVZRevisions2015 [Accessed 2015].

GOWER, J. 2004. SeaWiFS Global Composite Images Show Significant Features of Canadian Waters for 1997–2001. *Canadian Journal of Remote Sensing,* 30**,** 26-35.

GOWER, J. F. R., BROWN, L. & BORSTAD, G. A. 2004. Observation of Chlorophyll Fluorescence in West Coast Waters of Canada using the MODIS Satellite Sensor. *Canadian Journal of Remote Sensing,* 30**,** 17-25.

GREEN, D. 2010. Applying Geospatial Technologies to Weedmat Monitoring and Mapping: the Ythan Estuary, NE Scotland. *In:* GREEN, D. R. (ed.) *Coastal and Marine Geospatial Technologies*. Dordrecht: Springer Netherlands.

GREEN, K., KEMPKA, D. & LACKEY, L. 1994. Using Remote Sensing to Detect and Monitor Land-Cover and Land-Use Change. *Photogrammetric Engineering and Remote Sensing,* 60, 331-337.

GUILLAUMONT, B., CALLENS, L. & DION, P. Spatial Distribution and Quantification of Fucus Species and Ascophyllum Nodosum Beds in Intertidal Zones using SPOT Imagery. Fourteenth International Seaweed Symposium, 1993. Springer, 297-305.

HARRISON, P. J. & HURD, C. L. 2001. Nutrient Physiology of Seaweeds: Application of Concepts to Aquaculture. *Cahiers de Biologie Marine,* 42, 71-82.

HART, B., S. LAKE, P., WEBB, J. & GRACE, M. 2003. Ecological Risk to Aquatic Systems from Salinity Increase. *Australian Journal of Botany,* 51.

HAYES, D. J. & SADER, S. A. 2001. Comparison of Change-Detection Techniques for Monitoring Tropical Forest Clearing and Vegetation Regrowth in a Time Series. *Photogrammetric Engineering and Remote sensing,* 67, 1067-1075.

HöTZEL, G. & CROOME, R. 1994. Long-Term Phytoplankton Monitoring of the Darling River at Burtundy, New South Wales: Incidence and Significance of Cyanobacterial Blooms. *Marine and Freshwater Research,* 45, 747-759.

HSU, Y. L., DYKES, J. D., ALLARD, R. A. & KAIHATU, J. M. 2006. Evaluation of Delft3D Performance in Nearshore Flows. Available: https://apps.dtic.mil/dtic/tr/fulltext/u2/a460541.pdf [Accessed 2017].

HU, C. 2009. A Novel Ocean Color Index to Detect Floating Algae in the Global Oceans. *Remote Sensing of Environment,* 113, 2118-2129.

HU, C. & HE, M. X. 2008. Origin and Offshore Extent of Floating Algae in Olympic Sailing Area. *Eos, Transactions American Geophysical Union,* 89, 302-303.

HU, K., DING, P., WANG, Z. & YANG, S. 2009. A 2D/3D Hydrodynamic and Sediment Transport Model for the Yangtze Estuary, China. *Journal of Marine Systems,* 77, 114-136.

HU, L., HU, C. & MING-XIA, H. E. 2017. Remote Estimation of Biomass of Ulva Prolifera Macroalgae in the Yellow Sea. *Remote Sensing of Environment,* 192, 217-227.

HUANG, J., WANG, H., DAI, Q. & HAN, D. 2014. Analysis of NDVI Data for Crop Identification and Yield Estimation. *IEEE Journal of Selected Topics in Applied Earth Observations and Remote Sensing,* 7, 4374-4384.

HUME, T. M. & HERDENDORF, C. E. 1988. A Geomorphic Classification of Estuaries and its Application to Coastal Resource Management - A New Zealand Example. *Ocean and Shoreline Management,* 11, 249-274.

HUNTER, E. & POWER, C. 2002. An Assessment of Two Classification Methods for Mapping Thames Estuary Intertidal Habitats using CASI Data. *International Journal of Remote Sensing,* 23, 2989-3008.

HURD, C. L., HARRISON, P. J., BISCHOF, K. & LOBBAN, C. S. 2014. *Seaweed Ecology and Physiology,* Cambridge, Cambridge University Press.

HUSSAIN, M., CHEN, D., CHENG, A., WEI, H. & STANLEY, D. 2013. Change Detection from Remotely Sensed Images: From Pixel-Based to Object-

Based Approaches. *ISPRS Journal of Photogrammetry and Remote Sensing,* 80, 91-106.

HUTHOFF, F. & AUGUSTIJN, D. Channel Roughness in 1D Steady Uniform Flow: Manning or Chézy? NCR-days 2004, Research for managing rivers; present and future issues, 2004a Wageningen, The Netherlands. 98-100.

HUTHOFF, F. & AUGUSTIJN, D. Sensitivity Analysis of Floodplain Roughness in 1D Flow. The 6th International Conference on Hydroinformatics, 2004b World Scientific Publishing Company, Singapore. 301-308.

HWANG, P. A., KRABILL, W. B., WRIGHT, W., SWIFT, R. N. & WALSH, E. J. 2000. Airborne Scanning Lidar Measurement of Ocean Waves. *Remote Sensing of Environment,* 73, 236-246.

JAHNKE, L. S. & WHITE, A. L. 2003. Long-Term Hyposaline and Hypersaline Stresses Produce Distinct Antioxidant Responses in the Marine Alga Dunaliella Tertiolecta. *Journal of Plant Physiology,* 160, 1193-1202.

JASSBY, A. & VAN NIEUWENHUYSE, E. 2005. Low Dissolved Oxygen in an Estuarine Channel (San Joaquin River, California): Mechanisms and Models Based on Long-term Time Series. *San Francisco Estuary and Watershed Science,* 3.

JENSEN, J. R. 1987. Introductory Digital Image Processing: A Remote Sensing Approach. *Geocarto International,* 2, 65.

JOHNSTON, K., VER HOEF, J. M., KRIVORUCHKO, K. & LUCAS, N. 2001. *Using ArcGIS Geostatistical Analyst*, Esri Redlands.

JONES, M. & PINN, E. 2006. The Impact of a Macroalgal Mat on Benthic Biodiversity in Poole Harbour. *Marine Pollution Bulletin,* 53, 63-71.

KABBARA, N., BENKHELIL, J., AWAD, M. & BARALE, V. 2008. Monitoring Water Quality in the Coastal Area of Tripoli (Lebanon) using High-Resolution Satellite Data. *ISPRS Journal of Photogrammetry and Remote Sensing,* 63, 488-495.

KAZEMIPOUR, F., LAUNEAU, P. & MéLéDER, V. 2012. Microphytobenthos Biomass Mapping using the Optical Model of Diatom Biofilms: Application to Hyperspectral Images of Bourgneuf Bay. *Remote Sensing of Environment,* 127, 1-13.

KEESING, J. K., LIU, D., FEARNS, P. & GARCIA, R. 2011. Inter- and Intra-Annual Patterns of Ulva Prolifera Green Tides in the Yellow Sea during 2007–2009, their Origin and Relationship to the Expansion of Coastal Seaweed Aquaculture in China. *Marine Pollution Bulletin,* 62, 1169-1182.

KEITH, D. J. 2014. Satellite Remote Sensing of Chlorophyll a in Support of Nutrient Management in the Neuse and Tar-Pamlico River (North Carolina) Estuaries. *Remote Sensing of Environment,* 153, 61-78.

KENCH, P. S. 1999. Geomorphology of Australian Estuaries: Review and prospect. *Australian Journal of Ecology,* 24, 367-380.

KENNISH, M. J. 2002. Environmental Threats and Environmental Future of Estuaries. *Environmental Conservation,* 29, 78-107.

KERLE, N., BAKKER, W. H., GRABMAIER, K. A., HUURNEMAN, G. C., VAN DER MEER, F. D., PRAKASH, A., TEMPFLI, K., GIESKE, A. S. M., HECKER, C. A., JANSSEN, L. L. F., PARODI, G. N., REEVES, C. V., WEIR, M. J. C., GORTE, B. G. H., HORN, J. A., POHL, C., VAN RUITENBEEK, F. J. A. & WOLDAI, T. 2004. *Principles of Remote Sensing : An Introductory Textbook*, ITC.

KEYWORTH, S., JARMAN, M. & MEDCALF, K. 2009. Assessing the Extent and Severity of Erosion on the Upland Organic Soils of Scotland using Earth Observation: A GIFTSS Implementation Test. Available: http://www.gov.scot/Publications/2009/11/06110108/20 [Accessed 2017].

KIM, Y., LEE, C., HAN, D., KIM, Y. & KIM, Y. 2011. Improved Additive-Wavelet Image Fusion. *IEEE Geoscience and Remote Sensing Letters,* 8**,** 263-267.

KLEMAS, V. 2010. Remote Sensing Techniques for Studying Coastal Ecosystems: An Overview. *Journal of Coastal Research,* 27**,** 2-17.

KLEMAS, V. 2012. Remote Sensing of Algal Blooms: An Overview with Case Studies. *Journal of Coastal Research,* 28**,** 34-43.

KORIYAMA, M., KOGA, A., SEGUCHI, M. & ISHITANI, T. 2016. Factors Controlling Denitrification of Mudflat Sediments in Ariake Bay, Japan. *Environmental Monitoring and Assessment,* 188**,** 96.

KRAUSE-JENSEN, D., J. MCGLATHERY, K., RYSGAARD, S. & CHRISTENSEN, P. 1996. Production within Dense Mats of the Filamentous Macroalga Chaetomorpha Linum in Relation to Light and Nutrient Availability. *Marine Ecology Progress Series,* 134**,** 207-216.

KWON, B. O., LEE, Y., PARK, J., RYU, J., HONG, S., SON, S. H., LEE, S. Y., NAM, J., KOH, C. H. & KHIM, J. S. 2016. Temporal Dynamics and Spatial Heterogeneity of Microalgal Biomass in Recently Reclaimed Intertidal Flats of the Saemangeum Area, Korea. *Journal of Sea Research,* 116**,** 1-11.

LABEN, C. A. & BROWER, B. V. 2000. Process for Enhancing the Spatial Resolution of Multispectral Imagery using Pan-Sharpening. Us Patents.

LACHENDRO, T. 2016. *Natural and Anthropogenic Factors Controlling Algae Growth in the Ythan Estuary, Aberdeenshire*. Master Thesis, University of Glasgow.

LARGIER, J. L., HOLLIBAUGH, J. T. & SMITH, S. V. 1997. Seasonally Hypersaline Estuaries in Mediterranean-Climate Regions. *Estuarine, Coastal and Shelf Science,* 45**,** 789-797.

LARSON, M., HANSON, H. & KRAUS, N. C. 2003. Numerical Modeling of Beach Topography Change. *In:* LAKHAN, V. C. (ed.) *Elsevier Oceanography Series*. Elsevier.

LAVENS, P. & SORGELOOS, P. 1996. Manual on the Production and Use of Live Food for Aquaculture. Available: http://www.fao.org/3/W3732E/w3732e00.htm [Accessed 2015].

LAVERY, P. S. & MCCOMB, A. 1991. Macroalgal-Sediment Nutrient Interactions and their Importance to Macroalgal Nutrition in a Eutrophic Estuary. *Estuarine, Coastal and Shelf Science,* 32**,** 281-295.

LEACH, J. 1971. Hydrology of the Ythan Estuary with Reference to Distribution of Major Nutrients and Detritus. *Journal of the Marine Biological Association of the United Kingdom,* 51, 137-157.

LEE, T. M. & YEH, H. C. 2009. Applying Remote Sensing Techniques to Monitor Shifting Wetland Vegetation: a case Study of Danshui River Estuary Mangrove Communities, Taiwan. *Ecological Engineering,* 35, 487-496.

LEGLEITER, C. J., KYRIAKIDIS, P. C., MCDONALD, R. R. & NELSON, J. M. 2011. Effects of Uncertain Topographic Input Data on Two-Dimensional Flow Modeling in a Gravel-Bed River. *Water Resources Research,* 47.

LEMARIE, M., VAN DER ZAAG, P., MENTING, G., BAQUETE, E. & SCHOTANUS, D. 2006. The Use of Remote Sensing for Monitoring Environmental Indicators: the Case of the Incomati Estuary, Mozambique. *Physics and Chemistry of the Earth, Parts A/B/C,* 31, 857-863.

LEOTE, C., MULDER, L. L., PHILIPPART, C. J. M. & EPPING, E. H. G. 2016. Nutrients in the Western Wadden Sea: Freshwater Input Versus Internal Recycling. *Estuaries and Coasts,* 39, 40-53.

LESSER, G., ROELVINK, J., VAN KESTER, J. & STELLING, G. 2004. Development and Validation of a Three-Dimensional Morphological Model. *Coastal Engineering,* 51, 883-915.

LESSER, G., VAN KESTER, J., ROELVINK, J. & STELLING, G. 2001. Three-Dimensional Morphological Modelling in Delft3D-FLOW. Available: http://citeseerx.ist.psu.edu/viewdoc/download?doi=10.1.1.136.50&rep=rep1&type=pdf [Accessed 2015].

LI, F., ZHANG, H., ZHU, Y., XIAO, Y. & CHEN, L. 2013. Effect of Flow Velocity on Phytoplankton Biomass and Composition in a Freshwater Lake. *Science of the Total Environment,* 447, 64-71.

LI, X. & DAMEN, M. C. 2010. Coastline Change Detection with Satellite Remote Sensing for Environmental Management of the Pearl River Estuary, China. *Journal of Marine systems,* 82, S54-S61.

LILLEBø, A. I., NETO, J. M., MARTINS, I., VERDELHOS, T., LESTON, S., CARDOSO, P. G., FERREIRA, S. M., MARQUES, J. C. & PARDAL, M. A. 2005. Management of a Shallow Temperate Estuary to Control Eutrophication: the effect of Hydrodynamics on the System's Nutrient Loading. *Estuarine, Coastal and Shelf Science,* 65, 697-707.

LILLESAND, T., KIEFER, R. & CHIPMAN, J. 1994. *Remote Sensing and Image Interpretation,* Hoboken, New Jersey, USA, John Wiley & Sons.

LIN, H. J. & HUNG, J. J. 2004. Factors Affecting Macroalgal Distribution in a Eutrophic Tropical Lagoon in Taiwan. *Marine Biology,* 144, 653-664.

LIST, J. H., HANES, D. M. & RUGGIERO, P. Predicting Longshore Gradients in Longshore Transport: Comparing the CERC Formula to Delft3D. The International Conference on Coastal Engineering, 2006. American Society of Civil Engineers (ASCE), 3370.

LIU, D., KEESING, J. K., XING, Q. & SHI, P. 2009. World's Largest Macroalgal Bloom Caused by Expansion of Seaweed Aquaculture in China. *Marine Pollution Bulletin,* 58, 888-895.

LIU, X. 2008. Airborne LiDAR for DEM Generation: Some Critical Issues. *Progress in Physical Geography,* 32, 31-49.

LU, D., MAUSEL, P., BRONDIZIO, E. & MORAN, E. 2004. Change Detection Techniques. *International Journal of Remote Sensing,* 25, 2365-2401.

LUIJENDIJK, A. 2001. *Validation, Calibration and Evaluation of Delft3D-FLOW Model with Ferry Measurements.* Master Thesis, TU Delft.

LURTON, X. 2002. *An Introduction to Underwater Acoustics: Principles and Applications,* Berlin, Germany, Springer-Verlag Berlin and Heidelberg GmbH & Co.

LYONS, M., BALLS, P. & TURRELL, W. 1993. A Preliminary Study of the Relative Importance of Riverine Nutrient Inputs to the Scottish North Sea Coastal Zone. *Marine Pollution Bulletin,* 26, 620-628.

MACCREADY, P. 1999. Estuarine Adjustment to Changes in River Flow and Tidal Mixing. *Journal of Physical Oceanography,* 29, 708-726.

MACHIELS, O., ERPICUM, S., DEWALS, B., ARCHAMBEAU, P. & PIROTTON, M. 2009. Continuous Formulation for Bottom Friction in Free Surface Flows Modelling. *WIT Transactions on Ecology and the Environment* [Online], 124. Available: https://www.witpress.com/Secure/elibrary/papers/RM09/RM09008FU1.pdf.

MADDOCK, A. 2008. UK Biodiversity Action Plan: Priority Habitat Descriptions. Available: http://jncc.defra.gov.uk/PDF/UKBAP_PriorityHabitatDesc-Rev2011.pdf.

MAIER, G., GLEGG, G. A., TAPPIN, A. D. & WORSFOLD, P. J. 2012. A High Resolution Temporal Study of Phytoplankton Bloom Dynamics in the Eutrophic Taw Estuary (SW England). *Science of the Total Environment,* 434, 228-239.

MAIER, G., NIMMO-SMITH, R. J., GLEGG, G. A., TAPPIN, A. D. & WORSFOLD, P. J. 2009. Estuarine Eutrophication in the UK: Current Incidence and Future Trends. *Aquatic Conservation: Marine and Freshwater Ecosystems,* 19, 43-56.

MAIER, H. R., BURCH, M. D. & BORMANS, M. 2001. Flow Management Strategies to Control Blooms of the Cyanobacterium, Anabaena Circinalis, in the River Murray at Morgan, South Australia. *River Research and Applications,* 17, 637-650.

MANAVALAN, P., SATHYANATH, P. & RAJEGOWDA, G. 1993. Digital Image Analysis Techniques to Estimate Waterspread for Capacity Evaluations of Reservoirs. *Photogrammetric Engineering and Remote Sensing,* 59, 1389-1395.

MANTAS, V. M., PEREIRA, A. J. S. C., NETO, J., PATRíCIO, J. & MARQUES, J. C. 2013. Monitoring Estuarine Water Quality using Satellite Imagery. The

Mondego River Estuary (Portugal) as a Case Study. *Ocean & Coastal Management,* 72**,** 13-21.

MARCHISIO, G., PACIFICI, F. & PADWICK, C. On the Relative Predictive Value of the New Spectral Bands in the Worldview-2 Sensor. Geoscience and Remote Sensing Symposium (IGARSS), 2010 IEEE International, 2010. IEEE, 2723-2726.

MARTINS, I. & MARQUES, J. C. 2002. A Model for the Growth of Opportunistic Macroalgae (Enteromorpha sp.) in Tidal Estuaries. *Estuarine, Coastal and Shelf Science,* 55**,** 247-257.

MARTINS, I., PARDAL, M., LILLEBø, A., FLINDT, M. & MARQUES, J. 2001. Hydrodynamics as a Major Factor Controlling the Occurrence of Green Macroalgal Blooms in a Eutrophic Estuary: A Case Study on the Influence of Precipitation and River Management. *Estuarine, Coastal and Shelf Science,* 52**,** 165-177.

MASHAYEK, A., FERRARI, R., MERRIFIELD, S., LEDWELL, J. R., ST LAURENT, L. & GARABATO, A. N. 2017. Topographic Enhancement of Vertical Turbulent Mixing in the Southern Ocean. *Nature Communications,* 8**,** 14197.

MASTIN, M. & FOSNESS, R. 2009. Bathymetry and Near-River Topography of the Naches and Yakima Rivers at Union Gap and Selah Gap, Yakima County, Washington, August 2008. U.S. Department of the Interior, U.S. Geological Survey.

MATTHEW, M. W., GOLDEN, S. M. A., BERK, A., RICHTSMEIER, S. C., LEVINE, R. Y., BERNSTEIN, L. S., ACHARYA, P. K., ANDERSON, G. P., FELDE, G. W., HOKE, M. L., RATKOWSKI, A. J., BURKE, H. K., KAISER, R. D. & MILLER, D. P. Status of Atmospheric Correction using a MODTRAN4-Based Algorithm. AeroSense 2000, 2000. SPIE, 9.

MAURER, T. 2013. How to Pan-Sharpen Images using the Gram-Schmidt Pan-Sharpen Method-A Recipe. *ISPRS-International Archives of the Photogrammetry, Remote Sensing and Spatial Information Sciences,* XL-1/W1**,** 239-244.

MCCARTHY, M. J., MERTON, E. J. & MULLER-KARGER, F. E. 2015. Improved Coastal Wetland Mapping using Very-High 2-meter Spatial Resolution Imagery. *International Journal of Applied Earth Observation and Geoinformation,* 40**,** 11-18.

MCCARTHY, R. K. 1993. Residual Currents in Tidally Dominated, Well-Mixed Estuaries. *Tellus A,* 45**,** 325-340.

MCCLAIN, C., HOOKER, S., FELDMAN, G. & BONTEMPI, P. 2006. Satellite Data for Ocean Biology, Biogeochemistry,and Climate Research. *Eos, Transactions, American Geophysical Union* [Online], 87. Available: https://agupubs.onlinelibrary.wiley.com/doi/epdf/10.1029/2006EO340002.

MCFEETERS, S. K. 1996. The use of the Normalized Difference Water Index (NDWI) in the delineation of open water features. *International journal of remote sensing,* 17**,** 1425-1432.

MCLUSKY, D. S., ELLIOTT, M. & OXFORD UNIVERSITY, P. 2004. *The Estuarine Ecosystem: Ecology, Threats, and Management,* Oxford, Oxford University Press.

MéLéDER, V., BARILLé, L., LAUNEAU, P., CARRèRE, V. & RINCé, Y. 2003. Spectrometric Constraint in Analysis of Benthic Diatom Biomass using Monospecific Cultures. *Remote Sensing of Environment,* 88**,** 386-400.

MITCHELL, A. 1999. *The Esri Guide to GIS Analysis: Geographic Patterns & Relationships,* Redlands, CA, ESRI Press.

MOLLES, M. C. 2010. *Ecology Concepts & Applications,* Boston, MA, McGraw-Hill Higher Education.

MOORE, T. S., CAMPBELL, J. W. & DOWELL, M. D. 2009. A Class-Based Approach to Characterizing and Mapping the Uncertainty of the MODIS Ocean Chlorophyll Product. *Remote Sensing of Environment,* 113**,** 2424-2430.

MORRIS, C. T. & MORRIS, R. M. 2005. The Ythan Project: a Case Study on Improving Catchment Management through Community Involvement. *Journal of Environmental Planning and Management,* 48**,** 413-429.

MORRISSEY, J. F. & SUMICH, J. L. 2012. *Introduction to the Biology of Marine Life,* Burlington, MA, Jones & Bartlett Learning.

MUMBY, P. J., GREEN, E. P., EDWARDS, A. J. & CLARK, C. D. 1997. Coral Reef Habitat Mapping: How Much Detail can Remote Sensing Provide? *Marine Biology,* 130**,** 193-202.

MUMBY, P. J., GREEN, E. P., EDWARDS, A. J. & CLARK, C. D. 1999. The Cost-Effectiveness of Remote Sensing for Tropical Coastal Resources Assessment and Management. *Journal of Environmental Management,* 55**,** 157-166.

MURAI, S. 1993. *Remote Sensing Note,* Japan, Japan Association on Remote Sensing.

MUTANGA, O., ADAM, E. & CHO, M. A. 2012. High Density Biomass Estimation for Wetland Vegetation using WorldView-2 Imagery and Random Forest Regression Algorithm. *International Journal of Applied Earth Observation and Geoinformation,* 18**,** 399-406.

NATURE.SCOT. 2009. *Forvie National Nature Reserve: the Reserve Story* [Online]. Scottish Natural Heritage. Available: http://www.snh.org.uk/pdfs/publications/nnr/ForvieNNRTheReserveStory.pdf [Accessed 2015].

NEDWELL, D., DONG, L., SAGE, A. & UNDERWOOD, G. 2002. Variations of the Nutrients Loads to the Mainland UK Estuaries: Correlation with Catchment Areas, Urbanization and Coastal Eutrophication. *Estuarine, Coastal and Shelf Science,* 54**,** 951-970.

O'REILLY, J. E., MARITORENA, S., SIEGEL, D., O'BRIEN, M. O., TOOLE, D., MITCHELL, B. G., KAHRU, M., CHAVEZ, F., STRUTTON, P. G., COTA, G. F., HOOKER, S. B., MCCLAIN, C., CARDER, K., MULLER-KARGER, F., HARDING, L., MAGNUSON, A., PHINNEY, D., MOORE, G., AIKEN, J., ARRIGO, K. R., LETELIER, R. M. & CULVER, M. 1998. Ocean Color Chlorophyll Algorithms for SeaWiFS. *Journal of Geophysical Research: Oceans,* 103**,** 24937-24953.

OC.NPS.EDU. 2003. *Model Initialization and Spin-Up* [Online]. Available: http://www.oc.nps.edu/nom/modeling/initial.html [Accessed 2015].

OMAR, H. 2010. Commercial Timber Tree Species Identification using Multispectral Worldview-2 Data. *Digital Globe 8 Bands Research Challenge*.

OUELLETTE, W. & GETINET, W. 2016. Remote Sensing for Marine Spatial Planning and Integrated Coastal Areas Management: Achievements, Challenges, Opportunities and Future Prospects. *Remote Sensing Applications: Society and Environment,* 4, 138-157.

OUMAR, Z. & MUTANGA, O. 2013. Using WorldView-2 Bands and Indices to Predict Bronze Bug (Thaumastocoris Peregrinus) Damage in Plantation Forests. *International Journal of Remote Sensing,* 34, 2236-2249.

PAIVA, R. C., COLLISCHONN, W. & BUARQUE, D. C. 2013. Validation of a Full Hydrodynamic Model for Large-Scale Hydrologic Modelling in the Amazon. *Hydrological Processes,* 27, 333-346.

PANIGRAHI, K. & KHATUA, K. Analysis of Different Roughness Coefficients' Variation in an Open Channel with Vegetation. International Conference on Technologies for Sustainable Development (ICTSD), 2015. IEEE, 1-5.

PANNELL, D. J. 1997. Sensitivity Analysis: Strategies, Methods, Concepts, Examples. *Agric Econ,* 16, 139-152.

PARIDA, A. K. & DAS, A. B. 2005. Salt Tolerance and Salinity Effects on Plants: a Review. *Ecotoxicology and Environmental Safety,* 60, 324-349.

PEDERSEN, M. F. & BORUM, J. 1996. Nutrient Control of Algal Growth in Estuarine Waters. Nutrient Limitation and the Importance of Nitrogen Requirements and Nitrogen Storage among Phytoplankton and Species of Macroalgae. *Marine Ecology Progress Series*, 261-272.

PEDERSON, M. F. & BORUM, J. 1997. Nutrient Control of Estuarine Macroalgae: Growth Strategy and the Balance Between Nitrogen Requirements and Uptake. *Marine Ecology Progress Series*, 155-163.

PERILLO, G. M. E. 1995. Geomorphology and Sedimentology of Estuaries: An Introduction. *In:* PERILLO, G. M. E. (ed.) *Developments in Sedimentology*. Elsevier.

PETTORELLI, N., VIK, J. O., MYSTERUD, A., GAILLARD, J.-M., TUCKER, C. J. & STENSETH, N. C. 2005. Using the Satellite-Derived NDVI to Assess Ecological Responses to Environmental Change. *Trends in Ecology & Evolution,* 20, 503-510.

PIETRONIRO, A., LECONTE, R., PETERS, D. L. & PROWSE, T. D. 2001. Application of a Hydrodynamic Model in a Freshwater Delta using Remote Sensing. *IAHS Publication*, 519-525.

PRABHAKARA, K., HIVELY, W. D. & MCCARTY, G. W. 2015. Evaluating the Relationship between Biomass, Percent Ground Cover and Remote Sensing Indices Across Six Winter Cover Crop Fields in Maryland, United States. *International Journal of Applied Earth Observation and Geoinformation,* 39, 88-102.

PRANDLE, D. & LANE, A. 2015. Sensitivity of Estuaries to Sea Level Rise: Vulnerability Indices. *Estuarine, Coastal and Shelf Science,* 160**,** 60-68.

PUGH, K. 1998. Water Quality in the River Ythan. *The Natural History of the Ythan*. University of Aberdeen.

RAFFAELLI, D. 1995. Long-term Changes in Nutrients, Weed Mats and Shorebirds in an Estuarine System. *Environmental Pollution,* 90**,** 311-321.

RAFFAELLI, D. 1999. Nutrient enrichment and trophic organisation in an estuarine food web. *Acta Oecologica,* 20**,** 449-461.

RAFFAELLI, D. 2000. Interactions Between Macro-Algal Mats and Invertebrates in the Ythan Estuary, Aberdeenshire, Scotland. *Helgoland Marine Research,* 54**,** 71-79.

RAFFAELLI, D., BALLS, P., WAY, S., PATTERSON, I. J., HOHMANN, S. & CORP, N. 1999. Major Long-Term Changes in the Ecology of the Ythan Estuary, Aberdeenshire, Scotland; How Important are Physical Factors? *Aquatic Conservation: Marine and Freshwater Ecosystems,* 9**,** 219-236.

RAFFAELLI, D., RAVEN, J. & POOLE, L. 1998. Ecological Impact of Green Macroalgal Blooms. *In:* ALAN, A., MARGARET, B. & GIBSON, R. N. (eds.) *Oceanography And Marine Biology: An Annual Review*. CRC Press

RAO, A. R., DAYANANDA, C., SARADA, R., SHAMALA, T. R. & RAVISHANKAR, G. A. 2007. Effect of Salinity on Growth of Green Alga Botryococcus Braunii and its Contituents. *Bioresource Technology,* 98**,** 560-564.

RAPINEL, S., CLéMENT, B., MAGNANON, S., SELLIN, V. & HUBERT-MOY, L. 2014. Identification and Mapping of Natural Vegetation on a Coastal site using a Worldview-2 Satellite Image. *Journal of Environmental Management,* 144**,** 236-246.

READING, H. G. 1996. *Sedimentary Environments: Processes, Facies, and Stratigraphy,* Oxford, Blackwell Science.

RESHITNYK, L., COSTA, M., ROBINSON, C. & DEARDEN, P. 2014. Evaluation of WorldView-2 and Acoustic Remote Sensing for Mapping Benthic Habitats in Temperate Coastal Pacific Waters. *Remote Sensing of Environment,* 153**,** 7-23.

RICHARDS, J. A. 1999. *Remote Sensing Digital Image Analysis*, Springer.

RICHARDS, J. A. & JIA, X. 2006. Remote Sensing Digital Image Analysis. Berlin/Heidelberg: Springer.

ROBINS, P. E., SKOV, M. W., LEWIS, M. J., GIMéNEZ, L., DAVIES, A. G., MALHAM, S. K., NEILL, S. P., MCDONALD, J. E., WHITTON, T. A., JACKSON, S. E. & JAGO, C. F. 2016. Impact of Climate Change on UK Estuaries: A review of Past Trends and Potential Projections. *Estuarine, Coastal and Shelf Science,* 169**,** 119-135.

ROBINSON, I. S. 2004. *Measuring the Oceans from Space: The Principles and Methods of Satellite Oceanography*, Springer-Verlag Berlin Heidelberg.

RODI, W. 1993. *Turbulence Models and their Application in Hydraulics*, CRC Press.

ROELFSEMA, C. M., PHINN, S. R., DENNISON, W. C., DEKKER, A. G. & BRANDO, V. E. 2006. Monitoring Toxic Cyanobacteria Lyngbya Majuscula (Gomont) in Moreton Bay, Australia by Integrating Satellite Image Data and Field Mapping. *Harmful Algae,* 5**,** 45-56.

ROSS, D. A. 1995. *Introduction to Oceanography,* New York, NY, Harper Collins College Publishers.

ROUSE JR, J. W., HAAS, R., SCHELL, J. & DEERING, D. 1974. Monitoring Vegetation Systems in the Great Plains with ERTS. *Third Earth Resources Technology Satellite-1 Symposium.* Goddard Space Flight Center, NASA: Texas A&M University.

RUDDICK, K., PARK, Y., ASTORECA, R., BORGES, A., LACROIX, G., LANCELOT, C. & ROUSSEAU, V. 2008. Applications of the MERIS Algal Pigment Products in Belgian Waters. *The 2nd MERIS -(A)ATSR workshop.* Frascati, Italy: ESA Special Publication.

RYBAK, A. S. 2018. Species of Ulva (Ulvophyceae, Chlorophyta) as Indicators of Salinity. *Ecological Indicators,* 85**,** 253-261.

RYU, J. H., WON, J. S. & MIN, K. D. 2002. Waterline Extraction from Landsat TM Data in a Tidal Flat: a Case Study in Gomso Bay, Korea. *Remote Sensing of Environment,* 83**,** 442-456.

SALTELLI, A., RATTO, M., ANDRES, T., CAMPOLONGO, F., CARIBONI, J., GATELLI, D., SAISANA, M. & TARANTOLA, S. 2008. *Global Sensitivity Analysis: The Primer,* Chichester, UK, John Wiley & Sons.

SANTRA, A. & MITRA, S. S. 2016. *Remote Sensing Techniques and GIS Applications in Earth and Environmental Studies,* IGI Global.

SCHRAMM, W. & NIENHUIS, P. 1996. Marine Benthic Vegetation, Ecological Studies. *In:* WINFRID, S. & PIETER, H. N. (eds.) *The Ecological Studies (ECOLSTUD).* Springer Verlag, Heidelberg.

SEGURO, I., GARCíA, C. M., PAPASPYROU, S., GáLVEZ, J. A., GARCíA-ROBLEDO, E., NAVARRO, G., SORIA-PíRIZ, S., AGUILAR, V., LIZANO, O. G., MORALES-RAMíREZ, A. & CORZO, A. 2015. Seasonal Changes of the Microplankton Community along a Tropical Estuary. *Regional Studies in Marine Science,* 2**,** 189-202.

SELMAN, M., SUGG, Z., GREENHALGH, S. & DIAZ, R. 2010. Eutrophication and Hypoxia in Coastal Areas: a Global Assessment of the State of Knowledge *WRI Policy Notes* [Online], 1.

SHAERI, S., TOMLINSON, R., ETEMAD-SHAHIDI, A. & STRAUSS, D. 2017. Numerical Modelling to Assess Maintenance Strategy Management Options for a Small Tidal Inlet. *Estuarine, Coastal and Shelf Science,* 187**,** 273-292.

SHERMAN, B. S., WEBSTER, I. T., JONES, G. J. & OLIVER, R. L. 1998. Transitions Between Auhcoseira and Anabaena Dominance in a Turbid River Weir Pool. *Limnology and Oceanography,* 43**,** 1902-1915.

SICHANGI, A. W., WANG, L., YANG, K., CHEN, D., WANG, Z., LI, X., ZHOU, J., LIU, W. & KURIA, D. 2016. Estimating Continental River Basin Discharges using

Multiple Remote Sensing Data Sets. *Remote Sensing of Environment,* 179, 36-53.

SINGH, S. P. & SINGH, P. 2015. Effect of Temperature and Light on the Growth of Algae Species: a Review. *Renewable and Sustainable Energy Reviews,* 50, 431-444.

SMITH, V. H., TILMAN, G. D. & NEKOLA, J. C. 1999. Eutrophication: Impacts of Excess Nutrient Inputs on Freshwater, Marine, and Terrestrial Ecosystems. *Environmental Pollution,* 100, 179-196.

SORCE, C., PERSIANO LEPORATTI, M. & LENZI, M. 2018. Growth and Physiological Features of Chaetomorpha Linum (Müller) Kütz. in High Density Mats. *Marine Pollution Bulletin,* 129, 772-781.

SOULSBY, P. G., LOWTHION, D. & HOUSTON, M. 1982. Effects of Macroalgal Mats on the Ecology of Intertidal Mudflats. *Marine Pollution Bulletin,* 13, 162-166.

SOUSA, A. I., MARTINS, I., LILLEBø, A. I., FLINDT, M. R. & PARDAL, M. A. 2007. Influence of Salinity, Nutrients and Light on the Germination and Growth of Enteromorpha sp. Spores. *Journal of Experimental Marine Biology and Ecology,* 341, 142-150.

STUMPF, R. P. 2001. Applications of Satellite Ocean Color Sensors for Monitoring and Predicting Harmful Algal Blooms. *Human and Ecological Risk Assessment: An International Journal,* 7, 1363-1368.

SU, H. M., LIN, H. J. & HUNG, J. J. 2004. Effects of Tidal Flushing on Phytoplankton in a Eutrophic Tropical Lagoon in Taiwan. *Estuarine, Coastal and Shelf Science,* 61, 739-750.

SUN, W., ISHIDAIRA, H. & BASTOLA, S. 2010. Towards Improving River Discharge Estimation in Ungauged Basins: Calibration of Rainfall-Runoff Models Based on Satellite Observations of River Flow Width at Basin Outlet. *Hydrology and Earth System Sciences Discussions,* 7, 3803-3836.

SWIFT, D. A. 2002. *Provenance of Suspended Sediment in Subglacial Drainage Systems.* PhD Thesis, University of Glasgow.

SYMONDS, A., VIJVERBERG, T., POST, S., VAN DER SPEK, B. J. & HENROTTE, J. Comparison between MIKE 21 FM, Delft3D and Delft3D FM Flow Models of Western Port Bay, Australia. 35th Conference on Coastal Engineering, 2017 Antalya, Turkey. The International Conference on Coastal Engineering (ICCE).

TAPIA GONZáLEZ, F. U., HERRERA SILVEIRA, J. A. & AGUIRRE MACEDO, M. L. 2008. Water Quality Variability and Eutrophic Trends in Karstic Tropical Coastal Lagoons of the Yucatán Peninsula. *Estuarine, Coastal and Shelf Science,* 76, 418-430.

TARPANELLI, A., BARBETTA, S., BROCCA, L. & MORAMARCO, T. 2013. River Discharge Estimation by using Altimetry Data and Simplified Flood Routing Modeling. *Remote Sensing,* 5, 4145-4162.

TAYLOR, R. 1999. The Green Tide Threat in the UK-a Brief Overview with Particular Reference to Langstone Harbour, South Coast of England and the

Ythan Estuary, East Coast of Scotland. *Botanical Journal of Scotland,* 51, 195-203.

TENG, J., JAKEMAN, A. J., VAZE, J., CROKE, B. F. W., DUTTA, D. & KIM, S. 2017. Flood Inundation Modelling: a Review of Methods, Recent Advances and Uncertainty Analysis. *Environmental Modelling & Software,* 90, 201-216.

TETZLAFF, D., SOULSBY, C., HRACHOWITZ, M. & SPEED, M. 2011. Relative Influence of Upland and Lowland Headwaters on the Isotope Hydrology and Transit Times of Larger Catchments. *Journal of Hydrology,* 400, 438-447.

TIIT, K. 2004. Quantitative Detection of Chlorophyll in Cyanobacterial Blooms by Satellite Remote Sensing. *Limnology and Oceanography,* 49, 2179-2189.

TIKHOMIROV, V. M. 1991. Equations of Turbulent Motion in an Incompressible Fluid. *In:* TIKHOMIROV, V. M. (ed.) *Selected Works of A. N. Kolmogorov: Volume I: Mathematics and Mechanics*. Dordrecht: Springer Netherlands.

TRAAEN, T. & LINDSTRøM, E.-A. 1983. Influence of Current Velocity on Periphyton Distribution. *Periphyton of Freshwater Ecosystems*. Springer.

TRANCOSO, A. R., SARAIVA, S., FERNANDES, L., PINA, P., LEITãO, P. & NEVES, R. 2005. Modelling Macroalgae using a 3D Hydrodynamic-Ecological Model in a Shallow, Temperate Estuary. *Ecological Modelling,* 187, 232-246.

TRIBE, E. & BALL, D. 2005. A Review of the Hydrogeology Element of the Griffin Wind Farm Environmental Statement. British Geological Survey

TSUTSUI, I., MIYOSHI, T., AUEUMNEOY, D., SONGPHATKAEW, J., MEEANAN, C., KLOMKLING, S., SUKCHAI, H., PINPHOO, P., YAMAGUCHI, I., GANMANEE, M., MAENO, Y. & HAMANO, K. 2015. High Tolerance of Chaetomorpha sp. to Salinity and Water Temperature Enables Survival and Growth in Stagnant Waters of Central Thailand. *International Aquatic Research,* 7, 47-62.

TUCKER, C. J., GOFF, T. & TOWNSHEND, J. 1985. African Land Cover Classification using Satellite Data. *Science,* 227, 369-375.

TURNER, W., SPECTOR, S., GARDINER, N., FLADELAND, M., STERLING, E. & STEININGER, M. 2003. Remote Sensing for Biodiversity Science and Conservation. *Trends in Ecology & Evolution,* 18, 306-314.

UITTENBOGAARD, R. 1998. Model for Eddy Diffusivity and Viscosity Related to Sub-Grid Velocity and Bed Topography. WL| Delft Hydraulics.

UITTENBOGAARD, R. & VAN VOSSEN, B. 2004. *Subgrid-Scale Model for Quasi-2D Turbulence in Shallow Water*, Taylor and Francis.

UNDERWOOD, G. J. 2010. Microphytobenthos and Phytoplankton in the Severn Estuary, UK: Present Situation and Possible Consequences of a Tidal Energy Barrage. *Marine Pollution Bulletin,* 61, 83-91.

UPDIKE, T. & COMP, C. 2010. Radiometric Use of WorldView-2 Imagery Available: https://dg-cms-uploads-production.s3.amazonaws.com/uploads/document/file/104/Radiometric_Use_of_WorldView-2_Imagery.pdf [Accessed 2018].

USGS. 2016. LANDSAT-8 (L8) Data Users Handbook. Available: https://prd-wret.s3-us-west-2.amazonaws.com/assets/palladium/production/s3fs-

public/atoms/files/LSDS-1574_L8_Data_Users_Handbook.pdf [Accessed 2018].

VALLE-LEVINSON, A. 2010. Definition and Classification of Estuaries. *In:* VALLE-LEVINSON, A. (ed.) *Contemporary Issues in Estuarine Physics*. Cambridge: Cambridge University Press.

VALLE, M., PALA, V., LAFON, V., DEHOUCK, A., GARMENDIA, J. M., BORJA, Á. & CHUST, G. 2015. Mapping Estuarine Habitats using Airborne Hyperspectral Imagery, with Special Focus on Seagrass Meadows. *Estuarine, Coastal and Shelf Science,* 164**,** 433-442.

VALLINO, J. J. & HOPKINSON, J. C. S. 1998. Estimation of Dispersion and Characteristic Mixing Times in Plum Island Sound Estuary. *Estuarine, Coastal and Shelf Science,* 46**,** 333-350.

VAN DER MEULEN, M., KLEISSEN, F., EL SERAFY, G., STUPARU, D. & VETHAAK, A. Developing a Transport Model for Plastic Distribution in the North Sea. 36th IAHR World Congress, 2015 Delf, The Netherlands. Chemistry and Biology, Amsterdam Global Change Institute.

VAN DER WAL, D., VAN DALEN, J., WIELEMAKER-VAN DEN DOOL, A., DIJKSTRA, J. T. & YSEBAERT, T. 2014. Biophysical Control of Intertidal Benthic Macroalgae Revealed by High-Frequency Multispectral Camera Images. *Journal of Sea Research,* 90**,** 111-120.

VAN DER WAL, D., WIELEMAKER-VAN DEN DOOL, A. & HERMAN, P. M. 2010. Spatial Synchrony in Intertidal Benthic Algal Biomass in Temperate Coastal and Estuarine Ecosystems. *Ecosystems,* 13**,** 338-351.

VAN DONGEREN, A. 2009. Delft3D-Modelling of Hydrodynamic and Water Quality Processes in San Diego Bight. Deltares, The Netherlands.

VAN VOSSEN, B. 2000. Horizontal Large Eddy Simulations; Evaluation of Computations with DELFT3D-FLOW. Delft University of Technology.

VIGNAGA, E., SLOAN, D. M., LUO, X., HAYNES, H., PHOENIX, V. R. & SLOAN, W. T. 2013. Erosion of Biofilm-Bound Fluvial Sediments. *Nature Geoscience,* 6**,** 770.

VIGNUDELLI, S., KOSTIANOY, A. G., CIPOLLINI, P. & BENVENISTE, J. 2011. *Coastal Altimetry*, Springer Science & Business Media.

WALLACE, R. B. & GOBLER, C. J. 2015. Factors Controlling Blooms of Microalgae and Macroalgae (Ulva rigida) in a Eutrophic, Urban estuary: Jamaica Bay, NY, USA. *Estuaries and Coasts,* 38**,** 519.

WANG, R., GAMON, J. A., MONTGOMERY, R. A., TOWNSEND, P. A., ZYGIELBAUM, A. I., BITAN, K., TILMAN, D. & CAVENDER-BARES, J. 2016. Seasonal Variation in the NDVI-Species Richness Relationship in a Prairie Grassland Experiment (Cedar Creek). *Remote Sensing,* 8**,** 15.

WEBB, D. 2001. Numerical Models of Oceans and Oceanic Processes. *Journal of Fluid Mechanics,* 432.

WEHLAGE, D. C., GAMON, J. A., THAYER, D. & HILDEBRAND, D. V. 2016. Interannual Variability in Dry Mixed-Grass Prairie Yield: a Comparison of MODIS, SPOT, and Field Measurements. *Remote Sensing,* 8**,** 19.

WHITE, K. & EL ASMAR, H. M. 1999. Monitoring Changing Position of Coastlines using Thematic Mapper Imagery, an Example From the Nile Delta. *Geomorphology,* 29**,** 93-105.

WILLIAMS, R., BRASINGTON, J., HICKS, M., MEASURES, R., RENNIE, C. & VERICAT, D. 2013. Hydraulic Validation of Two-Dimensional Simulations of Braided River Flow with Spatially Continuous aDcp Data. *Water Resources Research,* 49**,** 5183-5205.

WOLANSKI, E., BOORMAN, L., CHíCHARO, L., LANGLOIS-SALIOU, E., LARA, R., PLATER, A., UNCLES, R. & ZALEWSKI, M. 2004. Ecohydrology as a New Tool for Sustainable Management of Estuaries and Coastal Waters. *Wetlands Ecology and Management,* 12**,** 235-276.

WOLANSKI, E. & ELLIOTT, M. 2016. Introduction. *Estuarine Ecohydrology (Second Edition)*. Boston: Elsevier.

WOLF, P. R. & GHILANI, C. D. 2008. *Elementary Surveying: An Introduction to Geomatics,* Prentice Hall.

WOO, I., STORESUND, R. & TAKEKAWA, J. Integrating Terrestrial LiDAR and Stereo Photogrammetry to Map the Tolay Lakebed in Northern San Francisco Bay. The Third Interagency Conference on Research in the Watersheds, 2018 Estes Park, CO, USA.

WOOLF, D. K. & GOMMENGINGER, C. 2008. Radar Altimetry: Introduction and Application to Air-Sea Interaction. *In:* BARALE, V. & GADE, M. (eds.) *Remote Sensing of the European Seas*. Dordrecht: Springer Netherlands.

WULDER, M. A., HALL, R. J., COOPS, N. C. & FRANKLIN, S. E. 2004. High Spatial Resolution Remotely Sensed Data for Ecosystem Characterization. *BioScience,* 54**,** 511-521.

XING, Q., HU, C., TANG, D., TIAN, L., TANG, S., HUA WANG, X., LOU, M. & GAO, X. 2015. World's Largest Macroalgal Blooms Altered Phytoplankton Biomass in Summer in the Yellow Sea: Satellite Observations. *Remote Sensing,* 7**,** 12297-12313.

XU, H. 2006. Modification of Normalised Difference Water Index (NDWI) to Enhance Open Water Features in Remotely Sensed Imagery. *International journal of remote sensing,* 27**,** 3025-3033.

XU, Y. & LIN, J. 2008. Effect of Temperature, Salinity, and Light Intensity on the Growth of the Green Macroalga, Chaetomorpha Linum. *Journal of the World Aquaculture Society,* 39**,** 847-851.

YEN, B. C. 2002. Open Channel Flow Resistance. *Journal of Hydraulic Engineering,* 128**,** 20-39.

YIN, K. & HARRISON, P. J. 2000. Influences of Flood and Ebb Tides on Nutrient Fluxes and Chlorophyll on an Intertidal Flat. *Marine Ecology Progress Series***,** 75-85.

YOUNG, K., MORSE, G., SCRIMSHAW, M., KINNIBURGH, J., MACLEOD, C. & LESTER, J. 1999. The Relation Between Phosphorus and Eutrophication in the Thames Catchment, UK. *Science of the Total Environment,* 228**,** 157-183.

YUHENDRA, J. & KUZE, H. 2011. Performance Analyzing of High Resolution Pan-sharpening Techniques: Increasing Image Quality for Classification using Supervised Kernel Support Vector Machine. *Research Journal of Information Technology,* 8**,** 12-28.

ZARZUELO, C., LóPEZ-RUIZ, A., DíEZ-MINGUITO, M. & ORTEGA-SáNCHEZ, M. 2017. Tidal and Subtidal Hydrodynamics and Energetics in a Constricted Estuary. *Estuarine, Coastal and Shelf Science,* 185**,** 55-68.

ZHANG, H., CHEN, R., LI, F. & CHEN, L. 2015. Effect of Flow Rate on Environmental Variables and Phytoplankton Dynamics: Results From Field Enclosures. *Chinese Journal of Oceanology and Limnology,* 33**,** 430.

ZHANG, X., HU, Y., ZHUANG, D., QI, Y. & MA, X. 2009. NDVI Spatial Pattern and its Differentiation on the Mongolian Plateau. *Journal of Geographical Sciences,* 19**,** 403-415.

ZHAO, F., HUAI, W. & LI, D. 2017. Numerical Modeling of Open Channel Flow with Suspended Canopy. *Advances in Water Resources,* 105**,** 132-143.

ZHOU, J., FALCONER, R. A. & LIN, B. 2014. Refinements to the EFDC Model for Predicting the Hydro-Environmental Impacts of a Barrage Across the Severn Estuary. *Renewable Energy,* 62**,** 490-505.

ZHOU, X., JANCSó, T., CHEN, C. & VERONE, M. Urban Land Cover Mapping Based on Object Oriented Classification Using WorldView 2 Satellite Remote Sensing Images. International Scientific Conference on Sustainable Development & Ecological Footprint, 2012. 26-27.

ZHU, G., QIN, B., GAO, G., ZHANG, L., LUO, L. & ZHANG, Y. 2007. Effects of Hydrodynamics on Phosphorus Concentrations in Water of Lake Taihu, a Large, Shallow, Eutrophic Lake of China. *Hydrobiologia,* 581**,** 53-61.

ZOU, T., ZHANG, H., MENG, Q. & LI, J. 2016. Seasonal Hydrodynamics and Salt Exchange of a Shallow Estuary in Northern China. *Journal of Coastal Research*, 95-103.

# Appendix

## Supplement Figures

### 1. Scatter plot of temperature against river flow 2009 and 2011

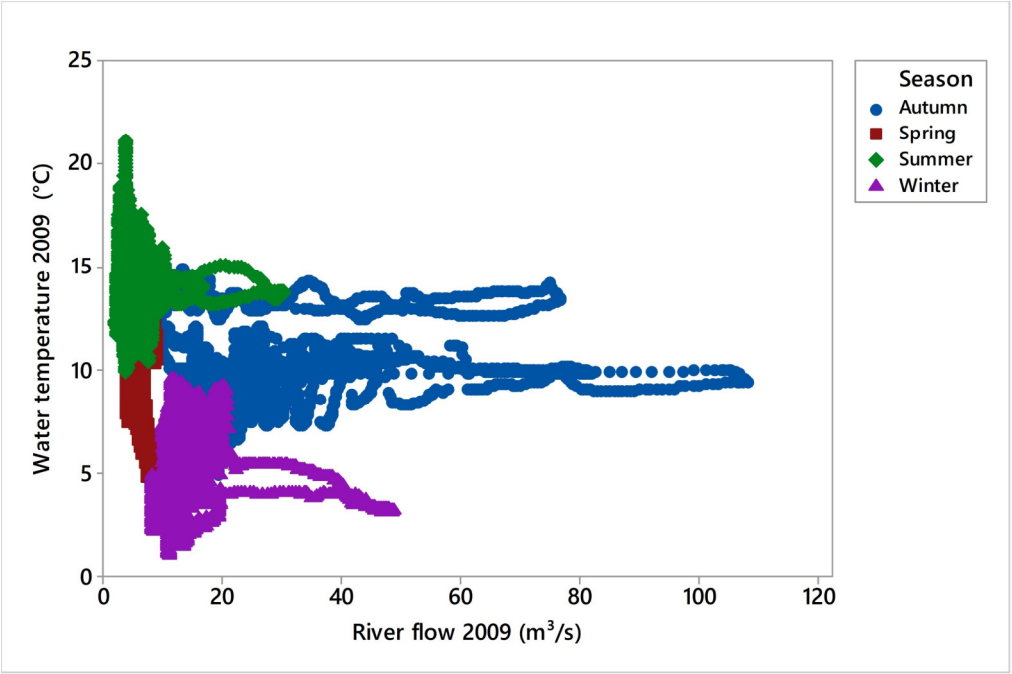


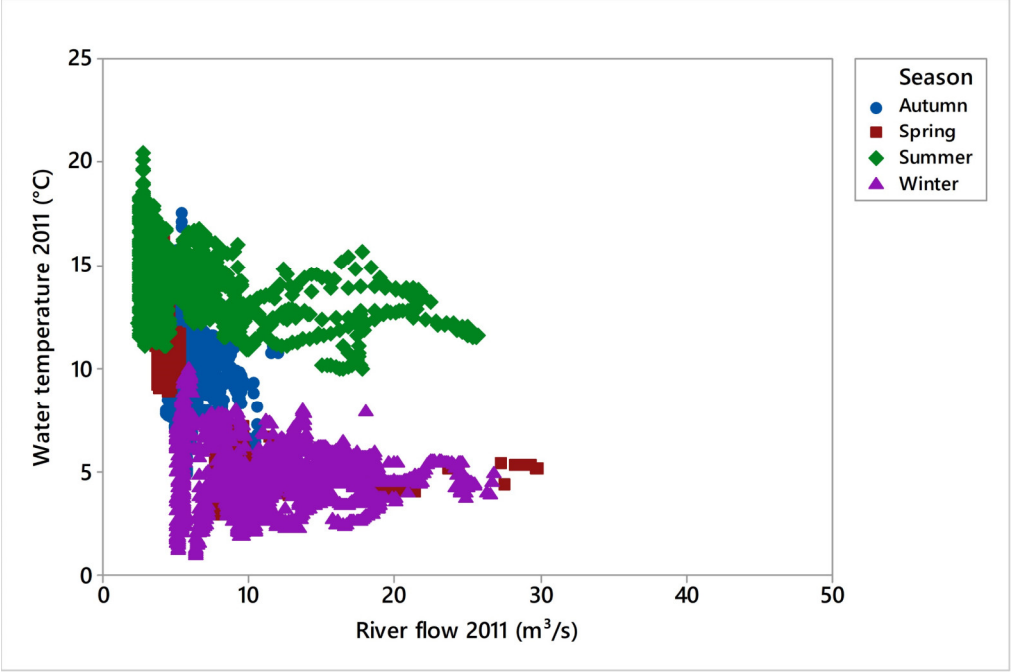

## 2. Scatter plot of pH against river flow 2009 and 2011

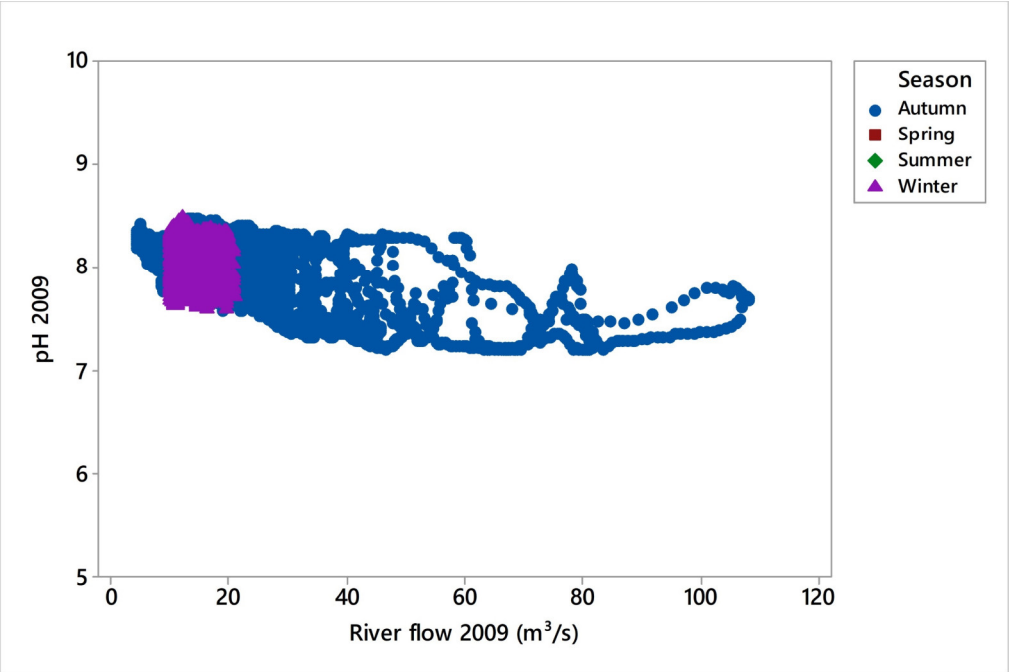


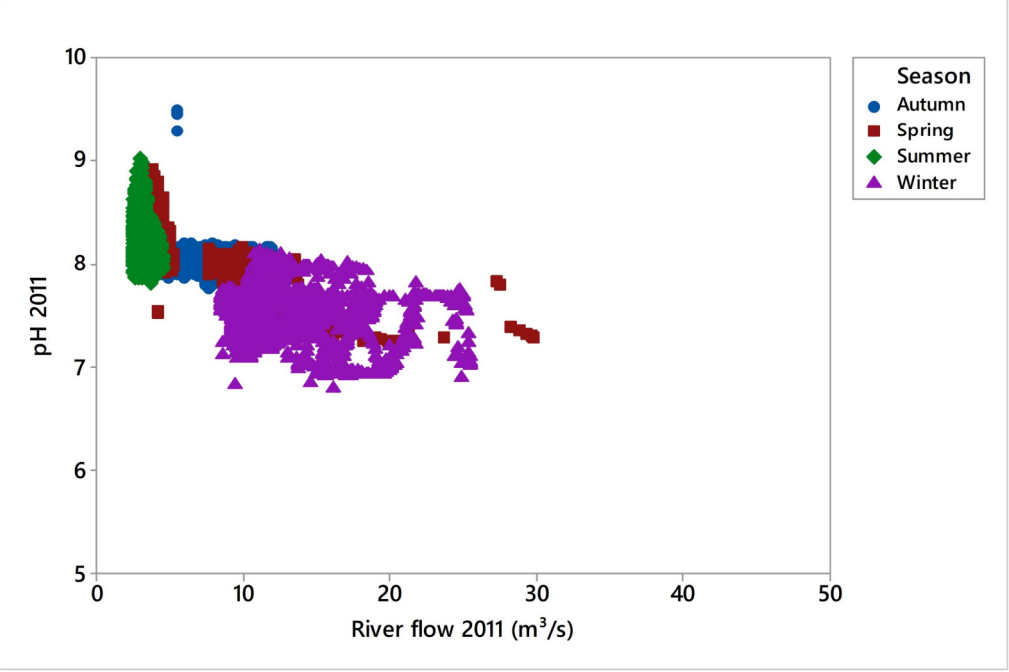

## 3. Scatter plot of DO against river flow 2009 and 2011

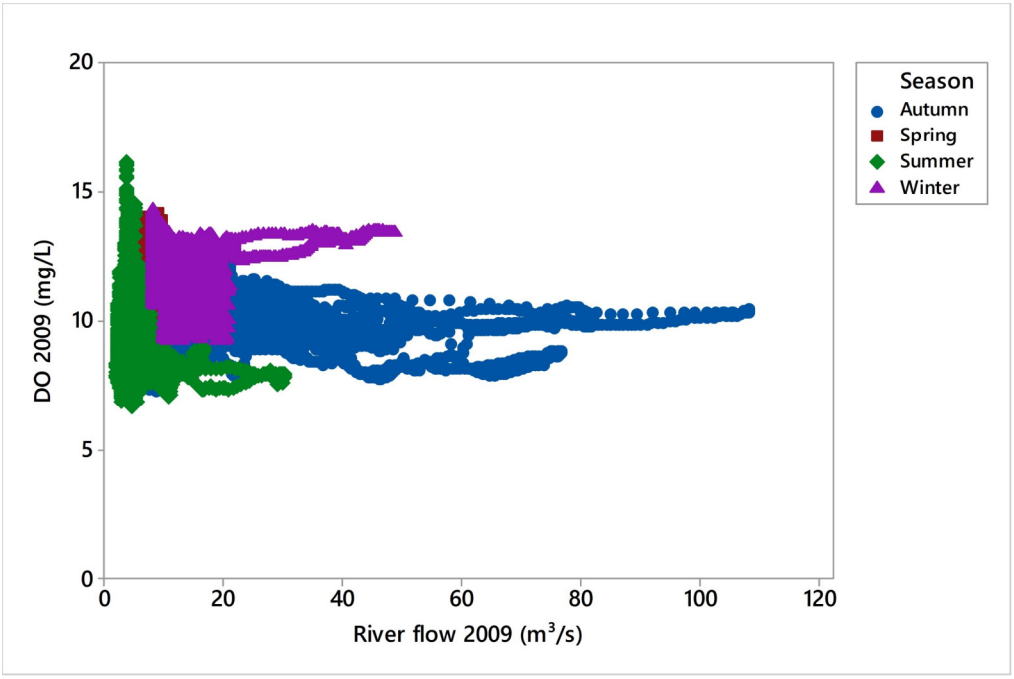


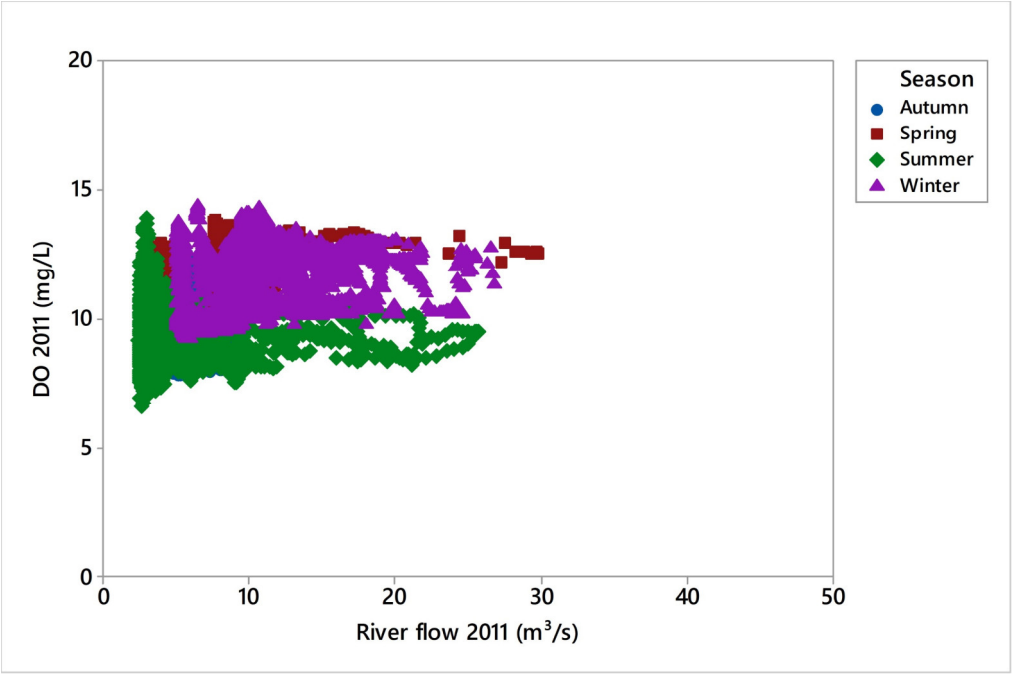

## 4. Scatter plot of turbidity against river flow 2009 and 2011

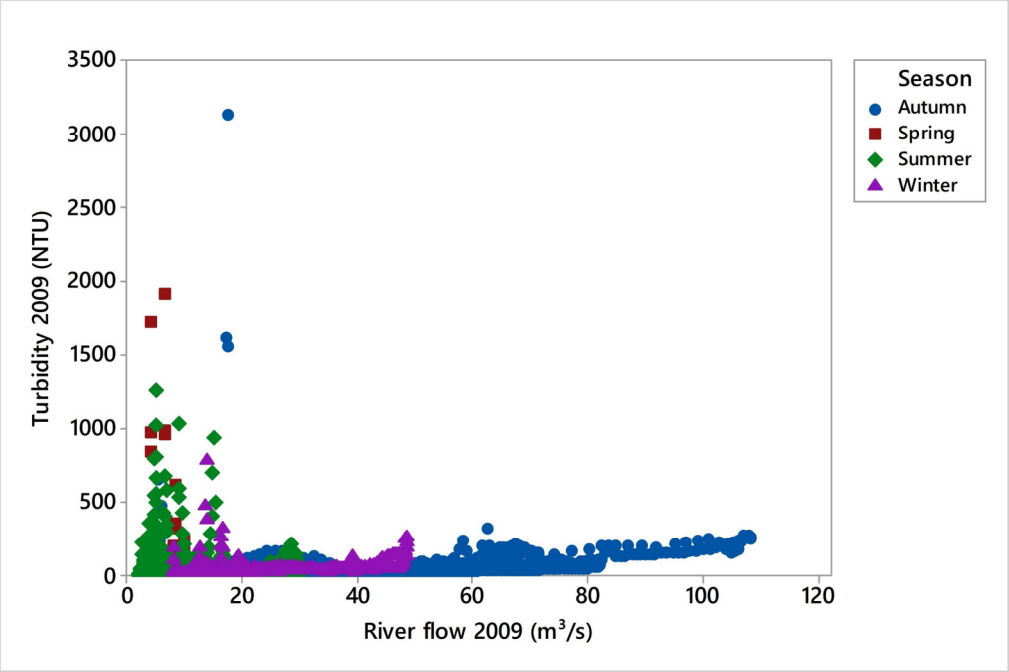


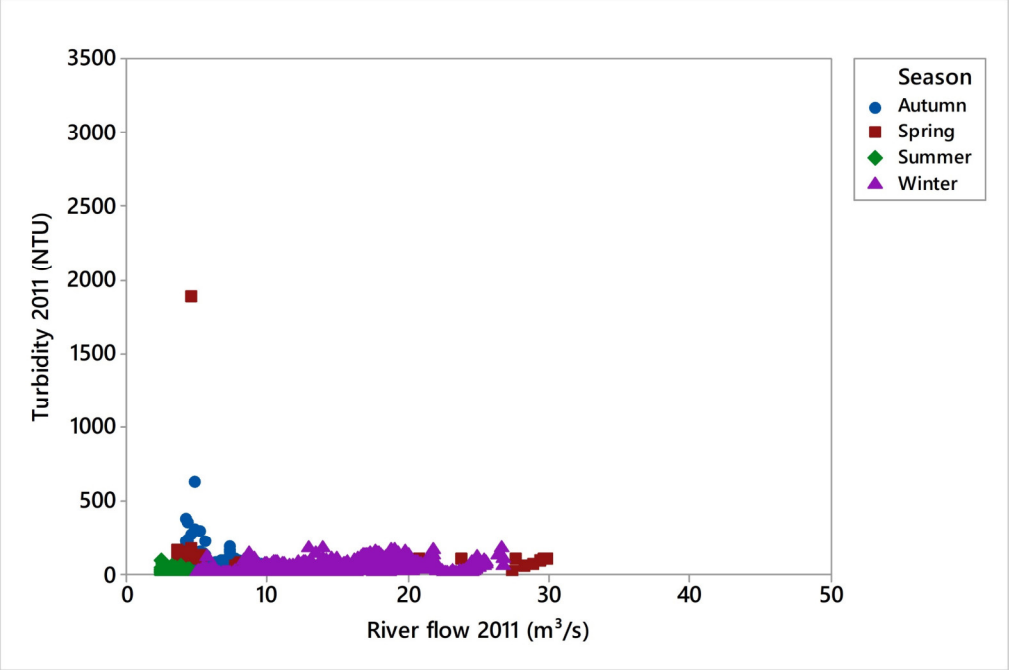

## 5. Scatter plot of chlorophyll-a against river flow 2009 and 2011

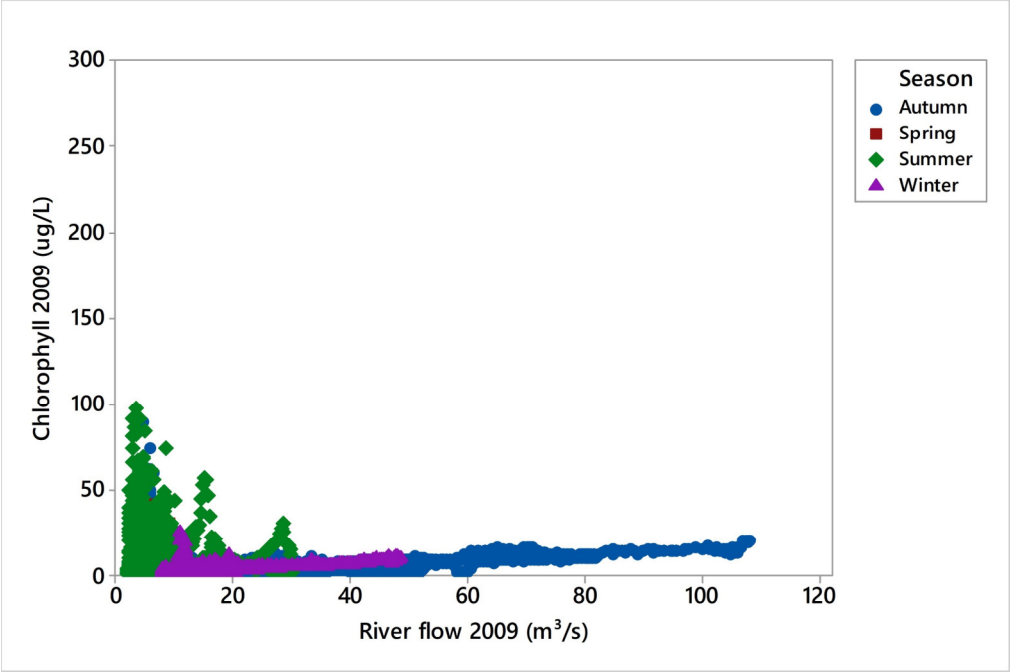


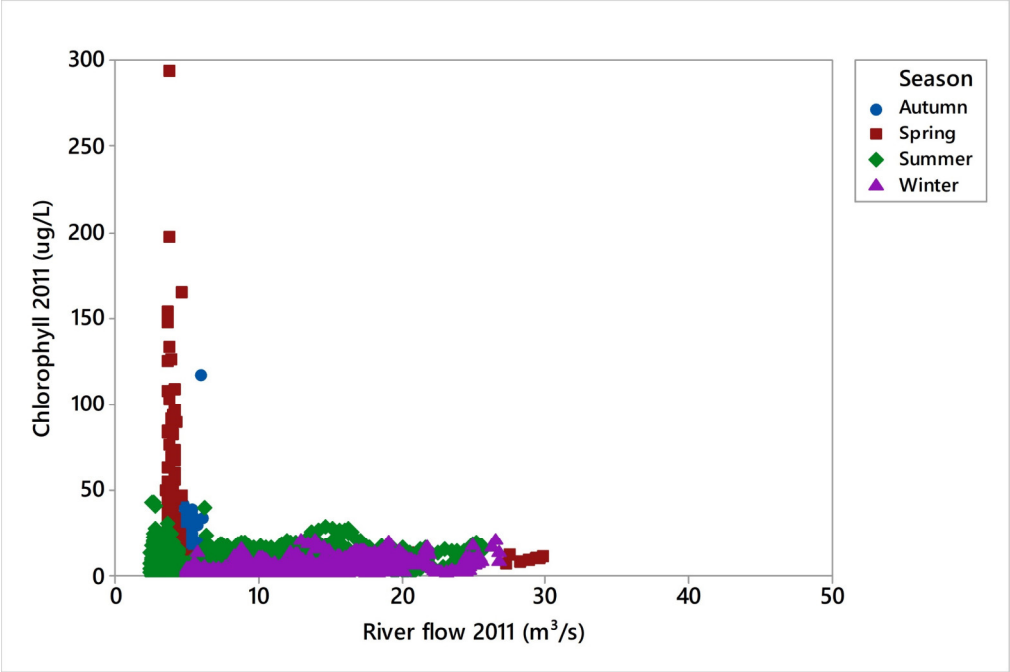

## 6. Scatter plot of temperature against chlorophyll-a 2009, 2010, 2011, 2013

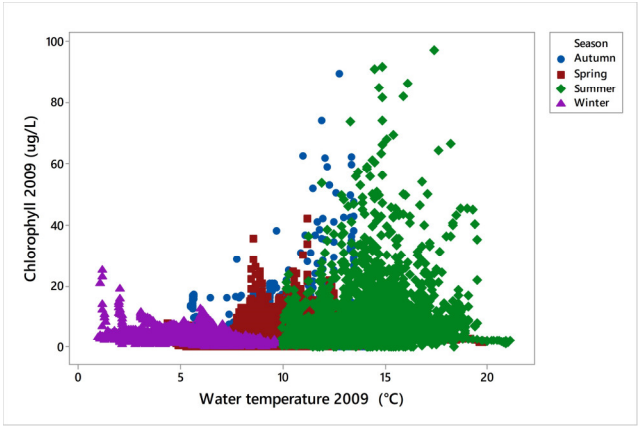


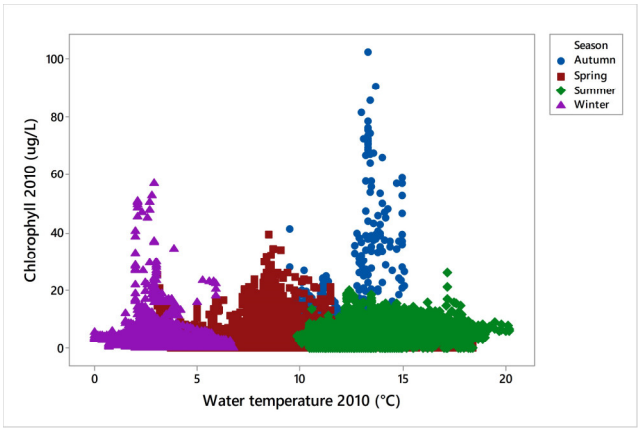


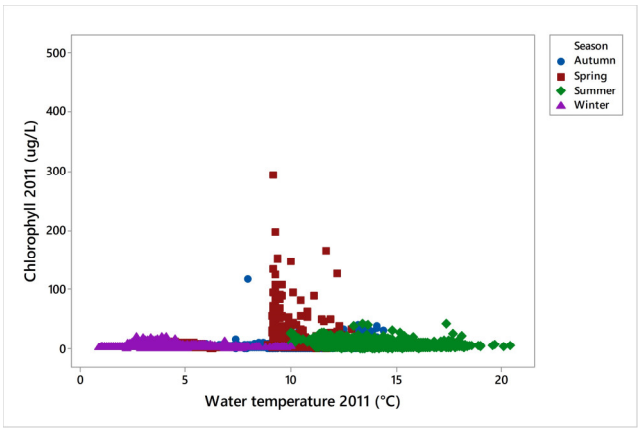


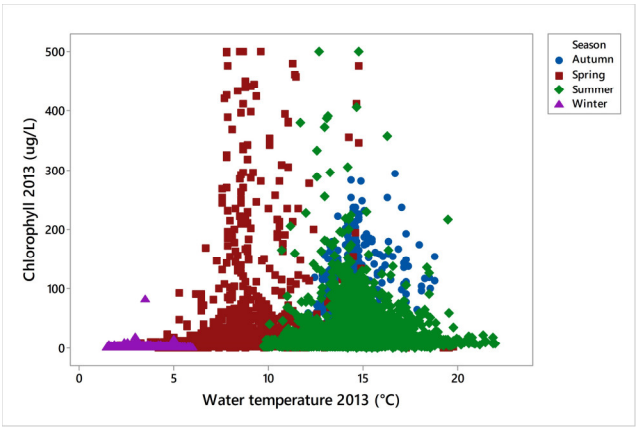

## 7. Scatter plot of pH against chlorophyll-a 2009, 2010, 2011, 2013

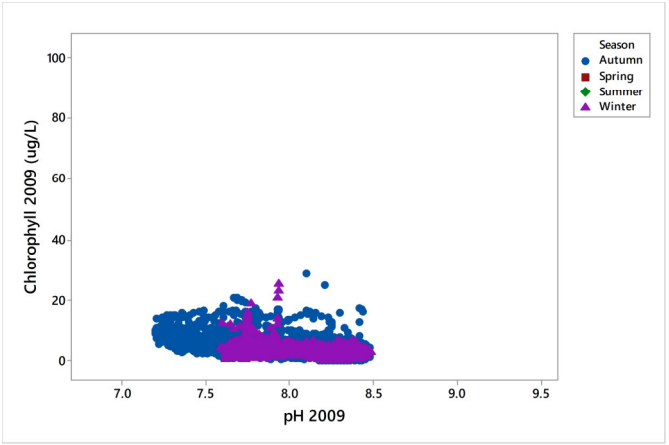


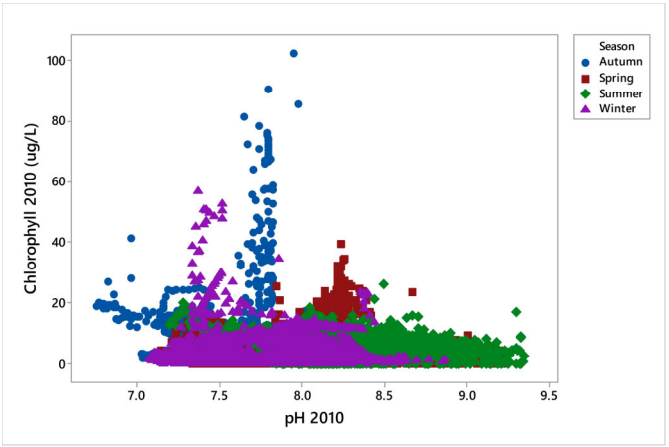


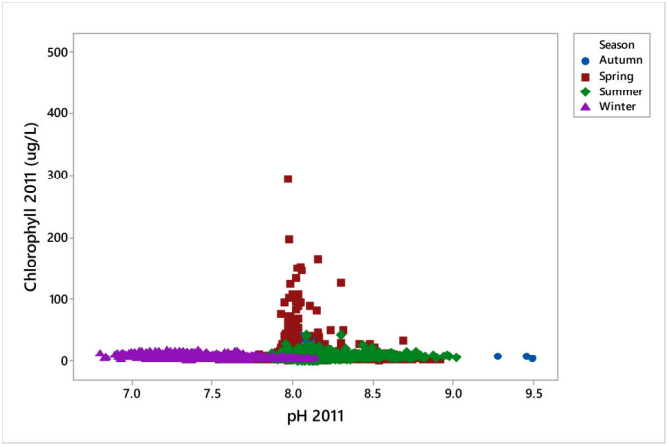


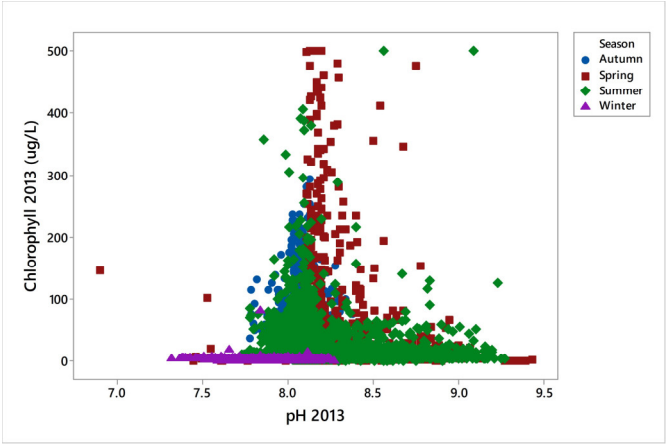

## 8. Scatter plot of DO against chlorophyll-a 2009, 2010, 2011, 2013

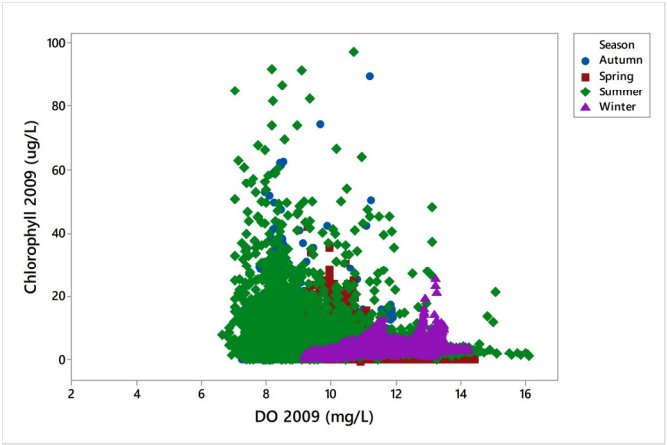


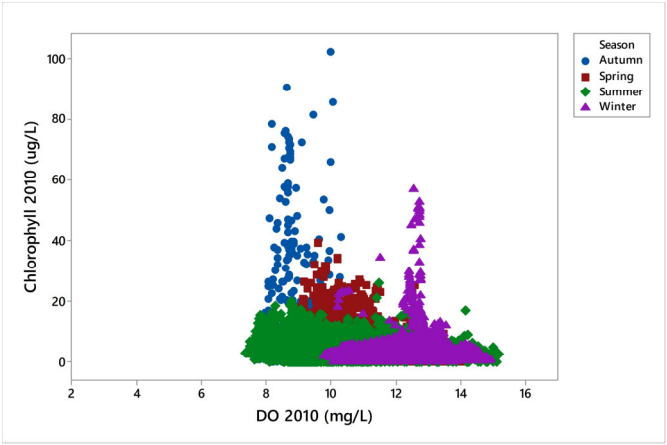


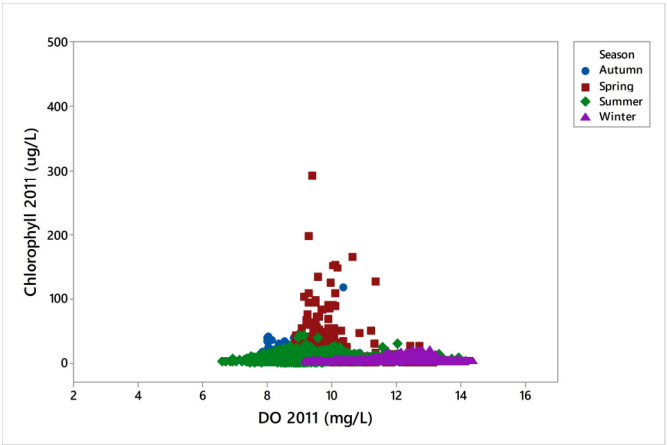


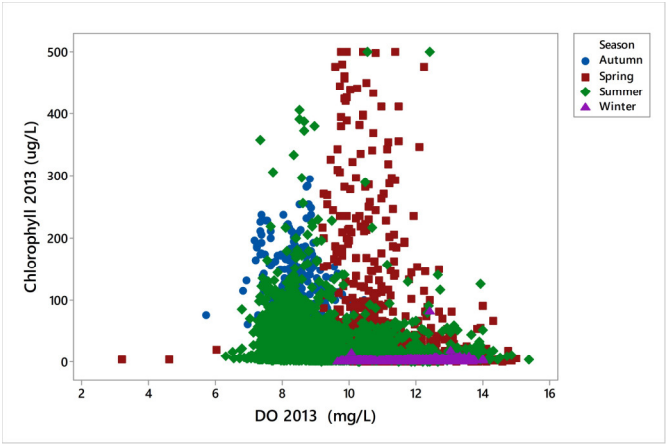

## 9. Scatter plot of turbidity against chlorophyll-a 2009, 2010, 2011, 2013

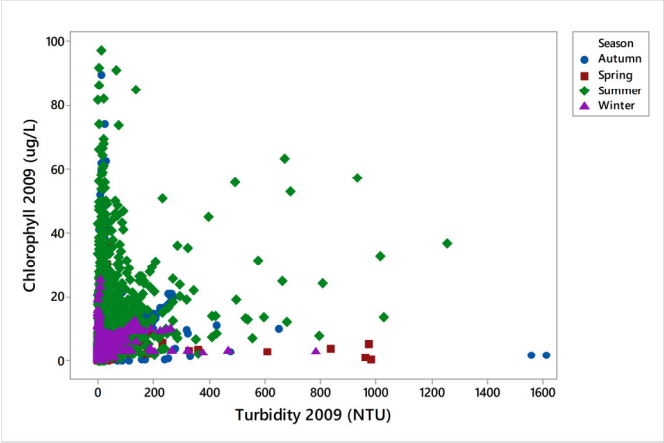


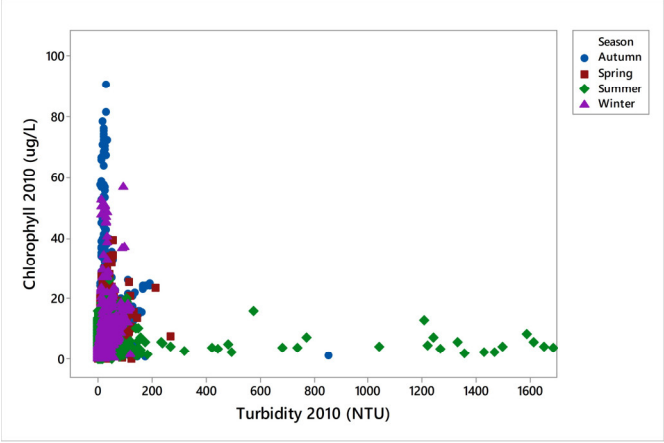


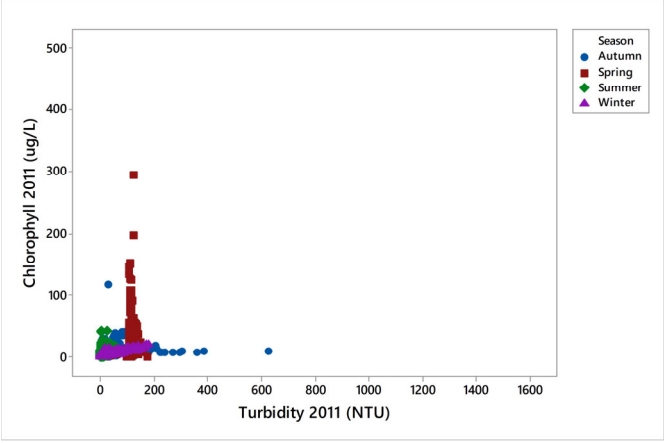


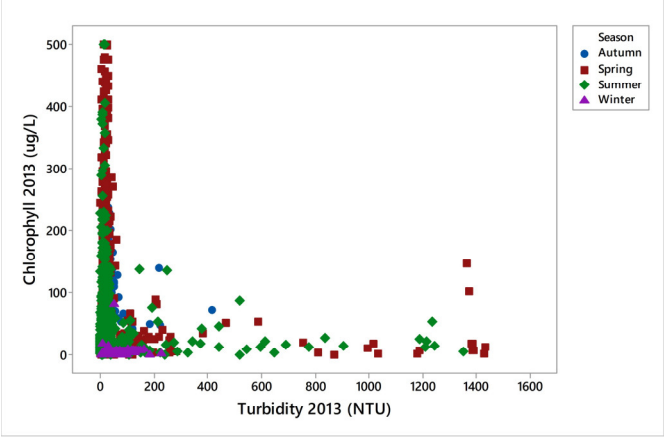

## 10. Scatter plot of turbidity against DO 2009, 2010, 2011, 2013

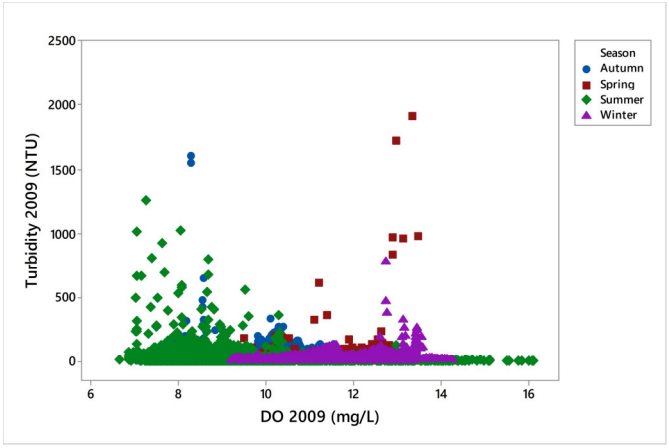


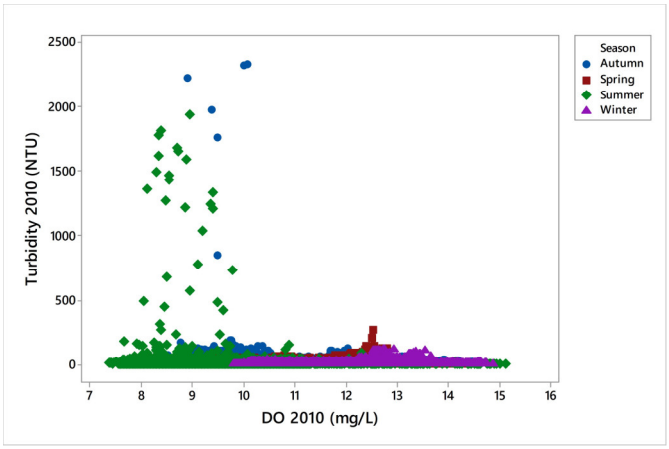


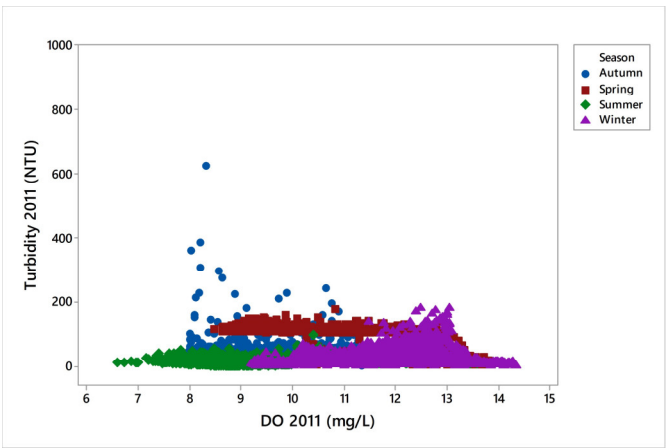


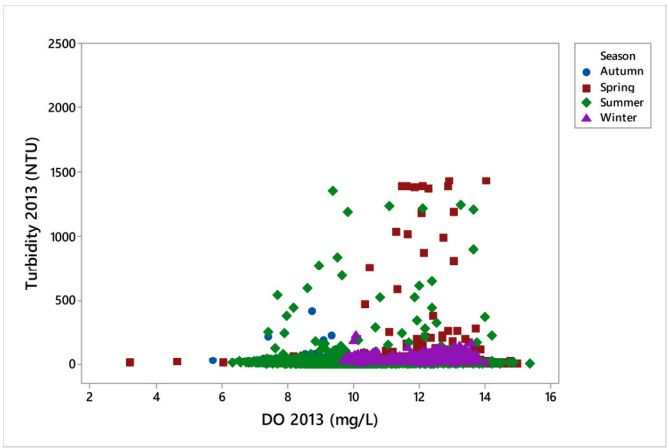

## 11. Scatter plot of NDVI against nutrient concentration 2009 and 2011